HIGH-TEMPERATURE CORROSION BEHAVIOR OF ALLOYS IN GASEOUS ENVIROMENTS WITH LOW-OXYGEN AND HIGH-SULFUR POTENTIALS

by

Xiaodan Wu

BS in Materials Science and Engineering,
University of Wuhan Science & Technology, Wuhan, China, 1998
MS in Materials Science and Engineering,
Pohang University of Science & Technology (POSTECH), South Korea, 2006

Submitted to the Graduate Faculty of

Swanson School of Engineering in partial fulfillment

of the requirements for the degree of

Doctor of Philosophy

University of Pittsburgh

2014

UNIVERSITY OF PITTSBURGH

SWANSON SCHOOL OF ENGINEERING

This dissertation was presented

by

Xiaodan Wu

It was defended on

December 17, 2013

and approved by

Judith C. Yang, PhD, Nickolas A. DeCecco Professor, Department of Chemical and Petroleum Engineering

Jörg M.K. Wiezorek, PhD, Associate Professor, Department of Mechanical Engineering and Materials Science

Guofeng Wang**,** PhD, Assistant Professor, Department of Mechanical Engineering and Materials Science

Dissertation Director: Brian M. Gleeson, Harry S. Tack Chair Professor, Department of Mechanical Engineering and Materials Science

HIGH-TEMPERATURE CORROSION BEHAVIOR OF ALLOYS IN GASEOUS ENVIROMENTS WITH LOW-OXYGEN AND HIGH-SULFUR POTENTIALS

Xiaodan Wu, PhD

University of Pittsburgh, 2014

To seek a better understanding of the compositional and environmental factors affecting the corrosion behavior of alloys in sulfur-rich atmospheres at temperatures above 600^{o}C, relevant to advanced combustion systems for power generation, eight chromia-scale-forming commercial alloys were tested at 750^{o}C in gases with a base composition of N_2-15%CO-3%H_2-0.12%H_2S. This base composition was made more oxidizing by introducing two different levels of water vapor, 0.6% and 3%, into the reaction gas. Five model alloys were also prepared to study and verify the effects of major alloying elements, Cr, Co and Ni, on sulfidation resistance. The additional three model alloys were prepared to systematically study the effects of minor alloying elements Ti, Al and Mo. Finally, another group of three model alloys was made to study the individual effect of titanium on sulfidation resistance.

All alloys eventually exhibited breakaway behavior. A protective Cr_2O_3 scale formed initially and then broke down. The mechanistic process of the breakaway corrosion was assessed. As for the effects of major alloying elements, it was found that the alloys with a Ni/Co mass ratio near to unity had less weight gain and hence, superior sulfidation resistance. This is because when the Ni/Co ratio is near unity, Ni and Co availability are both sufficiently low to suppress their external sulfidation and consequently extend the incubation period. In the range of the alloys studied, 10-40wt.%Co, weight gain decreased with an increase in the alloy cobalt content. Similarly, weight gain decreased with an increase in alloy chromium content in the range of 19-

28wt.%. Nickel was found to have a detrimental effect by increasing the tendency to form a liquid reaction product. This tendency increased with increasing nickel content in the alloy.

Besides major alloying elements, the judicious addition of minor alloying elements, Al, Ti and Mo, was found to have a significant effect to improve sulfidation resistance. This is because the minor additions promoted the formation of an oxide-enriched scale layer-comprised of Al_2O_3 and oxides containing Cr and Ti. This oxide-enriched scale layer was inferred to have inhibited the outward diffusion of base-metal elements, thus mitigating external sulfidation and consequently internal corrosion. It was found, based on the model alloys study, that remarkable sufidation resistance could be conferred to an alloy by maintaining an Ni/Co mass ratio near unity, and adding minor amounts of Al, Ti and Mo. A particularly sulfidation-resistant model alloy had the compostion of 33.1Ni-22Cr-34.9Co-2.5Al-2.5Ti-5Mo (in wt.%).

The individual effect of titanium was found to promote oxide-scale formation by shifting the kinetic boundary to a lower oxygen partial pressure. Titanium was observed to exist with Cr as complex oxides, which nevertheless acted as an effective barrier inhibiting the outward migration and subsequent external sulfidation of the base-metal elements.

In addition to the effects of major and minor alloying elements on sulfidation resistance, the mechanisms associated with the sometimes observed formation of whiskers, voids and nodules were assessed.

In the second part of this thesis, alloys Fe-30wt.%Mo-5wt.%Al and Fe-30wt.%Mo-10wt.%Al were studied in a simulated syngas atmosphere. It was found that alloy Fe-30Mo-10Al had better sulfidation resistance than conventional Ni-Cr-Co high-temperature alloys. The good corrosion resistance was attributed to the formation of a very thin Al_2O_3 layer on the surface of

the alloy, identified by XPS analysis. The effect of Al level on sulfidation resistance was also studied and explained.

TABLE OF CONTENTS

LIST OF TABLES

LIST OF FIGURES

ACKNOWLEDGEMENTS

I wish to offer my most sincere appreciation to my supervisor, Professor Brian Gleeson, for providing me the opportunity to study for a PhD degree in his well-established laboratory. I feel in great debt for the tremendous time he has spent in the direction of this study. I am extremely grateful for his patience, understanding, tolerance, and most importantly, his encouragement and scientific input which were invaluable during the course of my study. It was in such a flourishing research atmosphere that I was able to enjoy even the sometimes unbearable grind of my research study. His disciplined and exacting approach to scientific research has deeply influenced me and has become the main principles of my scientific pursuit. I also would like to thank Dr. Judith C. Yang, Dr. Jörg M.K. Wiezorek and Dr. Guofeng Wang for their sincere help with my academic advances.

I would like to thank Dr. James B. Miller at CMU for his help with the XPS analysis, and Mr. Albert Steward and Mr. Cole M. Van Ormer for their help with the SEM characterization. I also would like to thank Dr. Vinay Deodeshmukh at Haynes International for providing alloys and for insightful technical input.

Special appreciation is to Dr. K. Goldman for his generous help improving my English and my thesis writing. I would like to thank all my lab students and friends for their encouragement and many insightful discussions on some experimental or thesis work.

Finally, I would also like to thank my family members who motivated me to study abroad, shared all my feelings and sacrificed for my study. In particular, sincere appreciation is extended to my parents for their always unselfish and unrequited support and to my sister for her encouragement. Last but not the least, I want to express my thanks to my husband, Weiguo, and my son, Suhang, for their encouragement and expectations which always inspire me to face and overcome any difficulties. This work is dedicated to them.

1.0 INTRODUCTION

Since the energy crisis in the 1970s and subsequent price rise in the cost of fossil fuels, great efforts have been made to increase the efficiency of fossil-fuel burning power plants by increasing their operating temperature. The current operating temperature of the most efficient fossil-fueled power plants is around 600^{o}C, however, it is predicted that the operating temperature will increase by another 50 to 100^{o}C in the next 30 years[1]. Besides the effort to improve efficiency by increasing the operation temperature, environmental safeguards, such as reducing the emission of NO_x, have also been implemented in recent years[2]. Combustion at high temperature and low oxygen partial pressure is done to reduce the emission of NO_x. A low NO_x atmosphere usually contains about 15% carbon monoxide, 3% hydrogen, 0.12% hydrogen sulfide and 3% steam and nitrogen[3] , resulting in a very low oxygen partial pressure of about 10^{-20} atm, which is "reducing" from the standpoint of iron and nickel oxidation (i.e., FeO_x and NiO formation is thermodynamically not possible). The existence of a reducing atmosphere in the burner prevents the formation of NO_x. However, sulfur in the coal reacts to form H_2S under such conditions, which can accelerate the corrosion rate of the waterwall tubes, leading to a significant increase in structural materials wastage [3]. In addition to the accelerated wastage, commonly used overlay alloys, such as 309 stainless steel and alloy 622, also show circumferential cracking due to preferential sulfidation attack [4-6]. Some

Thyssenkrupp VDM alloys, such as Alloy 33, 50 and 59, were studied under this kind of atmosphere[3], but results on other commercially available alloys are generally limited. Some efforts conducted many decades ago, such as those stemming from EPRI and COST programs[7], have studied the available materials used at about 600^{o}C in the operating environments which have a combination of very low oxygen partial pressure and relatively high sulfur partial pressure. In general, however, there remains very limited understanding of corrosion processes of alloys exposed to environments relevant to low NO_x combustion systems, particularly at temperatures above 600^{o}C. To that end, the operation of fossil power plant at higher temperatures in the near future needs much more reliable guidance for material selection and alloy design.

Accordingly, the first aim of this thesis study is to seek a better understanding of the environmental and compositional factors affecting the corrosion behavior of some commercial alloys at temperatures above 600^{o}C. The results from this study will provide valuable guidance for material selection and design in the environments relevant to modern low-NO_x combustion systems. Model alloys will also be prepared to complement the testing and analyses of the commercial alloys.

As indicated above, most conventional oxidation-resistant alloys do not have acceptable sulfidation resistance under the condition where sulfidation is the favored mode of attack[8, 9]. This is because the sulfidation rate of most major metallic constituents in conventional high-temperature alloys are generally 10^4-10^6 times higher than their oxidation rate[10, 11]. The main reason for this is the greater extent of non-stoichiometry in sulfides compared with the oxides[12]. The defect concentration in common sulfides is orders of magnitude higher than in corresponding oxides.

Consequently, the diffusion through sulfide scales is very fast, and, hence, the growth rate of sulfides is fast. By contrast, a number of refractory metals, such as Mo and Nb, are highly resistant to sulfur corrosion, with the sulfidation rate comparable to the oxidation rate of Cr[13]. The excellent sulfidation resistance of refractory metals results from the very low deviations from stoichiometry, and thereby, the low defect concentrations in the sulfides of these metals. Research has shown that the predominant defects in these sulfides, as in refractory metal oxides, are S interstitials [12-14] . As a consequence, in contrast to common metals, sulfide scales on refractory metals grow relatively slowly by inward diffusion of sulfur. In 1974, Strafford et al.[15] was the first to systematically assess whether the addition of refractory metals is beneficial to the sulfidation resistance of the common base metal. Douglass and colleagues [11, 16-18] subsequently showed that refractory metal sulfides provide moderate protection when added to common base metals, cobalt, iron and nickel. A study by Kai and Douglass[19] assessed the effect of addition of Mo to pure iron over the temperature range 600-980^{o}C in a $H_2/H_2O/H_2S$ mixture having a sulfur pressure of 10^{-5}atm. The result showed that the addition of Mo can reduce the corrosion rate by about half an order of magnitude. However, even if the Mo content exceeds 30wt.%, the sulfidation rate of the Fe-Mo binary alloys cannot decrease further owing to the intercalated structure of MoS_2, which is consequently permeable to transition metals. Wang et al.[20] observed that there is a dramatic decrease in sulfidation rate when adding Al to an Fe-Mo alloy over the temperature range of 700-900 ^{o}C in 0.01atm sulfur vapor. The sulfidation rate of an Fe-Mo-Al alloy is even slower than that of pure Mo. The reason for this beneficial effect is

because of the formation of the spinel, $Al_xMo_2S_4$, which slows down the outward diffusion of the base-metal ions[20, 21].

However, all past research on the sulfidation of Fe-Mo-Al alloys was performed in sulfur vapor or H_2-H_2S mixed gas. Surprisingly, little work has been done in the past to investigate the corrosion behavior of Fe-Mo-Al alloys in other simulated high-sulfur and low-oxygen industrial atmospheres, such as syngas. Syngas, produced from coal gasification, is a mixture of gases, predominantly H_2S, CO, H_2, CO_2 and H_2O(g). There is variance in syngas compositions due to the differences in gasifier type, feedstock and operation parameters. A recent NETL study[22] provides the range of syngas compositions produced in various gasifier types.

Related to syngas technologies, hydrogen separation provides a pathway for economical hydrogen production. At present, the commonly used metallic materials for membranes are pure metals, such as palladium, vanadium and tantalum, or binary alloys of palladium, such as Pd-40Cu and Pd-23Ag[23]. They are not only expensive, but also susceptible to contaminants commonly found in syngas, sulfur in particular. Therefore, it would be greatly significant to find cheaper functional materials which have both good corrosion resistance and permeability to hydrogen. The Department of Energy (DOE), Energy & Environmental Research Center (EERC) and National Center for Hydrogen Technology (NCHT)[24-29] have been doing research to identify viable new hydrogen separation materials. However, little research has been done on the Fe-Mo-Al alloy, so it is highly worthwhile to investigate whether such an alloy system can offer a simple and inexpensive solution for hydrogen separation. Therefore, another goal of the current

study is to determine the possibility of functional usage of Fe-Mo-Al alloys as a membrane in syngas through studying their corrosion behavior.

2.0 BACKGROUND

Sulfur is generally present as an impurity in fuels or feed stocks. Sulfidation is a common corrosion attack. Many high-temperature commercial processes, such as oil refining, coal gasification and fossil-fuel conversion, contain both sulfur and oxygen. The high-temperature corrosion of metals and alloys in these oxidizing-sulfidizing environments has been reviewed by Gesmundo el al.[30], Stroosnijder and Quadakkers[31], Stringer[32] and Gleeson[10]. Sulfidation and oxidation have similar mechanisms, but they also have several differences. Firstly, sulfidation is more complex than oxidation because the number of stable sulfides is greater than that of the corresponding oxides. Secondly, the low melting point of some sulfide eutectics increases the complexity. For example, the melting point of the Ni, Co and Fe eutectic is 645^{o}C, 880^{o}C and 985^{o}C, respectively. The formation of liquid reaction products is catastrophic to corrosion resistance because they can penetrate down through the chromium oxide scale into alloy substrate, causing the early breakaway of the protective chromium oxide scale and severe internal corrosion. Furthermore, sulfidation rates of most alloying elements in high-temperature alloys are generally 10^4-10^6 times higher than their oxidation rate[10].

In environments with low-oxygen and high-sulfur potentials, sulfidation can be the main type of corrosion; although there can be a competition between sulfidation and oxidations since oxides are generally more stable thermodynamically than comparable

sufides. The following background consists of four topics: thermodynamic considerations, kinetic considerations, the effect of alloying elements on sulfidation resistance and test results of some high-temperature alloys.

2.1 THERMODYNAMIC CONSIDERATIONS

2.1.1 Gas phase equilibrium

Usually, the sulfidizing-oxidizing atmospheres can be classified into two types, SO_2 bearing gas (such as hot corrosion in gas turbines) and environments with low-oxygen and high-sulfur potentials. Many industrial atmospheres such as low NO_x burners in coal-fired boilers and coal gasification belong to the latter one. The two kinds of sulfidizing-oxidizing industrial operating conditions can be indicated in oxygen-sulfur-temperature diagram, as shown in Figure 2.1.

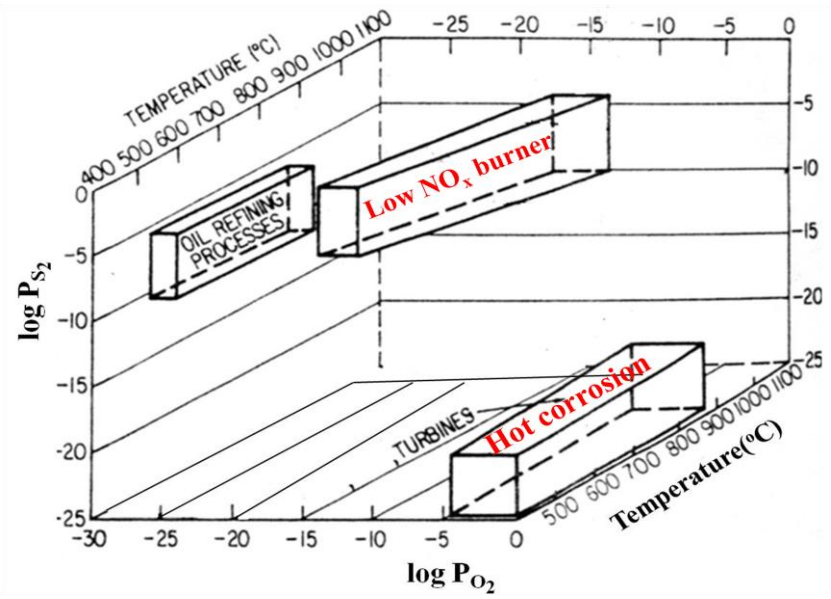

Figure 2.1 Oxygen-sulfur-temperature diagram indicating some industrial operating conditions[33]

The atmosphere with low-oxygen and high-sulfur potentials is of primary interest in this thesis study. It usually contains H_2O (g), H_2, H_2S and CO. It can be characterized by equilibrium partial pressures of oxygen (P_{O2}) and sulfur (P_{S2}), which are determined by the reaction (2.1) and (2.2), respectively.

$$H_2 + \frac{1}{2} O_2 = H_2O \tag{2.1}$$

$$H_2 + \frac{1}{2} S_2 = H_2S \tag{2.2}$$

The condition for equilibrium is given by equation (2.3) and (2.4),

$$K_1 = \frac{P_{H2O}}{P_{H2}\sqrt{P_{O2}}} = \exp\left(-\frac{\Delta G_1^o}{RT}\right) \quad (2.3)$$

$$K_1 = \frac{P_{H2S}}{P_{H2}\sqrt{P_{S2}}} = \exp\left(-\frac{\Delta G_2^o}{RT}\right) \quad (2.4)$$

K_1 and K_2 are equilibrium constants of reaction (2.1) and (2.2), ΔG_1^o and ΔG_2^o are the standard Gibbs free energy change for reaction (2.1) and (2.2) in the unit of J/mole, respectively. R is the gas constant and T is the absolute temperature. From equation (2.3) and (2.4), equation (2.5) can be obtained.

$$\frac{P_{O2}}{P_{S2}} = \left(\frac{K_2}{K_1}\frac{P_{H2O}}{P_{H2S}}\right)^2 \quad (2.5)$$

The ratio of P_{O2}/P_{S2} can be the measurement of the aggressiveness of a given environment. The lower the ratio, the more aggressive is the atmosphere.

The equilibrium sulfur and oxygen partial pressures can be calculated under the assumption of equilibrium conditions and the law of mass action using standard thermodynamic software, such as HSC software[34]. The P_{O2} and P_{S2} of low NOx burners are about 10^{-20}atm and 10^{-7}atm, respectively. Base metal oxides such as NiO, FeO are not stable, thus the environment is reducing. However, the oxygen partial pressure is high enough for Cr_2O_3 to be thermodynamically stable.

2.1.2 Equilibrium associated with gas-solid reactions

When a metal is put in the environment with high-sulfur and low-oxygen potential, the sulfidation reaction may occur according to reaction (2.6),

$$\frac{x}{y}\mathrm{M} + \frac{1}{2}\mathrm{S_2} = \frac{1}{\mathrm{y}}\mathrm{M_xS_y} \qquad (2.6)$$

The condition for equilibrium is given by Equation (2.7),

$$\mathrm{K_6} = \frac{\left(\mathrm{a_{M_xS_y}}\right)^{\frac{1}{y}}}{(\mathrm{a_M})^{\frac{x}{y}}\,(\mathrm{P_{S2}})^{\frac{1}{2}}} = \frac{1}{\mathrm{P_{S2}^{1/2}}} \qquad (2.7)$$

K_6 is equilibrium constant of reaction (2.6), $a_{M_xS_y}$ and α_M are the chemical activities of M_xS_y (metal sulfide) and M (metal), respectively, and can be taken to unity in the standard state condition. Equation (2.7) defines the sulfur partial pressure for equilibrium between metal and metal sulfide. This pressure is called the sulfide dissociation pressure. When the sulfur partial pressure in the environment is higher than the sulfide dissociation pressure, sulfide will form. The same sort of analysis can be applied to the formation of oxides. An Ellingham diagram, as shown in Figure 2.2, can help determine whether the sulfur potential in an environment is high enough to form sulfides[35]. "The sulfur partial pressure in equilibrium with a sulfide (dissociation pressure of sulfide) can be read from Figure 2.2 by drawing a straight line from point S through the free-energy line of the sulfide phase through the temperature of interest, and intersecting with the P_{S2} scale. The intersection at the P_{S2} scale gives the sulfur partial

pressure in equilibrium with the sulfide phase"[36]. For example, the dissociation pressure of CrS at 800 ^{o}C is indicated by the point 1 in Figure 2.2. An Ellingham diagram can also help to determine the relative stability of metal sulfides. The lower the free energy line the more stable is the sulfide. For example, Ni_3S_2 is less stable than FeS and CrS.

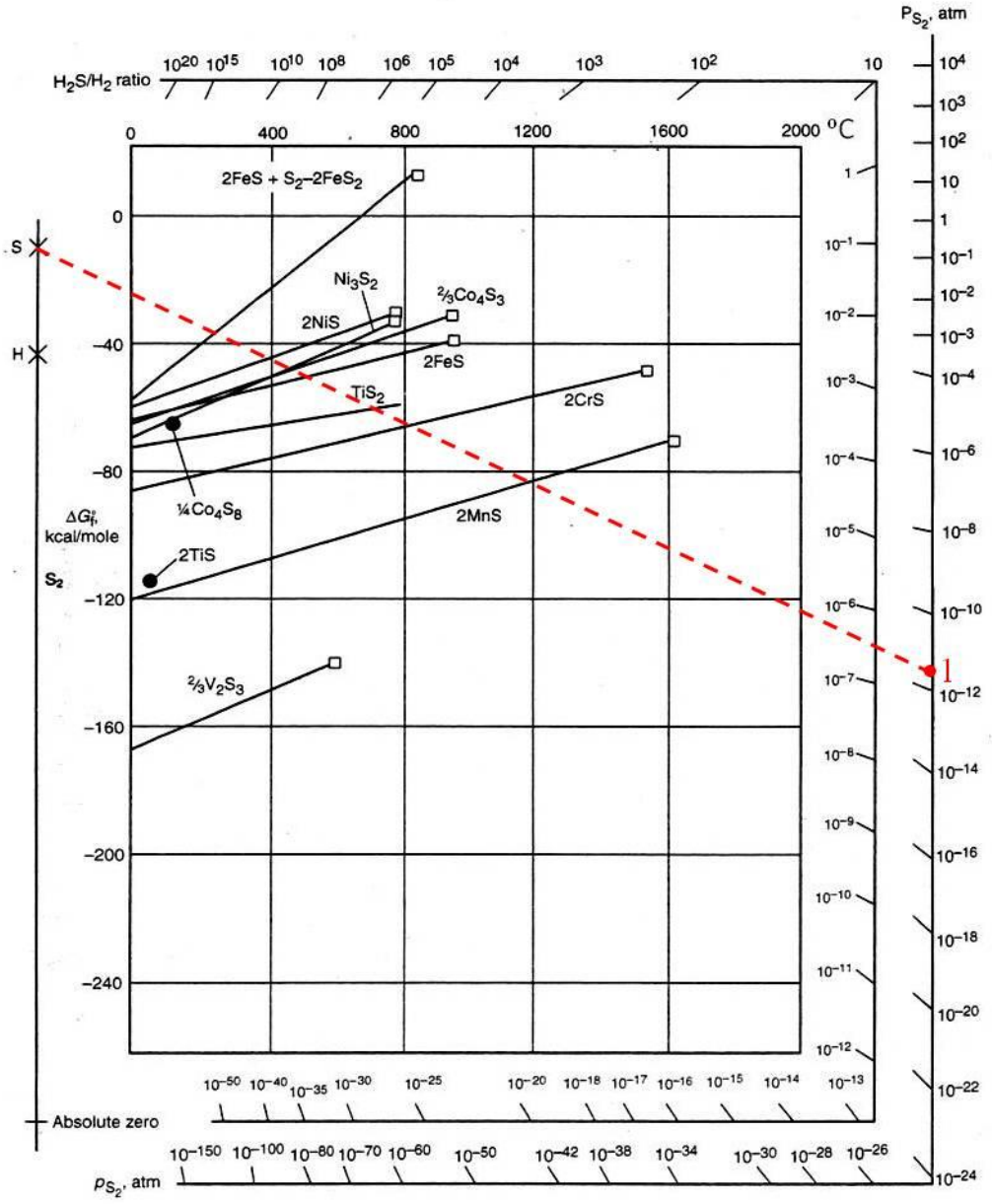

Figure 2.2 Standard free energy of formation of selected sulfides[35]

2.1.3 Stability diagrams

The thermodynamic relationship between the oxidants, such as oxygen and sulfur, and the metal can be expressed in the metal-oxygen-sulfur stability diagram. Perkins[37] , Hemmings and Perkins[38] discussed how the stability diagram can be used to aid the understanding of the corrosion behavior of metals in the environment containing both sulfur and oxygen.

The stability diagram for a metal, M, exposed to an atmosphere containing sulfur and oxygen, can be determined by considering the reactions as follows.

$$\mathrm{M} + \frac{1}{2}\,\mathrm{O_2} = \mathrm{MO} \tag{2.8}$$

$$\mathrm{M} + \frac{1}{2}\,\mathrm{S_2} = \mathrm{MS} \tag{2.9}$$

$$\mathrm{M} + \frac{1}{2}\,\mathrm{S_2} = \frac{1}{2}\mathrm{O_2} + \mathrm{M} \tag{2.10}$$

From reaction (2.8) and (2.9), dissociation pressure for M and MO, M and MS equilibrium can be obtained. From reaction (2.10), we know that the transition from oxidation to sulfidation should occur when:

$$\left(\frac{\mathrm{P_{O2}}}{\mathrm{P_{S2}}}\right)^{\frac{1}{2}} < \mathrm{K_{10}} \tag{2.11}$$

Where K_{10} is the equilibrium constant of equation (2.10). From equation (2.11), the thermodynamic boundary between sulfide and oxide in the Metal-S-O stability diagram can be determined.

Figure 2.3 is the stability diagram of the metal-S-O system. This is a simplified stability diagram; a complete diagram should include sulfates. However, only the simple diagram is discussed here since sulfate does not form in the gas atmosphere studied in this thesis. The atmosphere covered by the present study is located in the upper right area. Some industrial atmospheres, such as low NO_x burners and coal gasification, are located in this region. In the upper left region, sulfides are stable phases since the oxygen partial pressure in this region is too low to stabilize chromium oxides. The sulfur vapor and H_2-H_2S mixtures are located in this region.

The lines representing equilibrium between metal and metal sulfides, metal and metal oxide, metal sulfide and metal oxide are labeled in the figure. The equilibrium boundary between metal sulfide and oxide is called the thermodynamic boundary, as shown in Figure 2.3.

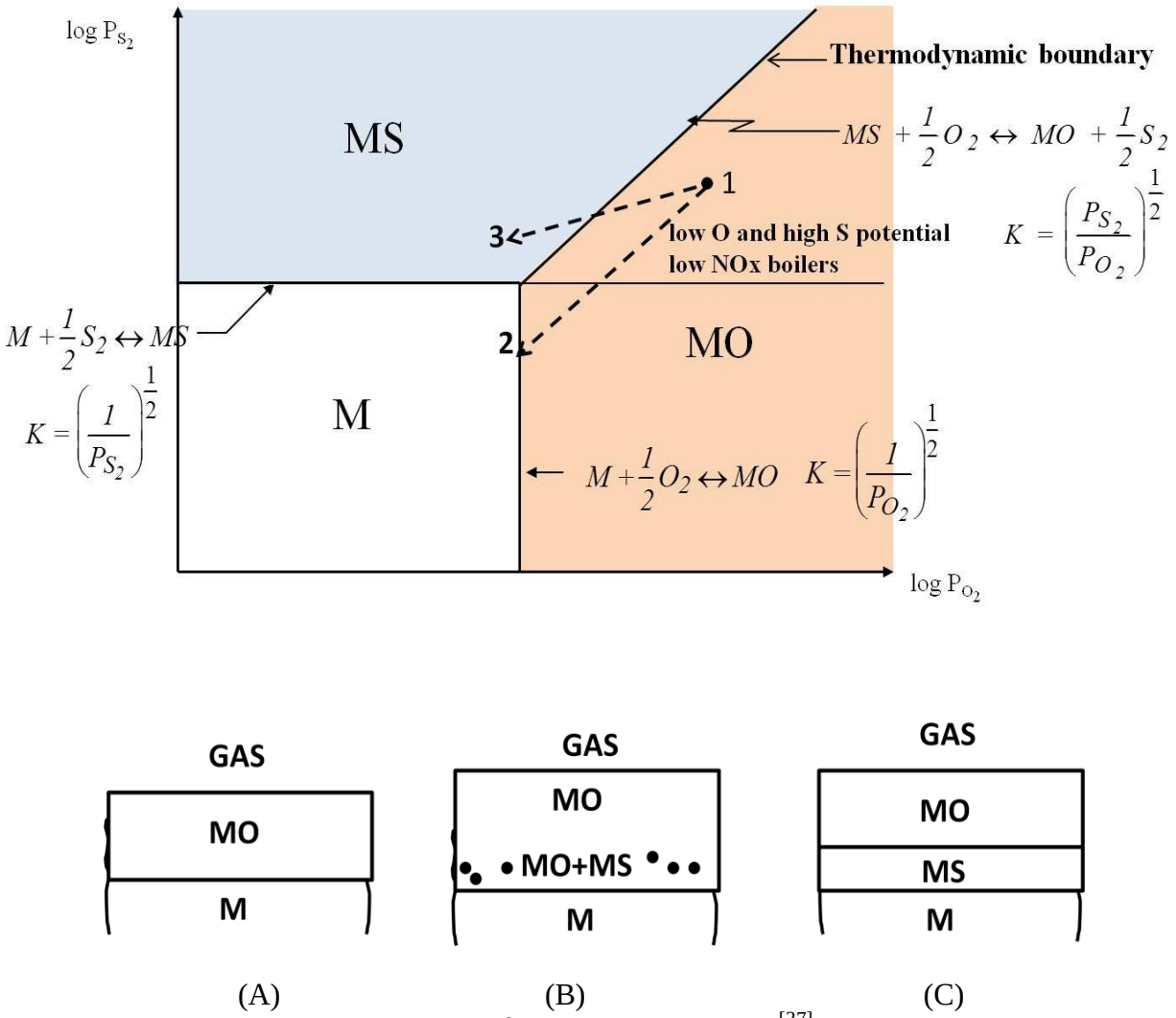

Figure 2.3 Schematic stability diagram for the M-S-O system[37] and possible reaction paths and products for a pure metal

The possible corrosion products cannot be predicted only by a stability diagram. Some kinetic factors are also important. Kinetic factors greatly influence the corrosion behavior of high-temperature alloys. They affect not only the reaction rate but also the morphology of the corrosion products. Due to kinetic factors the corrosion products formed may be different from what is predicted by thermodynamics. For example, a pure

metal exposed to a gas composition 1 in Figure 2.3 can form several types of corrosion products depending on the activity gradient of oxygen and sulfur developed in the surface scale. Since gas composition 1 is located in the metal oxide stable regime, the oxide of the metal will form. If the oxide is a good barrier to sulfur and oxygen, the activities of oxygen and sulfur will decrease rapidly through the scale from the surface to the scale metal interface along a reaction path from "1" to "2" in Figure 2.3. The sulfur activity at the scale/metal interface, as represented by point 2, is so low that metal sulfide cannot form beneath the oxide scale or internally in the metal. The scale structure is shown in Figure 2.3(A). If the oxide is not a good barrier to sulfur, the activities change along path "1" to "3" from the surface to the interface. In this case, metal sulfides form internally or as a sulfide layer beneath the oxide scale, as shown in Figure 2.3(B) and (C)[39].

The actual oxide to sulfide transition at a given P_{S2} actually occurs at a higher P_{O2} than that predicted from equilibrium calculations[40]. The experimentally determined boundary corresponding to a transition between sulfides and oxides is called the "kinetic boundary". Figure 2.4 shows the kinetic boundary for 310 SS at 875^{o}C .The actual P_{O2} values for the transition from chromium oxide to chromium sulfide formation are about three to four orders of magnitude higher than the equilibrium values. The location of the kinetic boundary depends on some kinetic factors such as: gas composition and flow rate, surface finish of the alloy, total pressure, and alloy composition. The gas flows through the testing system, the lower the flow rate, the closer to the equilibrium. At the surface of the reaction product, the dynamics is very different from that of the bulk gas. Theoretical prediction of the location of a kinetic boundary is currently not possible.

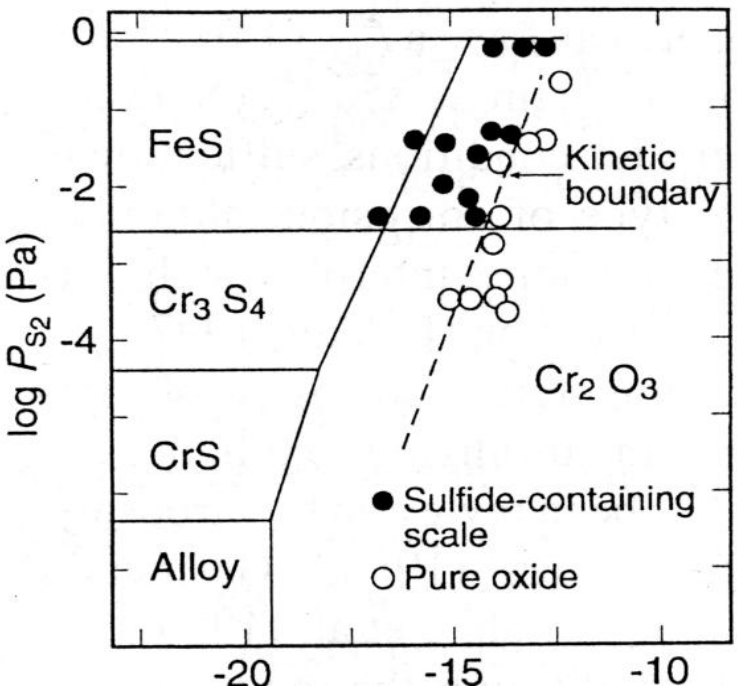

Figure 2.4 Kinetic boundary for 310 SS at 875°C

Why does the actual oxygen partial pressure to form chromia scale deviate so much from the equilibrium oxygen partial pressure of M and MO equilibrium? One explanation is the solid solution effect[41]. The other explanation is the reduction of sulfide activity to less than unity[42]. Another reason might be that the dissociation of H_2S is much easier than that of H_2O because the H-S bonding is weaker than the H-O bonding, reflected by the lower standard free energy of formation of H_2S compared to that of H_2O[43]. All these possible and proposed explanations reflect the fact that there is not a complete understanding of why the formation of MO occurs at higher oxygen partial pressure than that of M/MO equilibrium.

2.2 KINETIC CONSIDERATIONS

Although the thermodynamic considerations as discussed in the previous part are undoubtedly useful in the analysis of the likely mode of corrosion of a given alloy, kinetic factors such as diffusivity of the different alloying elements will influence the suitability of a material for long-term application.

In the absence of liquid formation, like oxides, most sulfide scales grow according to the parabolic rate law, reflecting rate control by solid-state diffusion. However, the sulfidation rate constants for most metals are much higher than their oxidation rate, as shown in Figure 2.5. This is because sulfides have the greater extent of non-stoichiometry than oxides, meaning that a higher defect concentration exists in common sulfides than in the corresponding oxides, thus leading to the rapid growth rate of sulfide scales. Solid-state diffusion, kinetic rate laws, defect structures and transport properties of some common metals are covered in this section.

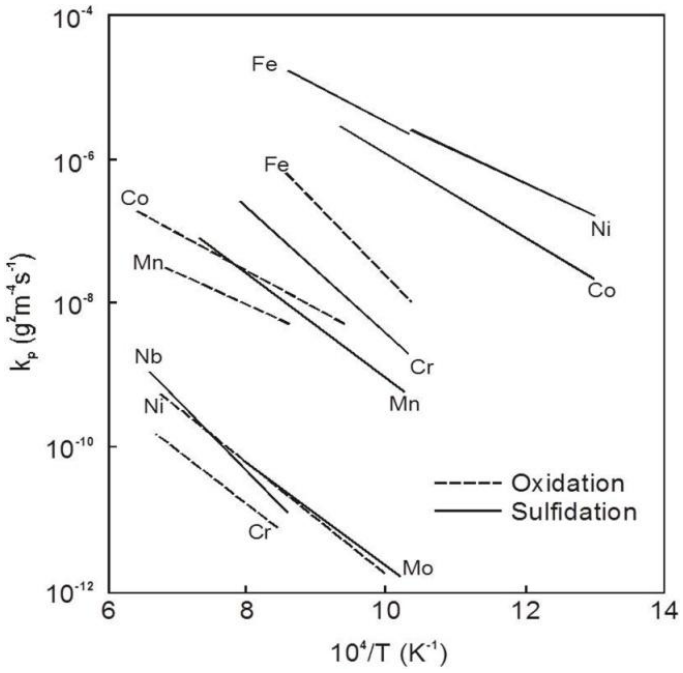

Figure 2.5 Collective plot of the temperature dependence of the sulfidation and oxidation rates of some metals[44]

2.2.1 Solid-state diffusion

In the solid state crystal, diffusion within the lattice occurs by either interstitial or vacancy mechanism and is referred to as lattice diffusion[45]. Atoms or ions are able to move because they vibrate around their mean position. The existence of point defects, such as vacancies and interstitials, permits the possibility for an atom to jump into an available lattice site. Figure 2.6 shows two common point defects in a pure, single-component solid: a vacancy and an interstitial atom.

Movement via vacancy mechanism is the most common way in which diffusion occurs. Clearly, diffusion by this way is proportional to the concentration of vacancies.

Another way of diffusion is by the movement of interstitial species to an adjacent interstitial site[46]. This is impossible in pure metals because the atoms are large, but operates for interstitial impurities such as C, H, N and O dissolved in metals. No matter which mechanism works, the concentration of defects is an important factor in the particle movement rate.

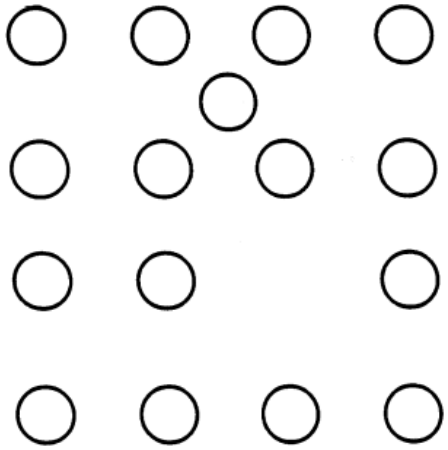

Figure 2.6 An vacancy and interstitial defect in a single-component crystal lattice

Self-diffusion in pure metals occurs via vacancies. It takes place in the absence of concentration (or chemical potential) gradient. This type of diffusion can be followed using radioactive isotopic tracers. The tracer diffusion is usually assumed to be identical to self-diffusion. In three dimensions, the diffusion coefficient can be related to the jump frequency of the atoms by Equation (2.12) that is

$$D_A^* = D_A = \frac{1}{6}\lambda\Gamma \qquad (2.12)$$

Where λ is jump distance, Γ is jump frequency. If an atom has enough thermal energy to overcome the activation energy barrier to migration, ΔG_m, it can make the

jump. The possibility of a successful jump is give by exp ($-\Delta G_m/RT$), the same for the case of interstitial migration. However, the adjacent sites are not always vacant. The possibility that an adjacent site is vacant is given by zX_v, where z is the number of the nearest neighbor, X_v is the possibility that a site is vacant, which is just the mole fraction of vacancies in the metal. Combining all these possibilities gives the possibility of a successful jump as Equation (2.13):

$$\Gamma = \nu z X_v \exp\left(\frac{-\Delta G_m}{RT}\right) \tag{2.13}$$

Where ν is vibration frequency of the atoms. If the vacancies are in thermodynamic equilibrium,

$$X_v = X_v^e = \exp\left(\frac{-\Delta G_v}{RT}\right) \tag{2.14}$$

Combining Equations (2.12), (2.13), (2.14) gives

$$D_A = \frac{1}{6}\alpha^2 z \nu \exp\frac{-(\Delta G_m + \Delta G_v)}{RT} \tag{2.15}$$

Substituting $\Delta G=\Delta H-T\Delta S$, and for most metals ν is ~10^{13}(S^{-1}). In fcc metals z=12 and $\lambda = a/\sqrt{2}$ the jump distance. Equation (2.15) can be rewritten as

$$D_A = D_o \exp\frac{-Q_{SD}}{RT} \tag{2.16}$$

Where $D_o = \frac{1}{6}\lambda^2 z \nu \exp\frac{\Delta S_m + \Delta S_v}{RT}$ and $Q_{SD} = \Delta H_m + \Delta H_v$.

Chemical diffusion occurs in a presence of concentration (or chemical potential) gradient and it results in net transport of mass. The diffusion coefficients for self-diffusion and chemical diffusion are generally different because the diffusion coefficient for chemical diffusion is binary and it includes the effects due to the correlation of the movement of the different diffusing species.

Defects in the solid-state crystals, such as dislocation, grain boundaries, and interfaces, have more open structures. As atom migration along these defects is faster than in the lattice, these defects become high-diffusivity paths. Figure 2.7[47] shows the diffusion results collected for NiO. Atkinson et al.[48] reported that the oxidation of NiO is controlled by the outward diffusion of Ni ions along grain boundaries in the NiO film at temperature below 1100°C. Whether the transport of atoms is via lattice diffusion or high-diffusivity path depends on temperature and grain size. Usually, small grain sizes and low temperature are favorable for grain boundary diffusion[47].

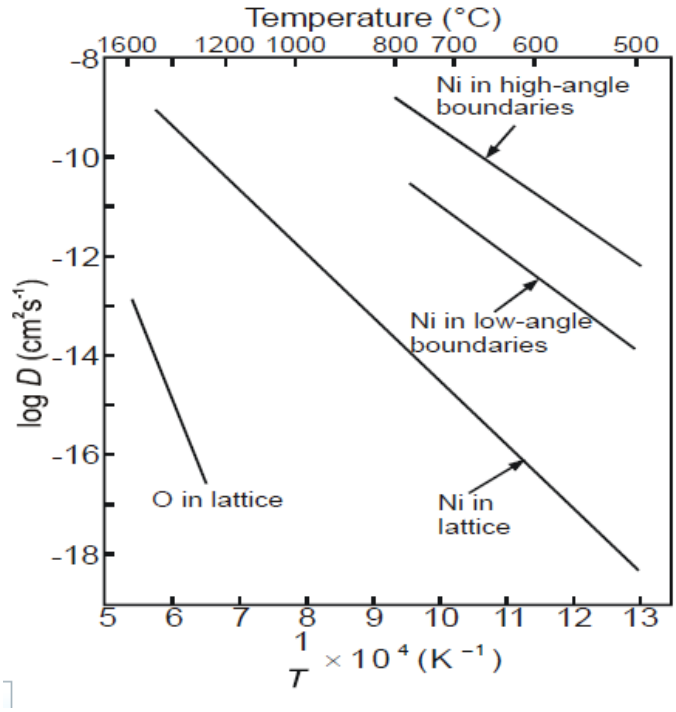

Figure 2.7 Transport paths for NiO[47]

2.2.2 Parabolic rate law and linear rate law

2.2.2.1 Parabolic rate law

When a metal is put in the sulfur-containing gas, the sulfide will form if the partial pressure of sulfur in the gas is above the dissociation pressure of the metal sulfide. When a sulfide layer develops to a relatively uniform thickness, its growth may be represented by a kinetic "law", typically parabolic for protective behavior, and linear for non-protective behavior. The two basic kinetic laws will be discussed in this part. Since sulfidation has similar mechanisms with oxidation, the growth of oxide can be used as an example to explain the growth process and rate.

Figure 2.8 is the schematic cross-sectional view of a growing oxide scale. The overall oxidation process includes the following steps [49].

(1) Delivery of oxidant to the scale-gas interface via transfer in the gas phase.

(2) Incorporation of oxygen into the oxide scale (scale gas interaction).

(3) Delivery of reacting metal from the alloy to alloy-scale interface.

(4) Incorporation of metal into the oxide scale.

(5) Transport of metal and/or oxygen through the scale.

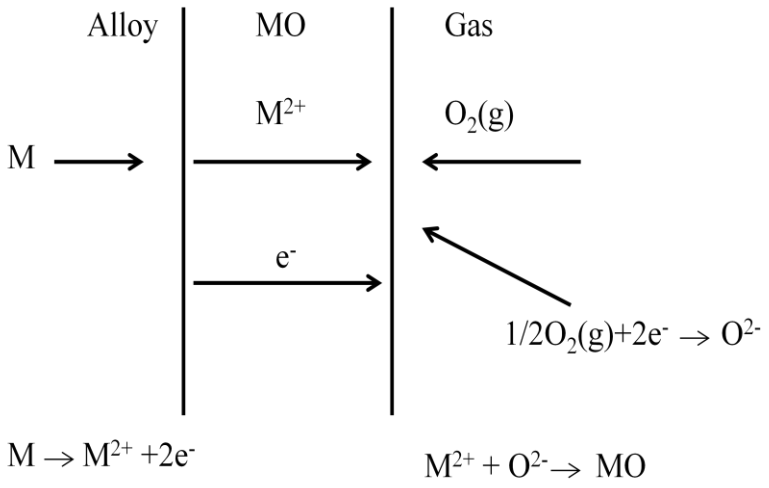

Figure 2.8 Reactions and transport processes involved in growth of an oxide scale

In step (1), the gas phase mass transfer rate can be calculated with the methods of fluid dynamics. In step (2), the surface chemistry can be used to analyze scale-gas interactions. In step (4), interfacial redox reactions are rapid and do not usually contribute to rate control. Although each step could become a rate-controlling process, step (3) and (5) related to the solid-state mass transfer by diffusion in the oxide and alloy, are commonly the rate control processes.

The parabolic rate law results, as shown in equation (2.18), when the growth rate of a compact scale is controlled by diffusion of some species through the scale. The concentrations of diffusing species at oxide-metal and oxide-gas interfaces are assumed to be constant. The diffusivity of the oxide layer is also assumed to be constant and therefore independent of composition. Increase in scale thickness, x, corresponds to an increase in the diffusion distance for O^{2-} and M^{2+}, so that,

$$\frac{dx}{dt} = \frac{k_p}{x} \qquad (2.17)$$

If no scale is present at t=0, this gives

$$x^2 = 2k_p t \qquad (2.18)$$

where k_p is the rate constant in the unit cm^2s^{-1}, and x=0 at t=0.

When weight change of the sample is measured,

$$(\frac{\Delta W}{A})^2 = 2k_w t \qquad (2.19)$$

K_w has the unit $g^2cm^{-4}s^{-1}$. For an oxide of stoichiometry M_xO_y, the relationship between k_p and k_w is

$$k_p = (\frac{V_{ox}}{16y})^2 k_w \qquad (2.20)$$

Figure 2.9 is the simplified diffusion model for mass transport through growing metal oxide scale. In the figure, C represents concentration of diffusing species, and C_1 and C_2 represent their boundary values.

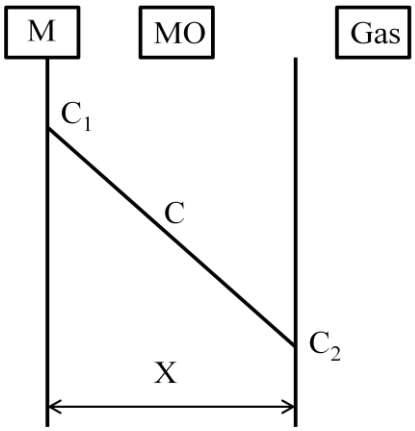

Figure 2.9 Simplified diffusion model for mass transfer through growing metal oxide scale

The rate of diffusion in one dimension is described by Fick's first law[50] as

$$J = -D\frac{\partial C}{\partial x} \qquad (2.21)$$

where J is flux, D is the diffusion coefficient and C is the concentration of a component. The partial derivation in Equation (2.21) is now approximated by the difference in boundary values

$$J = -D\frac{\Delta C}{\Delta x} = \frac{-D(C_2 - C_1)}{x} \qquad (2.22)$$

where C_1, C_2 are the diffusing component concentration at the scale-gas and scale-metal interfaces, respectively.

If diffusion is rate controlling, then the interfacial processes must be rapid and may be assumed to be locally at equilibrium. This is to say C_1, C_2 are time invariant. Equation (2.22 **(2.22)** is seen to be equivalent in the form to Equation (2.17), and we may write

$$k_p = \Omega D(C_1 - C_2) \qquad (2.23)$$

where Ω is the volume of oxide formed per unit quantity of diffusing species. Equation (2.23) was first derived by Wagner[51], who showed that the scaling rate was determined by oxide properties: its diffusion coefficient and its composition when at equilibrium with metal and oxidant. The rate constant by Wagner's theory of parabolic oxidation is

$$K_p = \frac{1}{RT}\int_{\mu_M''}^{\mu_M'} D_M d\mu_M \qquad (2.24)$$

Where D_M is the diffusion coefficient of metal through the scale, μ_M' μ_M'' are chemical potentials of metal at metal-scale and scale-gas interface.

2.2.2.2 Linear rate law

An oxidation process is controlled by gas-phase transport and /or phase boundary reaction in a certain stage before the transition to parabolic, solid-state diffusion controlled kinetics. The linear rate law, Equation (2.25), is usually observed at this initial stage of oxidation.

$$x = k_l t \qquad (2.25)$$

where k_l is the linear rate constant. The unit of k_l is cms^{-1} if scale thickness is measured, g $cm^{-2}s^{-1}$ if scale mass change is measured. Figure 2.10 shows the linear rate and parabolic rate regimes during oxidation of pure metal.

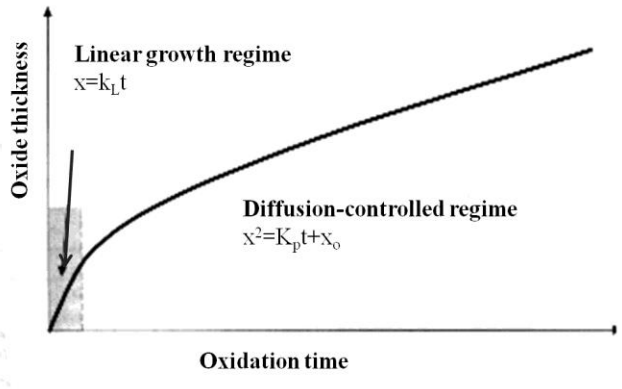

Figure 2.10 Illustration of the two oxidation rate regimes

In the initial stage of oxidation, the scale is so thin that diffusion through it is too fast to be rate limiting, and the phase boundary reaction is usually rate-controlling. In this case, the metal-oxide and oxide-gas interfaces cannot be assumed to be in equilibrium. It can be assumed that the reactions occurring at the metal-scale interface is fast and the process occurring at the scale-gas interface is rate controlling.

At the scale-gas interface, the processes of phase boundary reaction can be broken down into several steps, as shown in Equation (2.26), when oxygen molecules are the active oxidizing species in the gas phase. Step (1) shows that the adsorbed molecules split to form adsorbed oxygen, step (2) expresses that the adsorbed oxygen attracts electrons from the oxide lattice to become chemisorbed, step (3) means that the chemisorbed oxygen incorporates into the lattice.

$$\frac{1}{2}O_2(g) \underset{(1)}{\rightarrow} \frac{1}{2}O_2(ad) \underset{(2)}{\rightarrow} O(ad) \overset{e^-}{\underset{(3)}{\rightarrow}} O^-(chem) \overset{e^-}{\underset{(4)}{\rightarrow}} O^{2-}(latt) \qquad (2.26)$$

An example of linear rate law is oxidation at very high temperature in a dilute oxygen gas mixture. In this case, the surface process, such as molecular dissociation to produce adsorbed oxygen, $CO_2(g)=CO(g)+O(ad)$, is rate controlling.

2.2.3 Physicochemical properties of metal sulfides

The general properties of metal sulfides, and their non-stoichiometry, lattice defects and transport properties, have been reviewed by Rao and Pisharody[52], Mrowec and Przybylsk [13],[44].

Since the sulfur ions are larger than O^{2-}, this leads to M-S bond lengths larger than the corresponding M-O distances. Sulfides have smaller lattice energy than oxides, which is reflected in the lower free energy for the sulfide formation (as shown in Table 2.1) and generally lower melting points of sulfides (as shown in Table 2.2). The low stability of sulfides means that point defects are easily created.

Table 2.1 Free energy of formation for sulfides and oxides at 750^{o}C (KJ/ mole metal)

Sulfide	-ΔG	Oxide	-ΔG
FeS	96.8	FeO	197.6
NiS	65.3	NiO	146.6
CoS	77.9	CoO	161.9
Cr_2S_3	158.8	Cr_2O_3	432.7
MnS	210.0	MnO	309.7
MoS_2	212.0	MoO_2	402.2
TiS	247.8	TiO	444.2
TiS_2	357.9	TiO_2	758.6

Table 2.2 Melting points of some sulfides, oxides and metal-sulfide eutectics [53-58]

Sulfide	Melting point (K)	Oxide	Melting point (K)
TiS	2273	TiO	2023
La_2S_3	2353	La_2O_3	2490
Ce_2S_3	2333	Ce_2O_3	1963
NbS_2	?	NbO_2	2353
ThS_2	2198	ThO_2	3323
US_2	2123	UO_2	3113
Y_2S_3	1873	Y_2O_3	2683
CrS	1823	Cr_2O_3	2607
Cr_2S_3	?	MoO_2	2200
MoS_2	1431	MnO	2058
MnS	1598[b]	FeO	1697
FeS	1468	Cu_2O	1515
Cu_2S	1403	CoO	2083
CoS	1373	Al_2O_3	2319
Al_2S_3	1373	In_2O_3	2273
In_2S_3	1326	NiO	2230
NiS	1083	InO	1325
Ni_3S_2	1061		
InS	965		
Metal sulfide eutectics			
Mn-MnS	1513		
Cu-Cu_2S	1343		
Fe-FeS	1258		
Co-Co_4S_3	1153		
Ni-Ni_3S_2	918		

2.2.3.1 Defect structure

The deviations from stoichiometry and semiconducting properties have been investigated in many sulfides. Figure 2.11 shows a comparison of the non-stoichiometry of some sulfides and oxides. As shown in this figure, common metal sulfides have greater non-stoichiometry than oxides, so the defect concentration of metal sulfides is significantly higher than that in corresponding oxides. However, FeS and MnS are the exceptions.

$Fe_{1-y}S$ and $Fe_{1-y}O$ have similar non-stoichiometry while $Mn_{1-y}S$ shows smaller degree of non-stoichiometry than $Mn_{1-y}O$.

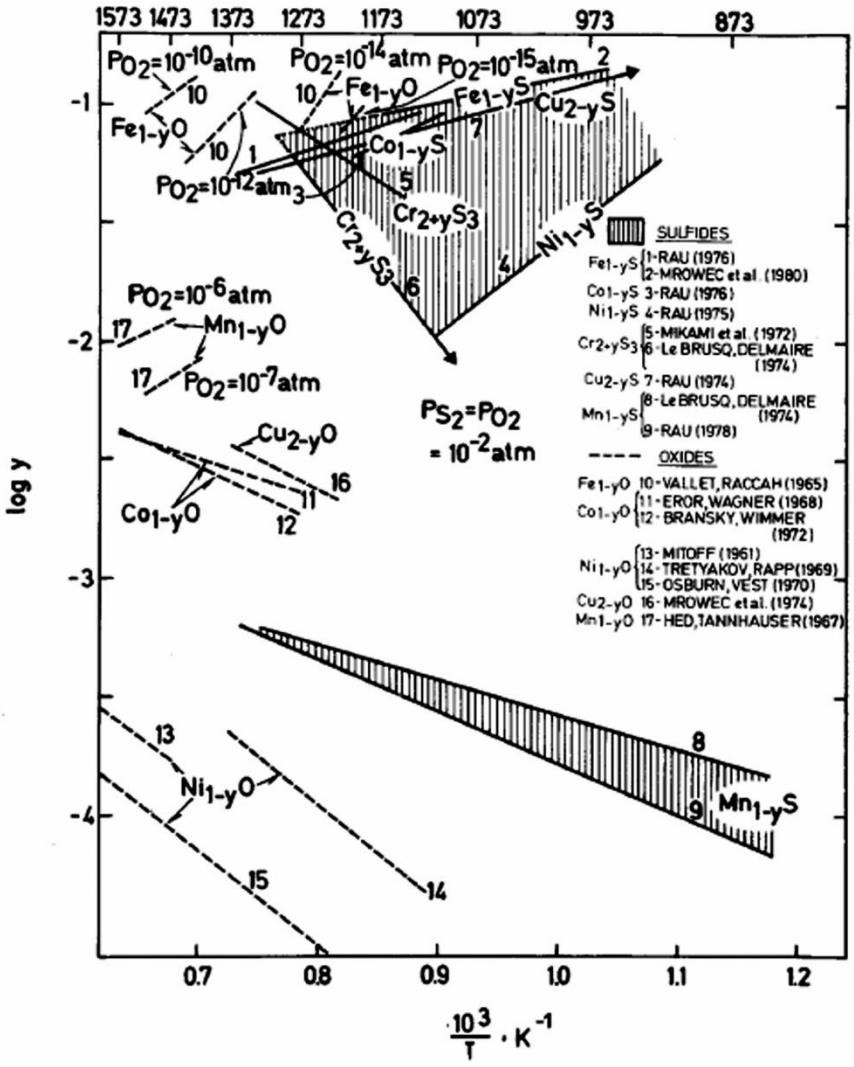

Figure 2.11 Comparison of non-stoichiometry of some metal sulfides and oxides[12]

The defects structure of some common metal sulfides will be discussed below, since the understanding of sulfide structure will help to learn about their diffusion behavior. This will be a further aid to explain the difference in the reaction rate between sulfides and oxides.

Ferrous sulfides

A number of researchers have studied the defect structure of ferrous sulfide, FeS[57-61].Iron sulfide is metal deficient with cation vacancies as predominant defects. Figure 2.12 shows the dependence of non-stoichiometry, y, in $Fe_{1-y}S$ on sulfur pressure for several temperatures. As shown in the figure, the dependence of y on sulfur pressure is not a simple power function as in the case of non-interacting defects. The defect concentration decreases with increasing temperature, similar to ferrous oxides, $Fe_{1-y}O$. Libowitz set up a model to deduce that this non-typical dependence of y on sulfur vapor pressure and temperature is due to the strong repulsive interactions between cation vacancies[62].

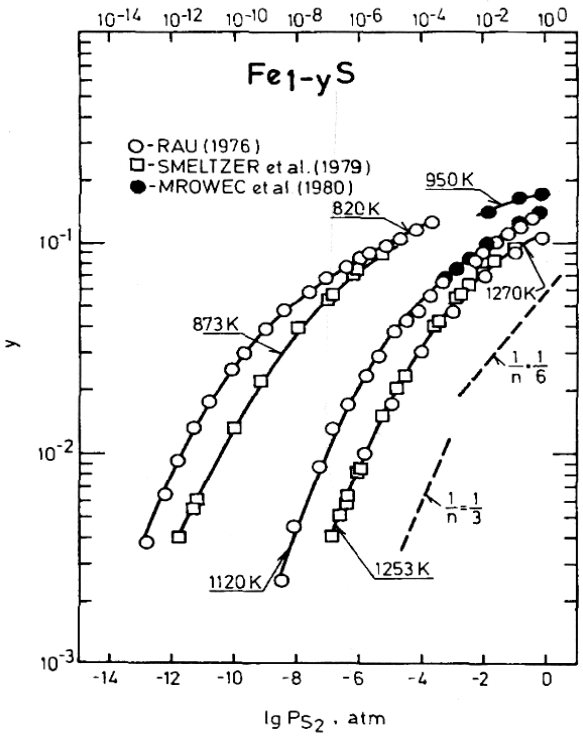

Figure 2.12 The dependence of non-stoichiometry, y, in $Fe_{1-y}S$ on sulfur pressure for several temperatures[57-59].

$Fe_{1-y}O$ and $Fe_{1-y}S$ have an analogous defect structure and comparable non-stoichiometry. However, it does not mean that the defect structures are exactly the same. In both compounds, the predominant defects are cation vacancies, but in FeO there are also interstitial cations of relatively high concentration. The interstitial cations together with cation vacancies form extended defects called Koch-Cohen type clusters. However, interstitial cations are not found in ferrous sulfides.

Nickel sulfides and cobalt sulfides

An analogous defect situation exists in $Ni_{1-y}S$ and $Co_{1-y}S$. They are metal deficient with cation vacancies as predominant defects. The nonlinear dependence of

non-stoichiomery on sulfur pressure can also be explained by the Libowitz's model. Figure 2.13 shows the dependence of non-stoichiometry, y, in $Ni_{1-y}S$ and $Co_{1-y}S$ on sulfur pressure for several temperatures.

It should be stressed that defect concentrations in the sulfides of Fe, Ni and Co decrease with increasing temperature. This behavior is due to strong repulsive interactions between cation vacancies.

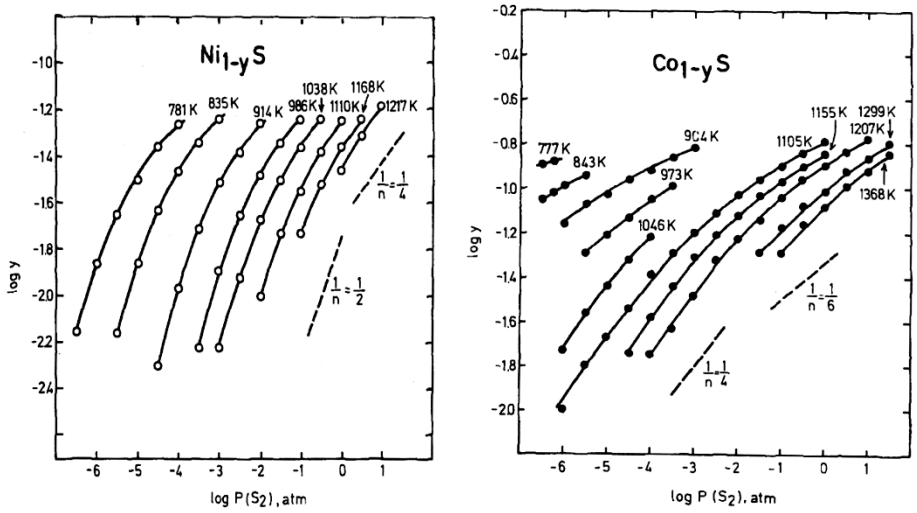

Figure 2.13 The dependence of non-stoichiometry, y, in $Ni_{1-y}S$ and $Co_{1-y}S$ on sulfur pressure for several temperatures[57, 63]

Manganous sulfides

Manganous sulfide is a metal-deficient, p-type semi-conductor, the predominant defects being cation vacancies[64, 65]. The non-stoichiometry of manganous sulfide is much smaller than in other sulfides. Manganous oxides have the same type of predominant defects, with the non-stoichiometry one order of magnitude higher than that

in manganous sulfide. Figure 2.14 shows the dependence of non-stoichiometry, y, in $Mn_{1-y}S$ on sulfur pressure for several temperatures.

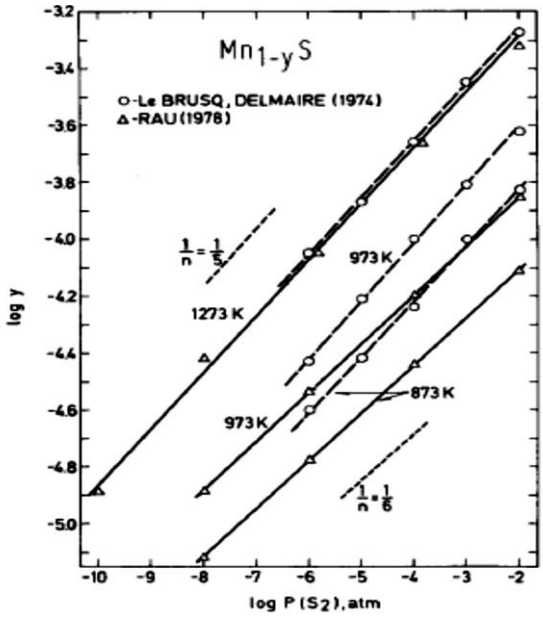

Figure 2.14 The dependence of non-stoichiometry, y, in $Mn_{1-y}S$ on sulfur pressure for several temperatures

Chromium sulfides

Cr_2S_3 is a metal-excess, n-type semi-conductor with interstitial cations as predominant defects[64, 66, 67]. Non-stoichiometry decreases with increasing sulfur pressure, as shown in Figure 2.15. It can be noticed that the value of 1/n decreases with increasing temperature. The degree of ionization of defects should therefore increase with temperature, as does the value, n.

Cr_2O_3 has a very small degree of non-stoichiometry. The defect concentration in chromium oxide is much smaller than that in chromium sulfides. The predominant defects are interstitial cations at low oxygen pressures and cation vacancies at high oxygen pressures[68] [69].

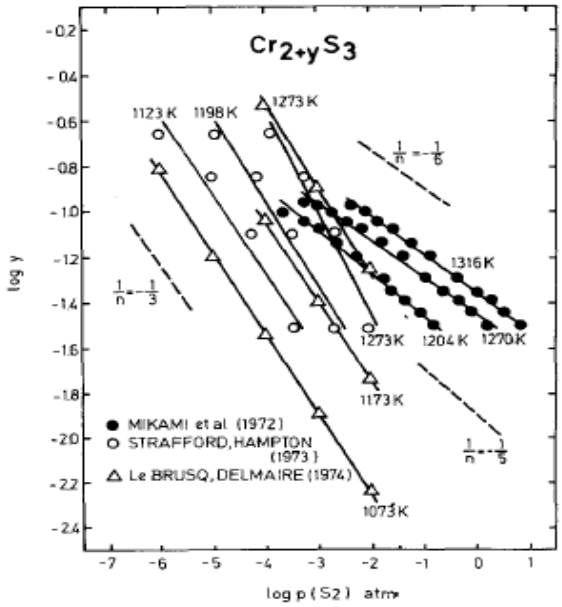

Figure 2.15 The dependence of non-stoichiometry, y, in $Cr_{2+y}S_3$ on sulfur pressure for several temperatures[64, 66, 67]

Refractory metal sulfides

Because of the very low deviation from stoichiometry in refractory metal sulfides, there is still insufficient information on defect structures and transport properties of refractory metal sulfides. Rau[70]has shown that the maximum non-stoichiometry of

molybdenum disulfides at 1373K (1100^{o}C) is smaller than 8 x 10^{-5} moles of sulfur per mole of MoS_2.

It has been shown by marker experiments that the sulfides formed on refractory metals, such as Mo and W, grow by inward diffusion of sulfur. This means that the predominant disorder in these sulfides, as in refractory metal oxides, is in the anion sublattice. As a consequence, in contrast with common metals, sulfide scales on refractory metals grow by inward diffusion of anions.

We can see from Figure 2.5 that some refractory metals, such as Mo and Nb, have low sulfidation rates. Refractory metals have sulfidation rates of the same order of magnitude as the rate of chromium oxidation. The slow sulfidation rate of refractory metals is due to their very low deviation from stoichiometry, that is, low defect concentration in these sulfides.

2.2.3.2 Transport properties

When considering transport properties, it is usually suggested that matter transport in metal sulfides is mainly via point defects at high temperature. Generally, sulfide scales on all common metals grow primarily by the outward diffusion of cations, and on refractory metals by inward diffusion of sulfur.

There is a difference in matter transport between metal sulfides and oxides because melting points of metal sulfides are lower than the corresponding oxides. In sulfides, volume diffusion is still the dominating method of matter transport at lower temperature than oxides[44, 71].

Transport properties of defects in sulfides may be described by self-diffusion coefficients and chemical diffusion coefficients. Figure 2.16 shows the collective plot of

self-diffusion coefficients in some metal sulfides and oxides. As shown in the figure, the activation energy of diffusion in sulfides is significantly smaller than that of oxides. Moreover, the self-diffusion rates of some important metal sulfides, such as Co, Ni, and Cr sulfides, are orders of magnitude higher than in the corresponding oxides[12]. It is also clearly seen from the figure that self-diffusion coefficients of cations in common metal sulfides are many orders of magnitude higher than those of anions in refractory-metal sulfides.[72]

Figure 2.17 shows a comparison of chemical diffusion coefficients in some oxides and sulfides. As shown in their figure, the chemical diffusion rate in metal sulfides and oxides do not differ greatly, therefore there is no big difference in the mobility of defects in metal sulfides and oxides. In fact, the rate of chemical diffusion in sulfides is generally higher than that in oxides, but this difference does not exceed one order of magnitude. The self-diffusion coefficient is a product of defect mobility and their concentration. It can therefore be concluded that, in general, the higher self-diffusion rate in metal sulfides results from the high defect concentration and not from the great defect mobility[12].

However, there are exceptions. The defect concentration of Mn sulfide is lower than its oxide, but the mobility of defects in Mn sulfide is higher than that in the oxide. Because of this compensation effect, the self-diffusion rates in Mn sulfide and oxide are similar. $Fe_{1-y}S$ and $Fe_{1-y}O$ have similar non-stoichiometry, but mobility of defects in $Fe_{1-y}S$ is higher than in $Fe_{1-y}O$, thus leading to higher self-diffusion rate of $Fe_{1-y}S$ than $Fe_{1-y}O$.

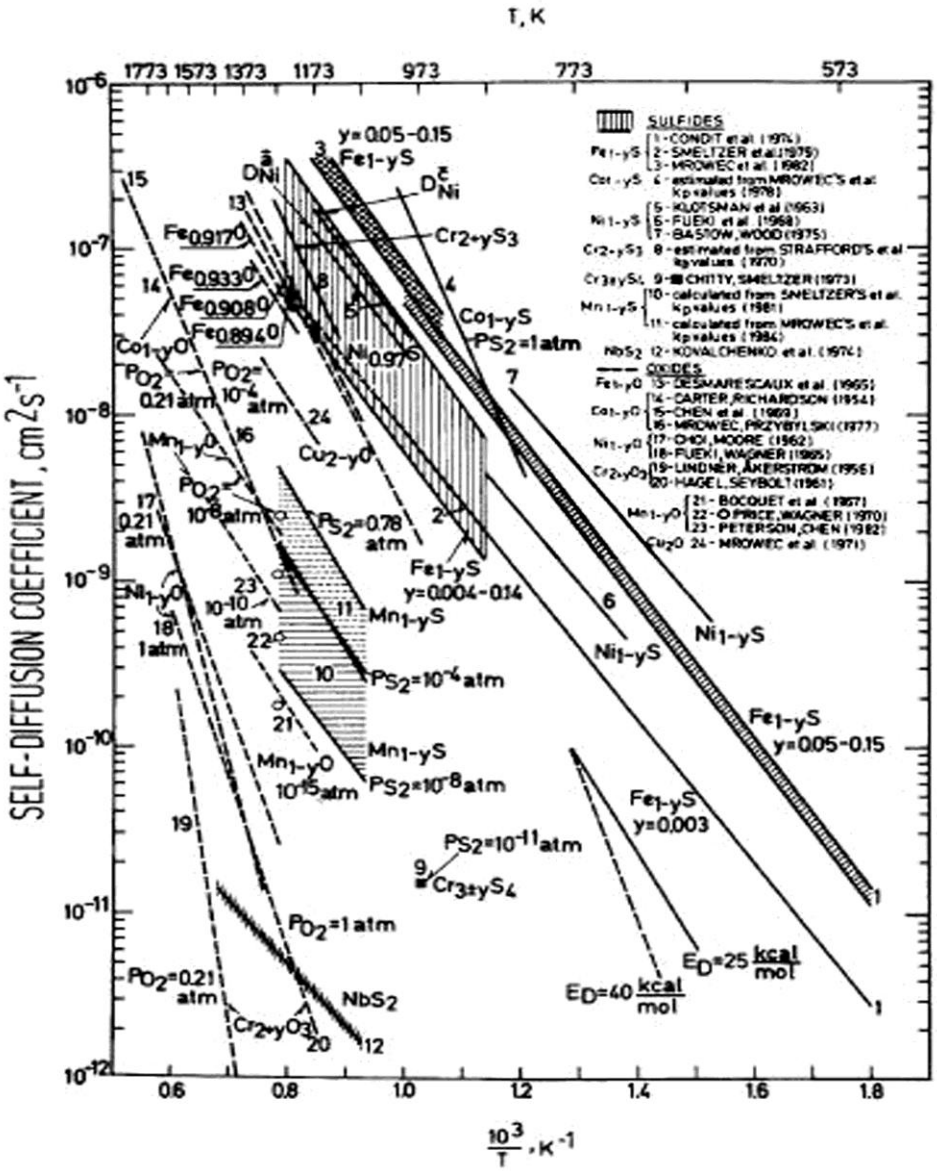

Figure 2.16 The collective plot of self-diffusion coefficients in some metal sulfides and oxides[12]

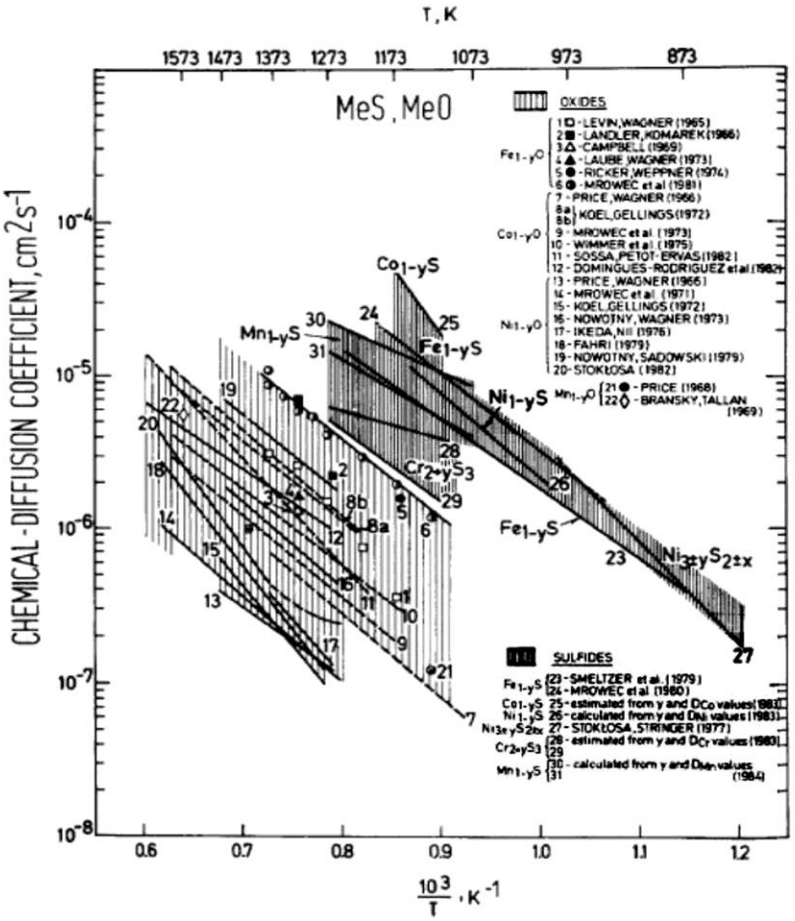

Figure 2.17 The comparison of chemical diffusion coefficient in some oxides and sulfides[12]

From the above discussion, it is clear that sulfidation rates of common metals are generally much faster than their oxidation rate. Figure 2.18 shows a collective plot of temperature dependence of sulfidation and oxidation rates of some metals. As shown in the figure, the sulfidation rates of some important metals, such as Ni, Co and Cr, are significantly higher than that of oxidation. Therefore, sulfide scales on common metals possess poor protective properties. However, refractory metals have good sulfidation

resistance because their sulfidation rate being comparable to the oxidation rate of chromium.

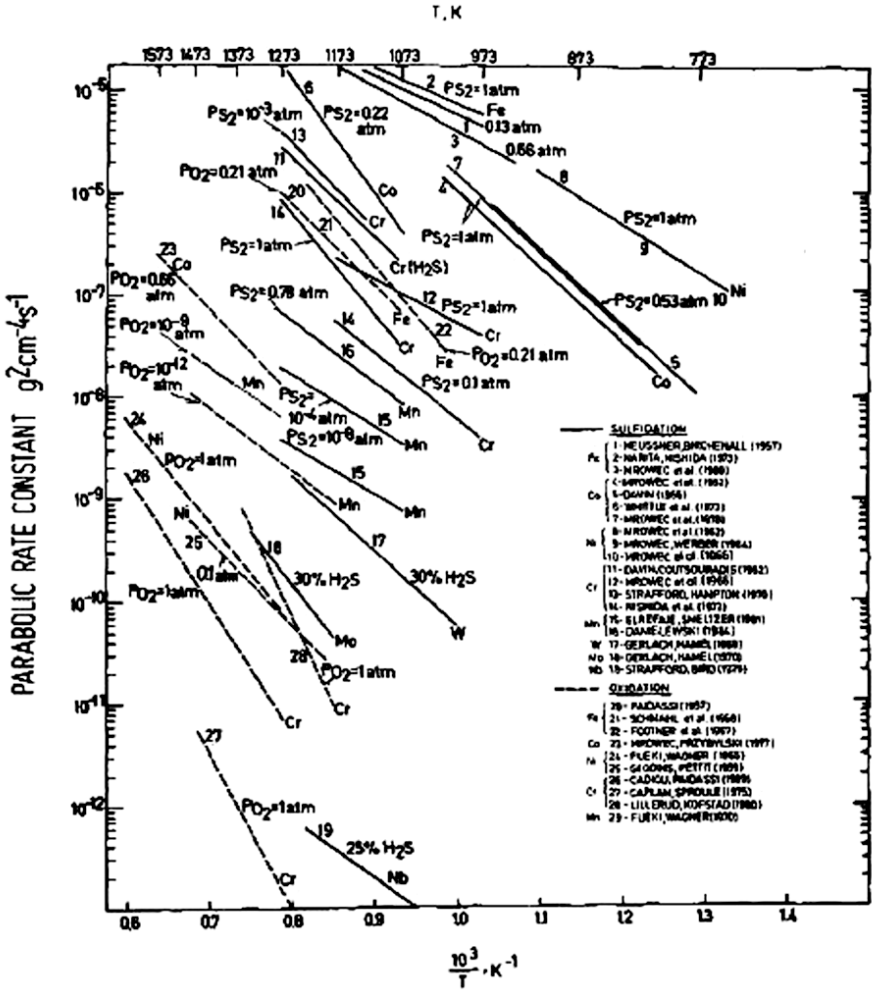

Figure 2.18 Collective plot of temperature dependence of sulfidation and oxidation rates of some metals[12]

2.3 ALLOY SELECTION AND DESIGN IN ENVIROMENTS WITH LOW-OXYGEN AND HIGH-SULFUR POTENTIALS

If alloys have long-term corrosion resistance in environments with low-oxygen and high-sulfur potentials, it is required that the alloy forms a slow-growing oxides, typically Cr_2O_3 (chromia) and Al_2O_3 (alumina), which act as barrier to the diffusion of metals or oxidants through the scale. This is because the rate constants of chromia and alumina are slower than those of Fe, Co and Ni oxides, as shown in Figure 2.19. Therefore, most commercial high temperature alloys rely on the formation of either chromia or alumina to provide corrosion resistance. Fe, Ni and Co are the common base metals for high temperature alloys. The alloys used in atmospheres with low-oxygen and high-sulfur potential are mostly chromia formers[73]. Even though alumina scale has superior corrosion resistance, alloys forming alumina layers are usually restricted to coatings of the M-Cr-Al type, where M is the base metal such as Ni, Fe or Co. This is because the aluminum content required for the formation of an alumina scale severely reduces the mechanical properties and the fabricability of these materials [74-77].

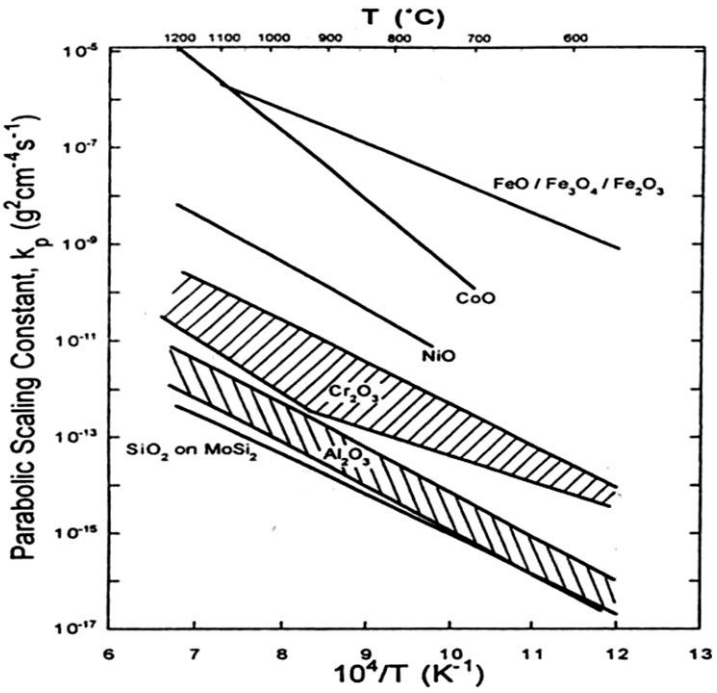

Figure 2.19 Rate constants of several metal oxides[73]

Gleeson[10] gave an example of alloy selection in this kind of sulfidizing-oxidizing environment. Alloy 600(mainly 72Ni-16Cr-8Fe,wt.%) can be used in the environment which is not very sulfidizing because it is susceptible to rapid sulfidation attack at temperature above 645^{o}C in highly sulfidizing atmospheres due to the formation of liquid corrosion products. With the increased amount of Cr and Fe, the melting points of sulfide scale increase to lower the risk of liquid products formation. Thus, stainless steel 309 and 310, mainly (Fe-(12-20) Ni-(22-26) Cr, wt.%), can be used where the atmosphere is more sulfidizing. The alloys with higher Cr and Co contents, such as Haynes 556(mainly 31Fe-22Cr-20Ni-18Co, wt.%), should be used if the environments become more severe. Co-rich alloys, such as alloy 160(mainly 37Ni-28Cr-30Co-2.7Si, wt.%) can be used if the severity of the environment keeps increasing[10].

Since the corrosion resistance of alloys in environments with low-oxygen and high-sulfur potential rely on the formation of the protective chromia scale, it is of significance to understand the compositional and kinetic factors which affect protective-scale formation to provide guidance for alloy design.

Figure 2.20 [78] schematically shows two limiting cases resulting from the oxidation of a binary A-B alloy in which AO, a non protective oxide, is less stable than BO, a protective oxide such as Cr_2O_3 or Al_2O_3. It is assumed that the difference in thermodynamic stability between AO and BO is large, the atmosphere is high enough to stabilize both AO and BO, and they are mutually insoluble. The two limiting cases shown are internal BO formation below a rapidly growing AO scale and the external protective BO scale formation.

The thickness of the internal oxidation region is

$$\xi = \left[\frac{2N_O^S D_O}{\nu N_B^o} t\right] \qquad (2.27)$$

where N_O^S is oxygen solubility in the alloy, N_B^o is the atomic concentration of B in the bulk alloy. Alloying additions which can effectively increase N_B^o or decrease N_O^S are beneficial in reducing ξ[79, 80].

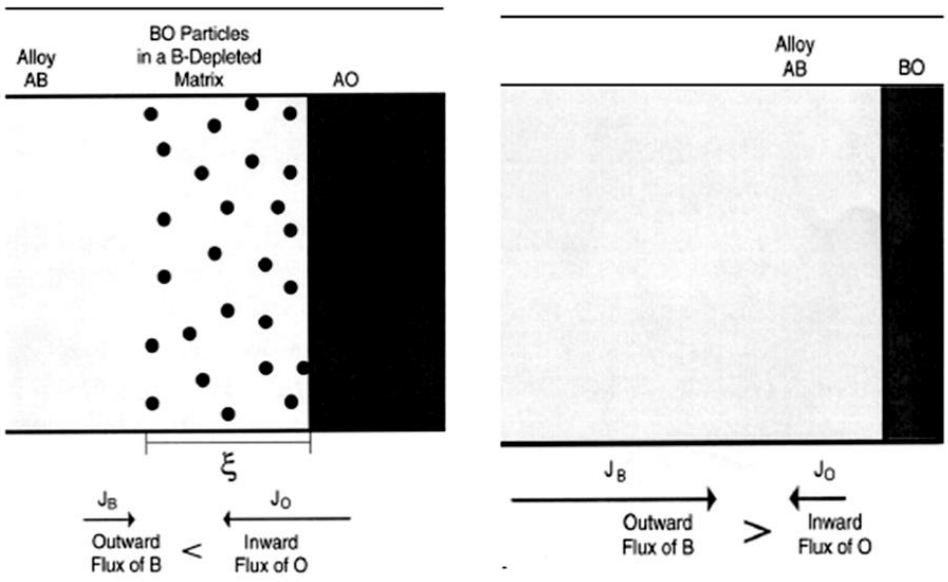

Figure 2.20 The schematic illustration of (a) internal BO formation below a rapidly growing AO scale; (b) external protective BO scale formation. BO is thermodynamically more stable than AO.

There is a critical B content, N_B^*, for the transition from internal to external BO, such as Cr_2O_3, formation.

$$N_B^* > [\frac{\pi g^*}{2v} N_o^s \frac{D_o V_m}{D_B V_{ox}}]^{1/2} \qquad (2.28)$$

where N_o^s is the oxygen solubility in the alloy, D_o is diffusivity of oxygen in alloy, D_B is diffusivity of B in alloy, V_m is the molar volume of alloy, V_{ox} is the molar volume of the oxide, g^* is a constant, v is the stoichiometric coefficient. This critical value is dependent on kinetic rather than thermodynamic factors. The value required by kinetics to form Cr_2O_3 or Al_2O_3 is much higher than that determined by thermodynamic consideration.

It can be inferred from Equation (2.28) that the formation of external BO is favored by a high value of D_B and a low value of $N_o^s D_o$. It is generally believed that the high diffusion path can increase D_B more than D_o. Therefore, the critical concentration for protective oxide can be greatly decreased by reducing grain size[81-83] or increasing the dislocation density at the alloy surface by mechanical deformation, such as abrasion, sand blasting and shot peening, and so on[83].

As was mentioned above, there is a critical Cr content for the transition from internal to external oxide. After the formation of the continuous Cr_2O_3 layer, it is necessary to determine if its growth can be sustained. The following example illustrates how that determination can be made.

An Alloy A-B, with BO more thermodynamically stable than AO, is pre-oxidized in a low P_{O2} gas where only BO is stable, followed by in-service exposure to a higher P_{O2} gas. It is clear that growth of a continuous BO scale requires a sufficient supply of B from within the alloy to alloy-scale interface. The resulting subsurface concentration gradient of B is schematically represented in Figure 2.21. The steepest possible diffusion gradient of B, or the maximum possible rate of supply of B in the alloy, can be obtained by setting N_B^i equal to zero. Under steady-state condition, this maxium supply of B would have to equal the rate of consumption of B as a result of the BO scale growth. Wagner(1952) determined the minimum B content, $N_{B,min}^o$, necessary for the sustained exclusive growth of a BO scale on an A-B alloy. Assuming that D_B is independent of concentration, that the growth of BO scale obeys the parabolic rate law, that solvent metal A is insoluble in BO, and that the recession of the alloy-scale interface can be neglected, Wagner derived the criterion shown in Equation (2.29).

$$N_{B,min}^{o} > \frac{V_m}{32}\left(\frac{\pi k_p}{D_B}\right)^{1/2} \quad (2.29)$$

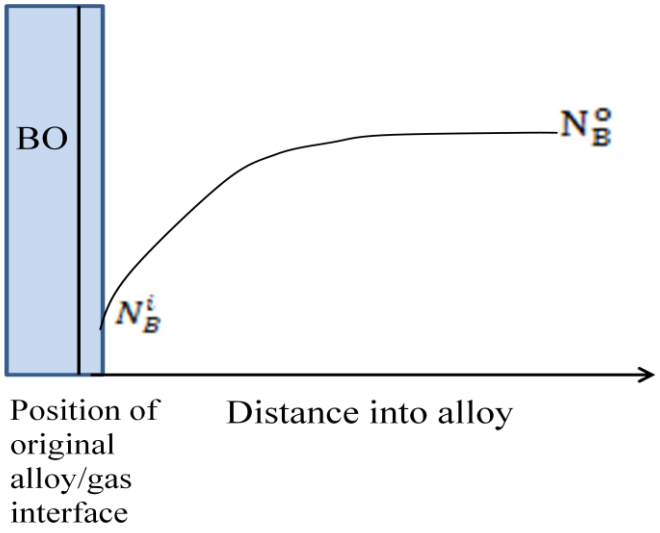

Figure 2.21 Schematic representation of the concentration profile of B in a binary alloy A-B which forms an exclusive scale of BO

This criterion, derived based on supply rather than establishment, gives only the minimum B content in the alloy necessary to supply B to the alloy-scale interface at a sufficient rate to sustain the growth of an established BO layer. The actual B content necessary for both the establishment and sustained growth of a BO scale will probably be higher than $N_{B,min}^{o}$ due to transient and kinetic effects.

Therefore, the critical amount of Cr in the alloy to form and maintain an external protective Cr oxide scale is determined by equations (2.28) and (2.29) together. Generally, Cr content in Fe-Ni alloys is above 18wt% to satisfy the requirements of Equation (2.28)

and (2.29). However, the Cr content in the alloy is typically kept below 30wt.% to avoid α'-Cr precipitation, which reduces both the workability and creep strength of the alloy.

2.4 EFFECTS OF ALLOYING ELEMENTS ON SULFIDATION RESISTANCE

High temperature alloys are typically based on Fe, Ni, Co or their combinations, with the addition of other alloying elements, invariably including chromium, to improve their chemical and physical properties[84, 85]. Iron-based alloys are the most common because of the low cost, but the usage is limited because their high-temperature corrosion resistance and mechanical properties are inferior to Ni- and Co- based alloys. Sulfidation resistance of Ni-based alloys is not as good as that of Co-base alloys because of the low melting point of the Ni-Ni_3S_2 eutectic mixture. The effects of alloying elements on sulfidation resistance will be discussed below.

Chromium

As mentioned in the previous part, the corrosion resistance of alloys in environments with low-oxygen and high-sulfur potential rely on the formation of the protective chromia scale. Chromium also has beneficial effect on corrosion resistance in purely sulfidizing atmosphere.

Many researchers studied the sulfidation behavior of Fe-Cr, Ni-Cr and Co-Cr alloys under a sulfur-vapor pressure of 1atm between the temperature range of 600-900^{o}C[56, 86-91]. Figure 2.22[44] shows the sulfidation rate of Fe-Cr, Co-Cr and Ni-Cr alloys as a function of Cr concentration. The alloys have similar kinetics and mechanisms

irrespective of the alloy composition and temperature. The corrosion rate is a diffusion-controlled process. The diffusing species are cations and electrons. Figure 2.23 schematically shows the dependence of sulfidation rate on chromium content at 1073K. The figure can be divided into three regimes. In regime 1, where the Cr content is below 2at.%, a monophase scale formed which consists of base metal sulfide doped with chromium. The sulfidation rates of Fe-Cr alloy is comparable to that of pure Fe, and sulfidation rate of Co-Cr and Ni-Cr alloys are higher than that of pure Co and Ni. The greater sulfidation rates of these alloys as compared to the pure base metal results from a higher concentration of cation vacancies in the scale due to the doping effect. In regime 2, a heterophase scale forms. The outer layer consists of base metal sulfide. The inner layer consists of chromium sulfide-base metal sulfide solid solution, acting as an inner barrier layer. So sulfidation rate decreases dramatically with Cr content in regime 2. In regime 3, the scale is single phase, consisting of Cr sulfide doped with base metals, so sulfidation rate is comparable to pure chromium[12]. It is worth noting that the minimum Cr content for selective sulfidation of chromium to form the single phase scale (chromium sulfide scale) in Co-Cr alloys is higher than that in Ni-Cr and Fe-Cr alloys[86].

It should be noted that the kinetics and mechanism of oxide scale formation on Fe-Cr, Ni-Cr and Co-Cr alloys depends similarly on chromium concentration, but the oxidation rate in regime 2 and 3 is many orders of magnitude smaller than that of sulfidation, as is illustrated in Figure 2.24. As shown in the figure, the oxidation rate of chromia formers (about 40% Cr) is four orders of magnitude lower than the sulfidation rate.

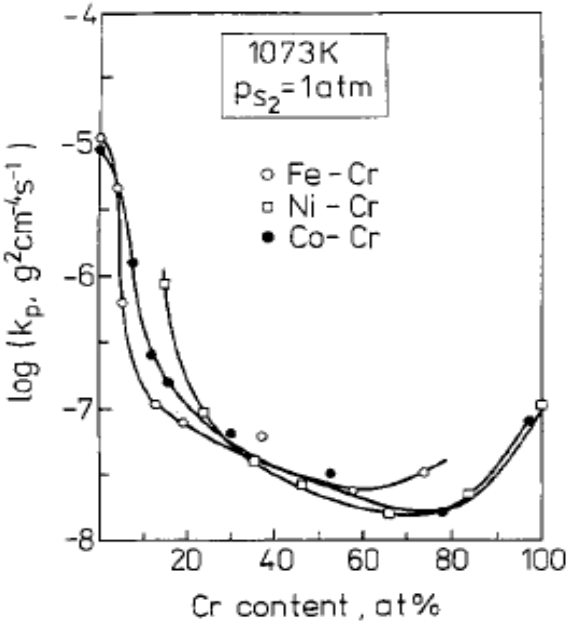

Figure 2.22 The dependence of sulfidation rate of Fe-Cr, Ni-Cr and Co-Cr alloys on Cr concentration

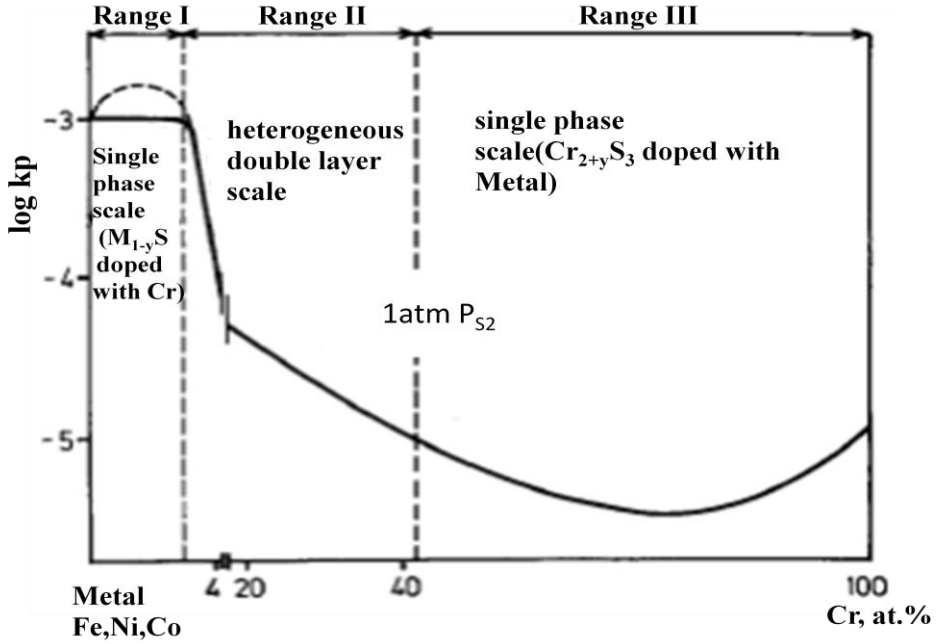

Figure 2.23 The dependence of sulfidation rate of Fe-Cr, Ni-Cr and Co-Cr alloys on Cr composition

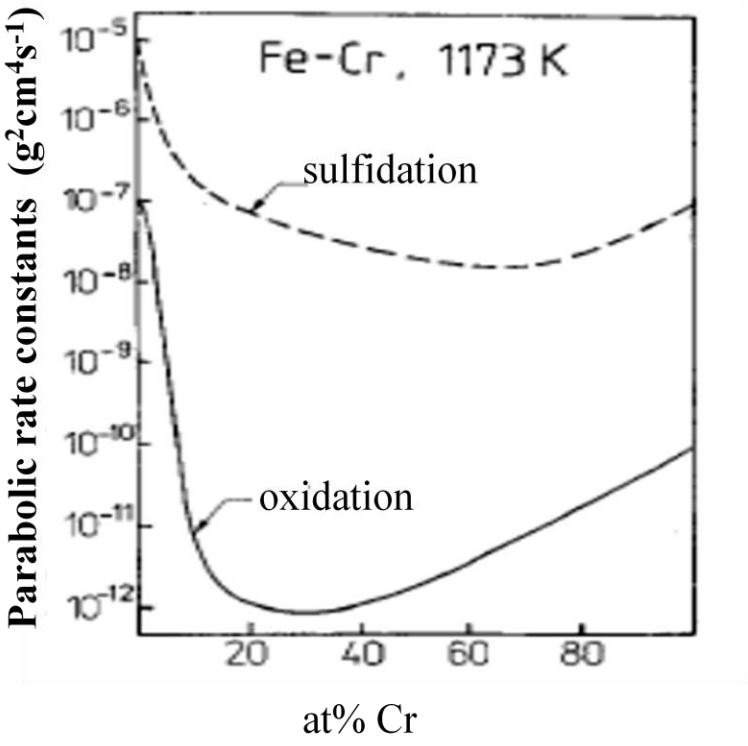

Figure 2.24 The dependence of sulfidation and oxidation rates of Fe-Cr alloys on Cr concentration

Cobalt

As for the effect of Co on sulfidation resistance, many studies have been performed on Co-based alloys[21, 86, 88, 92, 93]. The results showed that cobalt-based alloys generally have better sulfidation resistance than Ni-based alloys and Fe-Ni-Cr alloys. For example, A.Davin[56, 92] compared the sufidation resistance of alloy 80Co-20Cr with Alloy 80Fe-20Cr and 80Ni-20Cr in H_2S gas at 800^oC. Co-base alloys showed better sulfidation resistance than Fe and Ni-based alloys, as shown in Figure 2.25. Another example is the work done by Lai [94], as shown in Figure 2.26. Alloy 6B and 188(cobalt-

based alloys) are better than Alloy 800(Fe-Ni-Cr alloy), Alloy 214, 600(Ni-based alloy) and 310 stainless steel (Fe-Ni-Cr alloys). Generally, Co-based alloys and Co-containing alloys have higher temperature capabilities and are more resistant to breakaway corrosion. This is clearly shown in the study of Howes (Figure 2.27) [95] where Alloy 310 stainless steel, Alloy 800 and Alloy 6B were tested in the MPC coal gasification atmosphere ($24H_2$-18CO-$12CO_2$- $5CH_4$-$1NH_3$-0.5 H_2S-Bal. H_2O, P_{O2}=1.3 x 10^{-15}atm),PS_2=7.6 x 10^{-7}atm) at 980^{o}C. One reason for the beneficial effect of Co is that the high Co content in Ni-based alloys reduces the risk of Ni-Ni_3S_2 eutectic formation at 645^{o}C. Another reason is because of the lower diffusion rate of sulfur in Co than in Ni.

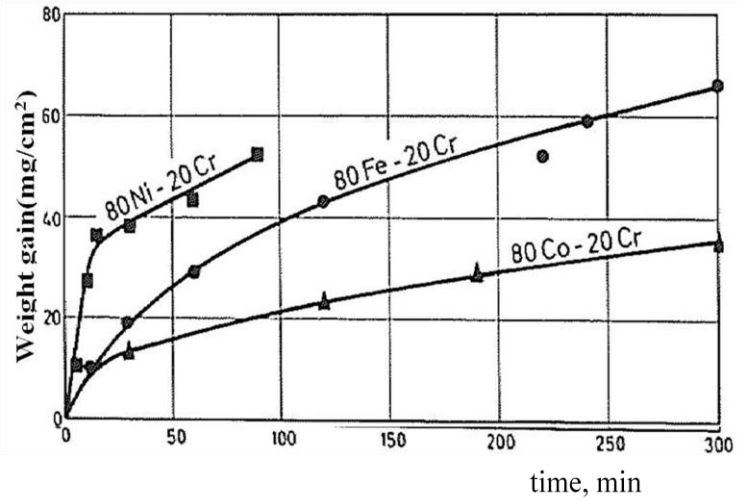

Figure 2.25 Sulfidation of binary alloys in H_2S at 800^{o}C

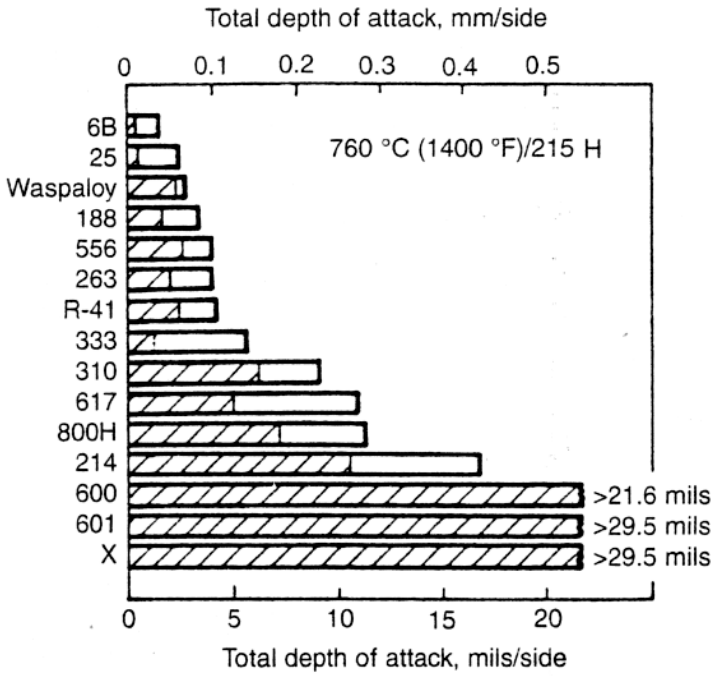

Figure 2.26 Corrosion of Fe-Ni-Cr,Ni-base and Co-base alloys at 980^{o}C in the MPC coal gasification atmosphere with 0.5%H_2S, P_{S2}=1x 10^{-7} atm , P_{O2}=1 x10^{-22} atm [94]

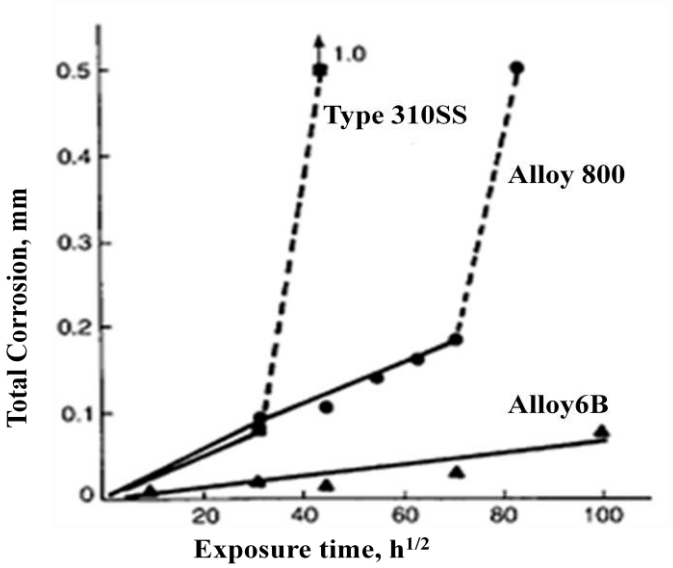

Figure 2.27 Corrosion behavior of several alloys

Nickel

For nickel based alloys, increasing nickel content greatly increases susceptibility to sulfidation attack. Figure 2.28 shows the corrosion rates of high-nickel alloy in the coal gasification atmosphere with 1.0% and 1.5%H_2S. As shown in the figure, sound metal loss increased with increase of Ni content. The detrimental effect of Ni on sulfidation resistance is due to the low melting point of Ni sulfide. The formation of liquid sulfide scale is catastrophic to corrosion resistance. As shown in Figure 2.29, the melting point of Ni sulfide is low. However, in Ni-based alloys, the melting points of sulfide scale generally increase with the increased addition of Cr and Fe.

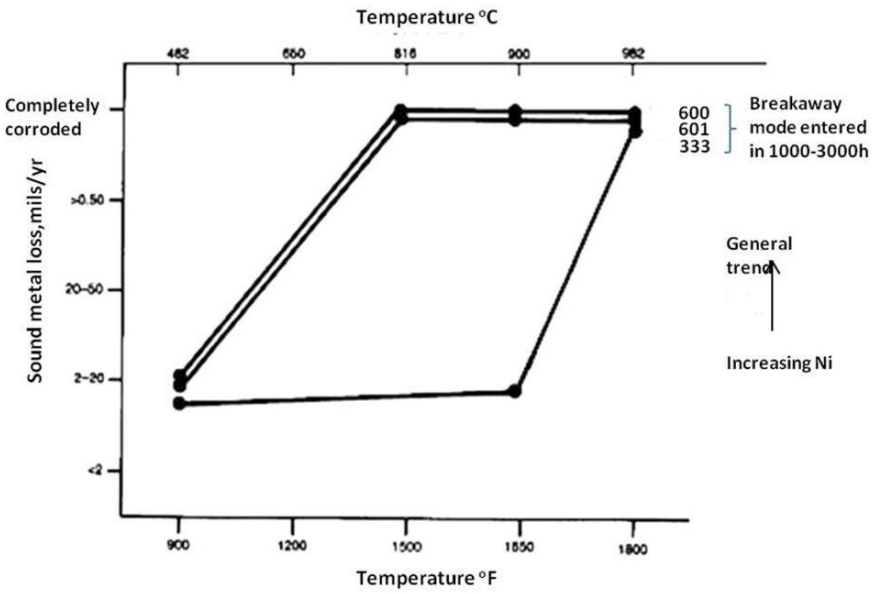

Figure 2.28 Corrosion rates of high-nickel alloys in the coal gasification atmosphere with 1.0% and 1.5%H_2S[8]

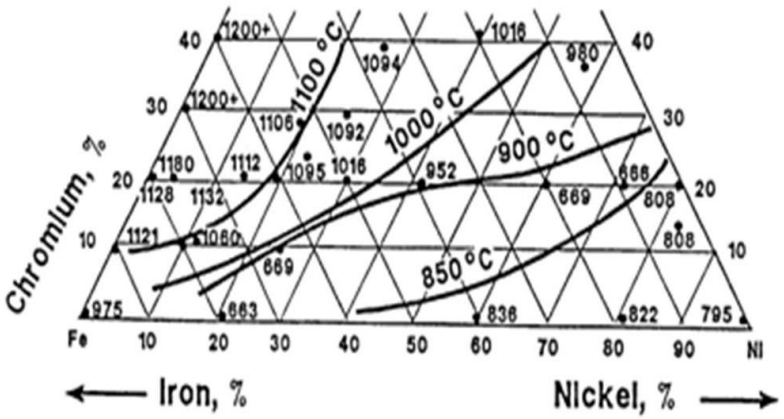

(Gaylord Smith, 1997)

Figure 2.29 Melting point of sulfide scale formed on Fe-Ni-Cr alloys

Silicon

Silicon is an important minor element frequently used in high-temperature alloys. Si addition can be used to improve corrosion resistance by forming a continuous silica layer, which has a very low growth rate, as shown in Figure 2.30. According to a study by Nagarajan et al. [96], the Fe-18Cr-2Si alloy exhibited significantly better sulfidation resistance than Fe-18Cr-0.5Si in $24H_2$-$39H_2O$-18CO-$12CO_2$-$5CH_4$-$1H_2S$-$1NH_3$ (P_{O2}=$9.9x10^{-16}$atm, P_{S2}=$2.4x10^{-6}$atm, α_c=0.3) at 980°C for 120 hours. When present in chromia-former alloys at low concentration (below 3wt%), silicon tends to segregate at the alloy-scale interface and form, under favorable conditions, a more or less continuous oxide sub layer below the main chromia[97, 98]. This may help to reduce both internal sulfidation and carburization. A study by G.Y.Lai[99]also showed the beneficial effect of Si in the Ni-27wt%Cr alloy in the gas mixture (5%H_2-5%CO-1%CO_2-

0.15%H_2S-Ar) at 760^oC for 500h, as shown in Figure 2.30. However, a large amount of Si should be avoided due to its detrimental effects on mechanical properties.

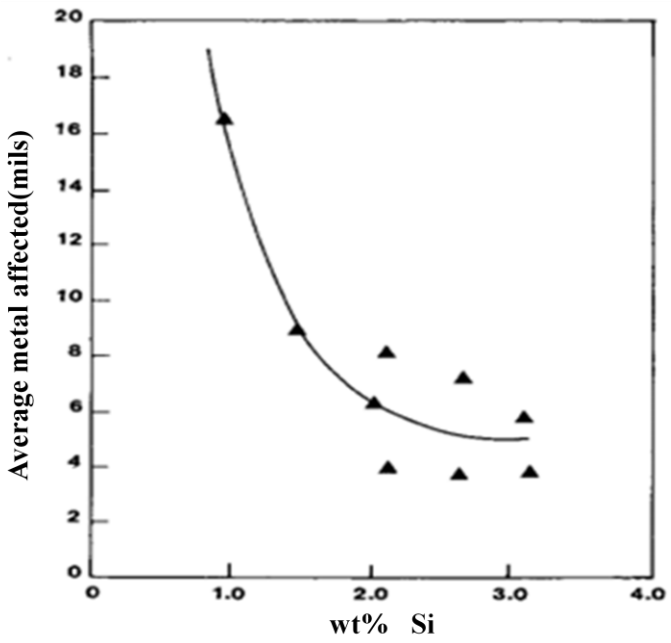

Figure 2.30 The effect of Si in the Ni -27wt%Cr alloy on sulfidation resistance

Manganese

Manganese is another common minor element. It acts as a deoxidizer and desulfurizer. Mn can have a deleterious effect on an alloy's sulfidation resistance because manganese diffuses quickly through the chromium oxide layer and reacts with the environment to form external sulfide, thus accelerating breakaway corrosion[37]. Azaroff[100] proposed a cation diffusion mechanism in close-packed anion lattices that involves the jump from alternative, adjacent octahedral to tetrahedral interstices. Cox et

al.[101] were able to calculate and show experimentally that the cation migration in chromium oxide by this diffusion mechanism decreases in the order: Mn^{2+}, Fe^{3+}, Fe^{2+}, Ti^{3+}, Co^{2+}, V^{3+}, Cu^{2+}, Mn^{3+}, Ni^{2+} and Cr^{3+}. This is quite in agreement with the results of Perkins et al. [102, 103] who showed that Mn and Fe are easily transported to the surface of chromia scale to form Mn and Fe rich sulfides. They also suggested that the Mn content in high-temperature alloys used for coal gasification plants should be kept below 0.1wt%[104].

Titanium

As for the effects of titanium on sulfidation resistance, many research has been done on Fe-based alloys. Bradshaw and Stoltz found that the addition of 3wt.% Ti to 310SS greatly enhanced sulfidation resistance[105]. They tested 310SS and 3wt.%Ti modified alloy in an MPC gas mixture with 1% H_2S at about 1 atm pressure for 100h at 980^{o}C. The 310SS sample showed some sulfide nodules as well as some spalled oxides, while Ti-modified 310 showed an adherent oxide scale with no sulfide nodules. They observed the presence of a significant concentration of Ti in the Cr_2O_3 layer. They also tested Alloy 800 and 801 in the same environment for 100 hours at 980^{o}C.The Alloy 800 was totally corroded, while Alloy 801 showed an adherent oxide scale with only about 1.4mg/cm^2 weight gain. The only difference in the composition of the two alloys is Ti content, 0.4% for alloy 800, and 1.1% for Alloy 801. Tiaearney and Natesan[106] also found that Ti promoted the formation of oxide instead of sulfide in the initial corrosion stage, thus leading to an increased tendency toward formation of oxide scales and reduced reaction rates. Table 2.3 contains the addition data showing the beneficial effect of Ti.

Table 2.3 Results of corrosion test at 1000 ^{o}C for 100h in Ar-30H_2-30H_2O-1H_2S [107]

Alloys	Total affected depth,um(mils)	Comments
310HP(b)	>1500(59.1)	Liquid sulfides
	650(25.6)	sulfide penetration
310HP+2%Ti	330(13.0)	sulfide penetration
	62(2.4)	Adherent oxide
310HP+3%Ti	38(1.5)	Adherent oxide
	34(1.3)	Adherent oxide

Test gas was at 1atm, P_{O2}=1.3 x 10^{-15}atm P_{S2}=1 x10^{-6} atm; HP indicates high-purity material.

Conversely, according to the study by Natesan[108] in the late 1970s, the addition of 3wt.% Ti to 310SS and Inconel X-750(mainly Ni-(14-17)wt.%Cr) alloy, increased the corrosion rate. Baxter and Natesan reported that the addition of 3wt.% Ti to a Fe-25Cr-20Ni alloy produced less protective scaling behavior than the corresponding pure ternary alloy[109]. The recent investigation showed that the addition of Ti to some Fe-Cr-Ni alloys has essentially no effect on the oxidation and sulfidation resistance in a mixed atmosphere at 700^{o}C[110]. To date, little work has been done on the effect of Ti in Ni-based alloys on sulfidation resistance.

Molybdenum

Molybdenum is used in many high-temperature alloys for solid solution strengthening. Research showed that refractory elements such as Mo are highly resistant to sulfur corrosion, with the sulfidation rate comparable to the oxidation rate of Cr, as shown in Figure 2.5. The excellent sulfidation resistance of refractory metals results from

the very low deviations from stoichiometry, and thereby, the low defect concentrations in the sulfides of these metals.

In 1974, Strafford et al.[15] was the first to suggest that addition of refractory-metals should be beneficial to the sufidation resistance of the common base metal. In 1989 or 1990, the work of Douglass, Chen et al.[17] , Gleeson et al.[11, 16], Wang et al.[18]showed that refractory metal sulfides provide moderate protection when formed in common base metals, cobalt, iron and nickel. For example, The study of W.Kai[19] showed that the addition of Mo to pure iron in the $H_2/H_2O/H_2S$ mixture can reduce the corrosion rate by about half an order of magnitude, as shown in Figure 2.31. When the Mo content is above the range of 10-40 wt%, the corrosion rate is relatively independent of the Mo content.

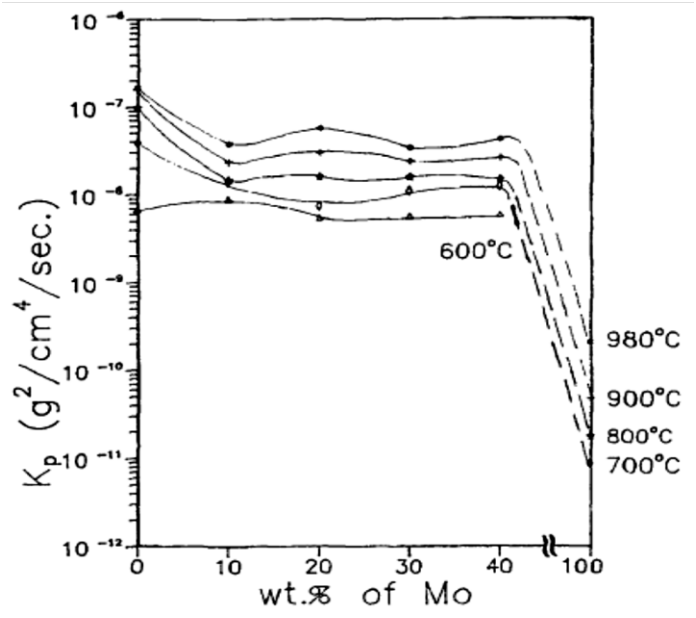

Figure 2.31 The effect of Mo in pure iron on rate constants[19]

An understanding of the structure of Mo sulfide (MoS_2) is essential to interpret the limited beneficial effect of Mo. MoS_2, in most cases with a hexagonal structure, is a layered compound consisting of trilayer S-Mo-S slabs held together by weak van der Wall interactions[111]. Each trilayer slab consists of two hexagonal (0001) planes of sulfur atoms and an intermediate hexagonal layer of Mo atoms, which are trigonally prismatic coordinated to the six surrounding sulfur atoms as shown in Figure 2.32(a)[112]. The most common allotrope of MoS_2 adopts 2H-stacking. In 2H- MoS_2 the unit cell extends over two S-Mo-S slabs, and the Mo atoms in one slab are placed on top of the S atoms in the other, and vice versa as shown in Figure 2.32[112]. Figure 2.32(a) shows the top and side view of the crystal structure of 2H- MoS_2. In the 2H-stacking, adjacent S-Mo-S slabs are rotated by 60^o with respect to each other and shifted so Mo atoms in one slab are placed over S atoms in the other and vice versa, as indicated by the black arrows. The distance between the Mo layers is 6.15 **Å**. The light gray parallel piping shows the unit cell. Figure 2.32(b) shows a ball model of hypothetical hexagonal MoS_2 cluster with the 2H-stacking. Notice the alternating edge termination. A $(\bar{\mathbf{1}}\mathbf{010})$ S edge in one layer is directly above a $(\mathbf{10}\bar{\mathbf{1}}\bar{\mathbf{0}})$ Mo edge in the layer below and vice versa.

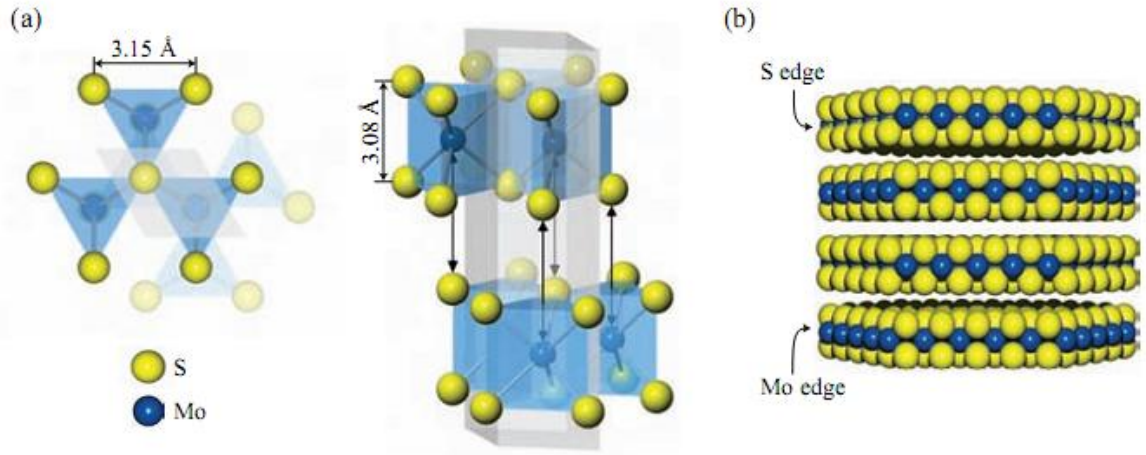

Figure 2.32 Structure of MoS_2 from several perspectives

The layered crystal structure of MoS_2 enables the intercalation of foreign ions of size similar to those of the common base metals. The intercalated foreign ions sit in the octahedral sites within the Van der Waals gap separating two loosely bound S-Mo-S sandwiches. The intercalated ions can diffuse at a reasonably rapid rate within the Van der Waals gap. Although MoS_2 is an ineffective barrier against the transport of intercalated metal ions, it is very protective on pure Mo because the diffusion of both Mo and S does not seem to occur along the open Van der Waals gap.

Aluminum

Since Mo offers only moderate resistance to sulfidation due to the layer structure of its sulfide, studies have been done to see if superior sulfidation resistance can be obtained by the addition of a ternary element which may form a protective inner layer or interact with MoS_2 in a synergistic manner to form a protective sulfide. The effects of some ternary additions (Al, Cr, Mn, Ti and V) on the sulfidation of Ni-Mo, Co-Mo and

Fe-Mo have been studied in sulfur vapor of 10^{-2}atm over the temperature range 600-900^{o}C, by Chen at el[113], Gleeson at el.[21], Wang and Najarajan[96]. Al was found to be the most effective addition to improve the sulfidation resistance of the ternary alloys. For example, Kai and Douglass[114] observed a dramatic decrease in sulfidation rate when adding Al to Fe-Mo alloys in a $H_2/H_2O/H_2S$ mixture over the temperature range 700-980^{o}C. The sulfidation rate of Fe-Mo-Al alloys is even slower than that of pure Mo, as shown in Figure 2.33. Wang et al.[20] also observed that there is a dramatic decrease in sulfidation rate when adding Al to an Fe-Mo alloy over the temperature range of 700-900 ^{o}C in 0.01atm sulfur vapor.

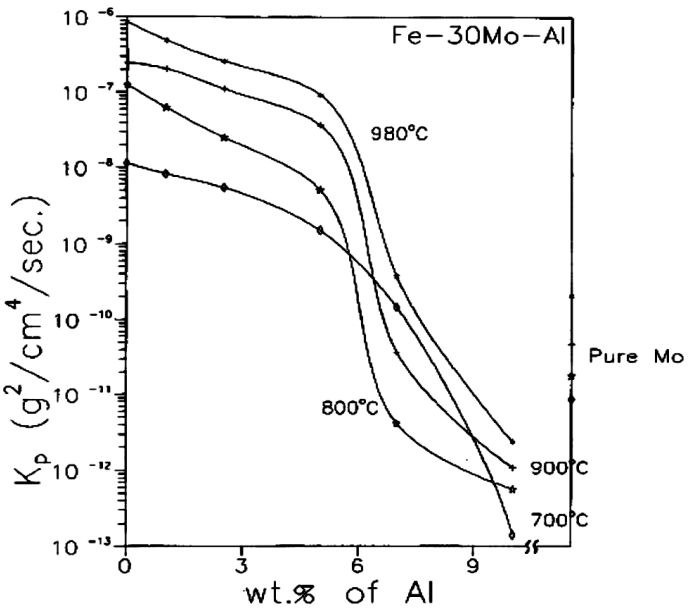

Figure 2.33 Effect of Al content on the corrosion kinetics of Fe-30Mo-yAl[114]

The reason for this beneficial effect is because of the formation of the spinel, $Al_xMo_2S_4$, which slows down the outward diffusion of the base-metal ions[20, 21]. Al can be intercalated into the Van der Waals gaps of MoS_2 [20]. When Al^{3+} is intercalated into the octahedral sites, considerable strain results because the ionic radius of Al^{3+}, 0.51**Å**, is smaller than the size of the octahedral site, 0.74**Å**. Intercalation of Al^{3+} leads to the formation of $Al_{0.5}Mo_2S_4$, which is more protective than MoS_2. On the other hand, Fe^{2+} with an ionic radius of 0.76**Å** fits readily into the octahedral sites with very little strain. The loosely-bound Fe^{2+} can readily diffuse through MoS_2 and leads to the formation of an outer layer of FeS. The presence of Al^{3+} in MoS_2 successfully block the diffusion path of iron through the sulfide, leading to the significant decrease of sulfidation rate.

2.5 INTRODUCTION TO SUPERALLOYS

Superalloys are used in high temperature applications requiring excellent creep resistance and high temperature strength in addition to good oxidation resistance and surface stability. Corrosion resistance relies on the formation of protective and slow-growing oxides scales such as Cr_2O_3 and Al_2O_3. Traditionally, superalloys are classified as Fe-, Ni-, and Co-based superalloys.

Superalloys are mainly strengthened by precipitation of intermetallic compounds, such as γ' and γ". Other strengthening mechanisms include solid-solution hardening, carbide precipitation and grain boundary control, directional solidification and single-crystal generation[115].

Superalloys have a close-packed FCC structure, which is capable of maintaining relatively high and reliable tensile, rupture, creep, and thermo-mechanical fatigue properties at temperatures much higher than BCC systems.

Ni-based superalloys contain Ni as base metal element, the reactive oxide formers (Cr, about 20wt.%), solid solution strengtheners(Mo, W), carbide formers (Ti, Ta), and deoxidizers/desulfidizers (Si, Mn). The general functions of alloying elements in Ni-based superalloys are summarized in Table 2.4[116].

Generally, Ni-based superalloy has a gamma Ni matrix with the garmar prime precipitates, such as Ni_3(Al,Ti), which act as coherent barriers to dislocation movement through the pinning effect. Therefore, Ni-based superalloys have good creep strength. The major phases in Ni-based superalloys are as follows[116]:

(1) Gamma Matrix (γ). The continuous matrix is an FCC nickel-base austenitic phase called gamma that usually contains a high percentage of solid-solution elements such as cobalt, chromium, molybdenum, and tungsten.

(2) Gamma Prime(γ'). Aluminum and titanium, for example, are added in amounts to precipitate high volume fraction of FCC γ', which invariably precipitates coherently with the austenite γ matrix.

(3) Carbides. Carbon, added at levels of about 0.05-0.2%, combines with reactive and refractory elements such as titanium, tantalum, and hafnium to form MC carbide. During heat treatment and service these begin to decompose and generate lower carbides such $M_{23}C_6$ andM_6C, which tend to populate the grain boundaries.

(4) Grain boundary γ'. For the stronger alloys, heat treatment and service exposure generate a film of γ' along grain boundaries; this is believed to improve rupture properties.

(5) Borides. They occur as infrequent grain boundary particles.

(6) TCP-Type Phase. Under certain conditions, platelike phases such as σ, μ, and Laves form; this can result in lowered rupture strength and ductility.

Table 2.4 The functions of alloying elements in Ni-based superalloys

Elements	Ni	Co	Fe	Cr	Mo,W	Cb,Ta,Ti	Al	C,B,Zr,Hf
Matrix class	×	×	×	×	×			
γ' class						×	×	
Grain boundary class								×
Carbide subclass				×	×	×		
Oxide scale subclass				×			×	

Ni-based superalloys are expensive compared to Fe-based superalloys, but they have excellent creep strength and toughness at high temperature, as shown in Figure 2.34. Most stainless steels are produced by AOD (argon-oxygen decarburization) steelmaking process, but some Ni-rich superalloys are produced by vacuum-induction melting(VIM) process where alloying, melt treatment, and ingot casting are conducted under vacuum. Chemical compositions can be better controlled by VIM compared to melting in air.

However, VIM is more expensive than AOD. For further alloy refinement the VIM or VAR (vacuum-arc remelting), ESR (electroslag remelting) are used. The ingot is then rolled, forged, drawn or a combination of these, to furnish a wrought products (eg. Strip, plate, tube, bar or wire). Thermomechanical treatments are typically utilized to produce a wrought product[73].

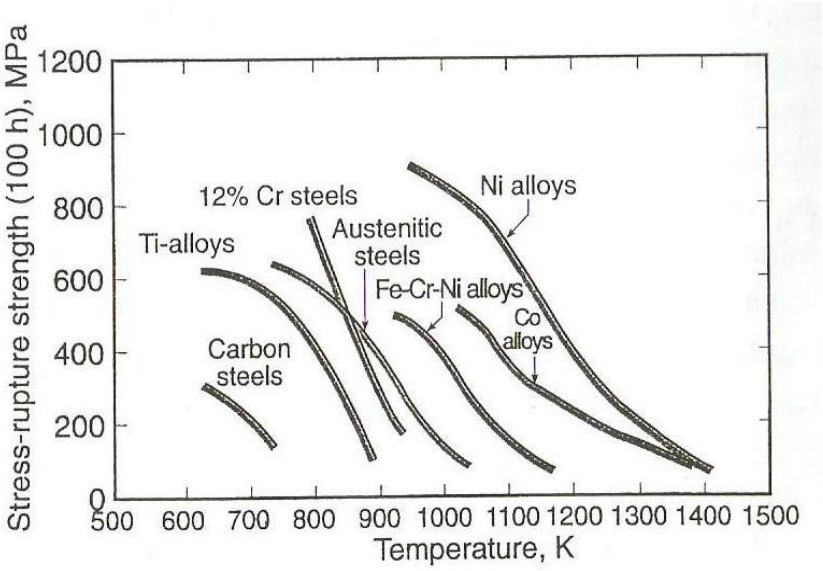

Figure 2.34 Stress required to produce creep-rupture in 100h for various alloys[117].

Iron-based superalloys are essentially compositional extensions of the austenite stainless steel. They are much cheaper than Ni-based surperalloys, but they have low creep strength. They are usually used in furnace, heat-treatment equipment(e.g., basket, trays),piping systems, domestic appliances.

Cobalt-based alloys are more expensive than Ni-based alloys. They have higher melting temperature, and thus provide useful stress capability to a higher absolute temperature than Ni- or Fe-base alloys. Cobalt alloys offer superior hot-corrosion resistance. Generally, nickel or iron is added to stabilize the high temperature austenitic FCC cobalt matrix, but the addition is usually limited to 10wt.% in the cast alloys because higher levels decrease rupture strength. 20-30wt% chromium is also added to impart oxidation and hot-corrosion resistance, and solid-solution strengthening to some extent. But higher chromium content should be avoided to restrain the formation of the detrimental sigma phase. Carbide strengthening is the primary precipitation hardening mechanism utilized in cobalt alloys. Another strengthening mechanism of cobalt alloys is solid-solution strengthening, mainly realized by the addition of refractory elements such as tungsten and molybdenum.

3.0 OBJECTIVES

In order to obtain a whole picture of the corrosion behavior of alloys in atmospheres with low-oxygen and high-sulfur potentials, and to enhance the present understanding of phenomena and mechanisms related to high-temperature alloys exposed to such atmospheres, the objectives of this thesis study are as follows.

3.1 OBJECTIVE I

In an effort to reduce the emission of NO_x in accordance with recently implemented environmental regulation, low NO_x burners are used in the coal-fueled power plants[2]. Besides the effort to reduce the emission of NO_x, improvement of efficiency by increasing the operation temperature is another consideration[1]. The combined effect of the increase in the operating temperature and the usage of low NO_x burners has led to cases of severe wastage of the structural materials. Much research has been done in the past to study the available materials used at about 600^{o}C in the operating environments that have a combination of very low oxygen partial pressure and relatively high sulfur partial pressure. In general, however, there remains very limited understanding of corrosion processes of alloys exposed to environments relevant to low NO_x combustion systems, particularly at temperatures above 600^{o}C. To that end, the operation of fossil

power plants at higher temperature in the near future needs much more reliable guidance for material selection and alloy design.

Accordingly, the first aim of this thesis study is to seek a better understanding of the environmental and compositional factors affecting the corrosion behavior of commercial alloys at temperatures above 600^{o}C. The results from this study will provide valuable guidance for material selection and design in the environments relevant to modern low-NO_x combustion systems. Model alloys will also be prepared to complement the testing and analyses of the commercial alloys. The specific objectives of this study are as follows:

1. Study the influence of compositional factors on reaction kinetics, e.g.

   - Influence of Cr on the location of the kinetics boundary separating sulfide formation from oxide formation, with the former being unwanted from a practical standpoint.

   - Effects of Ti addition on reaction kinetics (model alloys will be made for the study), as preliminary results have indicated that this element can confer improved sulfidation resistance to a base alloy.

   - Assess and elucidate the established benefit of using Co rather than Ni as a major alloying addition for improved sulfidation resistance.

2. Study the effects of gas composition on surface-reaction pathway, i.e., sulfidation, oxidation or both.

3. Provide mechanistic explanations on the formation of some morphological characteristics.

3.2 OBJECTIVE II

As indicated above, most conventional oxidation-resistant alloys do not have acceptable sulfidation resistance under the conditions in which sulfidation is the favored mode of attack[8, 9]. Past research has shown that a refractory element, such as Mo or Nb, has very good sulfdation resistance [12-14, 19, 118]. The addition of Al to an Fe-Mo alloy can further decrease the sulfidation rate[20]. However, all past research on the sulfidation of Fe-Mo-Al alloys was performed in sulfur vapor or H_2-H_2S mixed gas. Surprisingly, little work has been done in the past to investigate the corrosion behavior of Fe-Mo-Al alloys in other simulated high-sulfur and low-oxygen industrial atmospheres, such as syngas.

Related to syngas technologies, hydrogen separation provides a pathway for economical hydrogen production. At present, the commonly used metallic materials for membranes are not only expensive, but also susceptible to contaminants commonly found in syngas, sulfur in particular. Therefore, it would be greatly significant to identify cheaper functional materials which have both good corrosion resistance and permeability to hydrogen. Much research [24-29] has been done to identify viable new hydrogen separation materials. However, little research has been done on the Fe-Mo-Al alloy, so it is worthwhile to determine if such an alloy can offer a simple and inexpensive solution for hydrogen separation.

Therefore, another goal of the current study is to determine the possibility of functional usage of Fe-Mo-Al alloys as a membrane in syngas through studying their corrosion behaviors. The specific objectives are as follows:

1. Characterize the microstructure and phase constituents of the alloys and investigate the corrosion behavior and the corrosion mechanism.
2. Investigate the effect of different Al levels (5wt.%Al and 10wt.% Al) on the corrosion resistance and on the diffusion behavior of Fe.
3. Gain a better understanding of the corrosion behavior of two-phase alloys.

4.0 EXPERIMENTAL PROCEDURES

4.1 COMMERCIAL ALLOYS

Eight commercial Haynes alloys were chosen for testing in the simulated environments of low NO_x burners. The nominal compositions of alloys tested are listed in Table 4.1 The alloys were divided into four types for analysis: (1) Ni-based, (2) Ni-Fe-based, (3) Ni-Co-based, and (4) Co-based. All of the alloys tested are designated as being Cr_2O_3-scale forming when exposed to air.

The test samples were prepared from mill-annealed plates that were received from Haynes International (www.haynesintl.com). The samples had dimensions of about 10mm ×10mm× (1-3)mm (*i.e.*, the thickness of sheet varied). A 1mm diameter hole was drilled near the edge of a given sample so that it could be suspended in the furnace. Samples were polished to a 240-grit finish, cleaned in acetone and then weighed prior to testing. The laboratory testing system is shown schematically in Figure 4.1. The main part of this system is a horizontal furnace. The testing system was first vacuum pumped and then purged with argon gas for about 20 hours to remove oxygen prior to exposing the samples to the reaction gas. The reaction gas flowed through the system at a rate of $50cm^3$/min. After thermal exposure for a certain time, the samples were taken out of the hot zone and cooled to room temperature under an argon gas flow. The exiting test gas

was bubbled through Na_2CO_3 solution to trap H_2S and then through a Bunsen burner to burn CO to CO_2.

Table 4.1 Chemical composition

	Alloy	Composition(wt.%)									
		Ni	Fe	Co	Cr	Al	Si	Mo	Mn	C	Others
Nii-Fe based	HR-120	37	33	3*	25	0.1	0.6	2.5	0.7	0.05	2.5W*-0.7Nb-0.004B-0.2N
Ni- based	230	57	3*	5*	22	0.3	0.4	2	0.5	0.1	14W-0.02 La-0.015B*
Ni-Co-based	HR-160	37**	2*	29	28	-	2.75	1*	0.5	0.05	-
	263	52**	0.7*	20	20	0.6*	0.4*	6	0.6*	0.06	2.4Ti*-0.2Cu*
	617	54**	1	12.5	22	1.2	-	9	-	0.07	0.3Ti
	R-41	52**	5*	11	19	1.5	0.5*	10	0.1*	0.09	3.1Ti*-0.006B
	282	57**	1.5*	10	20	1.5	0.15*	8.5	0.3*	0.06	2.1Ti-0.005B
Co-based	188	22	3*	39**	22	-	0.35	-	1.25*	0.10	14W-0.03La

*maximum, ** as balance.

A premixed gas cylinder containing N_2-15%CO-3%H_2-0.12%H_2S was designated as being Gas 1. Gas 2 and Gas 3 were obtained by bubbling Gas 1 through distilled water at a controlled temperature of either 0^oC and 25^oC to obtain 0.6% or 3% water vapor, respectively. Gas 3, with 3% water vapor, represents the simulated gas of a low NO_x burner. The gas compositions used are the same as those used by Paul et al.[3].

Gases 1 and 2 were used to study in greater detail the influence of gas composition on the corrosion behavior. The exposures were at 750^{o}C (1382^{o}F) unless stated otherwise.

After thermal exposure, the samples were visually inspected and weighed. The samples were then examined using X-ray diffraction (XRD). Diffraction measurements were performed on as-formed reaction products and base alloys using a Bruker D8 Discover XRD with LynxEye detector. A Cu X-ray source operated at 40kV and 40mA was used. Patterns were recorded over a 2θ range of 15 to 95° at a scan speed of 0.4 sec/step with the increment of 0.04^{o}.

After XRD analysis, the samples were mounted with epoxy and then polished in a suspension to 1 um finish. The surfaces of the samples, as well as the cross-sections, were observed using scanning electron microscopy (SEM). X-ray energy-dispersive spectroscopy (EDS) was used to conduct semi-quantitative composition analysis.

Besides the above-mentioned analytical techniques, such as XRD, SEM and EDS, XPS (X-ray photoelectron spectroscopy) was used to assess the surface composition. The XPS measurements were performed using a PHI 5600ci instrument with monochromatic Al Kα X-rays and an analyzer pass energy of 58.7 eV. Elemental concentrations were calculated from O*1s*, Si*2p3*, and Zn*2p3* peak areas and calibrated sensitivity factors. Elemental depth profiles were acquired using argon ion sputtering. The differentially-pumped ion gun was operated at 1.5×10^{-2} Pa and 25 mA. The sputtering rate, calibrated using a 10 nm-thick Pt standard, was approximately 10 nm/min.

Finally, stability diagrams used to describe the equilibrium phases present at given temperature, pressure and oxidant (O_2, S_2) potential were constructed from thermodynamic data in the HSC software. The activity of metals was approximated to be

their mole fraction based on the assumption of ideal behavior. The stability diagrams of selected alloys are shown in Figure 4.2 and Figure 4.3.

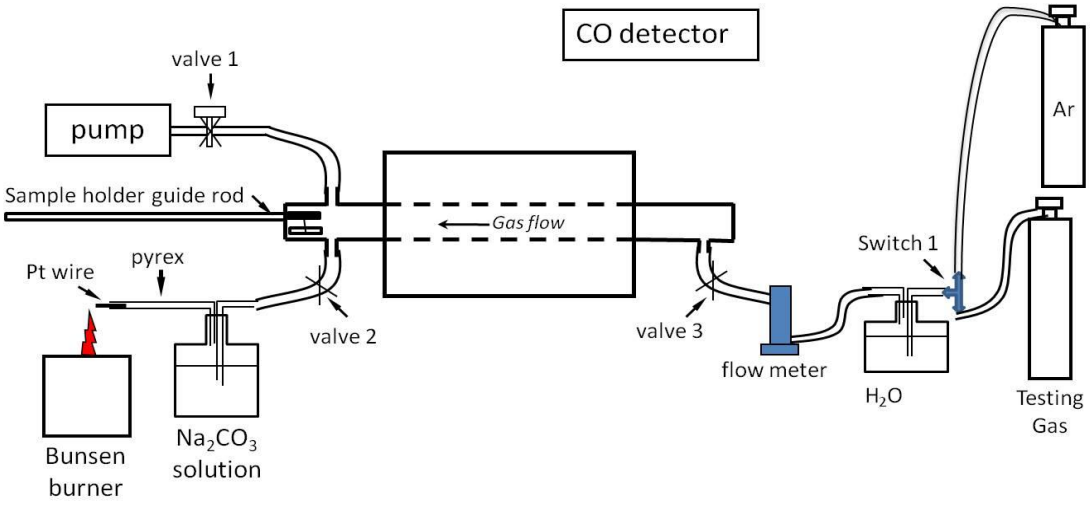

Figure 4.1 Schematic diagram of the apparatus used for corrosion studies

Table 4.2 Gas compositions and oxidant potentials in simulated low NO_x burners

Gas number	Gas composition, vol%	PS_2(atm)	PO_2(atm)	PH_2S(atm)
1	N_2-15%CO-3%H_2-0.12%H_2S	1.3×10^{-7}	1.0×10^{-25}	0.0012
2	N_2-14.91%CO-2.98%H_2-0.6%H_2O-0.119%H_2S	1.3×10^{-7}	1.1×10^{-21}	0.00119
3	N_2-14.55%CO-2.91%H_2-3%H_2O-0.116%H_2S	1.3×10^{-7}	2.9×10^{-20}	0.00116

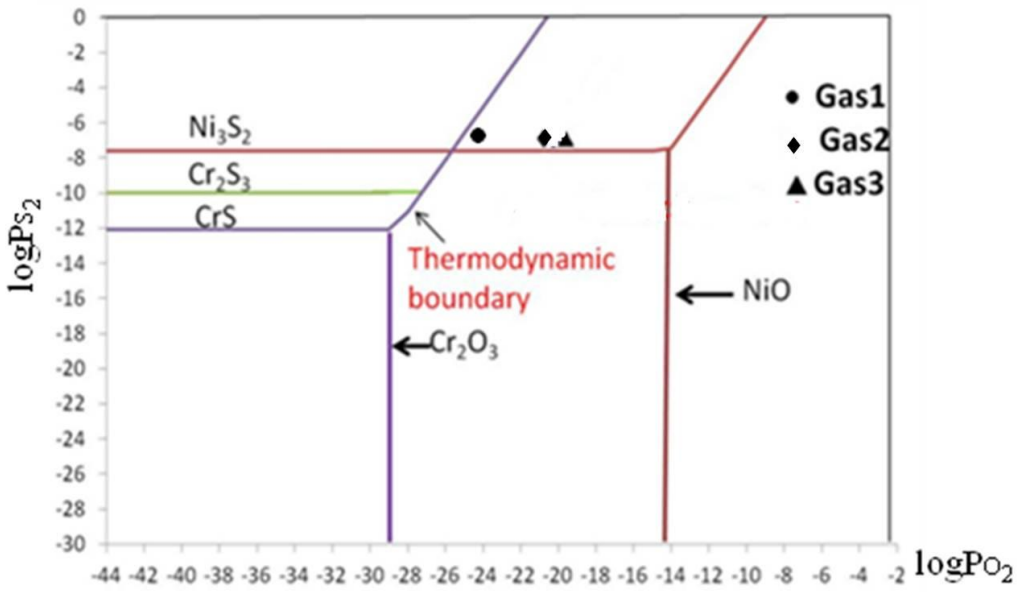

Figure 4.2 Stability diagram of Alloy HR-120 at 750℃

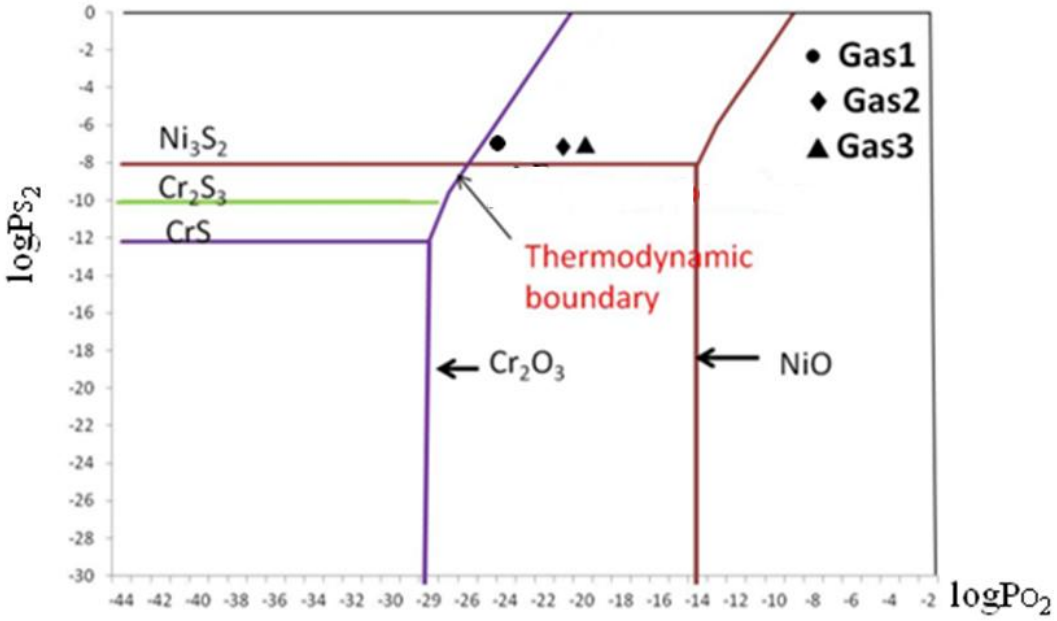

Figure 4.3 Stability diagram of Alloy 263 at 750℃

4.2 MODEL ALLOYS STUDY

Eleven model alloys in total were designed to complement the study on commercial alloys. All the model alloys were fabricated at the Materials Preparation Center of the Ames Laboratory (www.ameslab.gov). The alloys are prepared by arc-melting 99.95% purity particles of the constituent elements in a water-cooled copper hearth in an atmosphere of high-purity argon that was gettered by melted Ti. After melting for several times, a given alloy was drop-cast into a 10 mm diameter chilled copper mold. The resulting alloy bar was then annealed. As will be described in the following sections, the eleven model alloys were classified into three groups: alloys with different Cr and Co level (Alloys 1,2,3,4 and 5), alloys modified with minor alloying elements (Alloy 6, 7 and 8), and alloys with different Ti levels (Alloy 9, 10 and 11).

The testing system, test gases and test procedures were the same as those used for the commercial alloys. The procedures of sample preparation and analytical methods were also the same.

4.2.1 Model alloys with different Cr and Co levels

After melting and casting, model alloys with different Cr and Co levels were annealed at 1100^{o}C for 24 hours. The nominal compositions are listed in Table 4.3.

Table 4.3 The composition of model alloys with different Cr and Co level

Alloy	Composition (wt.%)		
	Ni (wt.%)	Cr (wt.%)	Co (wt.%)
1	58	22	20
2	38	22	40
3	32	28	40
4	52	28	20
5	62	28	10

4.2.2 Model alloys modified with minor alloying elements Al, Ti and Mo

The selected model Alloys 1, 2 and 4 were modified by adding minor amounts of Al, Ti and Mo. The nominal compositions of the three new model alloys are shown in Table 4.4. The alloys were annealed at 1100^{o}C for 24 hours.

Table 4.4 The composition of model alloys 6,7 and 8(wt.%)

Alloy	Ni	Cr	Co	Al	Mo	Ti	Ni/Co
6	50.6	22	17.4	2.5	5	2.5	2.9
7	44.8	28	17.2	2.5	5	2.5	2.6
8	33.1	22	34.9	2.5	5	2.5	0.95

4.2.3 Model alloys with different Ti levels

In order to study the effect of Ti on sulfidation resistance, three other model alloys were made with different Ti levels: 0.5wt.%Ti, 1.5wt%Ti and 3wt%Ti. The nominal compositions of the three model alloys are shown in Table 4.5. The alloys were also annealed at 1100^{o}C for 24 hours.

Table 4.5 The composition of model alloys with different Ti levels (wt.%)

Alloys	Ni	Fe	Co	Cr	Al	Si	Mo	Ti
9	56.5	3	13	20	1.5	0.5	5	0.5
10	55.5	3	13	20	1.5	0.5	5	1.5
11	54	3	13	20	1.5	0.5	5	3

4.3 IRON-MOLYBEDNUM-ALUMINUM ALLOYS

The preparation of Fe-Mo-Al alloys was the same as that with the models alloys mentioned above, except that annealing was performed at 1000^{o}C for 50 hours. The chemical compositions of the two alloys were Fe-30wt.%Mo-5wt.%Al and Fe-30wt.%Mo-10wt.%Al. Table 4.6 shows the composition of the simulated syngas atmosphere.

Table 4.6 Gas compositions of simulated syngas

Gas No.	Gas composition, vol%
4	30%CO_2-1%CO-0.005%H_2S-19%H_2O-H_2
5	30%CO_2-1%CO-0.01%H_2S-19%H_2O-H_2

The test temperature was 500^{o}C. The testing system was same as that used for the commercial and model alloys. The sample-preparation procedures were also same as those used for the commercial alloys.

Figure 4.4 presents the calculated stability diagram for alloy Fe-30Mo-5Al at 500℃, as determined on the assumption of ideal alloy behavior. Since there is not a significant difference in Al content between the two alloys, the diagram is considered suitable for both alloys.

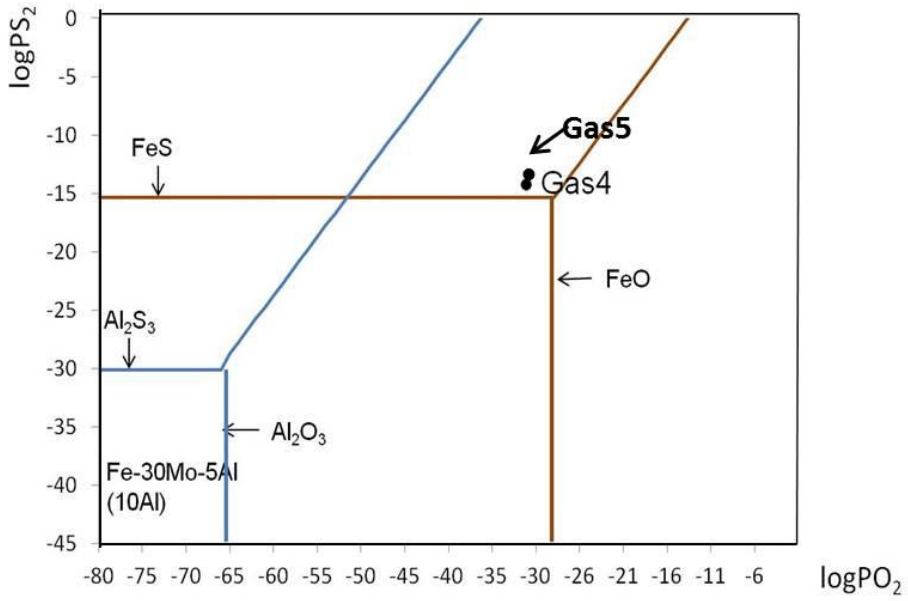

Figure 4.4 Stability diagram of alloy Fe-Mo-Al at 500℃

5.0 RESULTS AND DISCUSSION

5.1 CORROSION BEHAVIOR OF COMMERCIAL ALLOYS

5.1.1 The influence of composition on the kinetic boundary

Figure 5.1 summarizes the primary type of scale (oxide or sulfide) that formed on selected alloys after testing for 100 hours at 750^{o}C in the three gases. The dot and triangle represent oxides and sulfides, respectively. The dashed line represents an estimation of the threshold oxygen partial pressure above which a protective chromium oxide scale forms. As shown in this figure, and as would be expected, Cr content greatly affects this threshold P_{O2}. With an increase in chromium content, the threshold P_{O2} decreases. Low threshold oxygen partial pressure favors the formation of protective Cr oxide. This result verifies the established beneficial effect of Cr.

However, the trend shown in Figure 5.1 is not entirely straightforward, as a protective oxide scale formed on alloy 263, after testing for 100 hours in Gas 2, even though it contains only 20 wt.%Cr. As will be verified and discussed in more detail in a later chapter, this is due to the effects of minor alloying elements such as Al, Ti and Mo.

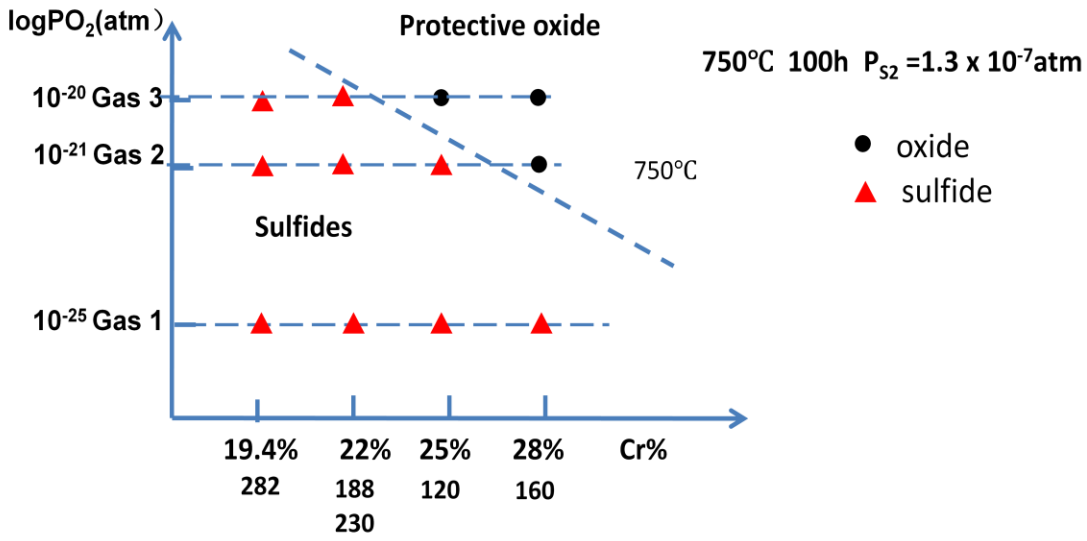

Figure 5.1 The influence of Cr content on the threshold oxygen partial pressure to form protective chromium oxide

The information of the primary scale type can also be used to determine the kinetic boundary in the oxide-sulfide stability diagram for a given alloy. The stability diagrams for Alloys 120 and 263 are shown in Figure 5.2. The alloys are assumed to be ideal, so that the activities of the alloying elements such as Cr are approximated to be equal to their mole fraction for the purpose of calculating equilibrium boundaries. Sulfides formed on Alloy 120 in Gases 1 and 2, while oxides formed in Gas 3. Therefore, the kinetic boundary is located somewhere between Gas 2 and Gas 3, as shown in Figure 5.2. For Alloy 263, sulfides formed in Gas 1, while oxides formed in Gases 2 and 3. Thus, the kinetic boundary for this alloy is located between Gas 1 and Gas 2, as shown in Figure 5.2.

Figure 5.2 clearly shows that the alloy composition greatly influences the location of the kinetic boundary. The kinetic boundary of alloy 263 favors the formation of Cr oxide at a lower oxygen partial pressure. It is obviously shown from this result that the location of kinetic boundary is alloy dependent, but not solely related to Cr content, as it also depends on other alloying elements such as Al, Ti and Mo. The effects of these elements will be discussed in more detail in a later chapter.

Since Gas 1 is the most reducing Gas, it is therefore expected to be the most aggressive. The results shown in the following are focused mainly on Gas 1.

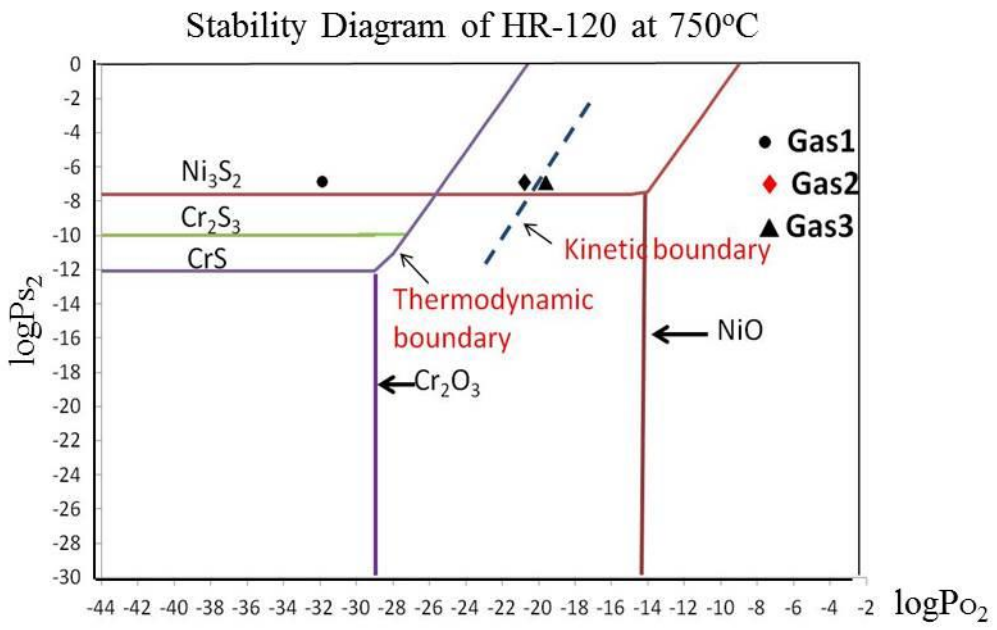

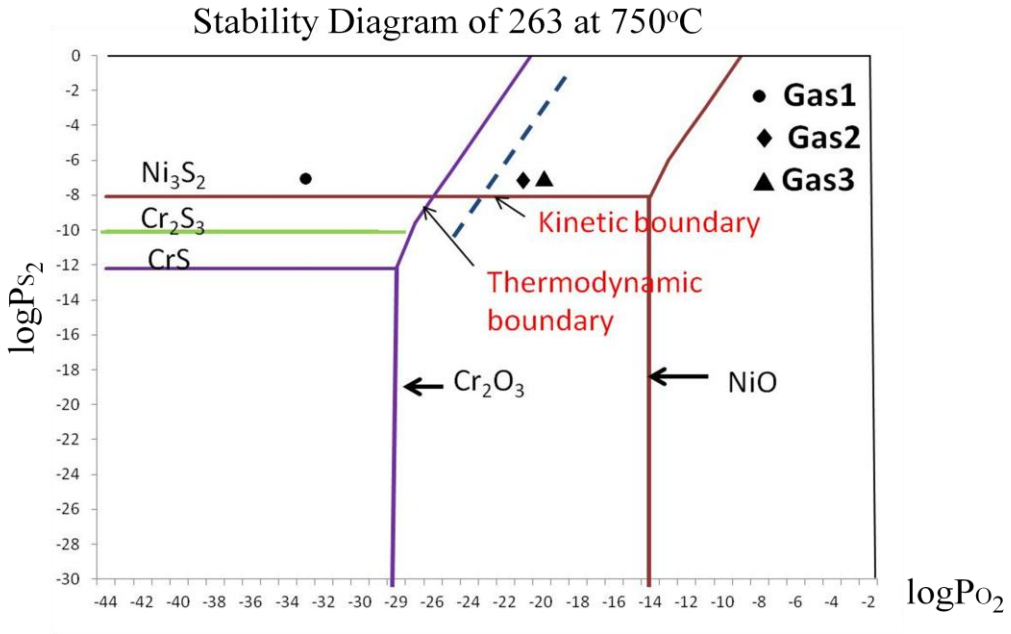

Figure 5.2 Kinetics boundaries of Alloy HR-120 and 263 at 750℃

5.1.2 The influence of composition on weight gain

Figure **5.3** compares the weight gains after testing for 100 hours in Gas 1. The figure shows that the Ni-based alloy has the greatest weight gain, followed by the Ni-Fe-based alloy and then the Co-based alloy. Ni-Co-based alloys exhibit the smallest weight gain. Weight gain can be a reasonable measure of corrosion resistance, thus it is inferred that the Ni-Co based alloys have the best corrosion resistance compared to Ni- based, Ni-Fe based and Co- based alloys.

It is common to consider Cr as the main variable for conferring sulfidation resistance, as well as Co[119]; however, the results of Alloys 160 and 263 highlight that there are more factors to consider. Alloy 160 contains high levels of Cr and Co, which contribute to the good corrosion resistance. But the Cr content of Alloy 263 (20wt.%) is not high and it has the least weight gain among all alloys tested(Figure 5.3) When comparing the compositions of the two alloys, it can be deduced that the minor amounts of Al, Ti and Mo in Alloy 263 play an important role to improve its sulfidation resistance.

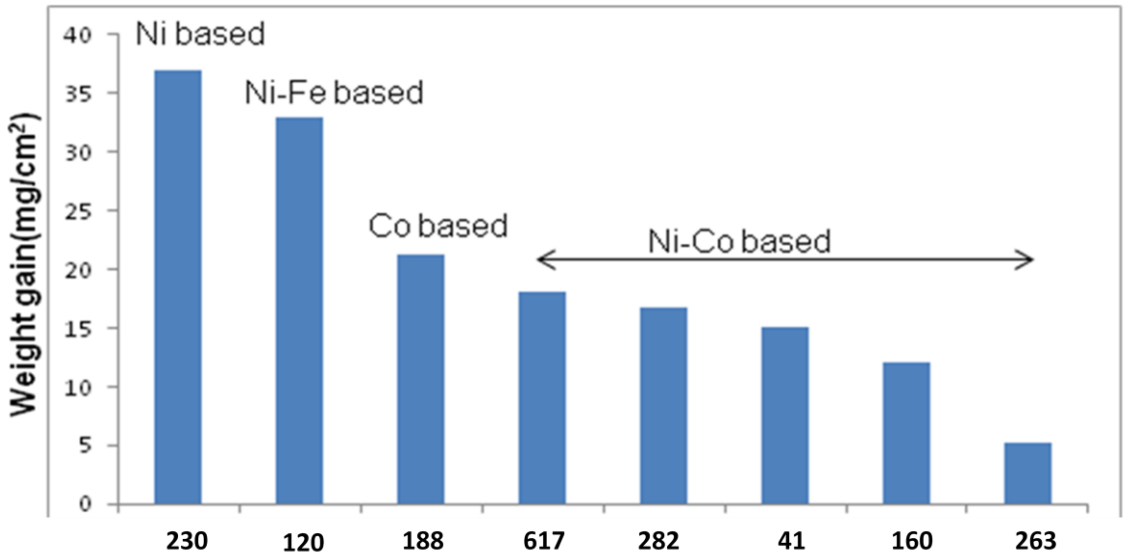

wt.%	Ni	Fe	Co	Cr	Al	Si	Mo	Mn	C	Others
160	37**	2*	29	28	-	2.75	1*	0.5	0.05	-
263	52**	0.7*	20	20	0.6*	0.4*	6	0.6*	0.06	2.4Ti*-0.2Cu*

Figure 5.3 Comparison of weight gains after testing for 100 hours for Gas 1

The collective influence of Co, Ni and Fe in imparting sulfidation resistance is shown in Figure 5.4, which plots in a Cr-Co-(Ni+Fe) Gibbs triangle the effective compositions of these alloys, along with the corresponding weight-gain values (mg/cm^2) after testing for 100 hours in Gas 1. As shown in this figure, Cr contents in the alloys are within a relatively narrow range of 19-28wt.%, but weight gains vary significantly. The results here show that not just Cr, but other alloying elements also affect the sulfidation resistance. For instance, it is clearly shown in Figure 5.4 that the weight gains tend to increase with the increase in (Ni+Fe) content. However, there is an exception indicated by the triangle in Figure 5.4 which is the Alloy 263 with a weight gain of 5.2 mg/cm^2.

This makes the story more complicated. There are other composition variables beyond just Cr content that affect sulfidation resistance.

Figure 5.5 shows the influence of Co content on weight gain after testing for 100 hours in Gas 1. As shown in this figure, the weight gain tends to decrease with increase in Co content. However, there appears to be a critical Co content above which the weight gain increases with increase in Co content.

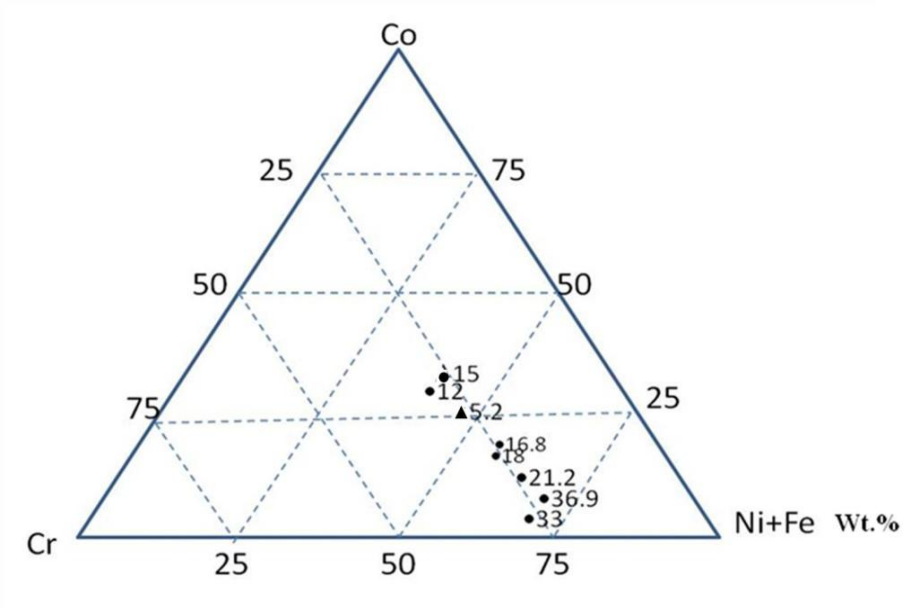

Figure 5.4 The Influence of Cr/Co ratios on weight gain (in mg/cm^2) after 100h exposure to Gas1

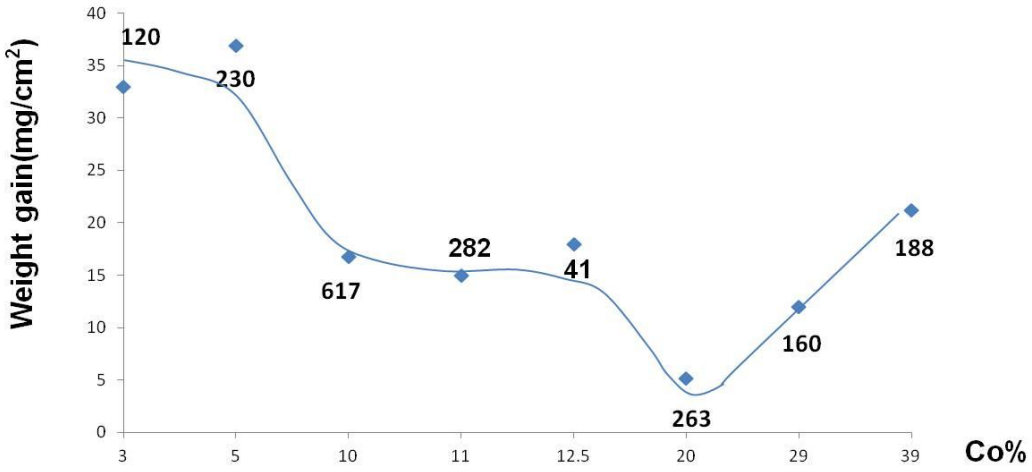

Figure 5.5 The Influence of Co content on weight gain

It is known that high Co content generally is good for sulfidation resistance[56, 95], so the trend shown in Figure 5.5 is at first glance somewhat unexpected. However, further assessment will show that the trend is due to the beneficial effects of certain minor alloying elements. The Co content in Alloy 263 is not as high as that in Alloy 160, but Alloy 263 contains 0.6wt.%Al, 6wt.%Mo and 2.4wt.%Ti, which are believed to contribute to its least weight gain (the compositions of Alloy 160 and 263 can be seen in Figure **5.3**).

Figure 5.6 compares the cross-sectional images of Alloys 160 and 263. The two cross-sections look similar in that they both formed sulfides with a multi-layered microstructure. The outer scale is comprised of Ni_3S_2 and Co_9S_8, as determined by XRD analysis summarized in Figure 5.7. The intermediate scale is mainly Cr sulfide, and the inner layer is the mixture of Cr oxide and sulfide, based on EDS composition analysis. However, the outer and inner layers of Alloy 263 are much thinner than those of Alloy

160. This implies that there must be some diffusional blocking effects in the product scale formed on Alloy 263. This blocking effect might come from the presence of Ti and Al in the inner layer of Alloy 263. These particular elements form even more stable oxides than Cr_2O_3, as can be seen in Figure 5.8. The compositions of the inner layers of Alloy 160 and 263 are indicated by points 1 and 2, respectively. As measured by EDS, point 1 has a composition of 26.5O-35.3S-23.6Cr-7.0Co-7.6Ni(at.%), while point 2 has the composition of 36.9O-25.6S-24.3Cr-3.0Co-3.1Ni-0.6Si-2.3Al-4.2Ti (at.%). Significant amounts of oxygen indicate the existence of metal oxides in the layer.

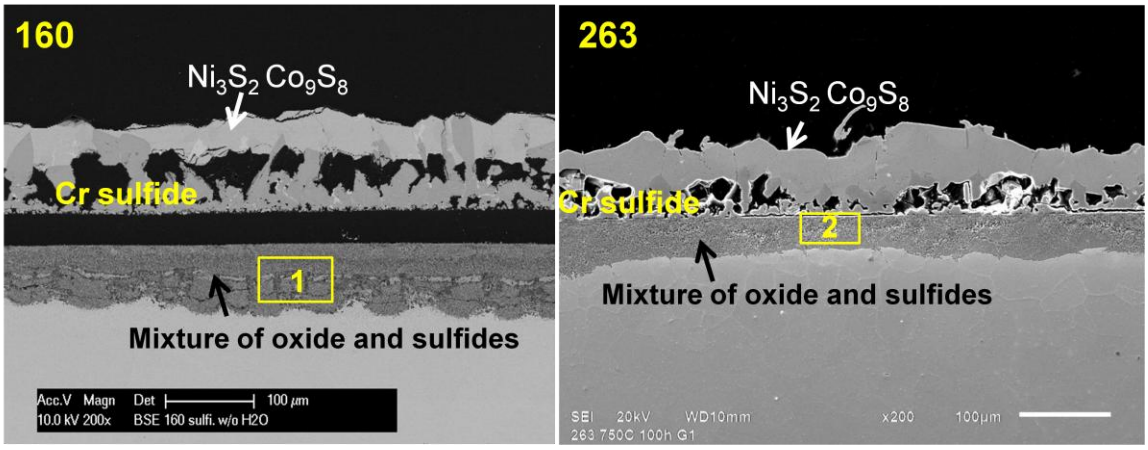

Figure 5.6 Cross-sectional images of Alloys 160 and 263 after testing for 100h in Gas 1

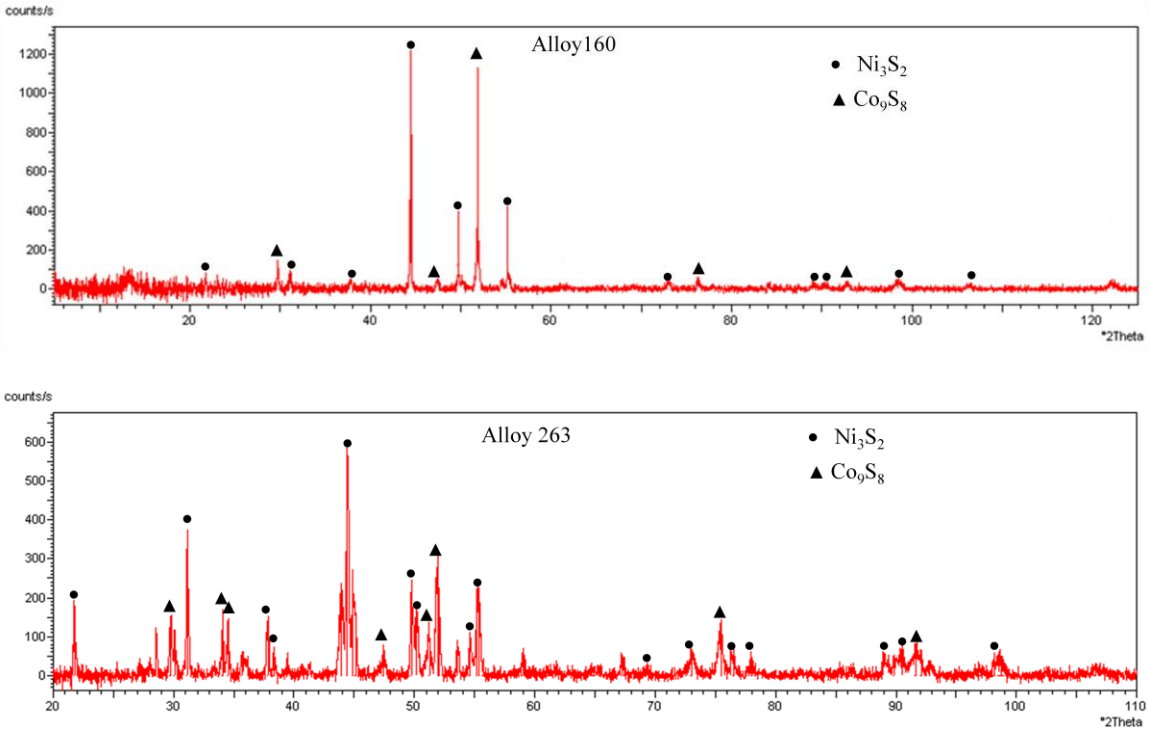

Figure 5.7 XRD analysis of Alloys 160 and 263 after 100 hours in Gas 1

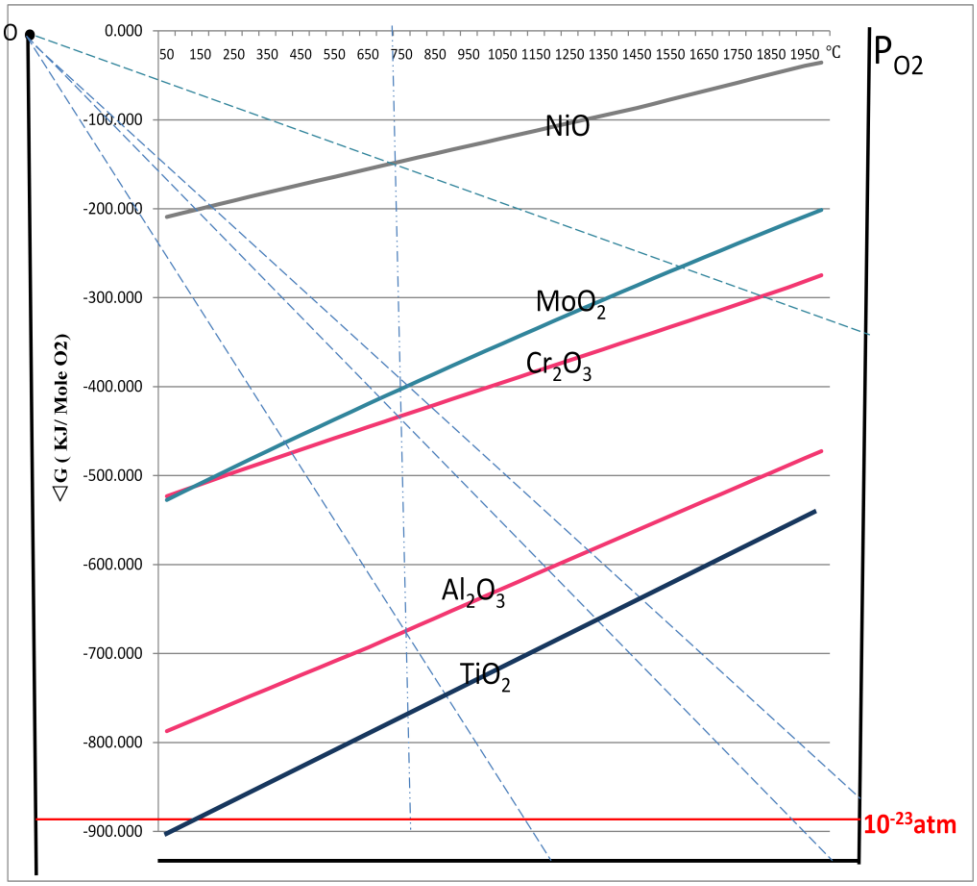

Figure 5.8 Elingham diagram for some oxides, showing that Al_2O_3 and TiO_2 are thermodynamically more stable than Cr_2O_3.

The current study shows that not just Cr and Co are important, but so too are minor alloying elements such as Al, Ti and Mo. A study by some Japanese researchers[120] also verified the beneficial effects of Ti and Al in conferring suflidation resistance. Figure 5.9 compares the weight gain of several Ni-based alloys after testing for 49h at 600°C in H_2-H_2S (Ps_2 is $10^{-10.5}$atm). As shown in this figure, weight gain decreases with the addition of Mo; while, weight gain further decreases with addition of Al and Ti.

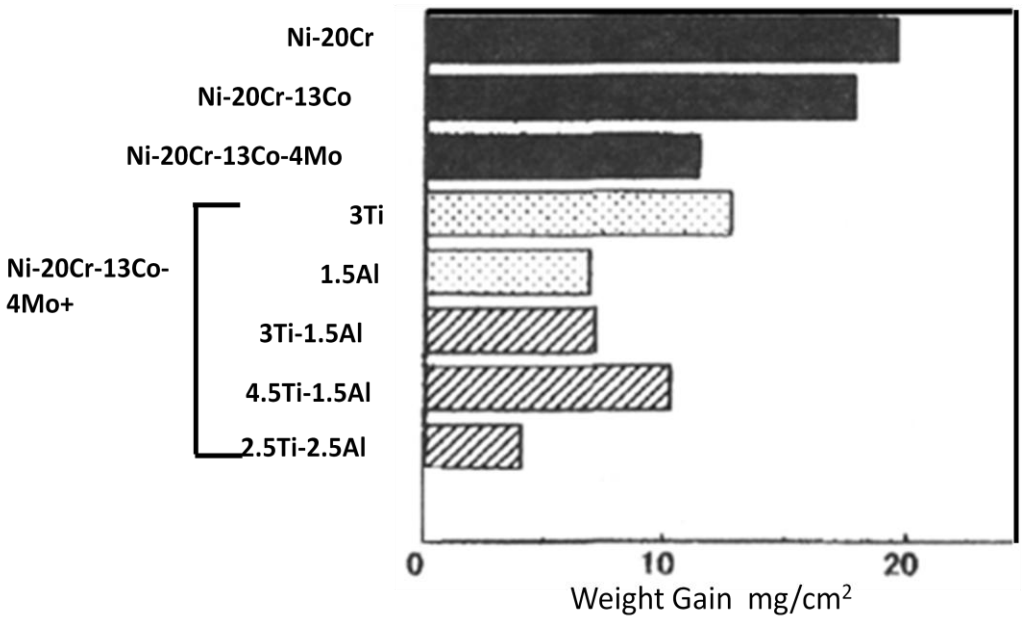

Figure 5.9 Weight gain of several Ni-based alloys after testing for 49h at 600°C in H_2-H_2S with P_{s2} is $10^{-10.5}$atm

In order to verify the effects of major alloying elements (Cr, Co) and minor alloying elements (Ti, Al and Mo), model alloys were made. Results for these alloys will be presented in chapter 5.2.1 and 5.2.2.

5.1.3 Breakaway corrosion

Until now, we have discussed the weight gain after testing for 100 hours. In this section, the weight changes as a function of time are studied. Figure 5.10 shows the weight gains of selected alloys as a function of time when exposed to Gas 1 at 750°C. As shown in this figure, the four alloys eventually suffered breakaway corrosion, *i.e.*, accelerated weight-gain kinetics, after a certain initial stage of relatively low weight gains. This latter

"protective" corrosion period lasted for 5 to 50 hours, depending on the alloy. HR-160 showed the slowest kinetics for the longest duration.

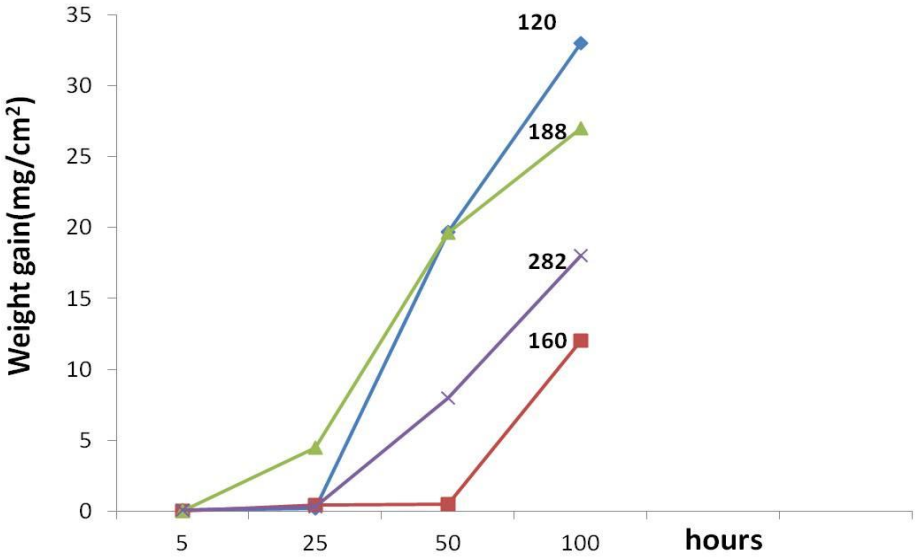

Figure 5.10 Weight gain vs. exposure time at 750 °C in Gas 1

The corrosion resistance of the alloys studied relies on the formation of a protective chromia scale. After formation of the chromia scale, the factor that determines the corrosion resistance is how long the scale can be maintained. It is therefore important to understand the process of the breakdown of the protective scale. Figure 5.11 illustrates cross-sectional images of Alloy 120 after different exposure times during the protective stage and after breakaway. After testing for 5 hours, it is showed that the alloy was protected by a continuous Cr-rich oxide layer. After testing for 25 hours, chromium

sulfides (Cr_2S_3) and iron sulfide (FeS) formed and reacted to form iron-chromium spinel sulfide ($FeCr_2S_4$) above the chromium oxide scale, which was detected by XRD (Figure 5.12).

After testing for 50 hours, nickel sulfide formed above the chromium sulfide layer. The process of breakaway on other alloys can be seen in Figure 5.13 to Figure 5.18, which show the cross-sectional images of the alloys after testing for various durations.

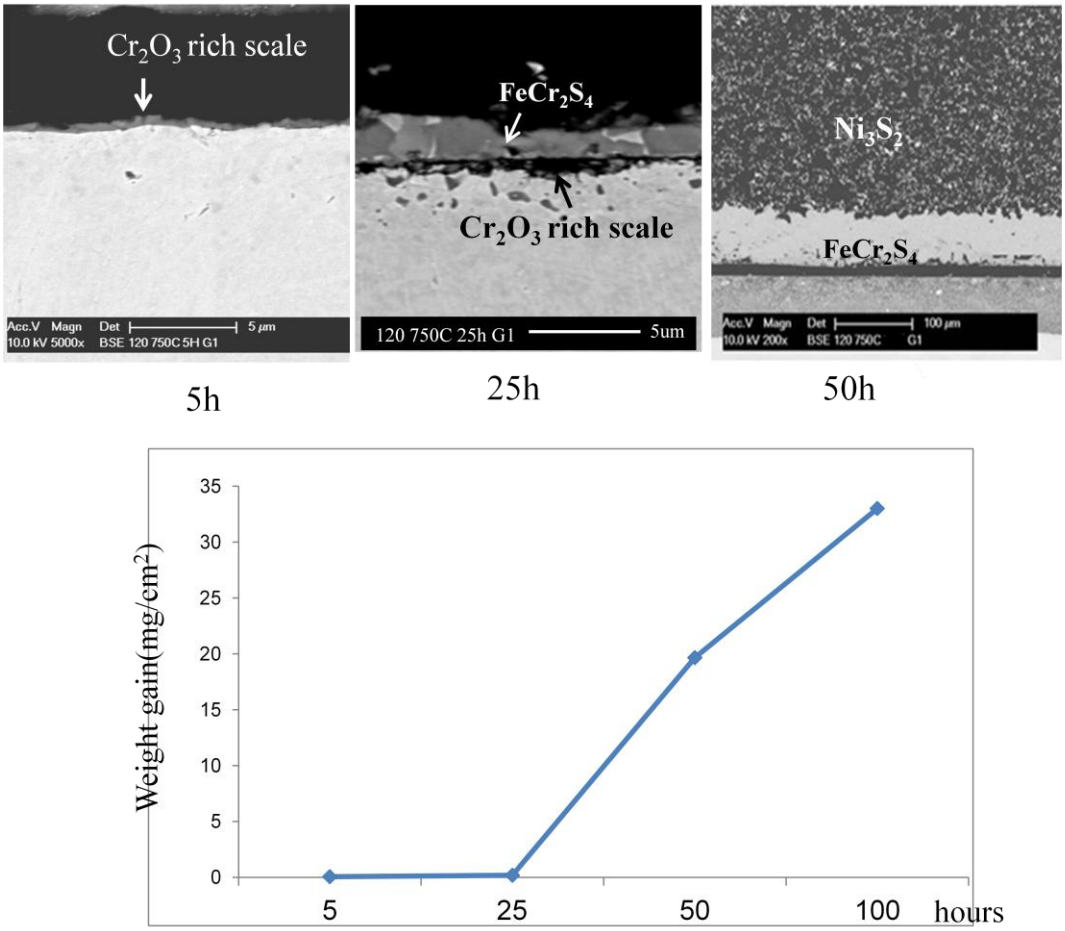

Figure 5.11 Corrosion behavior of Alloy HR-120 in Gas 1 at 750 °C showing oxides scales during the protective stage and after breakaway corrosion

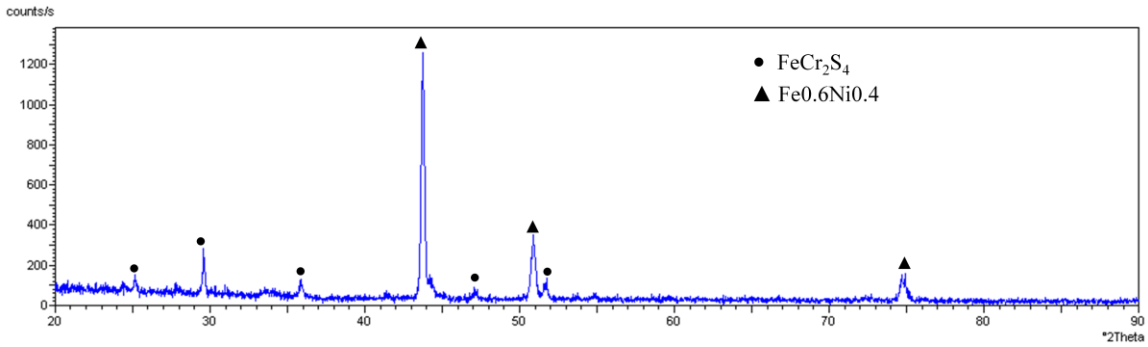

Figure 5.12 XRD pattern of Alloy 120 after 25h in Gas 1

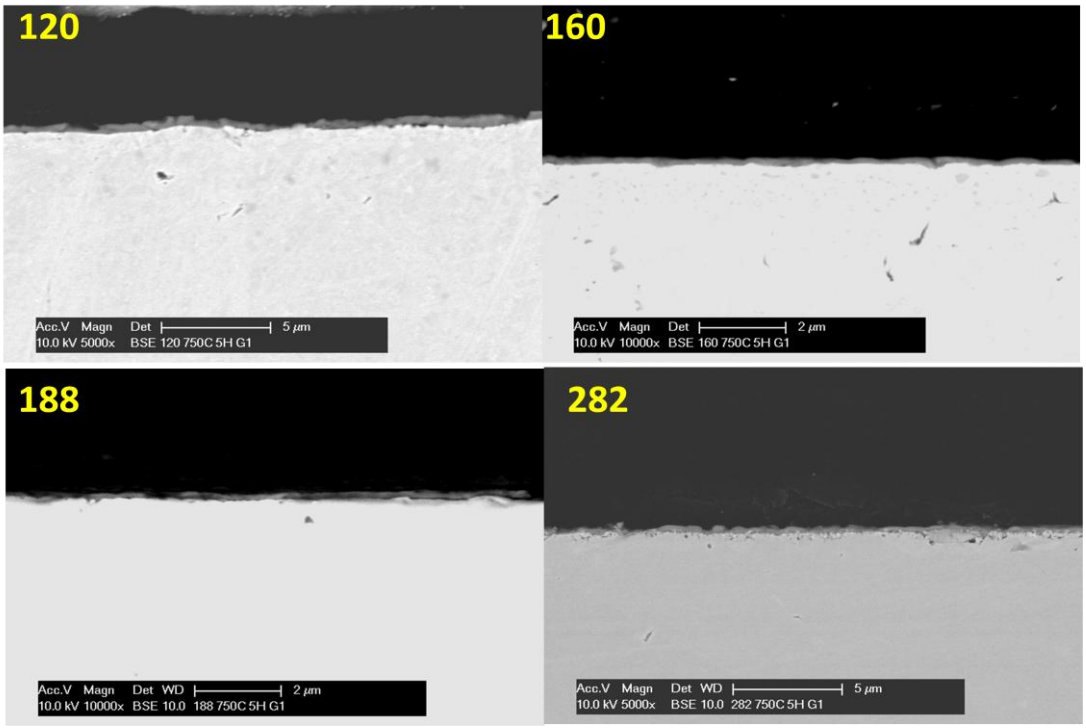

Figure 5.13 Cross-sectional images of some selected alloys after testing for 5 h in Gas1

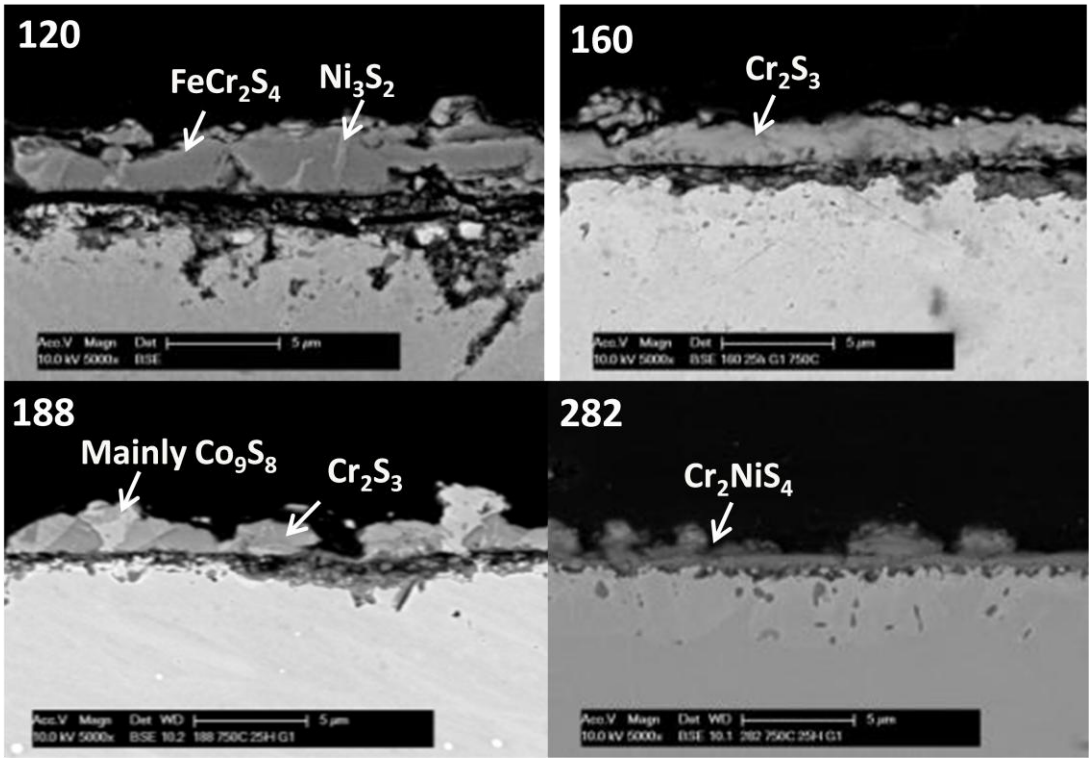

Figure 5.14 Cross-sectional images of some selected alloys after testing for 25 h in Gas 1

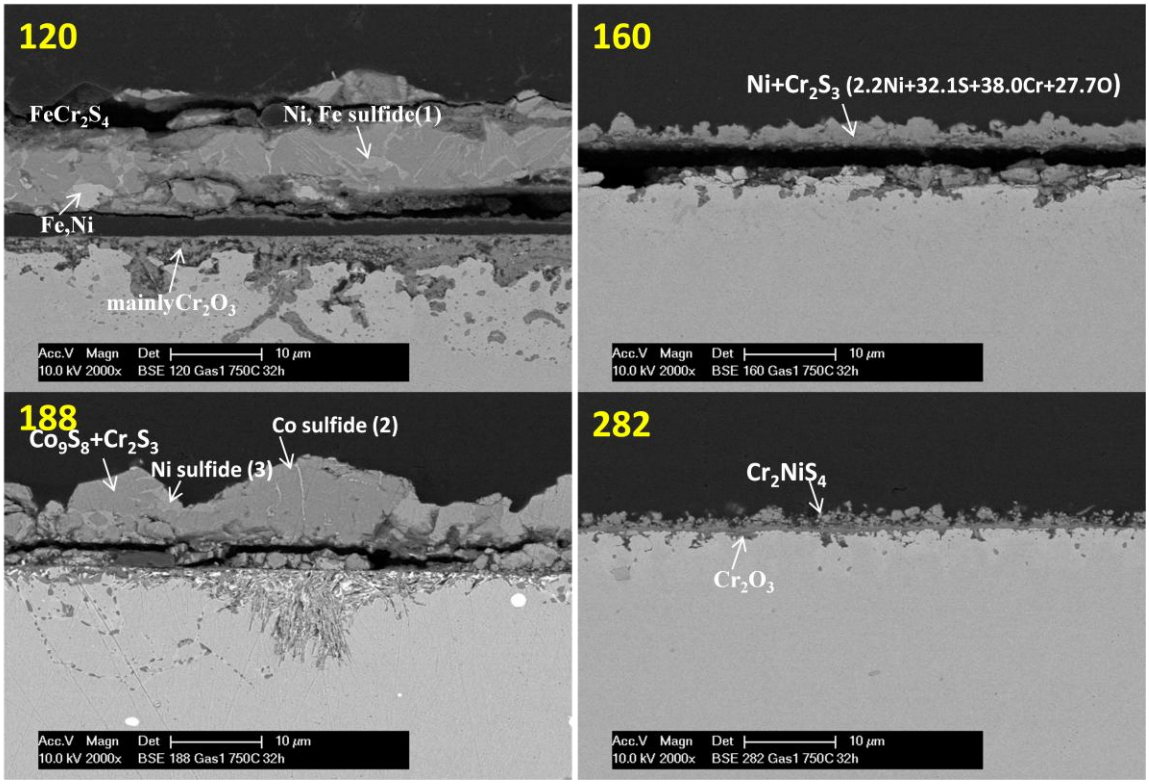

Figure 5.15 Cross-sectional images of some selected alloys after testing for 32h in Gas 1

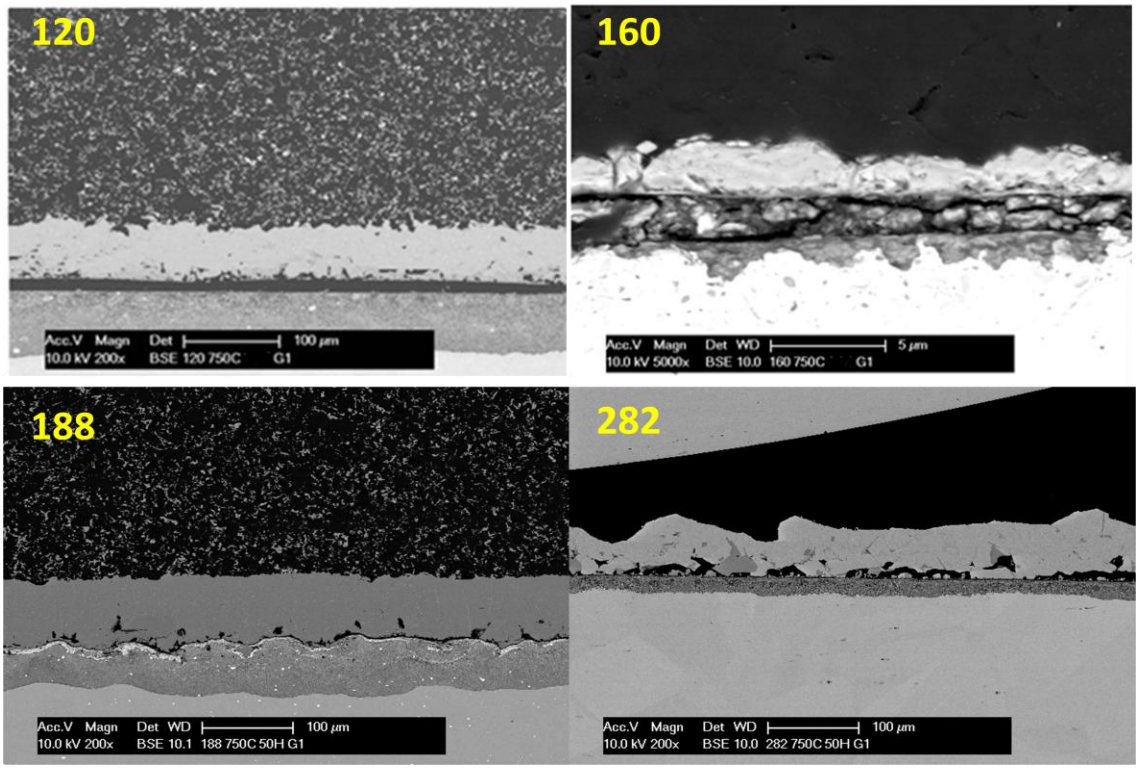

Figure 5.16 Cross-sectional images of some selected alloys after testing for 50h in Gas1

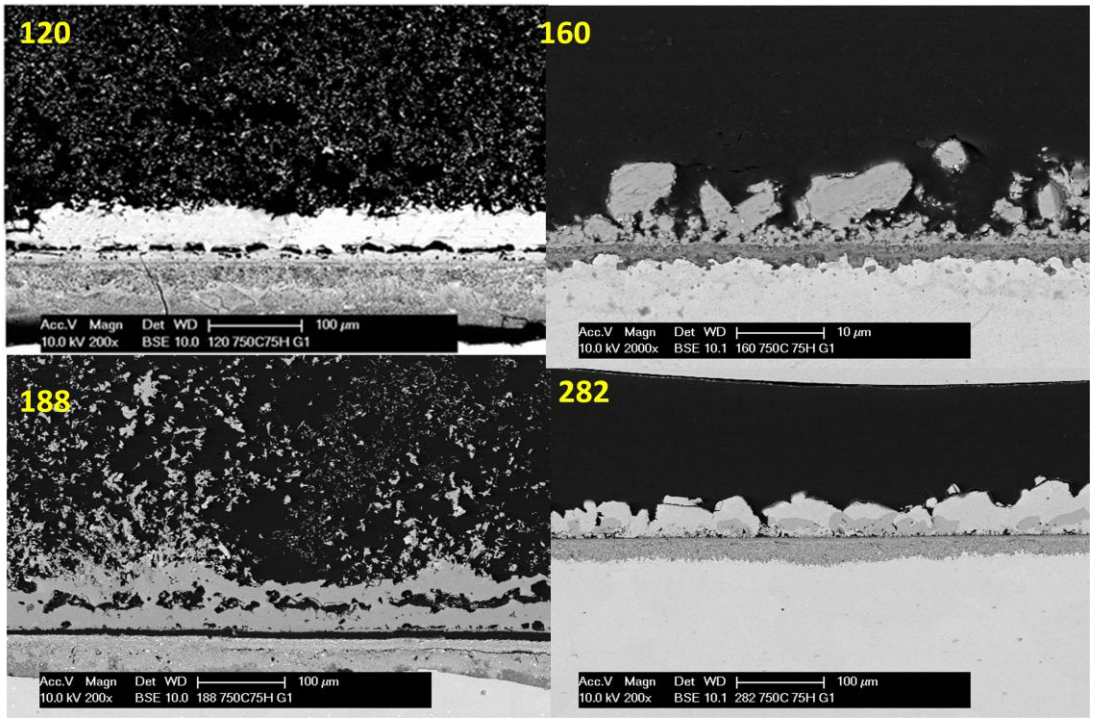

Figure 5.17 Cross-sectional images of some selected alloys after testing for 75h in Gas1

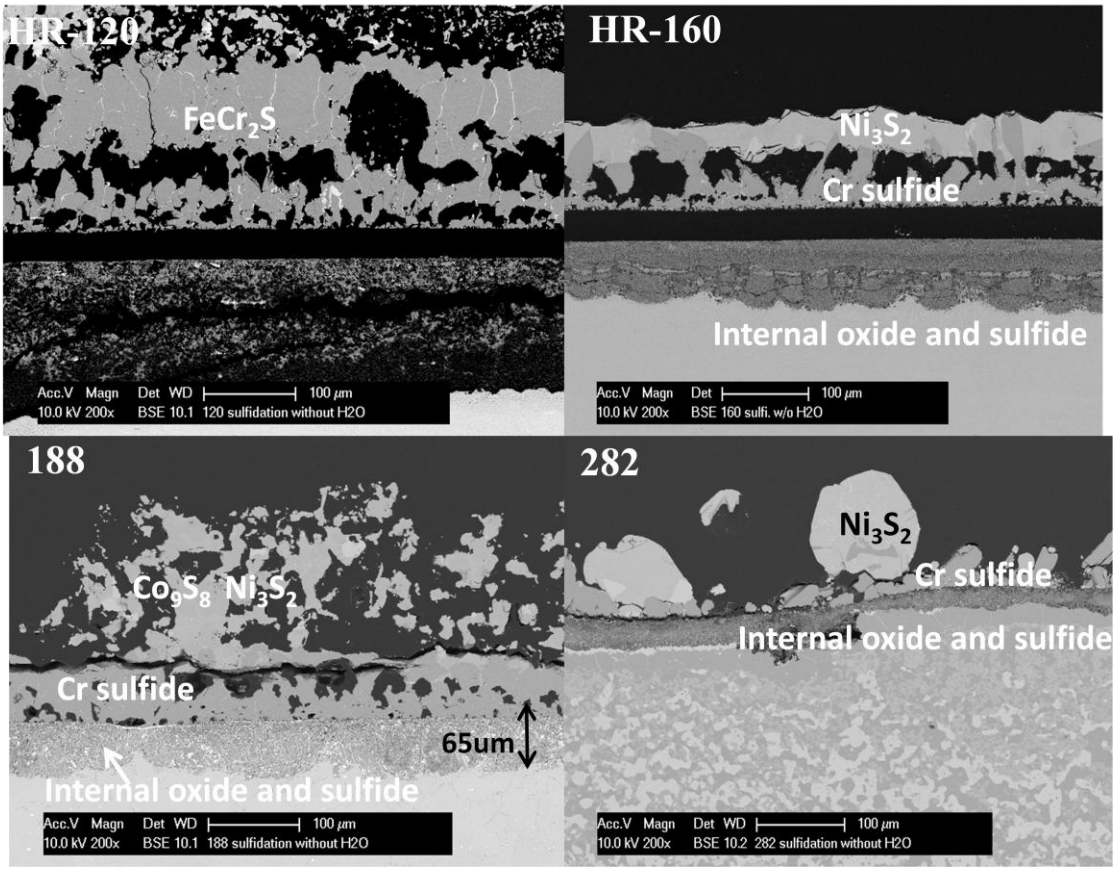

Figure 5.18 Cross-sectional images of some selected alloys after testing for 100h in Gas 1

How did sulfide form above the chromia scale from 5 to 25 hours? To date, a detailed understanding of the breakaway process has not been elucidated. However, there is a generally agreed mechanism that has been proposed[104, 121]. Figure 5.19 schematically shows the inferred process based on the current observations. During exposure for an initial period termed time 1 in Figure 5.19, a protective chromium oxide layer forms. Since the solubility of sulfur in the chromium oxide scale is extremely low, it is impossible to have any relevant amount of ionic diffusion of sulfur through the scale[122]. However, after some time, it is clear that sulfur does penetrate to the

alloy/Cr_2O_3 scale interface. This penetration is deduced to be due to the development of localized defects such as microcracks of fissures in the oxide scale. These defects provided short-circuit paths for molecular sulfur access to the alloy/scale interface. With the ingress of sulfur, its potential at the alloy/scale interface increased to a level sufficiently high to stabilize sulfide formation. The fast-growing sulfides developed into rapid transport channels through the chromia scale, thus providing easy paths for the further outward diffusion of the base-metal elements. Eventually, the chromia scale was covered by sulfides, leading to the breakdown of chromia scale and the acceleration of corrosion rate.

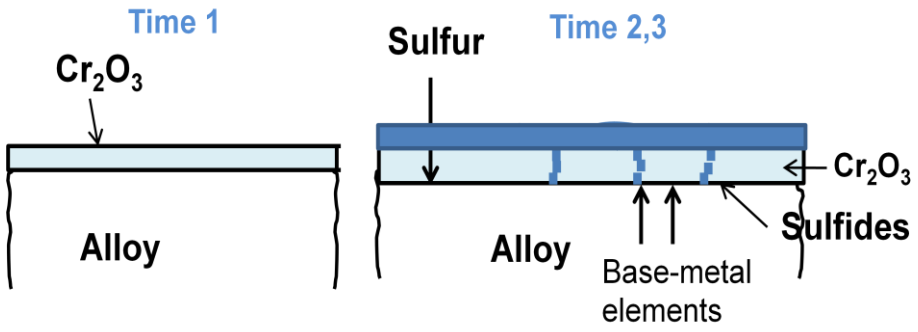

Figure 5.19 Schematic drawing of the process of breakaway corrosion

XPS analysis verified the existence of sulfur associated with the chromia scale. Figure 5.20 is the XPS depth profile of sulfur through the chromia-rich scale formed on alloy 120 after exposure for 5 hours in Gas 1. The Y-axis is the sulfur concentration, and the X-axis is the depth within the chromia-rich scale. It can be seen that the sulfur did not

reach the scale/alloy interface, and the oxide scale was still protective after 5 hours. The sulfur is surmised to have penetrated initially through the chromia scale by the penetration of molecular sulfur through physical defects such as microcracks. Detailed discussions of the possible ways in which sulfur could penetrate through the chromia layer have been presented by others[43, 123]. The formation of microcracks may be a result of strain relaxation of the scale caused by growth stresses [124-126]. A more detailed discussion will be presented in chapter 5.1.5.2.

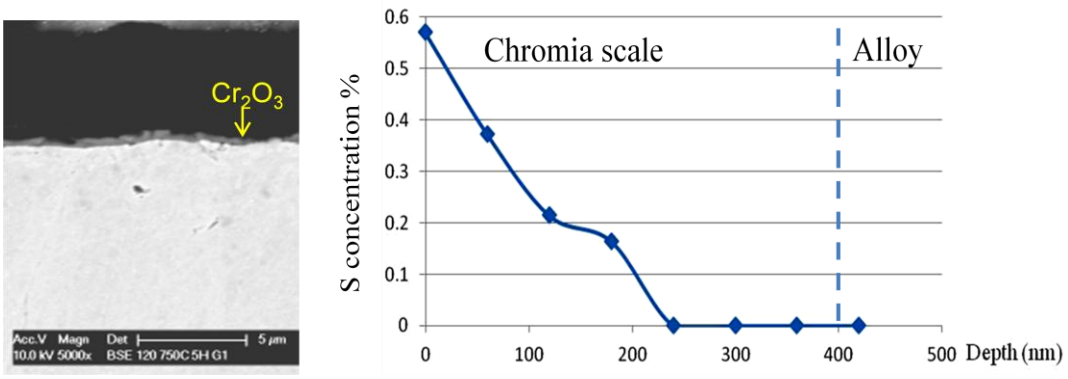

Figure 5.20 XPS depth profile of sulfur in the chromia scale on alloy120 after testing for 5 hours in Gas 1

The time to breakaway is very important because it is indicative of the useful service life of the alloy. In terms of corrosion products formed, the time to breakaway correlates with the time to when Ni-sulfide forms at the scale surface. To date, there has been little study on the environmental and alloy compositional factors that govern the time to breakaway. From Figure 5.10 it is clear that the time to breakaway is very

composition dependent. Figure 5.21 shows the influence of Co content on the time to breakaway. It is seen that the time to breakaway increases with increase in Co content. However, there is a critical Co content above which the time to breakaway decreases. The Alloy 160 with the critical Co content has the longest time to breakaway.

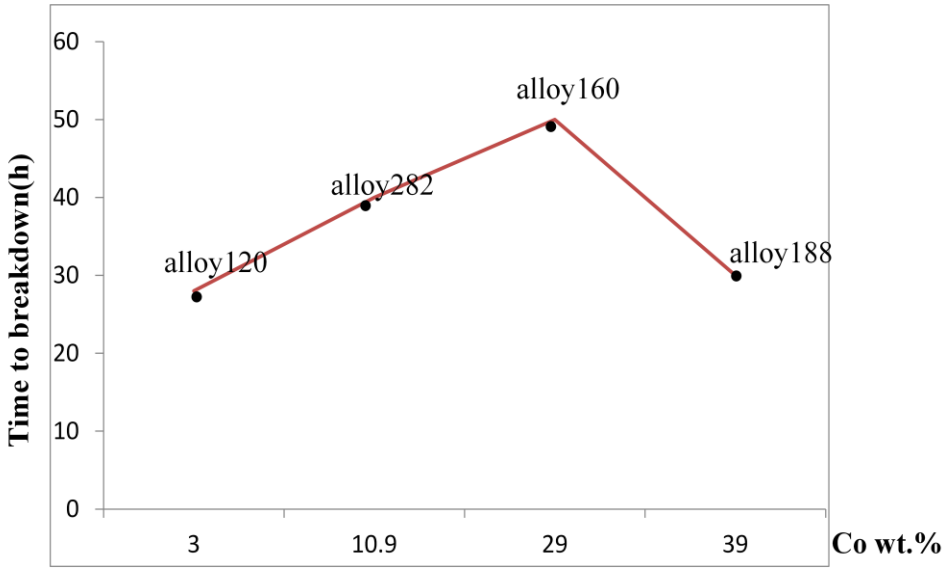

Figure 5.21 The Influence of Co on time to breakaway during 750^{o}C exposure to Gas 1

What are the reasons for the trend shown in Figure 5.21? Assessment of the cross- sectional images can aid in gaining an understanding. Figure 5.14 shows representative cross-sectional images of the four alloys after testing for 25 hours in Gas 1. A double-layered scale formed on all alloys. The inner layer is rich in Cr_2O_3, and the outer scale consists of sulfides. For Alloy 160 with the critical Co content, the outer scale is mainly Cr sulfide. For the two alloys having less than the critical Co content (alloy 120

and 282), Ni sulfide coexists with Cr sulfide in the outer sulfide scale. For Alloy 188 with greater than the critical Co content, cobalt sulfide was found to coexist with Cr sulfide. Therefore the critical amount of Co becomes the dividing line between two regimes of sulfidation behavior. In the "Co-lean" regime, Ni reaction becomes dominant. While in the "Co-rich" regime, Co reaction becomes dominant. At the critical Co level, both Ni and Co reactions are minimal, as shown in Figure 5.22.

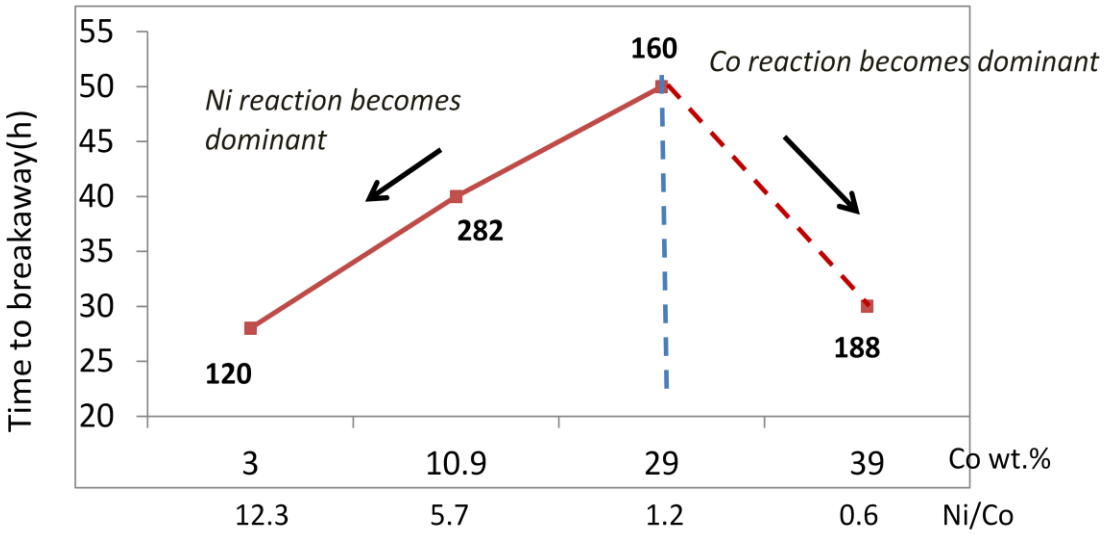

Figure 5.22 The different reaction regimes divided according to Ni/Co ratio

XPS analysis of the chromia-rich scale formed on the various alloys after 5 hours in Gas 1 also verified the inferred trend. As shown in Figure 5.23, a significant amount of Ni was observed in the oxide scale on alloys 120 and 282. For Alloy 188, instead of Ni, a considerable amount of Co exists in the Cr oxide scale. However,

negligible amounts of Ni and Co were observed in the chromium-oxide scale on Alloy 160.

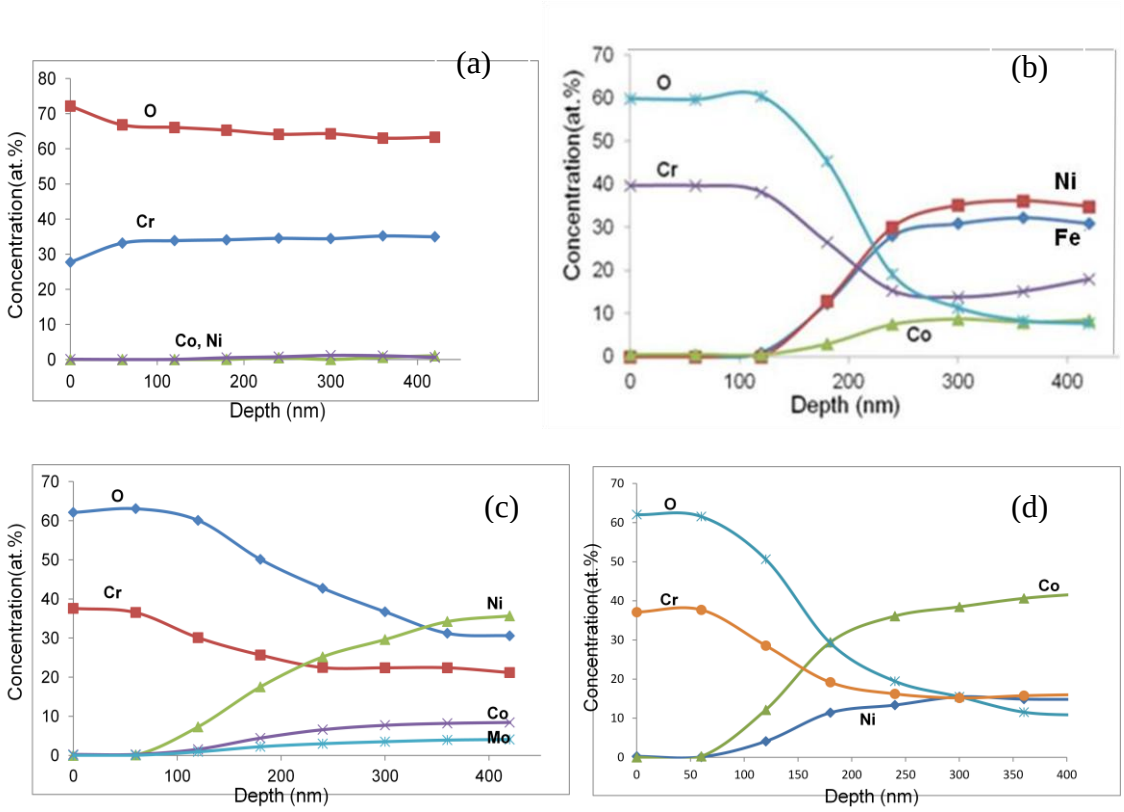

Figure 5.23 XPS depth profiles of (a) Alloy 160, (b) Alloy 120, (c) Alloy 282, (d) Alloy 188 after testing for 5 hours in Gas 1

We can also use Ni/Co ratio as the variable. Ni/Co ratio is relatively high in the Ni-reaction dominant regime, which corresponds to a relatively high availability of Ni. By contrast, when the Ni/Co ratio is low, Ni content is low but Co content is high, so that Co availability is high. Accordingly, Co reaction becomes more dominant. At the critical Co content where Ni/Co is near unity, both Ni and Co availabilities are low, so both Ni

and Co reactions are minimal. This result leads to the hypothesis that when the Ni/Co major-element ratio is near unity, the alloy should have less weight gain, hence better sulfidation resistance. Such a hypothesis has not been previously reported in the literature. In order to verify this hypothesis, model alloys were made and the verifying results will be presented in section 5.2.1.

The Cr-rich sulfide scale that formed above the chromia, shown in Figure 5.14, can also serve to act as the barrier to prohibit the outward diffusion of base metals such as Ni and Co. Indeed, Biegun et al.[86] studied the sulfidation behavior of Co-Cr binary alloys in 1 atm sulfur vapor and found that the sulfidation rate progressively decreased with increase in Cr content. According to their study, the decreasing sulfidation rate was due to a blocking effect of the Cr sulfide-rich layer.

When Ni sulfide formed and co-existed with the Cr sulfide, as was the case for alloys 188, 120 and 282 in Figure 5.14, this marked the commencement of breakaway attack.

5.1.4 Influence of gas composition on sulfidation resistance

Figure 5.24 shows the weight gain of selected alloys after testing for 100 hours at 750℃ as a function of $\log P_{O2}$ of the three gases. The three gases have a relatively constant sulfur pressure of 1.3×10^{-7}atm. As shown in this figure, all four alloys had a highest weight gain in Gas 1, which is the most reducing gas and hence has the lowest oxygen partial pressure. The least weight gain was always with Gas 3, in which the oxygen partial pressure is the highest. Weight gain can again be used as a metric for assessing

corrosion resistance, so that it can be concluded that for given sulfur potential, the alloys are less corroded in the environments with higher oxygen partial pressure.

In gas 3, where oxidation dominated over sulfidation, a chromium-oxide layer formed and provided protection against corrosion. Alloys had the highest weight gain in Gas 1 where sulfidation dominated. The interaction between oxidation and sulfidation is indicated in Figure 5.25. In all three gases, HR-160 and 263 had the lowest weight gain primarily due to them having the highest Cr and Co contents.

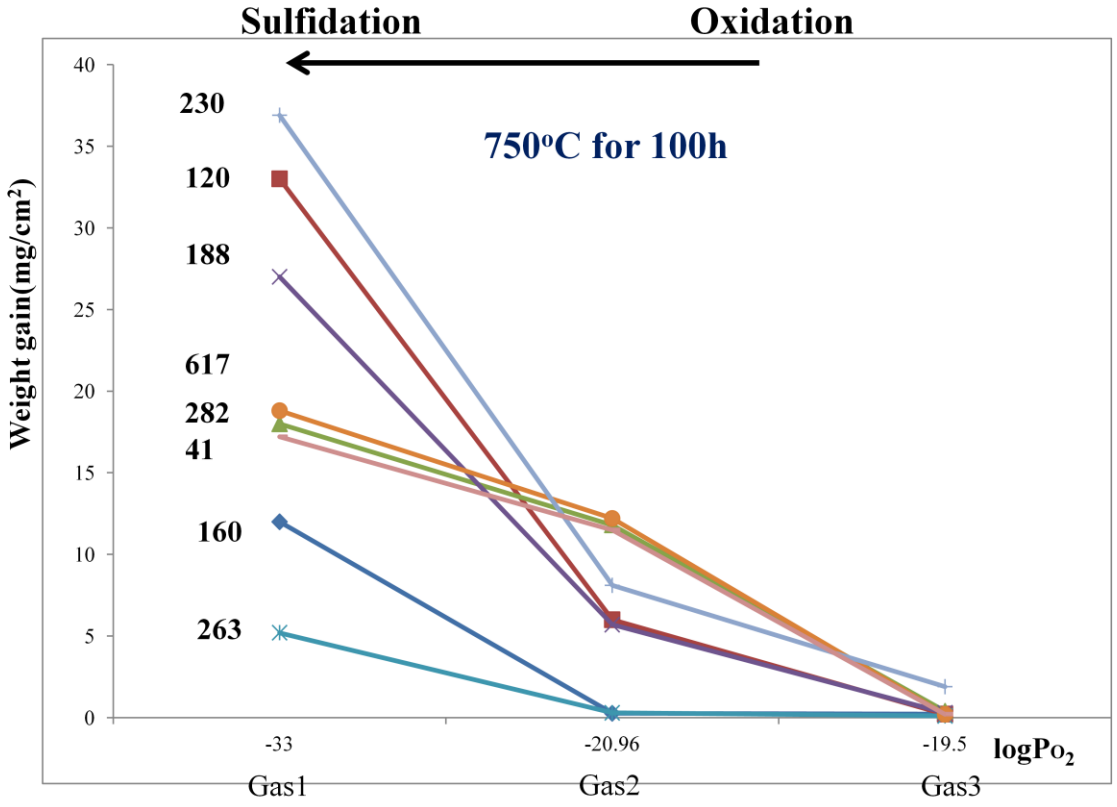

Figure 5.24 Weight gains as a function of oxygen activity at constant sulfur pressure, after testing at 750℃ for 100 hours

The cross-sectional images of Alloys 120, 160,188 and 282 after testing for 100 hours in Gas 1 are shown in Figure 5.18, and those of Alloys 263, 617, 230 and 41 after 100 hours in Gas 1 are shown in Figure 5.26. The cross-sectional images of alloys tested in Gases 2 and 3 for 100 hours are shown Figure 5.27 and Figure 5.28, respectively. All alloys were completely sulfidized after 100 hours in Gas 1. In Gas 2, sulfides formed locally above the Cr oxide scale on most alloys. While in Gas 3, a protective Cr oxide scale formed on most alloys.

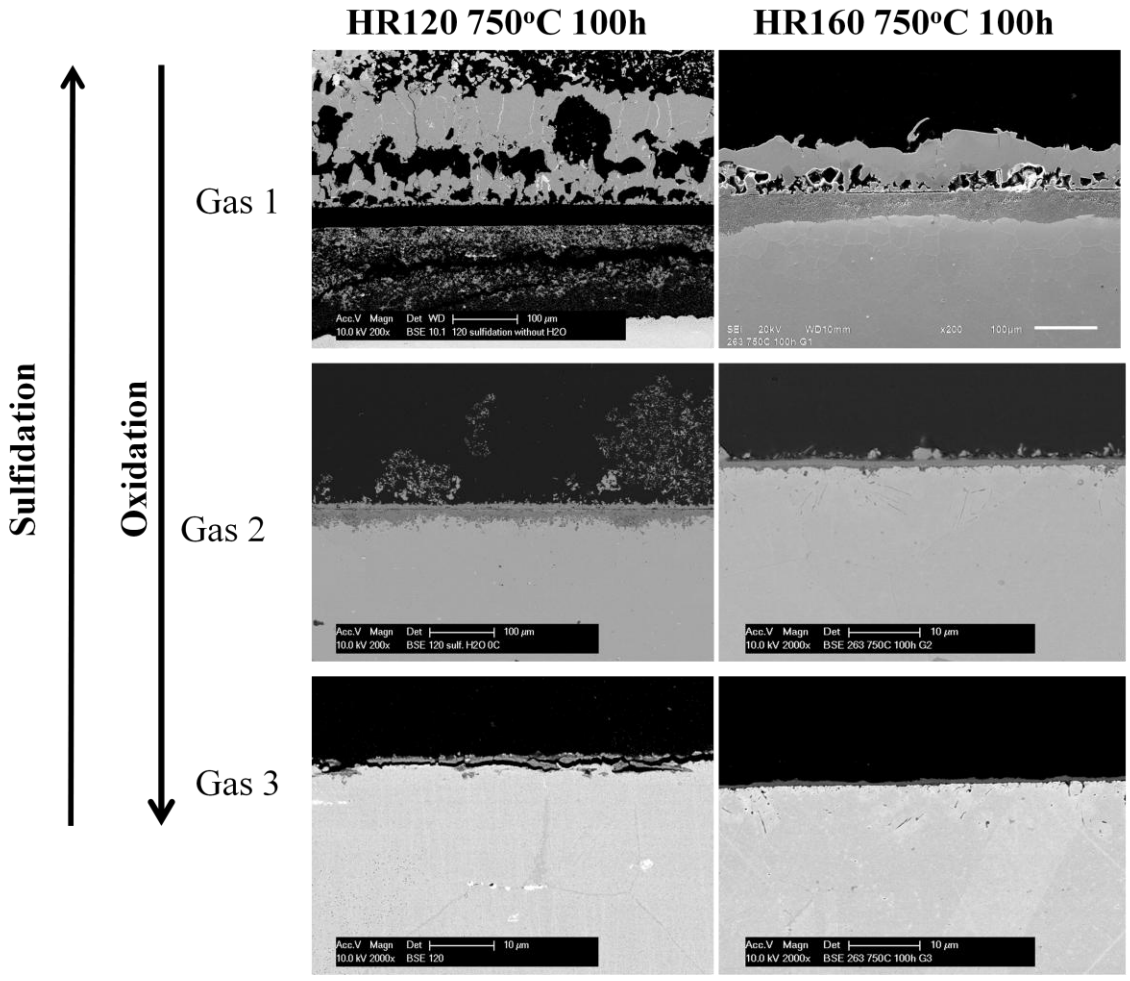

Figure 5.25 Interrelation between oxidation and sulfidation

.

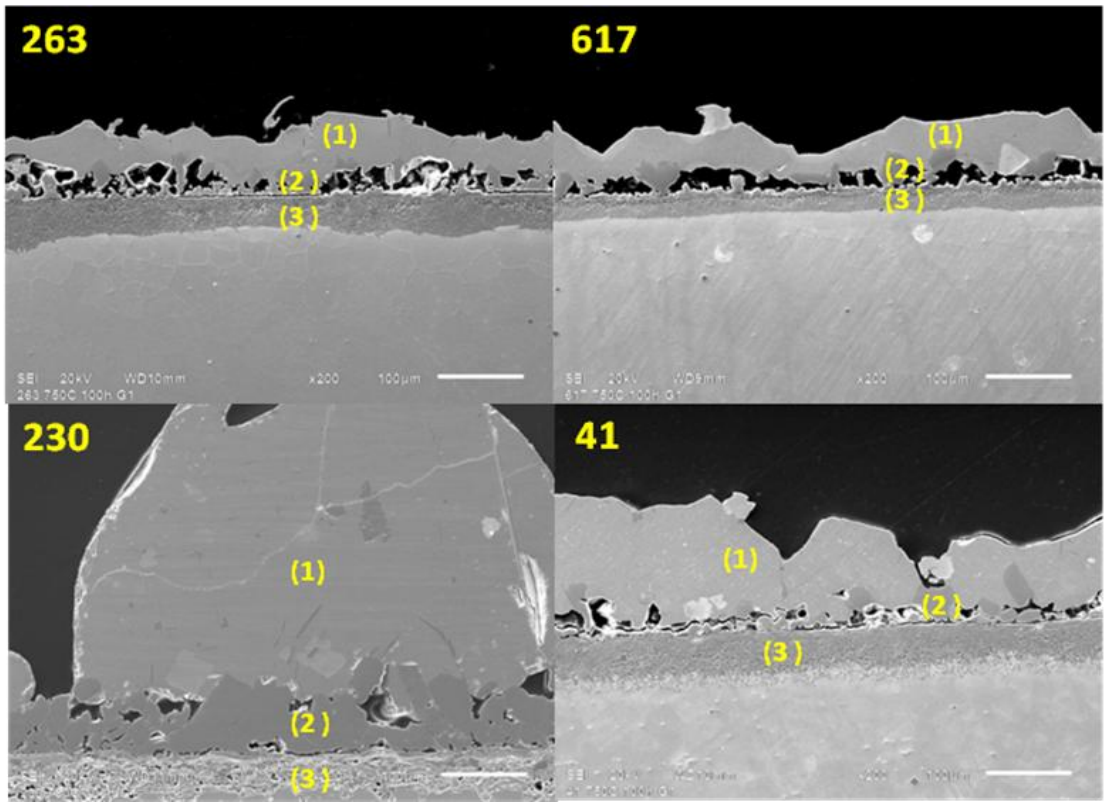

Figure 5.26 Cross-sectional images of Alloy 263, 617,230 and 41 after testing in Gas 1 for 100 hours

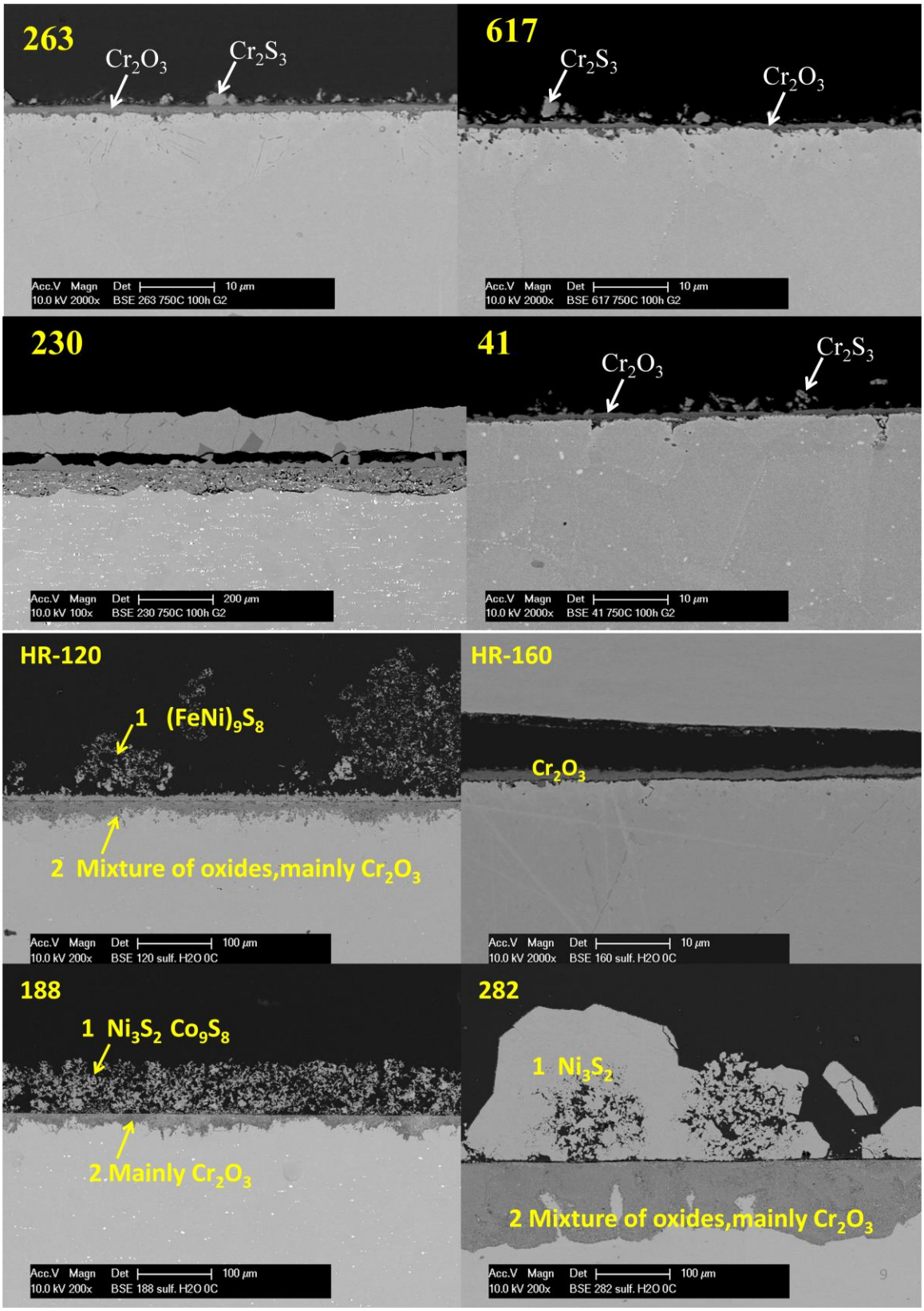

Figure 5.27 Cross-sectional images of alloys after testing in Gas 2 for 100 hours

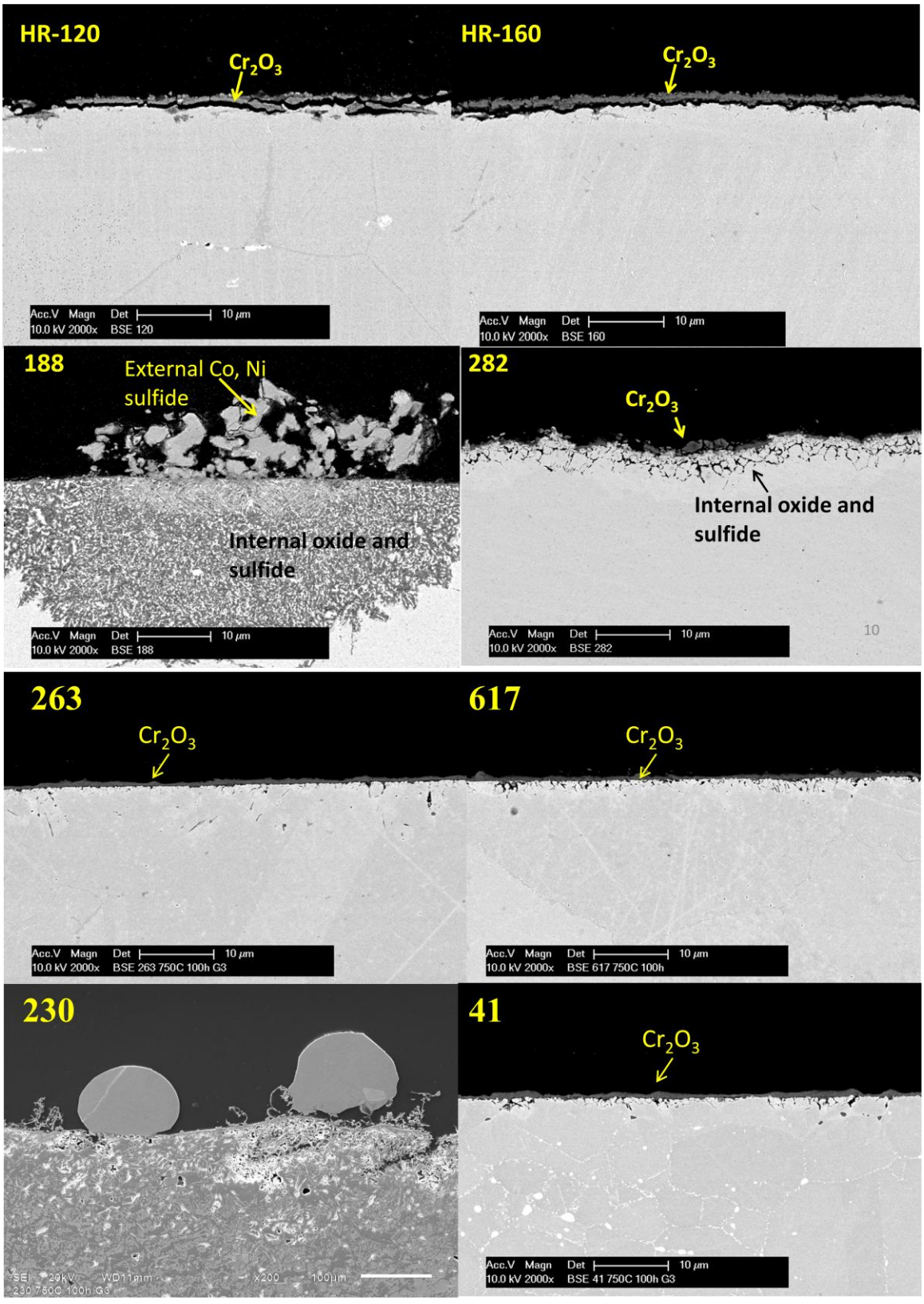

Figure 5.28 Cross-sectional images of alloys after testing in Gas 3 for 100 hours

5.1.5 Morphological characteristics

Since Gas 1 is the most sulfidizing, the discussion of morphological characteristics will mainly focus on the samples exposed for 100 hours to this gas at 750°C. Figure 5.18 and Figure 5.26 show resulting cross-sectional images of the various alloys. All alloys are seen to have similar multi-layered scale microstructures. The top layer (1) is nickel sulfide, the second layer (2) is Cr- and/or Co-enriched sulfide, and the third layer (3) is the mixture of internal oxide and sulfide. Figure 5.29 is a schematic representation of the sulfide structure after testing at 750^{o}C for 100h in Gas1.

It is noticed that some white particles are present in the top sulfide layer. According to EDS analysis, these are metallic Ni or/and Co. These particles might have formed during the relatively slow cooling process - after testing for a certain time, the samples were taken out of the hot zone of the furnace and cooled under an Ar gas flow. To verify this possibility, selected alloys were quenched to room temperature after 100 hours in Gas 1. No metallic Ni or Co particles were observed, as shown in Figure 5.30. This observation verifies that the metallic Ni and Co particles precipitated during the relatively slow-cooling process after testing.

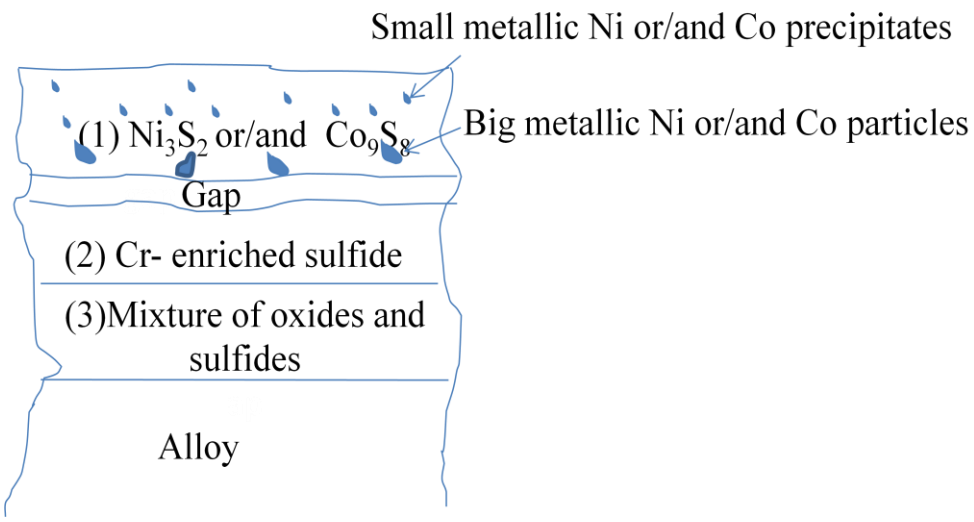

Figure 5.29 Schematic drawing of the scale structure after testing for 100h in Gas 1 at 750^{o}C

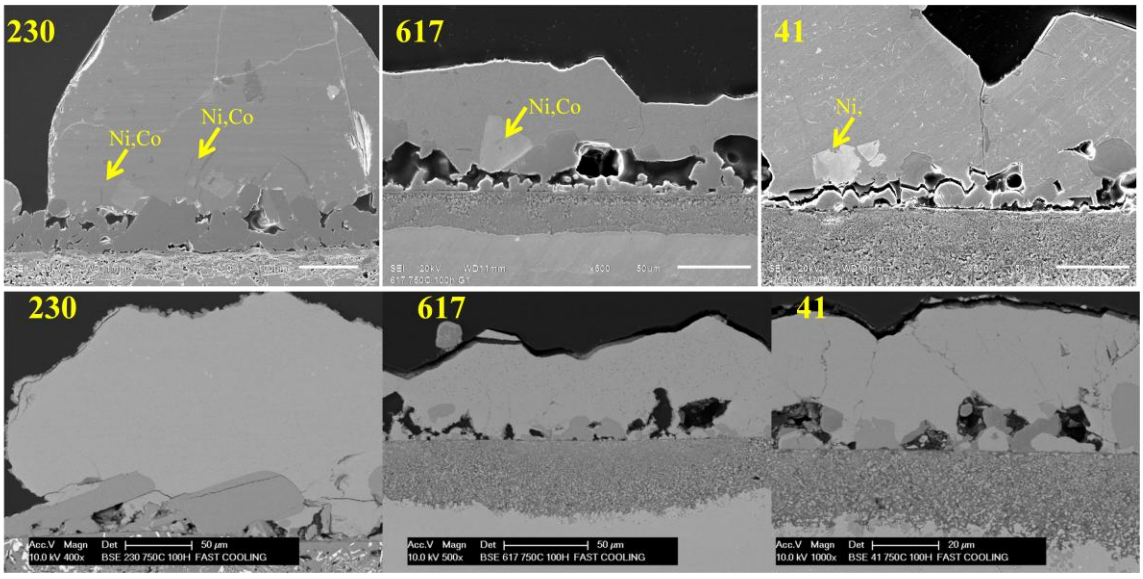

Figure 5.30 Cross-sectional images of some alloys after slow cooling (top three photos) and fast cooling (bottom three photos)

Figure 5.31 is the 700°C Ni-Cr-S isothermal section showing the compositions of points 1 and 2 in the SEM image of alloy 230 after 100 hours in Gas 1. As shown in this figure, point 1 is located in the Ni_3S_2 phase region, and point 2 is located in the Cr_2S_3 region.

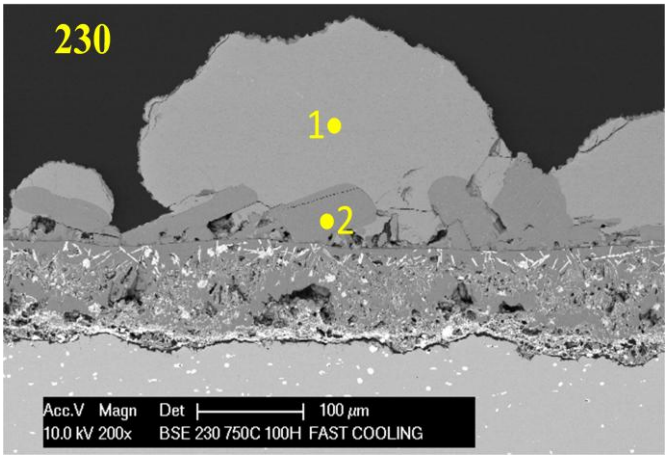

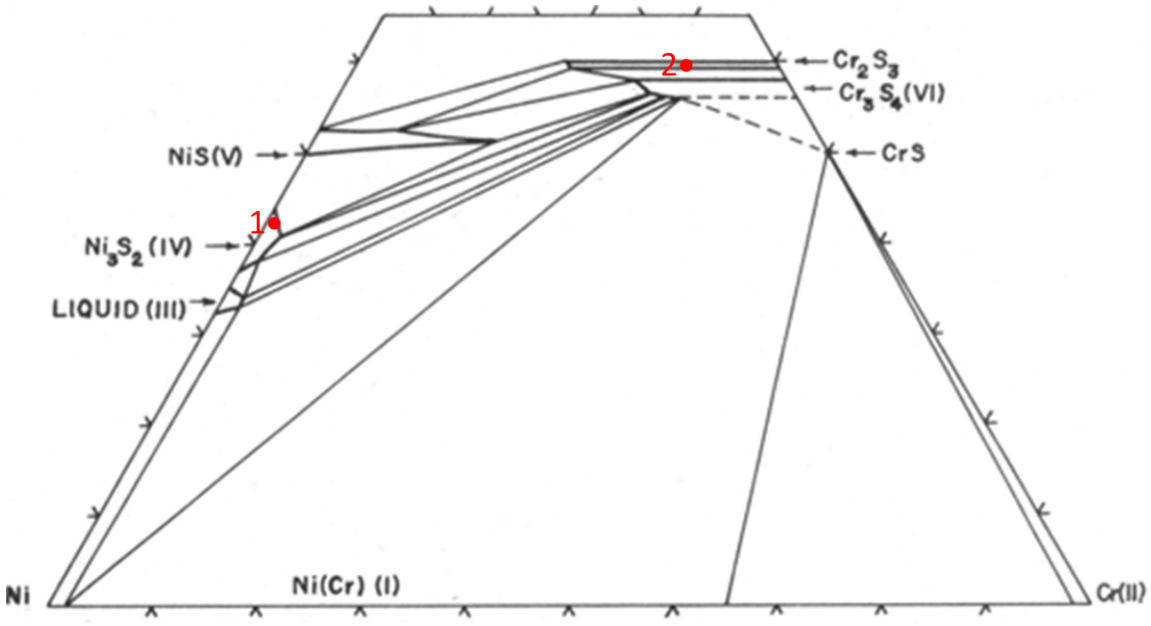

Figure 5.31 Ni-Cr-S isothermal section for 700°C showing composition measured on the scale

Several interesting morphological characteristics were observed, including the formation of Ni_3S_2 whiskers on Alloy 120, massive void formation in the sulfide layer of Alloy 120 and the formation of nodules (consisting of Ni-N_3S_2) on Alloys 282 and 230. All these morphological characteristics are discussed in the following section. The internal sulfidation zone is also considered.

5.1.5.1 Whisker formation

(1) Whisker morphology and composition

Whiskers were observed on the surface of Alloy 120. Figure 5.32 shows surface images of Alloy HR-120 after testing for various times at 750°C in Gas 1. As seen in this figure, whiskers started to form after 42 hours. The sample surface was completely covered by whiskers after 100 hours. Figure 5.33 shows surface SEM images after testing for 50 hours. An area of compact $FeCr_2S_4$ layer was covered by whiskers, as shown in Figure 5.33(a). The enlarged image (b) shows occasional coarse whiskers among a tangle of much finer whiskers. The thickness of the whiskers after 50 hours is as much as 640um measured from the side view of the image shown in Figure 5.33(c). Figure 5.34 shows a magnified side view of whiskers after testing for 50 hours in Gas 1.

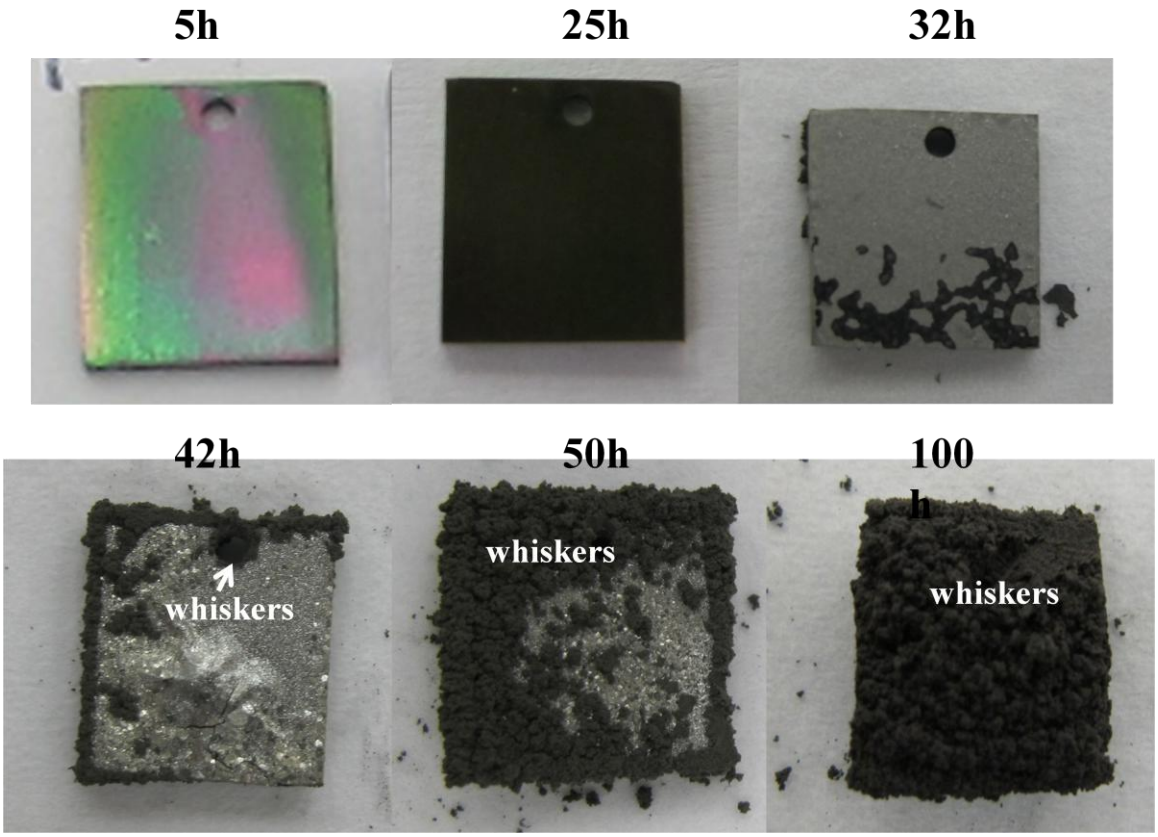

Figure 5.32 Surface images of Alloy HR-120 after testing for different times at 750°C in Gas 1

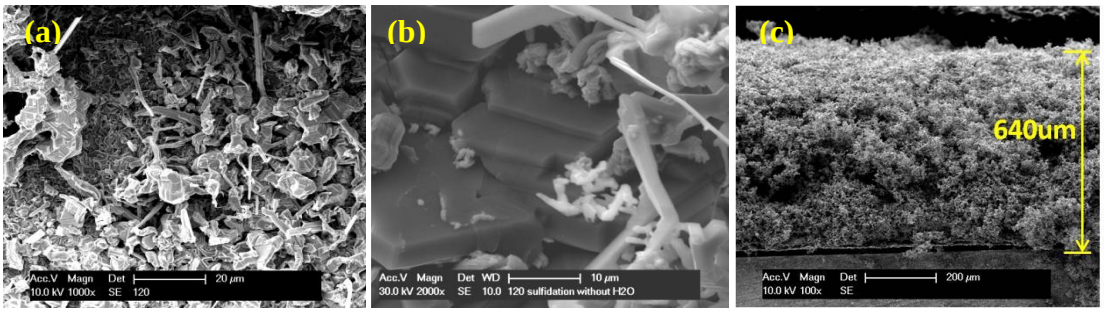

Figure 5.33 Images of Ni sulfide whiskers on Alloy 120 after 50 hours in Gas 1, (a) surface view of whiskers, (b) magnified surface view of whiskers, (3) side view of whiskers

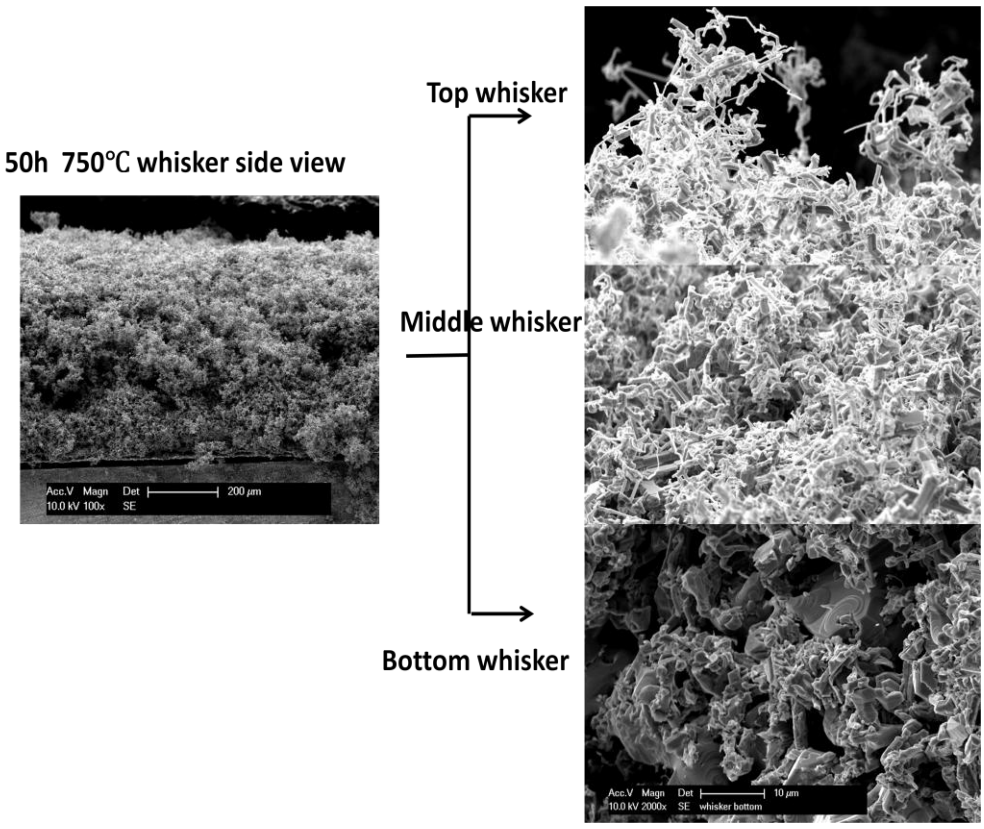

Figure 5.34 Magnified side view of whiskers

XRD analysis showed that the top whisker consists of $(FeNi)_9S_8$ and Ni_3S_2, as indicated in Figure 5.35. It is known from the isothermal section of the Fe-Ni-S phase diagram at 700°C and 500°C, shown in Figure 5.36 and Figure 5.37, respectively, that $(FeNi)_9S_8$ does not exist at 700°C, but it exists at 500°C. Thus, it can be inferred that $(FeNi)_9S_8$ may have formed by decomposition of $Ni_{3 \pm x}S_2$ during subsequent cooling since Ni_3S_2 is stable at 750°C in gas 1 ($P_{S2}=10^{-7}$atm, $P_{O2}=10^{-25}$atm), as shown in Figure 5.38.

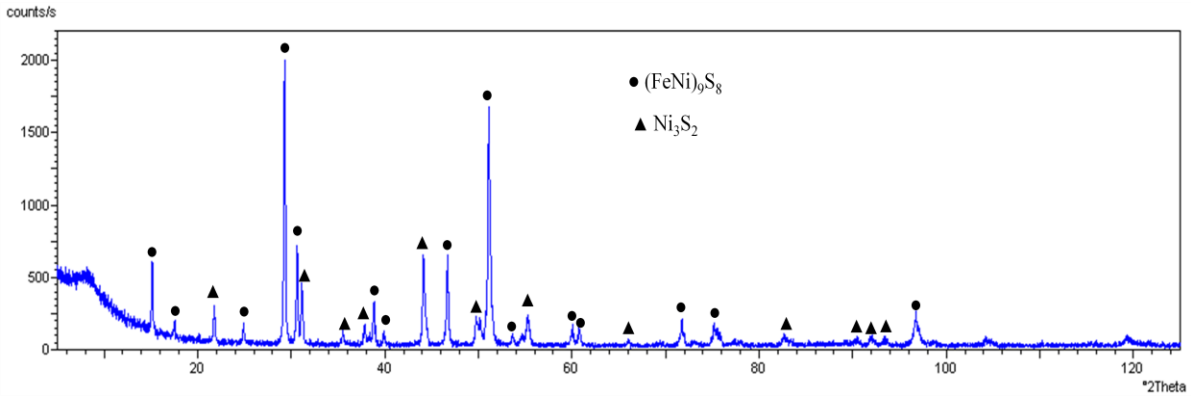

Figure 5.35 XRD pattern of Alloy 120 after 100h in Gas 1

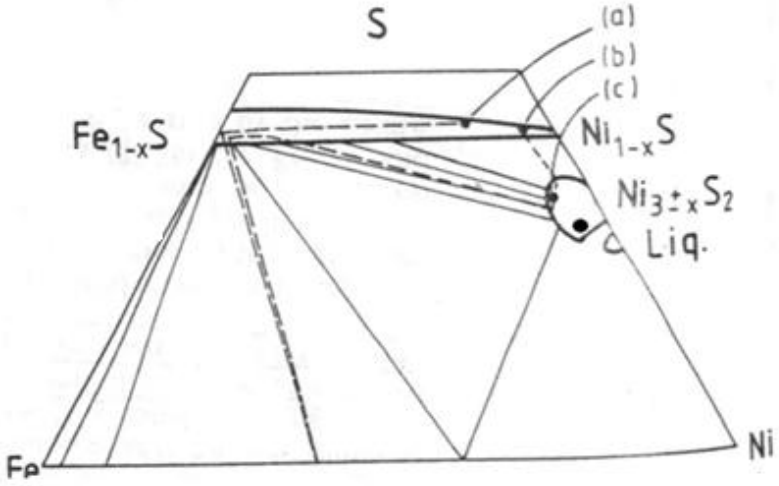

Figure 5.36 Isothermal section of Fe-Ni-S pase diagram at 700°C

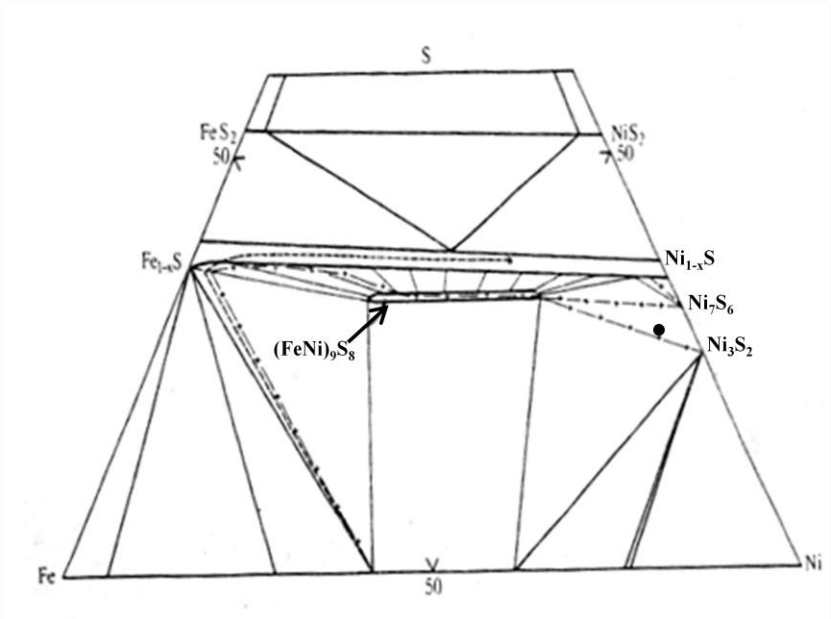

Figure 5.37 Isothermal section of Fe-Ni-S phase diagram at 500 ^{o}C

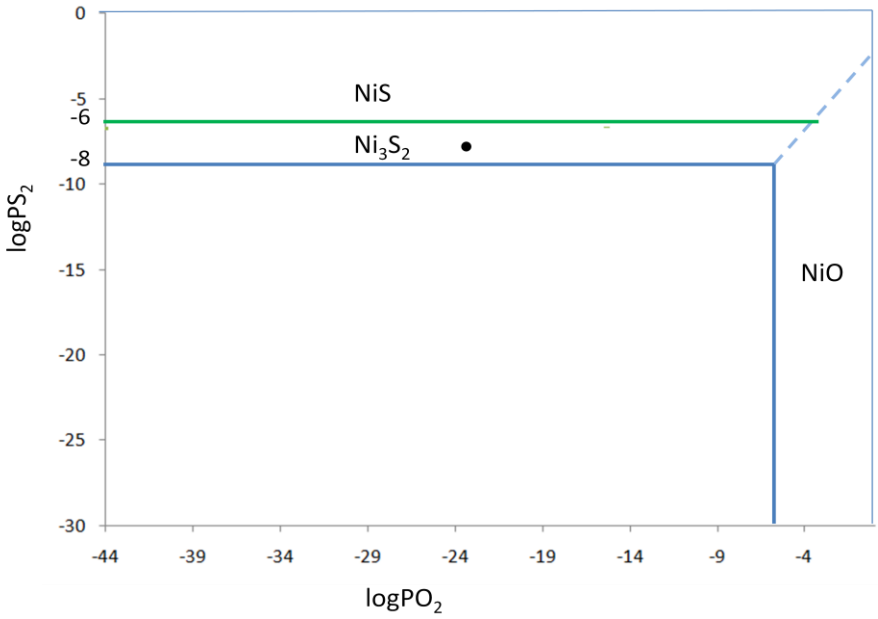

Figure 5.38 Ni-O-S stability diagram at 750^{o}C, the data point represents the equilibrium P_{S2} and P_{O2} in Gas 1

(2) The growth of whiskers supplied by the outward diffusion of Ni

The measured thicknesses of whiskers after exposure for 50, 75 and 100 hours are shown in Table 5.1. If the growth of the Ni_3S_2 whisker is controlled by the outward diffusion of Ni, then the diffusion coefficient of Ni in Ni_3S_2 layer can be approximately calculated knowing the thickness of the Ni_3S_2 layer according to equation (5.1) [127].

$$X = (2Dt)^{\frac{1}{2}} \qquad (5.1)$$

The resulting calculated diffusion coefficients of Ni are also shown in Table 5.1. According to a study by Lillerud [128], the self-diffusion coefficient of Ni in Ni_2S_3 at 700^oC is $8.6 \times 10^{-7} cm^2 sec^{-1}$, which is reasonably within an order of magnitude of the calculated diffusion coefficient of Ni shown in Table 5.1. This agreement supports the postulation that the growth of the porous outer Ni_3S_2 layer is supplied primarily by the outward solid-state diffusion of Ni.

Table 5.1 The measured thickness of whiskers

Ni_2S_3 layer	50h	75h	100h
Measured thickness (um)	640±15	858±15	1030±15
Calculated D_{Ni} through whisker (cm^2 /Sec) based on measured value	~1.1 x 10^{-8}	1.4 x 10^{-8}	1.5 x 10^{-8}
Calculated thickness (um)	572	818	978
Calculated D_{Ni} through whisker (cm^2 /Sec) based on calculated value	2.2 x 10^{-8}	2.8x 10^{-8}	2.9 x 10^{-8}

Since the whisker is easily spalled, there might be error in the measurement. To verify the measured value, the thickness was calculated as follows.

The weight gain due to the inner $FeCr_2S_4$ layer growth (ΔW^I) may be estimated from the measured inner $FeCr_2S_4$ layer thickness (X^I) using equation (**5.2**)[129].

$$\Delta W^I = \frac{32\rho X^I}{288} \qquad (5.2)$$

Here, ρ is the density of $FeCr_2S_4$, 32 is the atomic weight of sulfur and 288 is the atomic weight of $FeCr_2S_4$. Knowing the total weight gain (ΔW) and the weight gain due to inner

$FeCr_2S_4$ (ΔW^I), the weight gain of outer whisker layer can be calculated using equation (5.3).

$$\Delta W^o = \Delta W - \Delta W^I \qquad (5.3)$$

The measured total weight gain and the calculated weight gain of the inner $FeCr_2S_4$ layer after sulfidizing for 25, 50, 75 and 100 hours are summarized in Figure 5.39. As shown in this figure, the total weight gain is mainly due to the growth of the outer Ni sulfide whiskers.

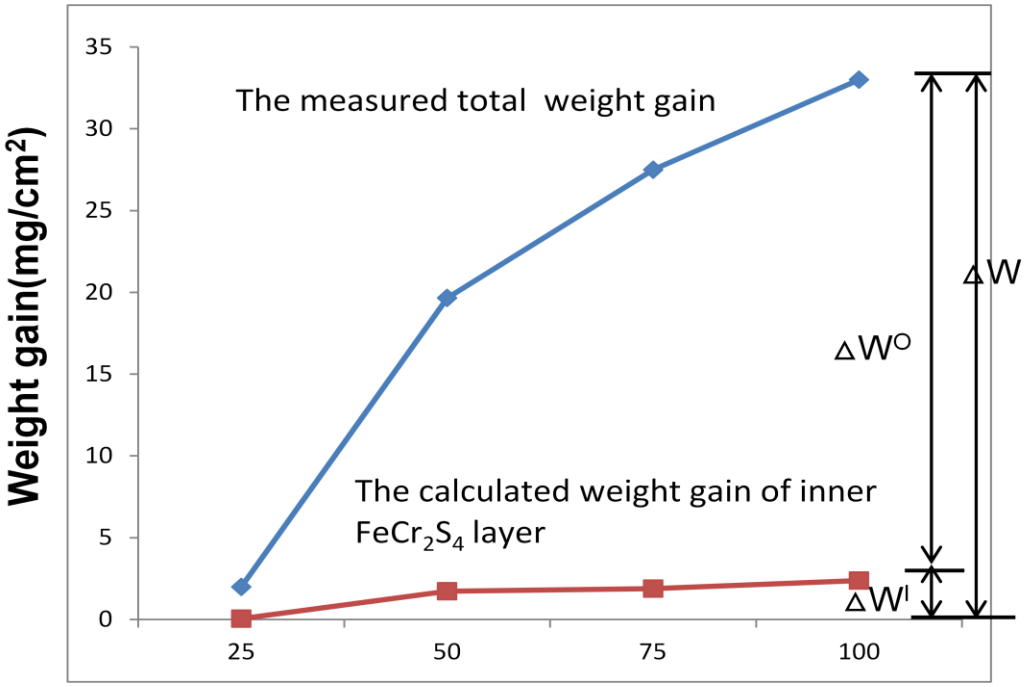

Figure 5.39 Total weight gain and the calculated weight gain of the inner $FeCr_2S_4$ layer

The porous outer Ni_3S_2 layer is estimated to have 60% porosity; thus the thickness of this layer can be calculated from equation (**5.4**).

$$\Delta W = \frac{0.4 * 32\rho X}{241} \qquad (5.4)$$

where ρ is density of Ni_2S_3, 5.89g/cm^3 and X is the thickness of the Ni_3S_2 layer. The calculated thickness of the outer Ni_3S_2 whisker layer is shown in Table 5.1 and also compared to the measured thickness. There is no significant difference between the calculated and measured thicknesses, though the latter was always greater. The calculated diffusion coefficients of Ni though the whisker based on either the measured thickness or calculated value are thus comparable.

(3) Proposed mechanisms for whisker formation

Orchard and Young[129] also observed whisker formation when they studied the 520^{o}C sulfidation of Fe-41Ni in a N_2-H_2-H_2S mixture having a P_{S2} of 10^{-9} atm. Figure 5.40 compares cross-sectional images from the current study to that presented by Orchard and Young. In their test, a compact Ni sulfide layer formed in the gas with a higher P_{H2S}. According to their explanation, the whisker formation in low P_{H2S} gas is related to the surface reaction control of H_2S dissociation**.**

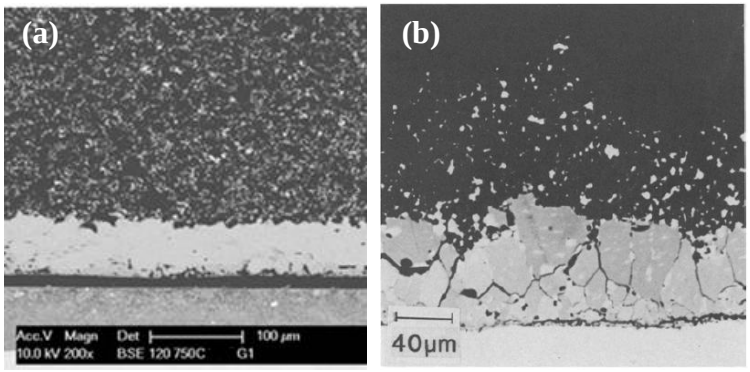

Figure 5.40 Cross sections of alloys in the current test and Orchard's test,(a)Alloy HR-120, 750°C , Gas 1, (b) Alloy Fe-41Ni, 520°C, $P_{S2}= 10^{-9}$ atm

If the surface reaction is rate controlling, the reaction kinetics should obey the linear rate law. To verify if Orchard and Young's explanation is suitable for the current study, the reaction kinetics were checked. Since the data points for the reaction kinetics of Alloy 120 shown in Figure 5.11 are not enough to closely investigate the kinetics, additional tests for 32 and 40 hours were conducted. The resulting weight gain vs. time plot is shown in Figure 5.41. As shown in this figure, the corrosion rate is linear for up to 50 hours, and then transitions to parabolic beyond 50 hours. The reaction kinetics therefore verifies that surface reaction is rate controlling until about 50 hours.

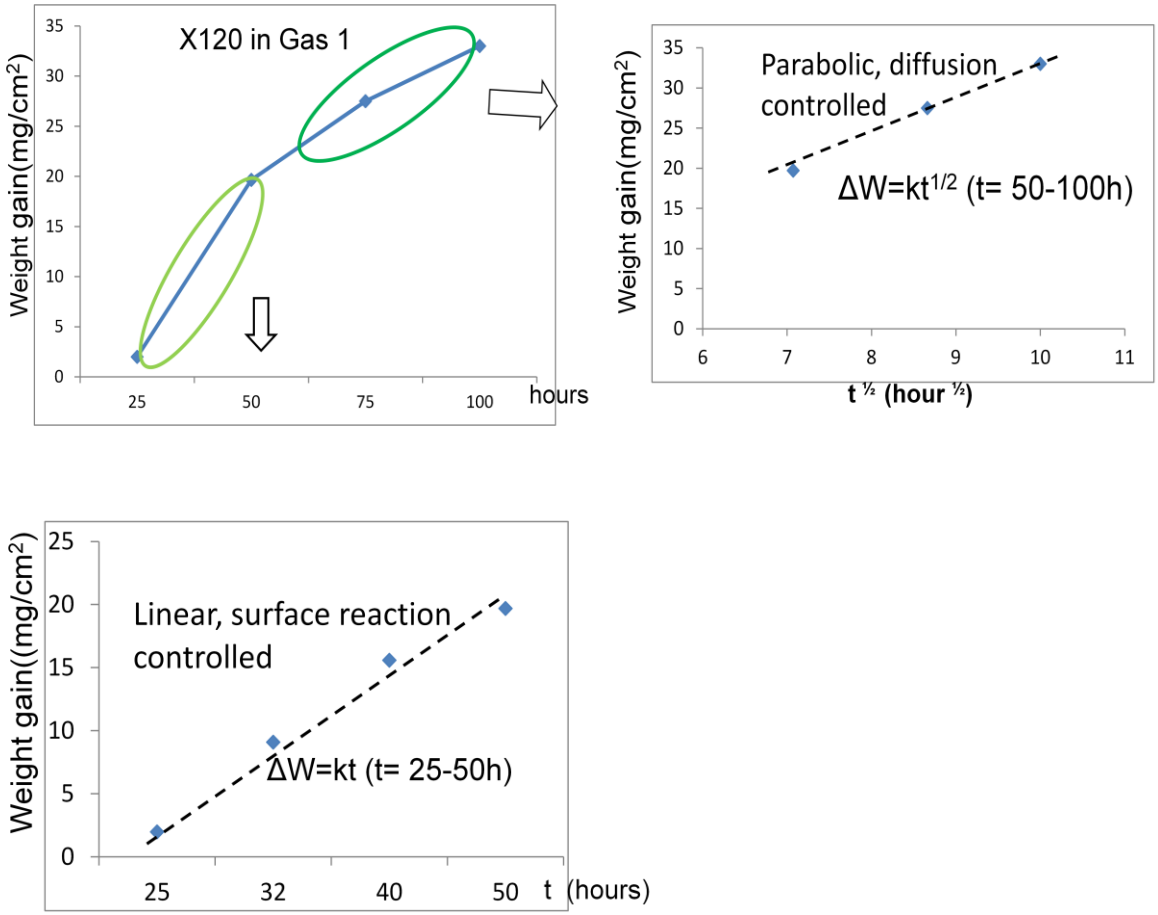

Figure 5.41 Weight gain as a function of time after testing for 25 to 50 hours

In Orchard and Young's reaction gas, the principal reaction route was not inferred to involve $S_2(g)$, but rather involved the direct interaction of $H_2S(g)$ with the solid sulfide surface according to their calculations. The present case for the Gas 1, the composition is N_2-15%CO-3%H_2-0.12%H_2S and the equilibrium sulfur partial pressure is 1.3×10^{-7}atm at 750°C. The principal reactant may be either S_2 or H_2S, as shown in Figure 5.42. Since the equilibrium sulfur partial pressure was known, the sulfur delivery rate, J_S, can be calculated.

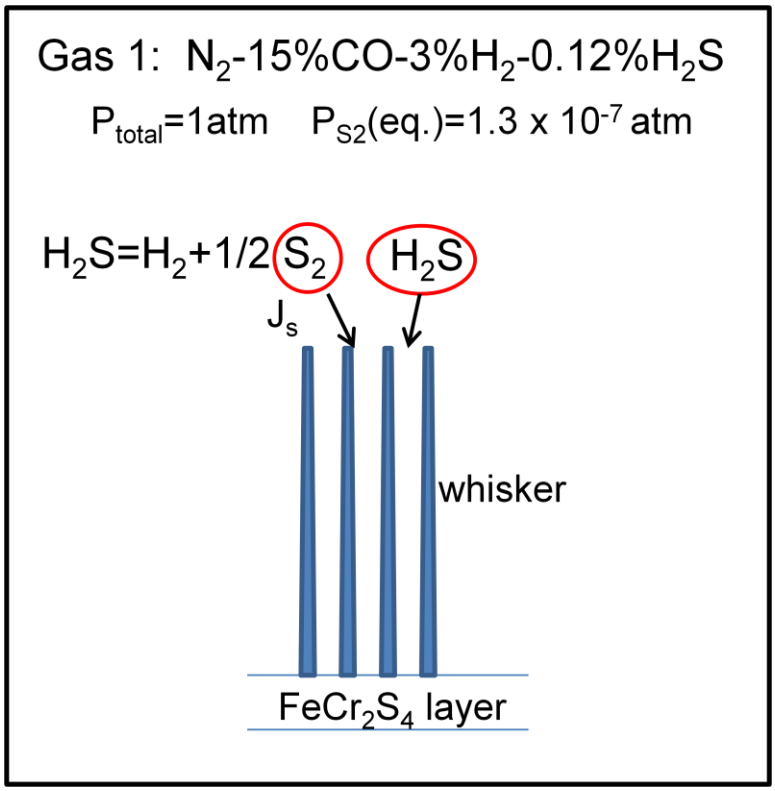

Figure 5.42 The principal reactants in Gas 1

According to gas transfer theory in the viscous flow regime, the calculated sulfur delivery rate is 2.1 x10^{-11} mole/cm^2 min. The calculation will be shown in the following. For now, however, it is useful to compare sulfur delivery rate with the actual sulfur consumption rate. Knowing that the actual weight-gain value of Alloy 120 after 25 hours was 2 mg/cm^2, the actual sulfur consumption rate is calculated to be 4x10^{-8}mole/cm^2 min, which greatly exceeds the calculated sulfur delivery rate of 2.1 x10^{-11} mole / cm^2 min. Therefore, it is inferred that the principal reaction route does not involve S_2(g), but rather occurs via direct interaction of H_2S(g) with the solid product surface in the reaction with Gas 1. The detailed calculation of sulfur delivery rate is as follows.

The supply of sulfur is calculated using equation (5.5).

$$J_s = \frac{k_m}{RT}(P^{(o)} - P^{(i)}) \qquad (5.5)$$

where k_m is mass transfer coefficient, P^i and P^o are the partial pressures of the gas species at the solid surface and in the bulk gas, respectively. P^i is assumed to be zero if all the oxidant is consumed by the corrosion reaction. For simplification, the gas atmosphere is assumed to be N_2-H_2S. The mass transfer coefficient, k_m, for this binary system is given by equation (5.6):

$$k_m = 0.664(\frac{D_{AB}^4}{v_g})^{\frac{1}{6}}(\frac{v}{l})^{\frac{1}{2}} \qquad (5.6)$$

where v_g is the kinematic viscosity, v is linear velocity of the gas, l is the length of the sample surface (it is 1.5cm in the current experiment), and D_{AB} is binary gas diffusion coefficient. Since there is a small amount of H_2S in the gas, the self-diffusion coefficient of N_2 can be used instead of $D_{N2\text{-}H2S}$. From some reports [130-132], the self-diffusion coefficient of N_2 is about $2.1cm^2S^{-1}$. v_g is given by equation(5.7):

$$v_g = \frac{\eta}{\rho} \qquad (5.7)$$

where ρ is density in the unit of g/cm^3 and η is the viscosity, which is given by equation (5.8):

$$\eta = \frac{2.6693 \times 10^{-5}\sqrt{MT}}{\sigma_i^2 \Omega_i} \qquad (5.8)$$

Since the majority of the gas is N_2, the viscosity and density are assumed to be the values for N_2. The data for N_2 are shown in Table 5.2.

Table 5.2 Some parameters for N_2

	M	σ_i (Å)	Ω_i(Å)
N_2	28	3.681	0.7837

Then $\eta = \frac{2.6693\times10^{-5}\sqrt{28\times1023}}{3.681^2 \times 0.7837} = 4.2 \times 10^{-4}$ Pois

The kinematic viscosity of N_2 is $v_g = \frac{\eta}{\rho} = \frac{4.2\times10^{-4}}{\frac{28}{1.1\times10^5}} = 1.65$

Here, the density is calculated assuming the gas to be ideal.

The sample length was about 1.5cm, linear gas flow rate v was 10cm/min, and thus k_m can be calculated as follows:

$$k_m = 0.664(\frac{2.1^4}{1.65})^{\frac{1}{6}} \left(\frac{\frac{10}{60}}{1.5}\right)^{\frac{1}{2}} = 0.222 cm/sec$$

Therefore,

$$J_s = \frac{k_m}{RT}\left(P^{(o)} - P^{(i)}\right) = \frac{0.222 \times 10^{-2}}{8.314 \times 1023} (1.3 \times 10^{-7} \times 1.013 \times 10^5)$$

$$= 3.437 \times 10^{-13} \frac{\text{mole}}{\text{cm}^2\text{sec}} = 2.06 \times 10^{-11} \frac{\text{mole}}{\text{cm}^2\text{min}}$$

The above calculation assumes that the principal reaction route does not involve $S_2(g)$ but occurs via direct interaction of $H_2S(g)$ with the solid surface in the reaction Gas 1. A change in gas flow rate had no effect on weight gain, which indicates that gas phase diffusion of H_2S to the sample surface is not the rate-controlling step (this is explained in Appendix A of this thesis). Clearly then, it is the surface reaction that is rate-controlling in the linear kinetics regime (< 50 hours). Equation (5.9) shows the H_2S dissociation reaction. It is believed that the formation of whiskers is related to the slow approach of the H_2S dissociation reaction to equilibrium.

$$H_2S(\text{adsorbed}) \rightarrow S(\text{adsorbed}) + H_2(g) \qquad (5.9)$$

The formation of whiskers indicates the occurrence of preferential growth. Obviously, the whisker formation requires the preferential growth longitudinally instead of laterally. The orientation dependence of surface reactivity might be the possible explanation for this anisotropic growth. Orchard and Young [129] proposed that the whisker tip is a catalyst to the H_2S dissociation reaction, thus sulfur activity is higher at the tip than at the side, producing a greater driving force for diffusion, and hence, growth in the longitudinal direction than in the lateral direction, as indicated in Figure 5.43.

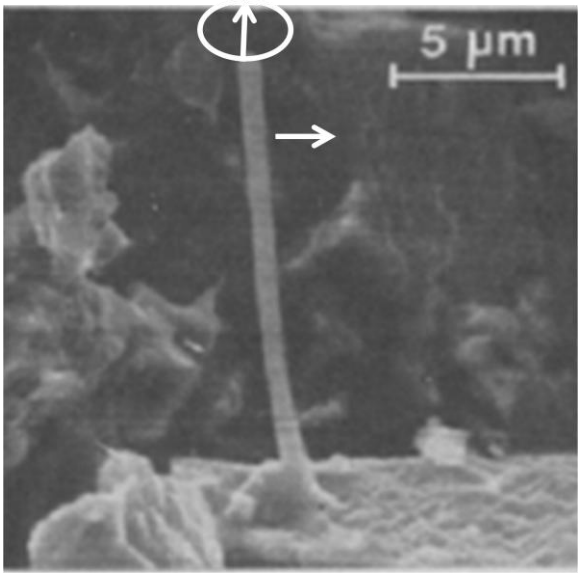

Figure 5.43 The localized catalysis phenomenon leading to asymmetric growth

The explanation here is different from those provided for the growth of CuO and NiO whiskers[133][134]. In these cases, the existence of an axial screw dislocation was believed to provide preferential diffusion path. Whisker growth was also extensively studied in semiconducting industry, for example, whisker formation on high-purity Sn. It was believed that oxygen diffuses in and reacts with metal, thus resulting in volume expansion which creates a compressive stress that pushes up the whisker[134] .

5.1.5.2 Extensive void formation

As shown in Figure 5.18 and Figure 5.26, massive voids were observed in the sulfide scale formed on some alloys, especially on alloy 120. The formation of such massive voids occurred in several steps. Firstly, growth stresses were produced in the scale as the sulfidation reaction proceeded. The voids then formed as a result of the Kirkendall effect

or diffusional creep. After the formation of voids, a dissociation process eventually led to the massive void formation in the scale.

Before discussing the mechanism for void formation, the origin of stresses in the scale should be reviewed. Usually, there are two types of stresses that develop in a scale: growth stress and thermal stress. Growth stress is associated with the isothermal formation of the scale. Thermal stress arises from different thermal expansion or contraction between the alloy substrate and scale and arise during thermal cycling[47]. Growth stress and thermal stress in an oxide scale are discussed in the following. The stress developed in oxide scale applies to that produced in sulfide scale.

Growth stress arises from several sources, such as[126]: volume difference between the sulfide and the metal from which it forms; epitaxial stress; compositional changes in the alloy or scale; point defect stresses; recrystallization stresses; product formation within the scale; and specimen geometry. Although there are many sources of growth stress, only volume difference between the sulfide and metal will be discussed here as it is the most common reason for the growth stress[126]. If the sulfide growth is controlled by the inward diffusion of sulfur, and sulfides form at or near metal/scale interface, the cause of stress in this case is the volume difference between the sulfide and the metal which is consumed to form sulfide. The Pilling-Bedworth ratio (PBR)[135], shown in equation (5.10), can be used to characterize the stress. Compressive stress develops in the scale if the PBR is greater than unity (this is the case for most metals); tension develops in the scale if the PBR is less than unity.

$$\mathrm{PBR} = \frac{V_{ox}}{V_m} \qquad (5.10)$$

If sulfide grows by outward diffusion of metal ions, the new sulfide forms at the scale/gas interface. In this case, it seems that the new sulfide forms in a stress-free manner. However, as metal diffuses outward, the volume of the metal core decreases, and growth stress still arises. The receding metal core with adhering sulfide will produce compressive stress in the scale parallel to, and tensile stress normal to the metal surface, as shown in Figure 5.44. The growth stress in the sulfide scale on most metals (Ni, Co, Fe, Cr, Al, etc.) is caused by this mechanism. [126]

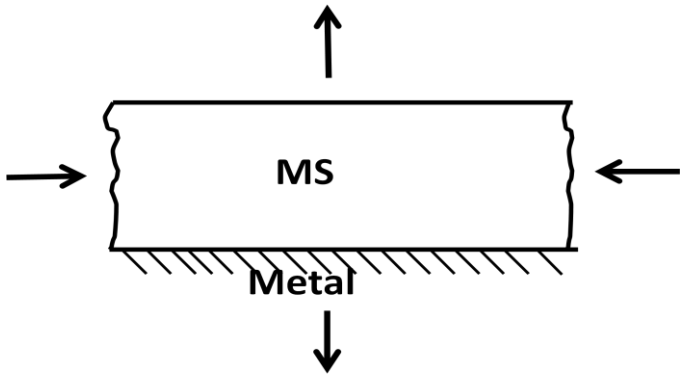

Figure 5.44 Growth stress in sulfide scale produced by outward diffusion of metal ions

Thermal stress originates during cooling and heating because of the difference in thermal-expansion coefficient of the metal and oxide. The thermal stress retained in the scale can be measured by X-ray diffraction[47].

With this understanding of the origin of stresses in the scale, the formation of voids as a result of diffusional creep caused by the stresses in the scale can be discussed.

Diffusional creep, either Nebarro-Herring creep or Coble creep, is a main source of deformation that occurs in a scale[136]. Both modes of creep involve the non-random motion of point defects and thus cause a change in the shape of a crystal.

The model for Nabarro-Herring creep is that deformation occurs by a flux of vacancies through the crystal lattice, that is, volume diffusion. Figure 5.45(a) schematically shows the flux of vacancies in a homogeneous single crystal due to an imposed stress. Figure 5.45 (b) shows the vacancies diffusing along the grain boundaries. Vacancies diffusing along the grain boundaries are the case of Coble creep. For both creep mechanisms, diffusion of vacancies toward one direction results in a flux of atoms in the opposite direction, thus causing an elongation of the crystal in the direction normal to the compressive stresses. Diffusion along grain boundaries is more rapid than through the volume, largely because the activation energy for grain-boundary diffusion is roughly two thirds that for volume diffusion[47]. Thus, "although the diffusion path for an atom or ion around the sides of a grain may be longer than the path directly through the volume, the higher rate of grain-boundary diffusion can make it the more efficient mechanism of the two. Coble creep is more effective at low temperatures than Nabarro-Herring creep because of its lower activation energy."[136]

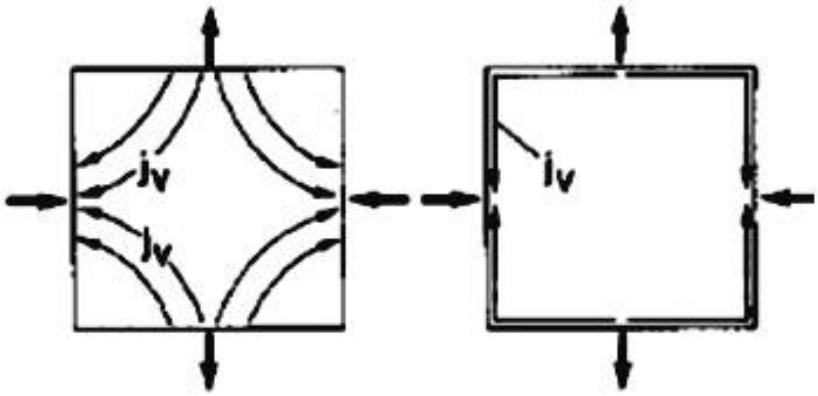

(a) (b)

Figure 5.45 Vacancies flux j_v, in single grains due to imposed stress, (a) through lattice diffusion (Nabarro-Herring creep), (b) through diffusion along grain boundaries (Coble creep).

When volume diffusion and grain-boundary diffusion take place in a polycrystalline, homogeneous material, each grain is deformed as shown in Figure 5.46. Figure 5.46(a) shows grains before deformation, (b) shows the grains after diffusional deformation of the single grains without relative grain movement (grain boundaries sliding), (c) shows grains after diffusional deformation and grain-boundaries sliding[137]. The overall creep process eventually leads to the formation of voids and porosity at grain boundaries or dislocations [126, 136] .

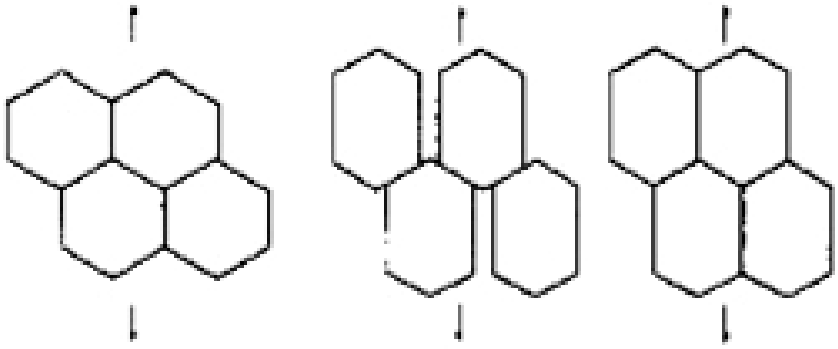

(a) (b) (c)

Figure 5.46 High-temperature deformation of grains under stresses

Another reason for the voids formation is the Kirkendall effect. During the sulfidation reaction, base metal ions and electrons diffuse outward and vacancies diffuse inwards, as shown in Figure 5.47. These vacancies condense to form voids when their concentration is high enough.

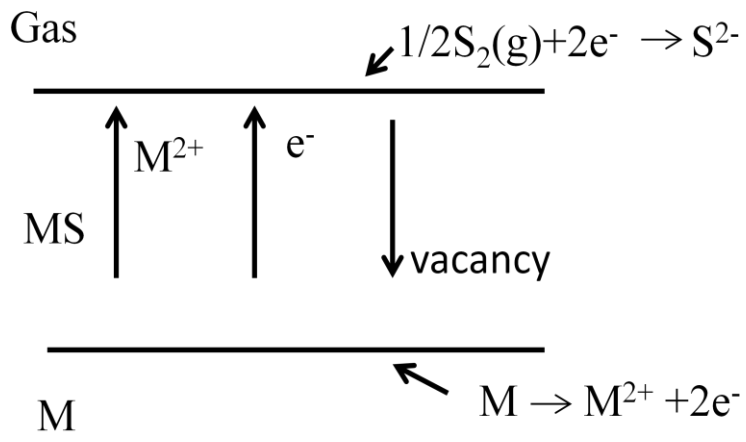

Figure 5.47 The outward diffusion of metal ions and inward diffusion of vacancies through the scale

As shown in Figure 5.48, voids first formed at the interface between the $FeCr_2S_4$ scale and internal corrosion zone after 75 hours. This is because the vacancies condense at the inter-phase boundary to minimize the overall free energy of the system[138].

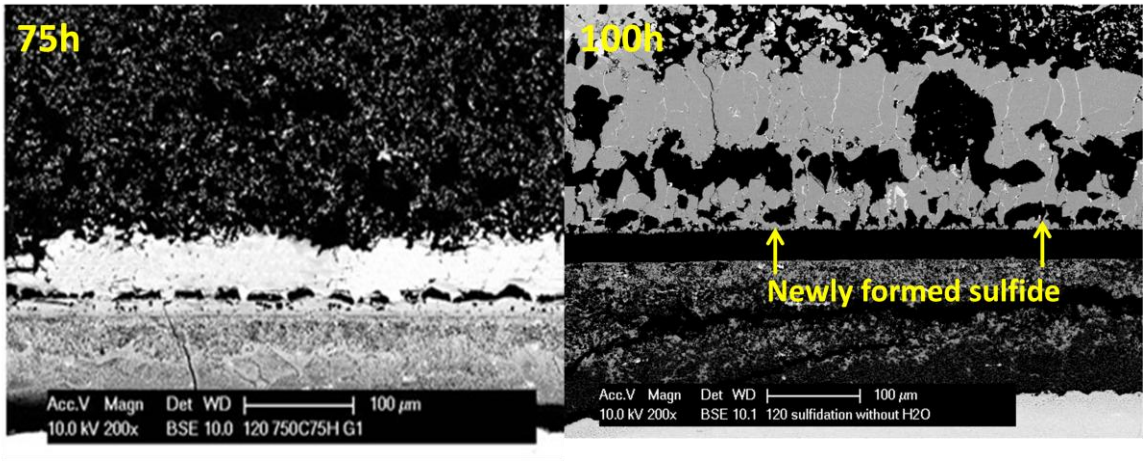

Figure 5.48 Cross sectional image of Alloy 120 after 50, 75 and 100 hours

After the formation of voids, a dissociation process occurs[139, 140], as shown in Figure 5.49. The voids impede the outward transfer of metal ions, such as iron ions, and electrons from the alloy into the scale, so there is an increase in the sulfur vapor pressure at the inner surface of $FeCr_2S_4$ scale, which is separated from the base metal by pores, above the dissociation pressure of FeS, as shown in Figure 5.49(A). The sulfur migrates across the pore or gap and begins to form new sulfides on the metal surface, as shown in Figure 5.49(B). The newly formed sulfides within the pore are indicated in the image of the alloy exposed for 100 hours in Figure 5.48. With the formation of now sulfides, the vapor pressure of sulfur decrease below the FeS dissociation pressure, and FeS begins to dissociate to produce gaseous sulfur for the growth of inner layer, as shown in Figure 5.49(C).

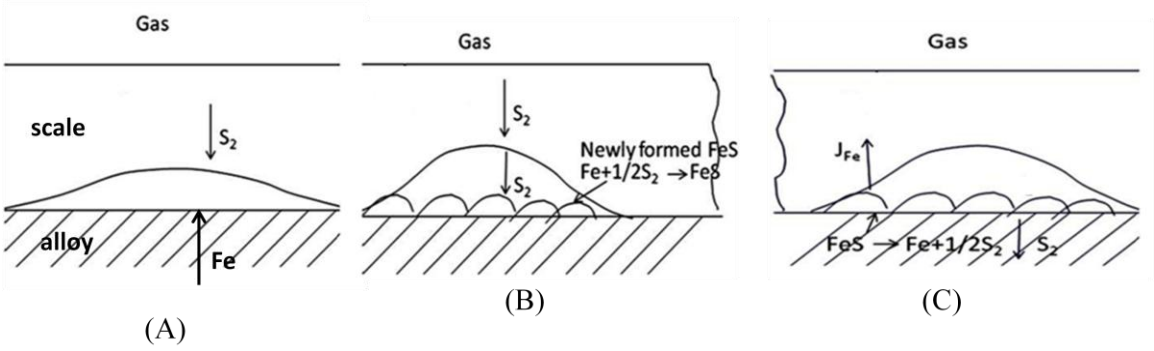

Figure 5.49 The schematic drawing of the dissociation process

5.1.5.3 Nodules formation

As shown in Figure 5.18 and Figure 5.26, nodules were observed on alloy 282 and 230 after testing at 750^{o}C for 100 hours in Gas 1. Figure 5.50 shows the surface image of nodule formed on Alloy 282 after 100h in Gas 1. According to the XRD analysis shown in Figure 5.51, the nodules consist of Ni_3S_2 and metallic Ni. This observation is in agreement with the study by Harper[141], who showed that nodules form on Alloys 310 and 556 after thermal exposure in H_2-25%CH_4-14.8%N_2-4%CO-0.6%CO_2-0.6%H_2S for 500 hours at 900°C. Harper explained that the nodules formed during fast cooling, and might disappear during slow cooling. To verify if this explanation is applicable to the current study, sample 282 was slow cooled in the furnace after testing for 100 hours instead of taking samples out of the furnace and cooling down under the Ar gas flow. The nodules were still observed as shown in Figure 5.52. This suggested that the formation of nodules is not caused by the cooling process.

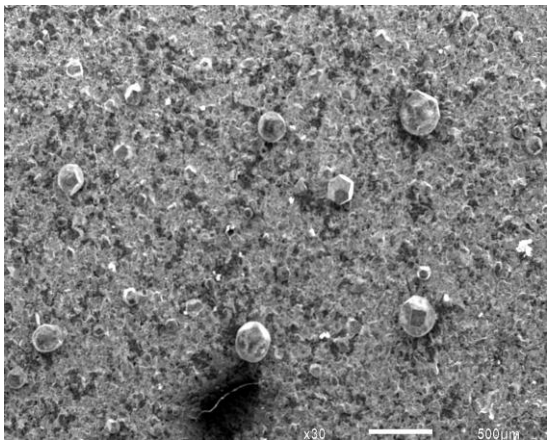

Figure 5.50 Surface images of nodules formed on Alloy 282 after 100h in Gas 1

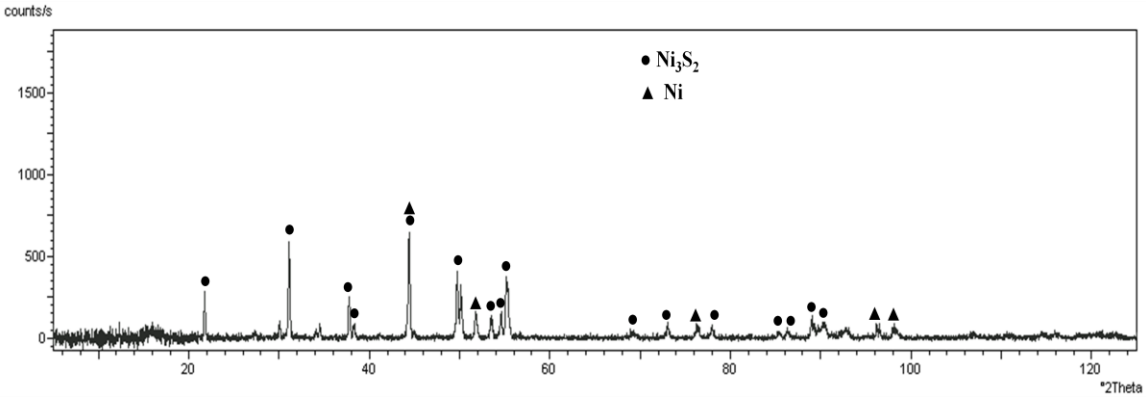

Figure 5.51 XRD pattern of Alloy 282 after 100 hours in Gas 1

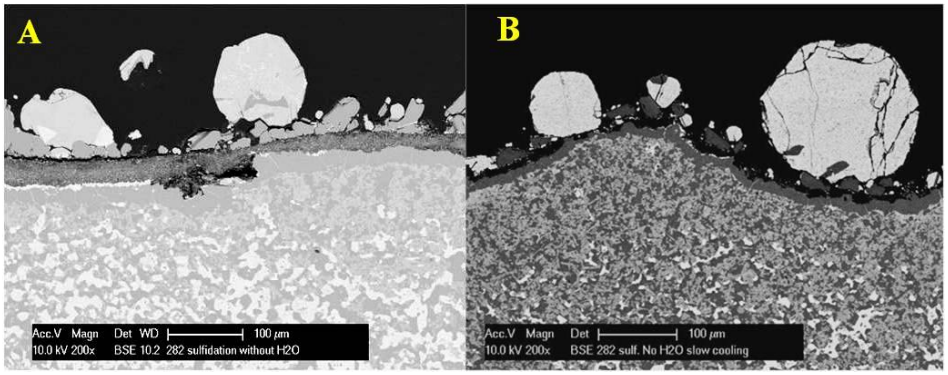

Figure 5.52 Cross section of Alloy 282 after testing at 750^{o}C for 100 hours in Gas 1, (A) relatively fast cooling, (B) slow cooling.

Figure 5.53 presents a magnified image of the nodules. The nodules consist of two phases, the gray matrix phase is Ni_3S_2, and the white phase is metallic nickel. The average composition of the nodules is 66.4Ni-35.6S (at%) which is located within the Ni-Ni_3S_2 eutectic transition range of the Ni-S phase diagram, as shown in Figure 5.54. During the test at 750^{o}C, the liquid Ni-Ni_3S_2 eutectic formed, since T_m=645°C, and during cooling transformed to Ni_3S_2 and metallic Ni.

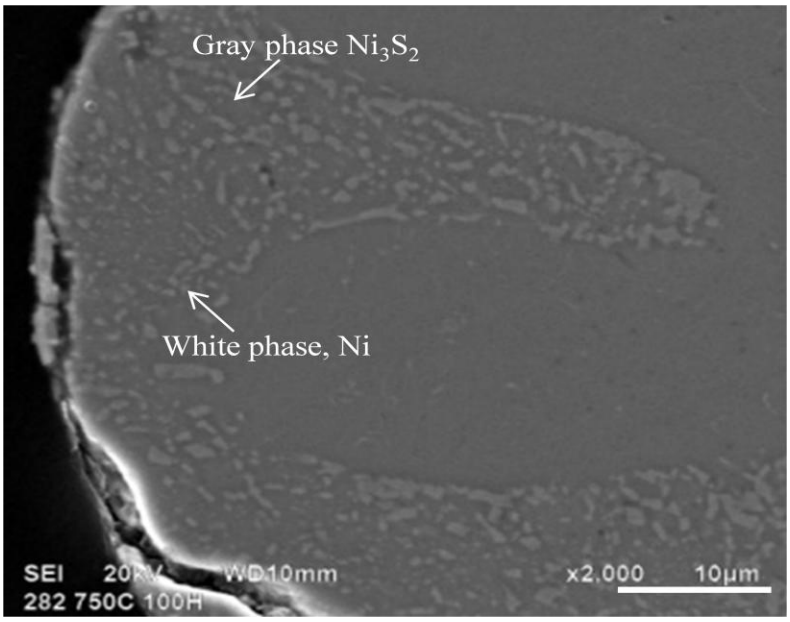

Figure 5.53 Magnified image of nodules formed on Alloy 282

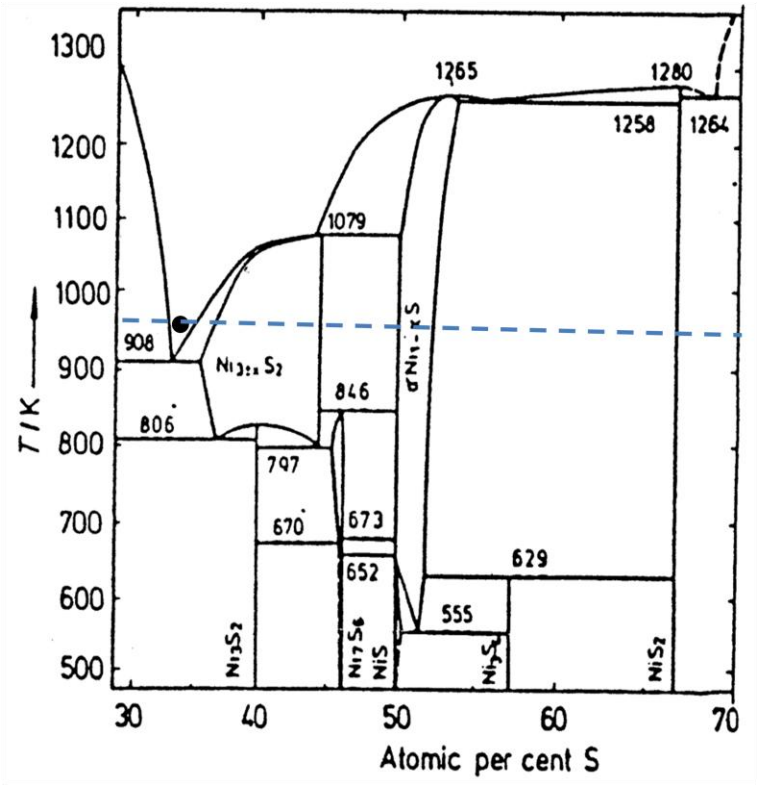

Figure 5.54 Phase diagram for the Ni-S system.[15]

Since non-wetting was observed after cooling to room temperature, it is inferred from the wetting process shown in Figure 5.55 that $\theta > 90^o$ and so the solid-vapor surface energy must be less than liquid-solid surface energy

Specifically, since non-wetting occurs, it must be that

$$\cos\theta = (\gamma_{S.V} - \gamma_{l,S})/\gamma_{l,V} < 0,$$

so that

$$\gamma_{S.V} < \gamma_{l,S}$$

where $\gamma_{S,V}$, $\gamma_{l,S}$, $\gamma_{l,V}$ are solid-vapor, liquid-solid and liquild-vapor surface energies, respectively.

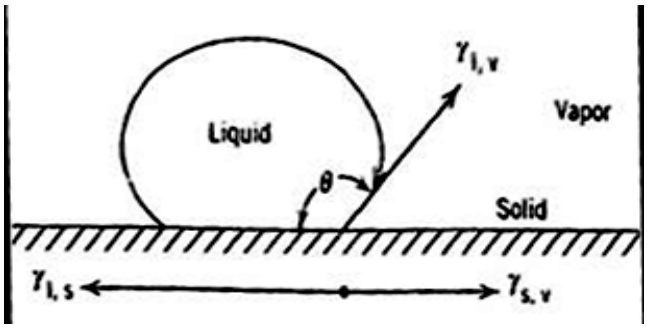

Figure 5.55 solid-vapor, liquid-solid and liquild-vapor surface energy

There is another question of why nodules were observed only on certain alloys such as Alloy 282 and 230. We know from Table 4.1 that Ni content in Alloy 230 and 282, 57wt.%, is the highest among all the alloys studied, which contributes to the

formation of the low-melting Ni-Ni_3S_2 eutectics. As would be expected, it was found from model alloys that Ni increases the tendency to form liquid Ni-Ni_3S_2 eutectics during the test. This will be presented in section 5.2.1.2.

In order to further explore the reason for nodule formation, the composition of regions in the scales formed on alloy 282 was carefully analyzed and compared to measurements made on several other alloys. Figure 5.56 shows detailed analysis of the composition of each layer on the selected samples, Alloy 120, 160, 188 and 282. Noticeably, a large amount of Co was observed in the outer and intermediate sulfide layers on Alloy 160 and 188, while only a small amount of Co existed in the sulfide layers on Alloy 282. For Alloy 120, although Co content in the sulfide scales is not very high, the existence of Fe in sulfide scales might have a similar effect as Co to reduce the risk of Ni-Ni_3S_2 eutectic formation.

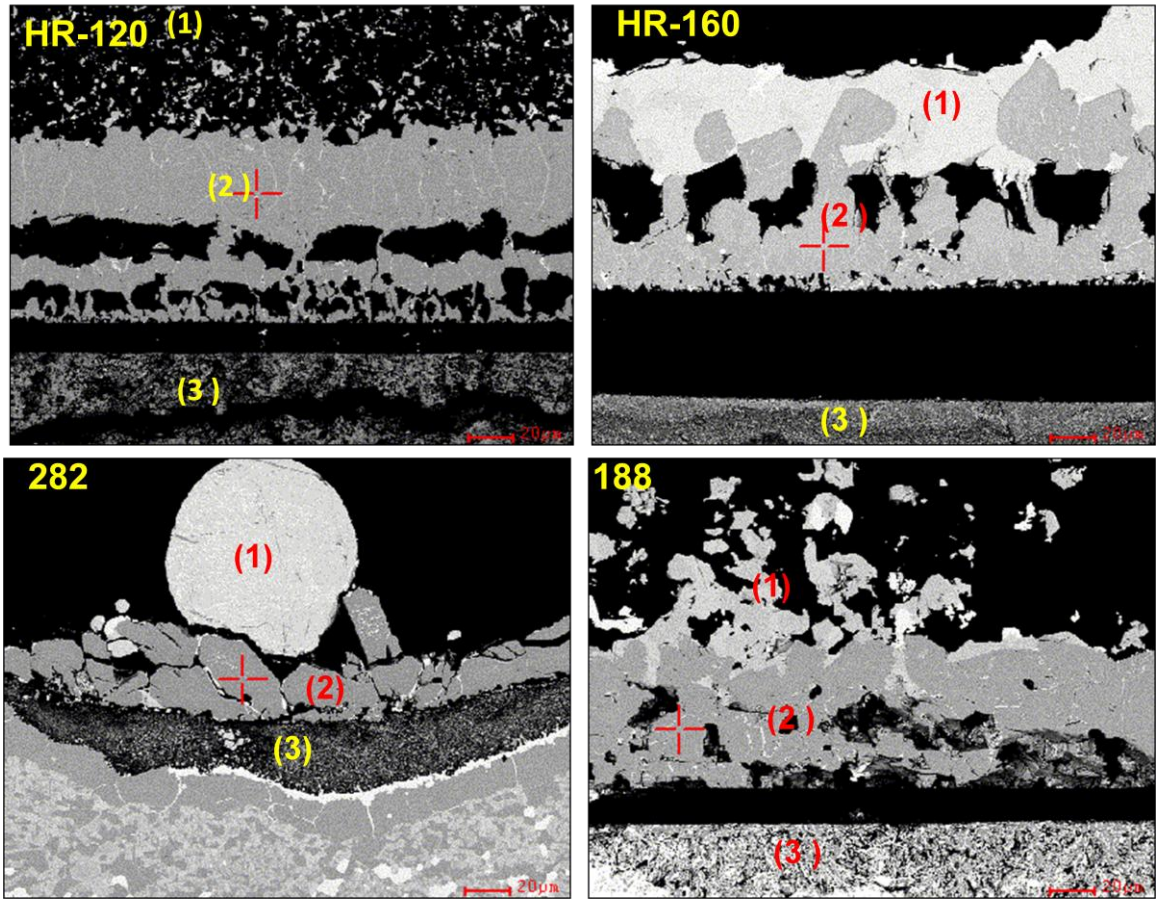

	Composition of outer layer (1) (at%)	Composition of intermediate layer (2) (at%)	Composition of inner layer (3) (at%)
HR-120	Ni sulfide Ni_3S_2 34.9Ni-49.1S-13.9Fe-1.1Cr-1.0Mn	Cr ,Fe sulfide($FeCr_2S_4$) 18.3Fe-14.9Cr-46.9S-7.5Ni-4.6Co-7.9O	Internal oxide and sulfides of Cr, Fe and Ni 14.8Cr-4.2Fe-6.5Ni-32.5O-38.9S-2.1Si-1Mn
HR-160	Ni sulfide Ni_3S_2 39.5Ni-38.2S-18.3Co-4O	Cr ,Fe sulfide($FeCr_2S_4$) 2.6Fe-21.7Cr-46.9S-6.5Ni-14.5Co-7.9O	Internal oxide and sulfides of Cr, Fe and Ni 26.5O-35.3S-23.6Cr-7.0Co-7.6Ni
188	Ni_3S_2 41.4Ni-36.5S-16Co-3.4O-1.9Fe	(2) Cr and Co sulfide 49.3S-20.5Cr-14.1Co-8.4O-7Ni-0.7Fe	Internal sulfide and oxide of Cr, Co 13.5O-8Co-19.2W-48.5S-10.8Cr
282	Ni sulfide 55.3Ni-33.7S-5.1Co-3.7O-1.2Fe	49.9S-26.8Cr-3.9Co-8.6Ni-9.5O-0.8Fe	Internal oxide and sulfides of Cr, Al and Ni 22.3O-40.5S-17.5Cr-5.5Ni-9.4Al-4.2Ti-0.7V

Figure 5.56 Detailed analysis of scale compositions

5.1.6 Internal Sulfidation zone

Figure 5.57 and Figure 5.58 show the cross-sectional images of Alloy 282 and 120 after testing in Gas 1 for different times, respectively. The top scale is Ni sulfide, intermediate scale is Cr sulfide, below which is the internal corrosion zone where sulfidation occurs within the metal-consumption zone. The internal corrosion zone contains a mixture of oxide and sulfide. As shown in the figures, the interface between the internal corrosion zone and the alloy after testing for 50 hours was quite planar.

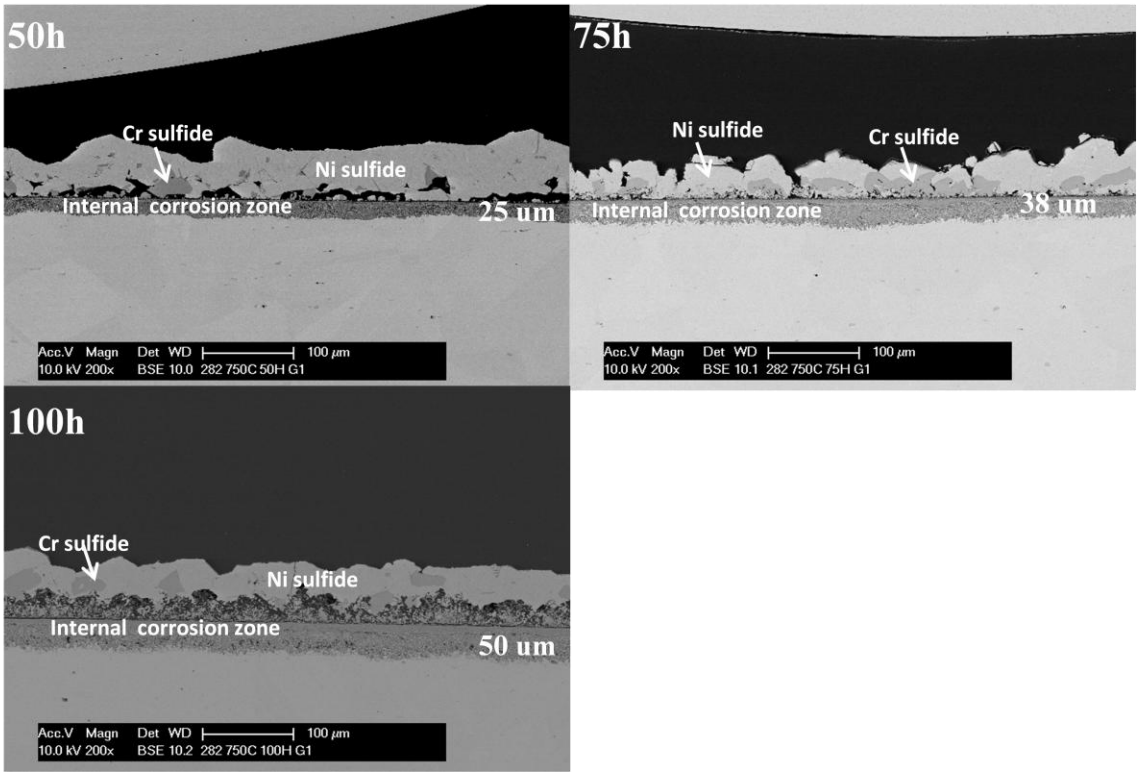

Figure 5.57 The internal corrosion zone of Alloy 282 after various times in Gas 1

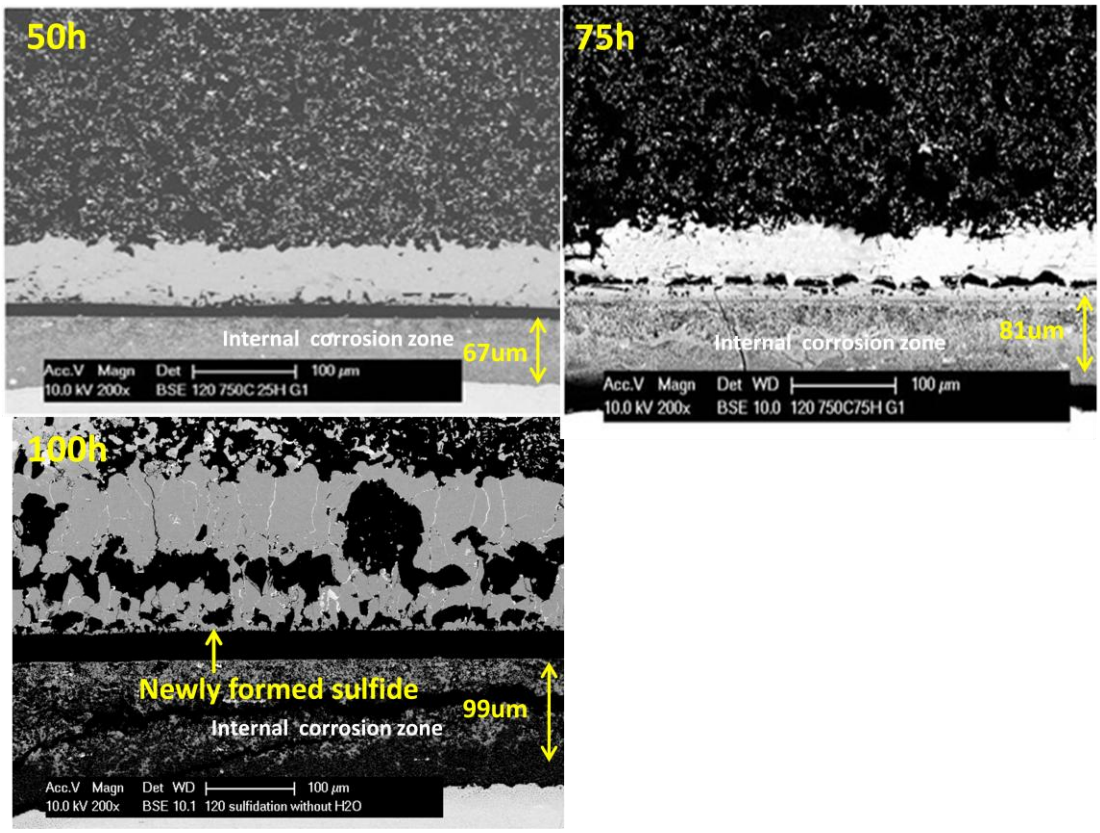

Figure 5.58 The internal corrosion zone of Alloy 120 after various times in Gas 1

Figure 5.59 schematically shows two kinds of interfaces between substrate Alloy A-B and sulfide BS: a non-planar interface and a planar interface. When the scale growth is controlled by diffusion in the alloy, the scale–alloy interface can become unstable, as illustrated in Figure 5.59 (a). Since any inward protuberance of the scale–alloy interface will shorten the diffusion distance across the zone depleted in B, such a protuberance will grow and result in a wavy scale–alloy interface[139]. When the interface between alloy and scale is planar, it suggests that either outward diffusion of metal B or inward diffusion of oxygen through the BS scale is rate controlling.

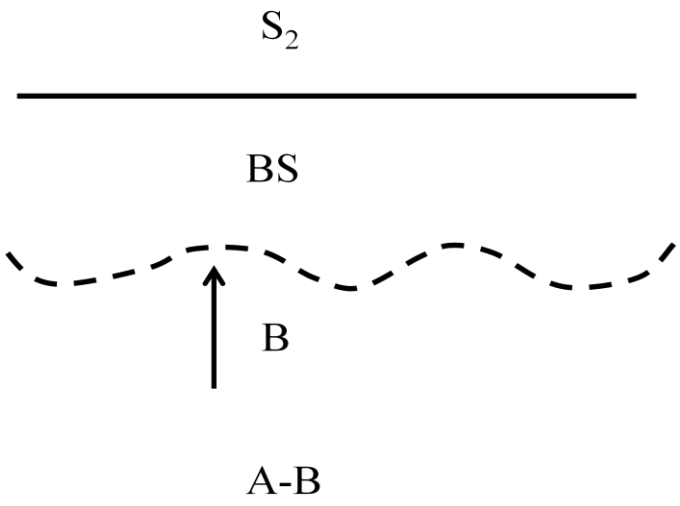

(a) Unstable interface: B diffusion through A-B is rate controlling

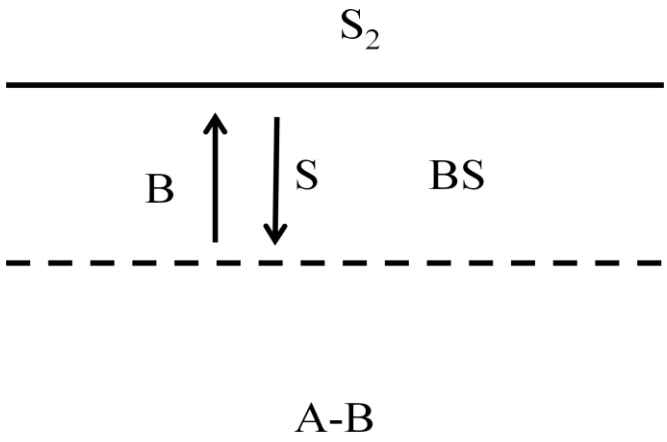

(b) Stable interface: either B or S diffusion through BS is rate controlling

Figure 5.59 Schematic drawing of the planar and non-planar alloy-scale interface

Figure 5.60 and Figure 5.61 show the thickness of internal corrosion zone with time of testing in Gas 1. These figures show that the growth of internal corrosion zone obeyed parabolic kinetics after 50 hours.

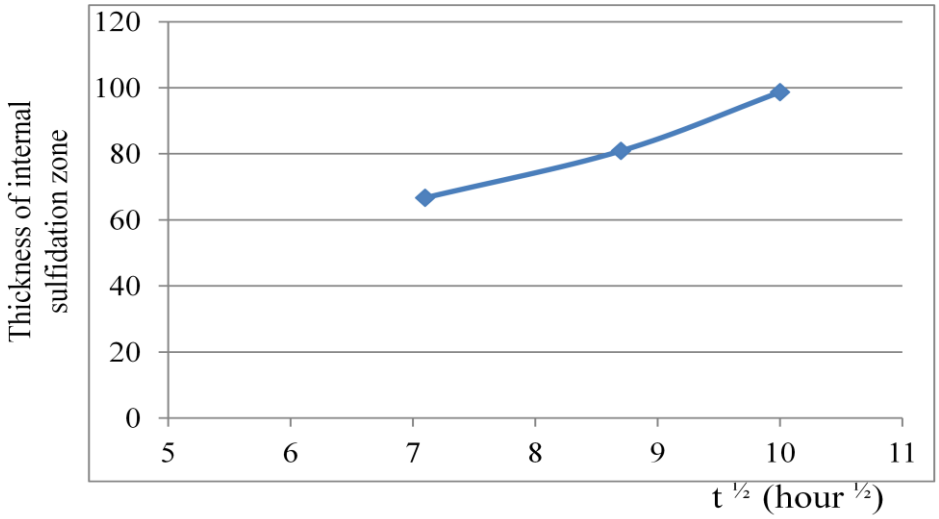

Figure 5.60 The growth of internal sulfidation zone with time for alloy 120

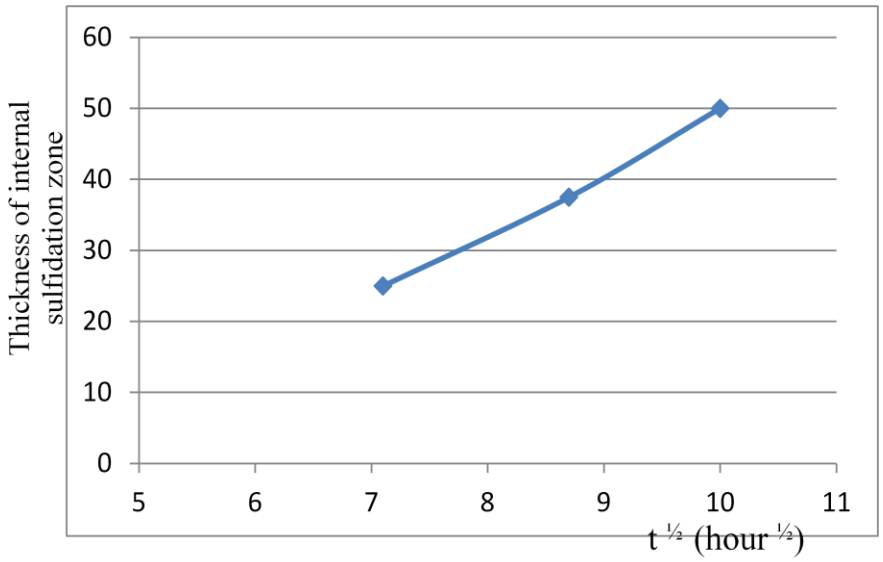

Figure 5.61 The growth of internal sulfidation zone with time for Alloy 282

Alloys 120 and 282 showed no indication of internal sulfide precipitates, as evidenced in Figure 5.57 and Figure 5.58. This is likely because the rate at which an alloy is consumed by scaling exceeds the rate at which sulfur can diffuse into the alloy. The rapidly receding scale-alloy interface sweeps up and incorporates any internal precipitates. Mrowec and Przybylski[13] reported that internal sulfide precipitates were generally absent when they studied the sulfidation of Fe-, Co- and Ni-based alloys with additions of reactive metals such as Cr and Al.

5.1.7 Preliminary conclusions

After testing the various Haynes alloys in the simulated atmosphere of a low NO_x burner, the following conclusions can be drawn.

(1) Compared to Ni-Fe-based and Co-based alloys, the Ni-rich Ni-Co-based alloys studied showed the best corrosion resistance, with alloys 160 and 263 exhibiting the best sulfidation resistance in all the three gases.

(2) In the case of Ni-based alloys, at a certain Cr level (~25wt. %), the Co content influences the weight gain and the onset of breakaway corrosion. An alloy has the longest time to breakaway when Ni/Co major element ratio is near unity, because both Ni and Co availability are low in such a case.

(3) Alloy 263 does not have high Cr and Co contents compared to Alloy 160, but the former has less weight gain due to relatively minor addition of Ti, Al and Mo. These elements can play an important role to improve sulfidation resistance due to their ability to promote and/or maintain protective oxide scale formation.

(4) At a given sulfur pressure, there is a threshold oxygen partial pressure beyond which a continuous protective chromia scale is developed. This threshold pressure decreases with the increase in the alloy Cr content. Even so, the kinetic boundary between sulfidation and oxidation is highly alloy dependent, beyond just total Cr content.

(5) In Gas 3, which has the highest oxygen potential, oxidation dominated over sulfidation; the chromium oxide layer formed to provide protection against corrosion. In Gas 1, where sulfidation dominates, all the alloys showed the worst corrosion resistance due to the sulfides formed over chromium oxide layer.

(6) The growth of an external whisker is maintained by the outward diffusion of Ni. The whisker formation on Alloy 120 is believed to be related to surface-reaction control of the H_2S dissociation. The formation of whiskers indicates the occurrence of preferential growth, which can be explained by an orientation dependence of the H_2S dissociation reaction.

(7) The Kirkendall effect and diffusional creep as a result of the stress produced in the scale probably account for the formation of voids in the scale, and the dissociation process eventually leads to the massive void formation.

(8) The formation of nodules on some alloys is due to melting via Ni-Ni_3S_2 eutectic formation during the test.

5.2 CORROSION RESISTANCE OF MODEL ALLOYS

5.2.1 Model alloys with different Cr and Co levels

5.2.1.1 Phase identification

The phase constitution of the model alloy systems was firstly predicted by utilizing thermodynamically computed phase diagrams. Direct comparison was then made to experimentally determined phase compositions.

The Pandat 8.0 software together with the Ni8 database were used to compute the Ni-Cr-Co phase diagram at 750^{o}C. The resulting phase diagram is shown in Figure 5.62.

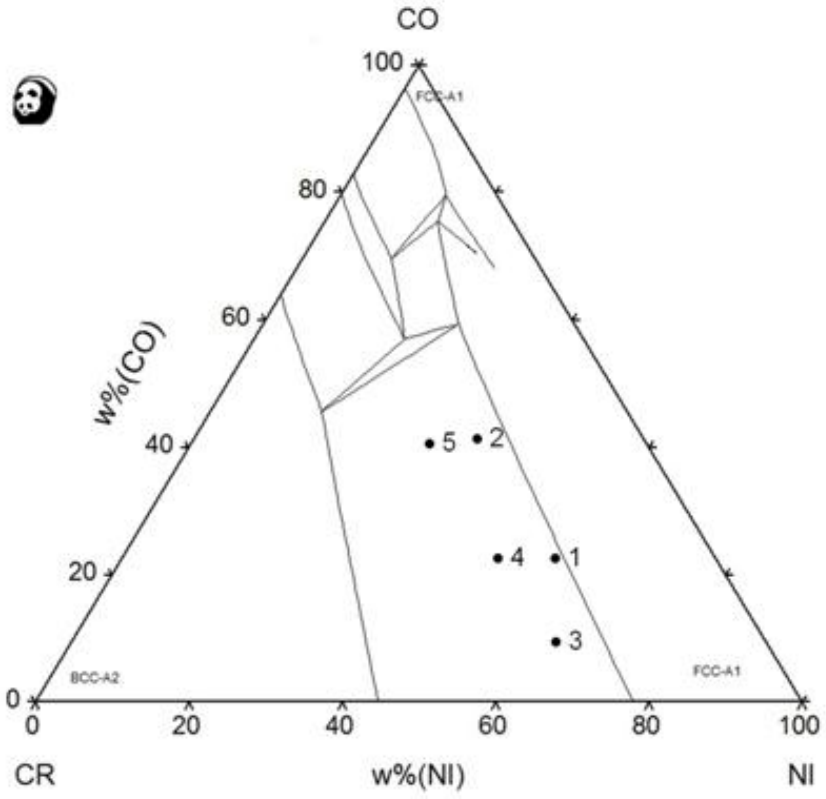

Figure 5.62 750 ^{o}C phase diagram of the Ni-Cr-Co system

The Co-rich portion of the phase diagram in Figure 5.62 is not complete due to the database being insufficient. The five model alloys are indicated in this diagram. They are all located in the FCC+BCC two phase region.

Binary Ni-Cr and Ni-Co phase diagrams can also be used to help analyze the possible phases that exist at 750^{o}C. It is known from the Ni-Cr phase diagram, shown in Figure 5.63, that the Ni content should be above 68wt% to have single phase FCC (Ni) at 750^{o}C. Since the maximum Ni content of the five model alloys (62wt %) is below this value, it is plausible that the model alloys are located in the FCC+BCC two phase region. It is clear from the Co-Ni phase diagram in Figure 5.64 that the single phase FCC phase exists at 750^{o}C (1023K). Therefore, analysis from Ni-Cr and Ni-Co binary phase diagrams concur with the calculated Ni-Co-Cr isotherm that the model alloys should have a FCC+BCC phase constitution at 750^{o}C. Figure 5.65 shows the XRD pattern of Alloy 1 after annealing at 750 ^{o}C and subsequent water quenching. Only FCC peaks are observed in the pattern. Although XRD analysis only showed FCC peaks, it is possible that the volume fraction of BCC phase is too small to be detected.

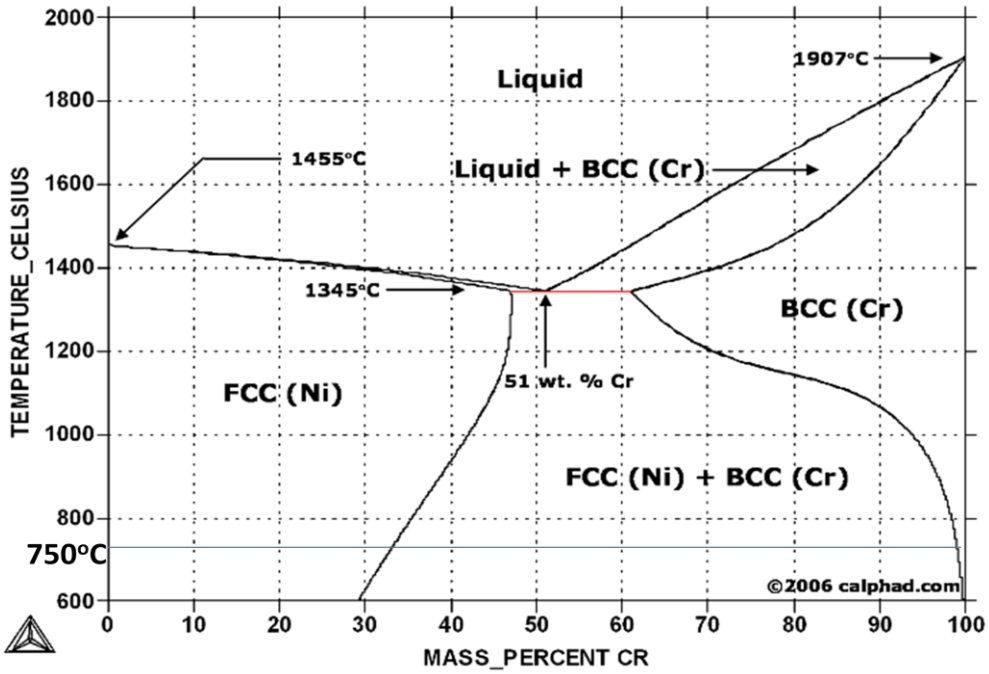

Figure 5.63 Binary Ni-Cr phase diagram

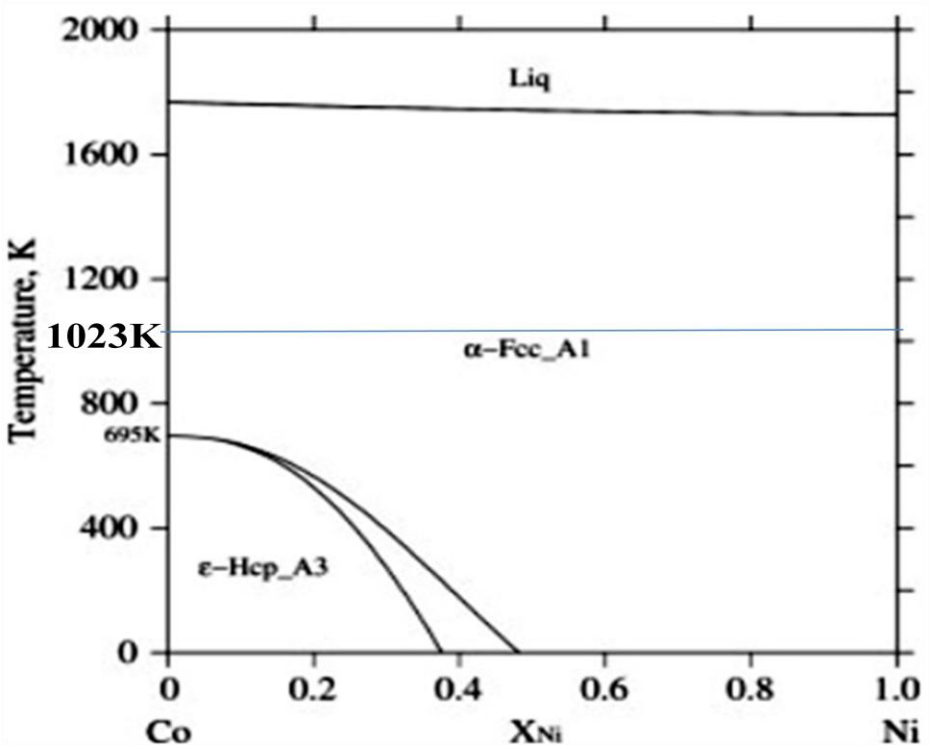

Figure 5.64 Binary Co-Ni phase diagram

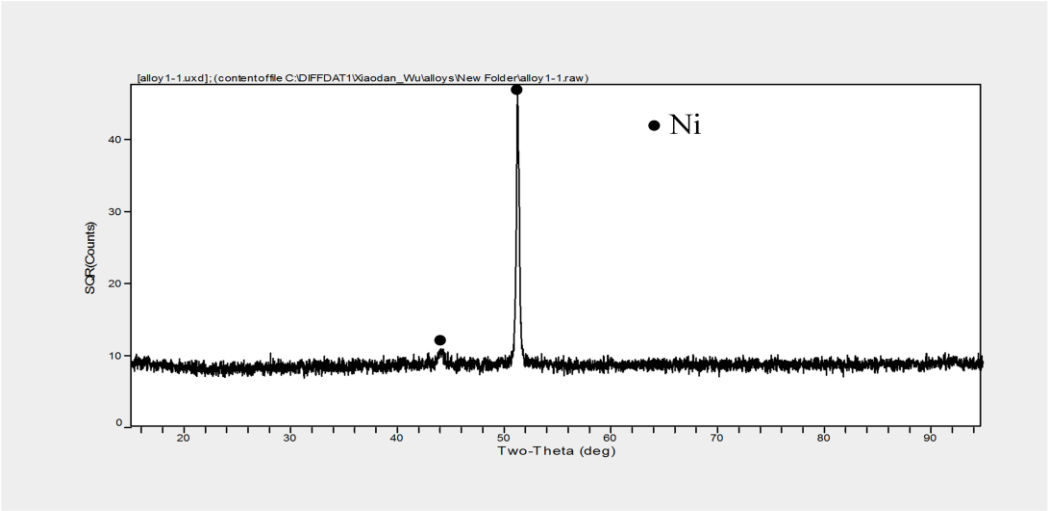

Figure 5.65 XRD pattern of Alloy 1

To verify the phase constitutions, the alloys were annealed at 750^{o}C and water-quenched to room temperature. The alloys were then etched in Marble reagent (4g $CuSO_4$+20 ml HCl+20ml H_2O) for 10 seconds. The microstructures were analyzed using optical microscopy, and representative images are shown in Figure 5.66.

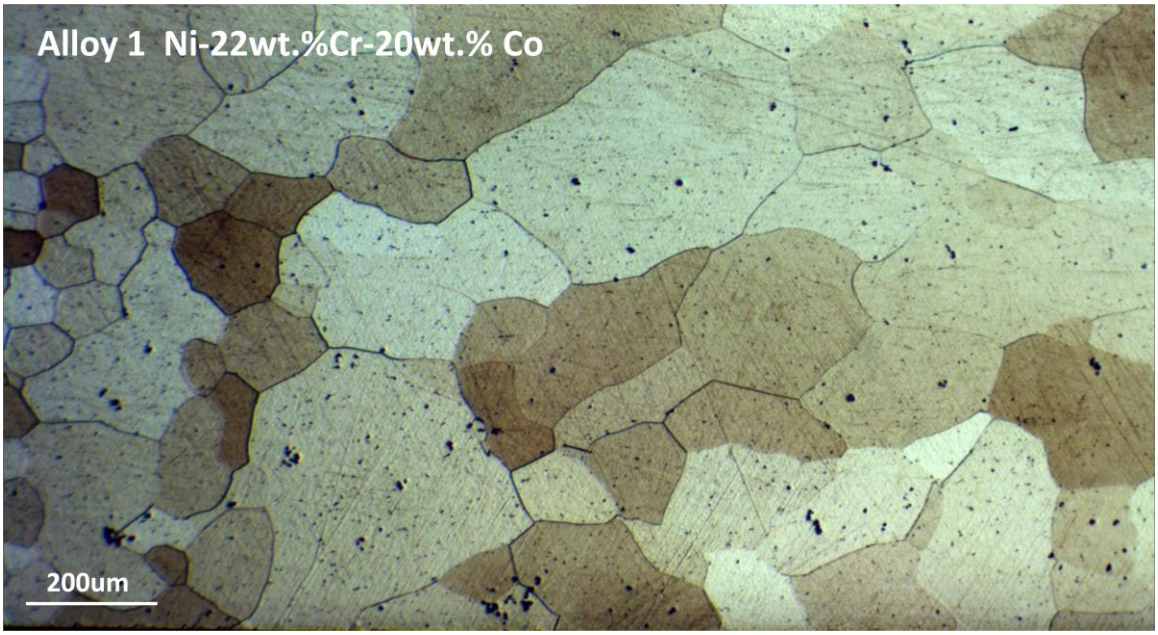
Alloy 1 Ni-22wt.%Cr-20wt.% Co
200um

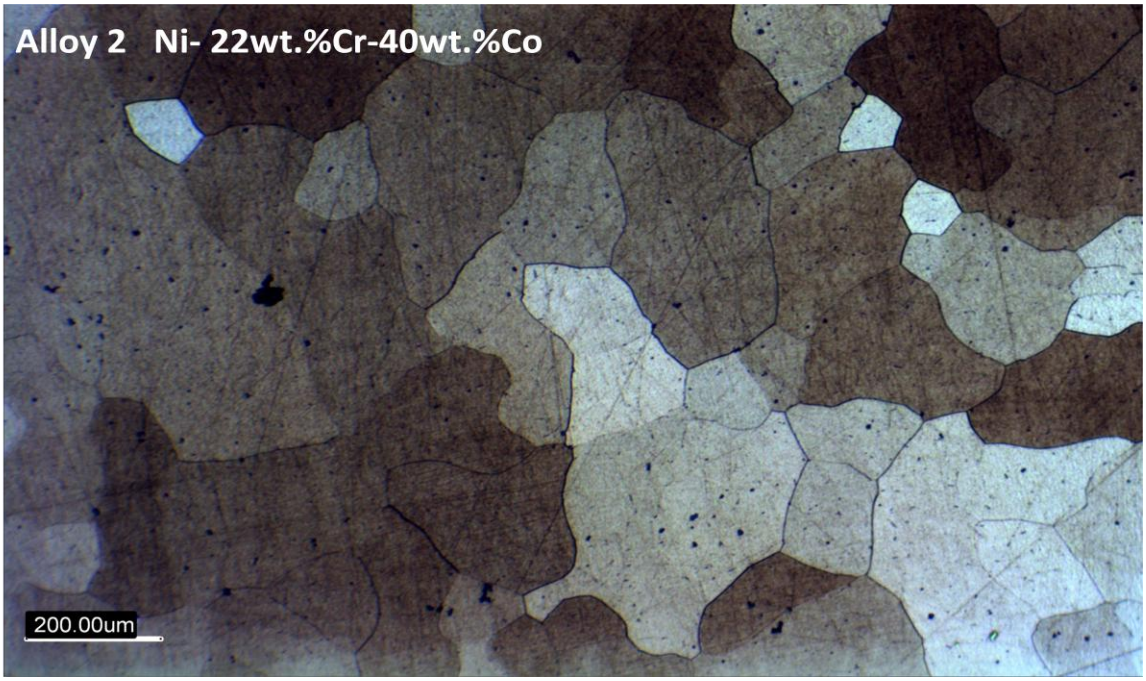
Alloy 2 Ni- 22wt.%Cr-40wt.%Co
200.00um

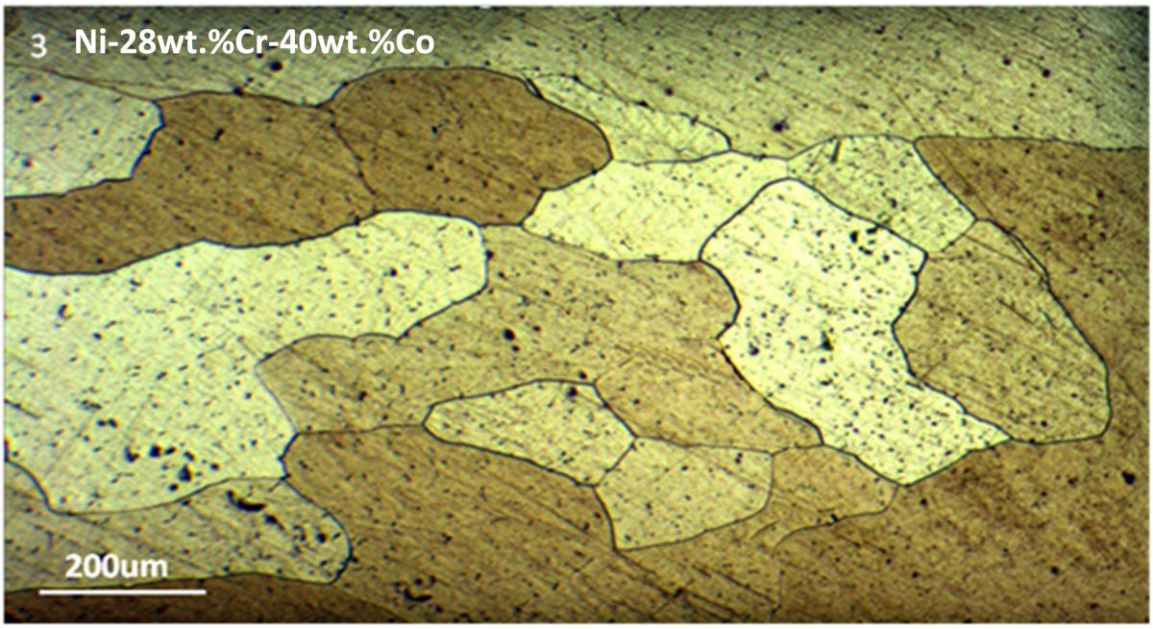
3 Ni-28wt.%Cr-40wt.%Co
200um

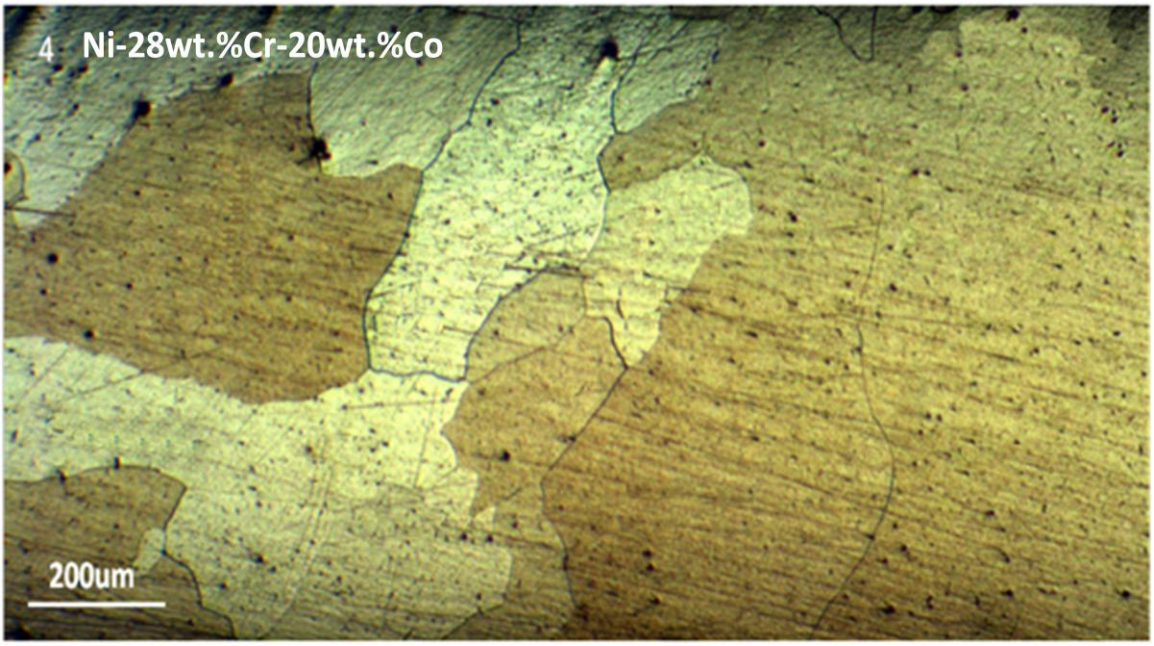
4 Ni-28wt.%Cr-20wt.%Co
200um

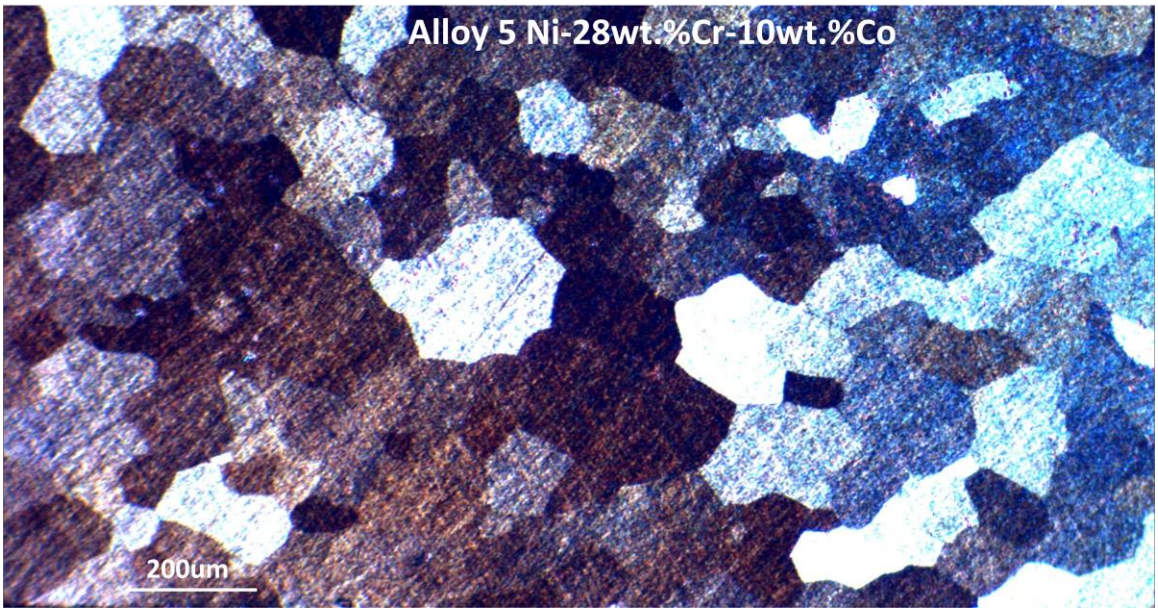

Figure 5.66 Optical micrographs of the model alloys studied

5.2.1.2 Sulfidation resistance in Gas 1

One purpose for making the five model alloys was to verify the observed effect of Ni/Co major element ratio in the study of the commercial alloys (chapter 4). The five model alloys were tested in Gas 1 for 25, 50 and 100 hours. Figure 5.67 shows the weight gains as a function of testing time. In agreement with the trend found with the commercial alloys, Alloys 2 and 5 with Ni/Co near unity have less weight gain and thus better sulfidation resistance.

Figure 5.68 clearly shows the effect of Cr on sufidation resistance. As seen in this figure, weight gain decreases with increase in alloy Cr content at two Co levels, 20 and 40 wt.%. Similarly, weight gains decrease with the increase in alloy Co content, as shown in Figure 5.69. This verifies the established beneficial effects of Cr and Co on sulfidation resistance.

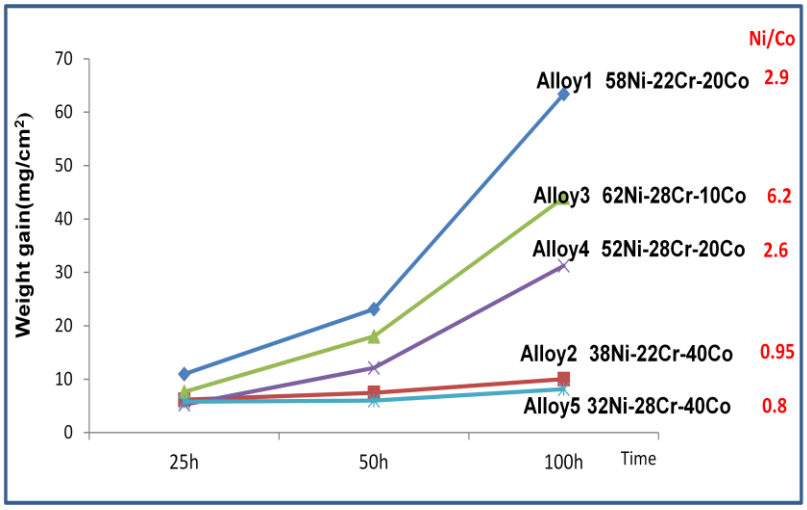

Figure 5.67 The weight gain as a function of time in Gas 1

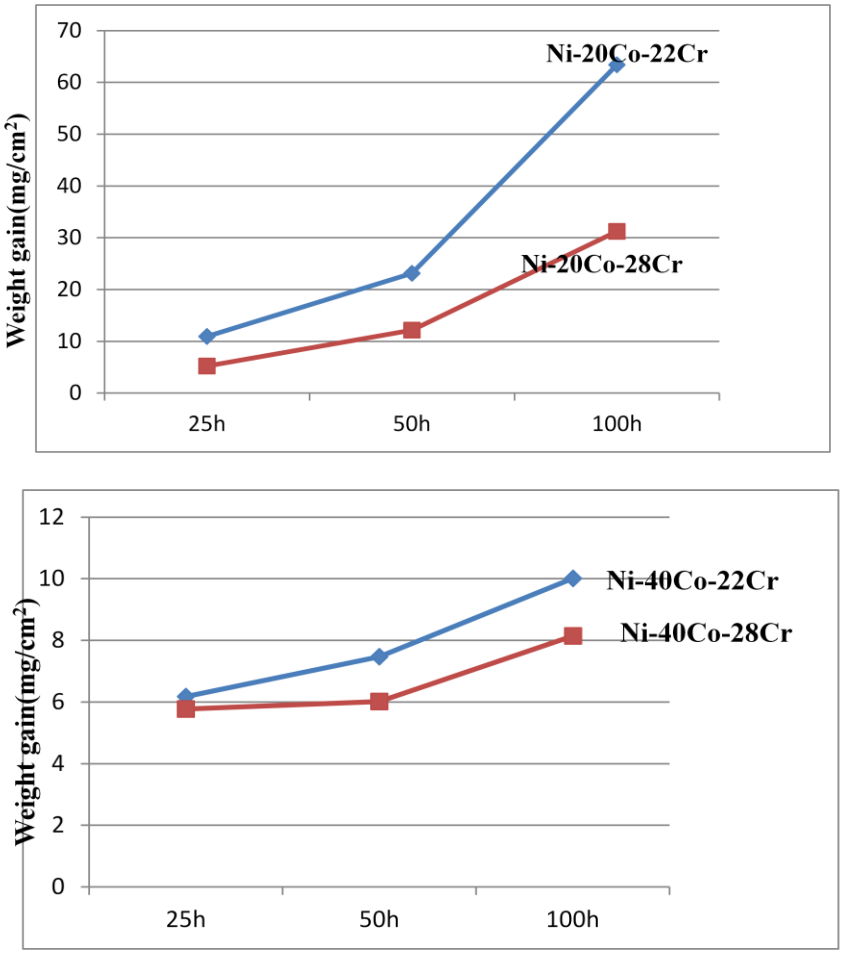

Figure 5.68 Effect of Cr content on weight gain at two constant Co level

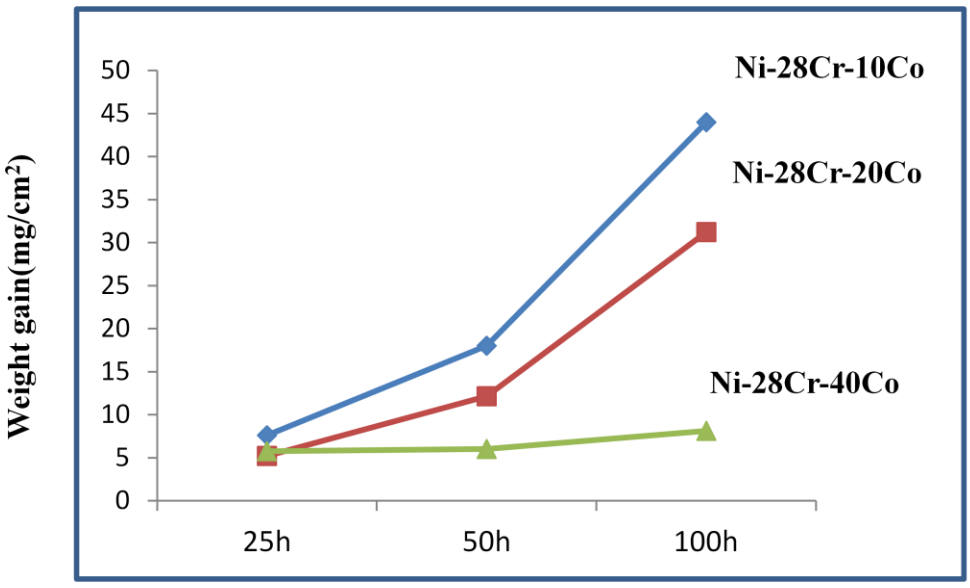

Figure 5.69 Effect of Co content on weight gain at constant Cr level

Figure **5.70** shows surface images of the five alloys after testing for 25h, 50h and 100h in Gas 1 at 750^{o}C. Figure 5.71 shows cross-sectional images of alloys after 25 hours in Gas 1.

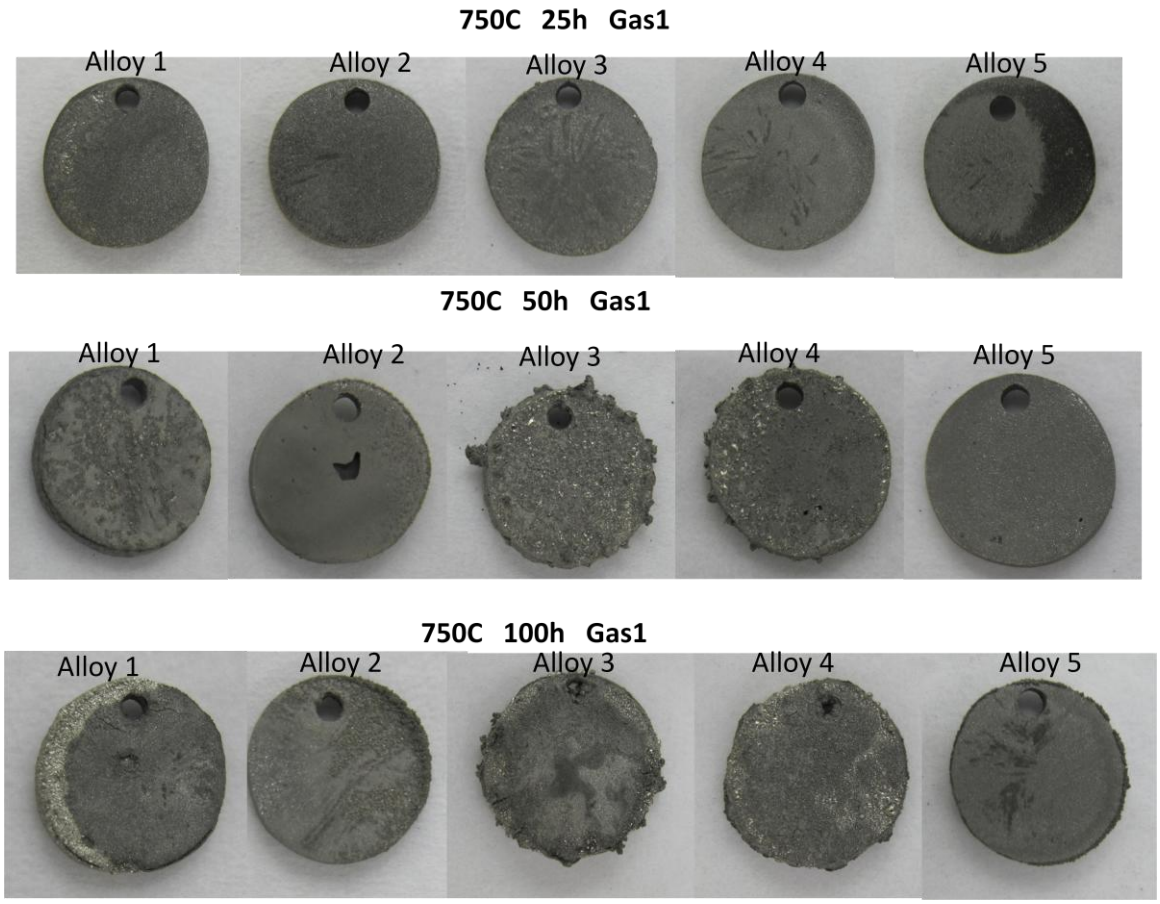

Figure 5.70 Surface images after testing for 25, 50 and 100 hours in Gas 1 at 750^{o}C

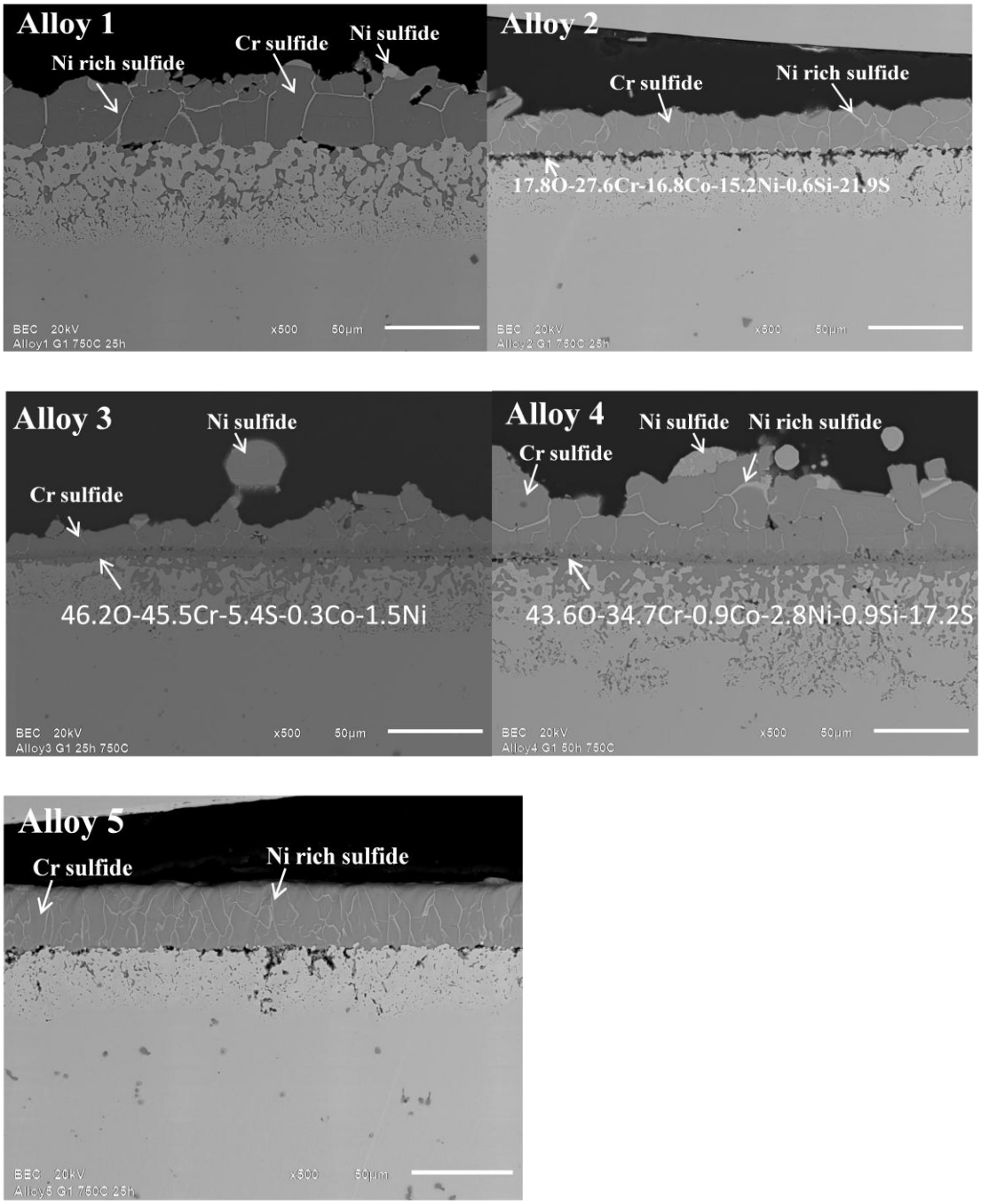

Figure 5.71 Cross-sectional SEM images of the model alloys after testing for 25 hours in Gas1

As indicated in Figure 5.71, Cr sulfide formed on all the alloys. Cr sulfide also formed internally, which is shown in the magnified SEM images of Alloy 1 and 2 in Figure 5.73. The measured compositions of the Cr sulfides are summarized in Table 5.3. All alloys are located in the region where Cr_2S_3 and Cr_3S_4 coexist. It is hard to determine the exact portion of Cr_2S_3 and Cr_3S_4 since there are uncertainties in the XRD analysis due to the similar lattice parameters of Cr_2S_3 and Cr_3S_4. Other researchers also found similar difficulty to determine the exact type of Cr sulfide[142].

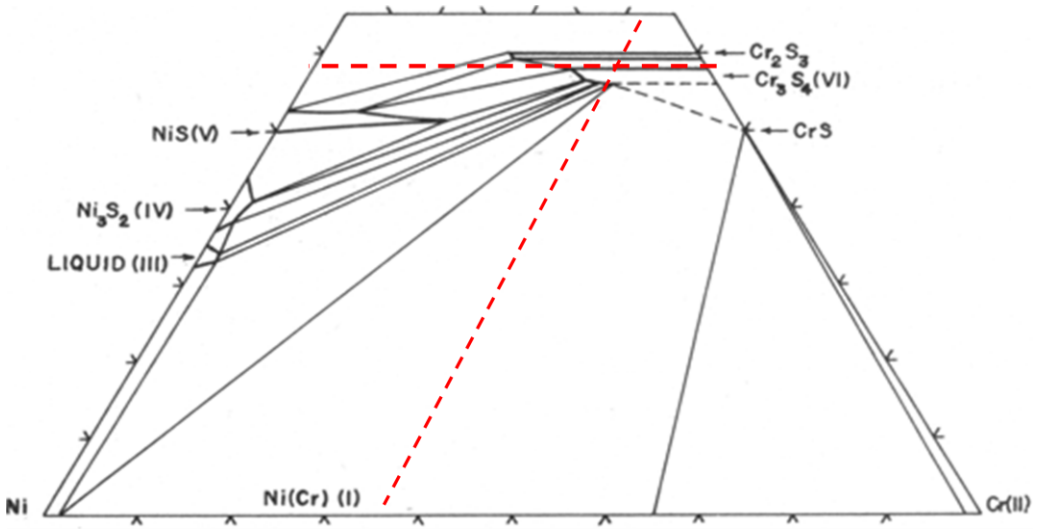

Figure 5.72 S-Ni-Cr phase diagram at 700°C

The white phase in the Cr sulfide is Ni-enriched sulfide. It is seen that Ni content in the Cr sulfide formed in Alloy 3 is the highest, 5.6wt%. This is likely because Alloy 3 has the highest Ni content, 62wt%. The Ni content in the Cr sulfide generally trended with the Ni in the alloy, seen in Figure 5.74.

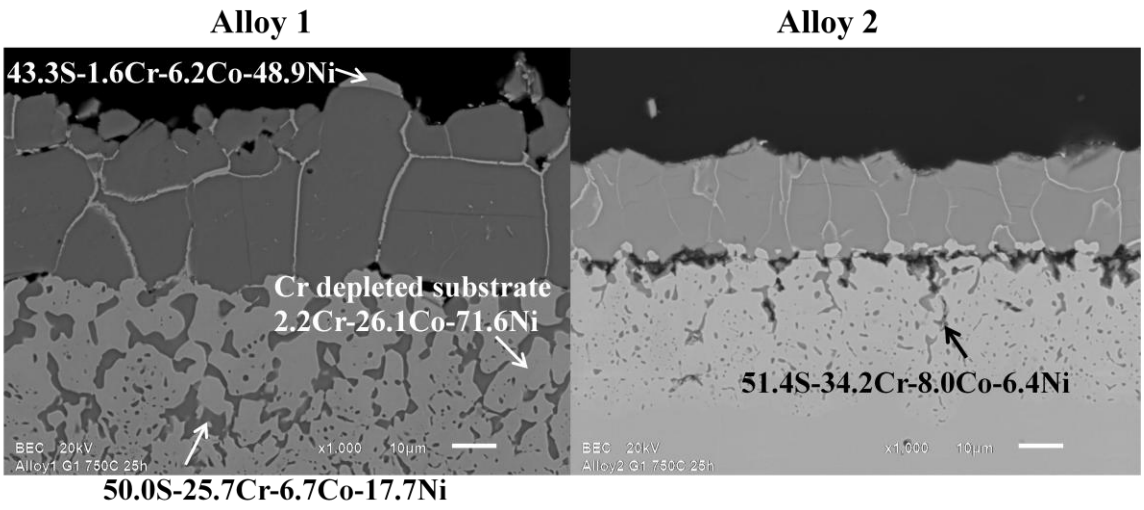

Figure 5.73 The magnified images of Alloy 1 and 2 after 25 hours in Gas 1

Ni sulfide nodules were observed on Alloys 1, 3 and 4, which all contain greater Ni than Alloys 2 and 5. As discussed earlier in section 5.1.5.3, nodule formation indicates the formation of liquid during testing due to the relatively low of Ni- Ni_3S_2 eutectic temperature. The results for the model alloys show that the tendency to form liquid reaction product increases with increase in the alloy's Ni content, thus verifying the detrimental effect of Ni on sulfidation resistance.

Table 5.3 The composition of sulfide scale formed after 25 hours in Gas 1

Cr sulfide	S(at.%)	Cr(at.%)	Co(at.%)	Ni(at.%)
Alloy1	58.0	32.7	4.0	5.4
Alloy2	59.2	35.8	4.4	0.6
Alloy3	58.9	33.3	2.2	5.6
Alloy4	58.9	35.3	2.5	3.4
Alloy5	58.3	37.8	3.5	0.3

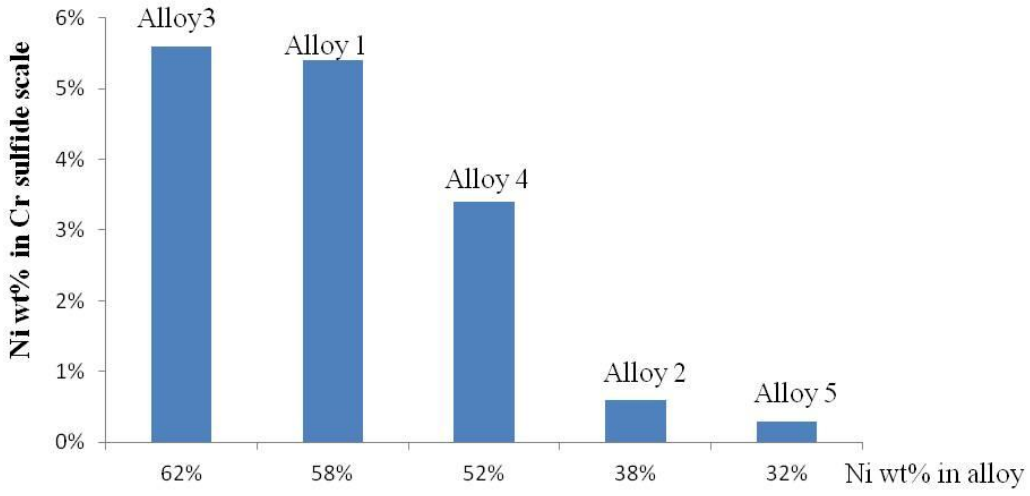

Figure 5.74 Ni content in the Cr sulfide scales as a function of Ni content in the alloy

Figure 5.75 shows cross-sectional images of the model alloys after 50 hours exposure in Gas 1. The cross-sections look similar to those after 25 hours of exposure. A multi-layered structure formed: outer Ni-sulfide nodules (except Alloy 5), an intermediate layer of Cr-rich sulfide, an inner layer mixture of Cr oxide and Cr sulfide and an innermost internal Cr sulfide.

Figure 5.76 shows magnified images of the five model alloys. The composition of each layer is indicated in the images. The nodule morphology and composition are similar to those observed with the commercial alloys. The internal corrosion zone can be clearly seen in Alloy 1 of Figure 5.76. The gray phase is Cr sulfide, the light phase is occluded metal rich in the more noble alloy constituents (i.e., Ni and Co).

Figure 5.77 shows the cross-sectional images after 100 hours in Gas 1. The morphologies are analogous to those after 50 hours of exposure.

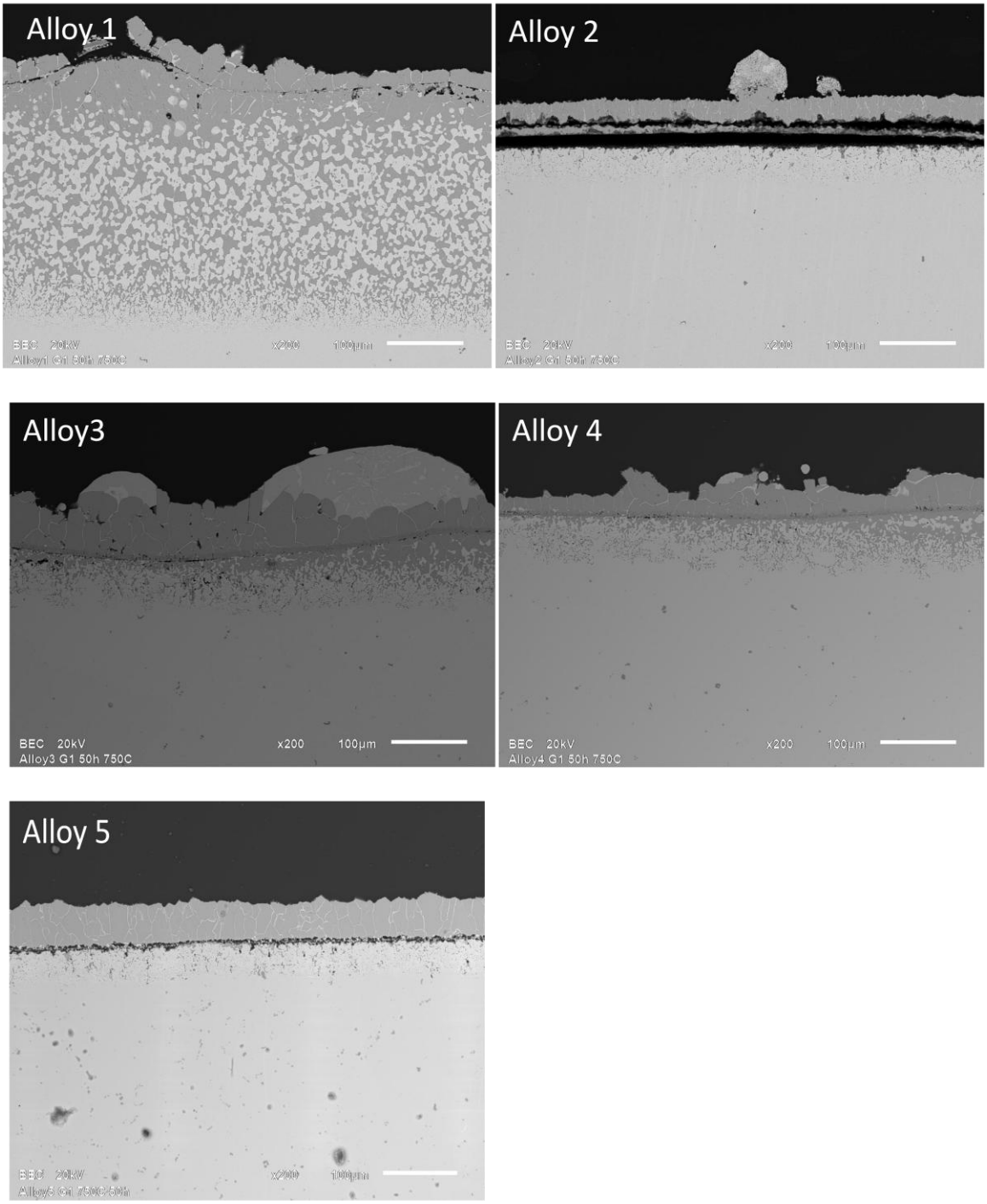

Figure 5.75 Cross-sectional images of the model alloys after testing for 50 hours in Gas1

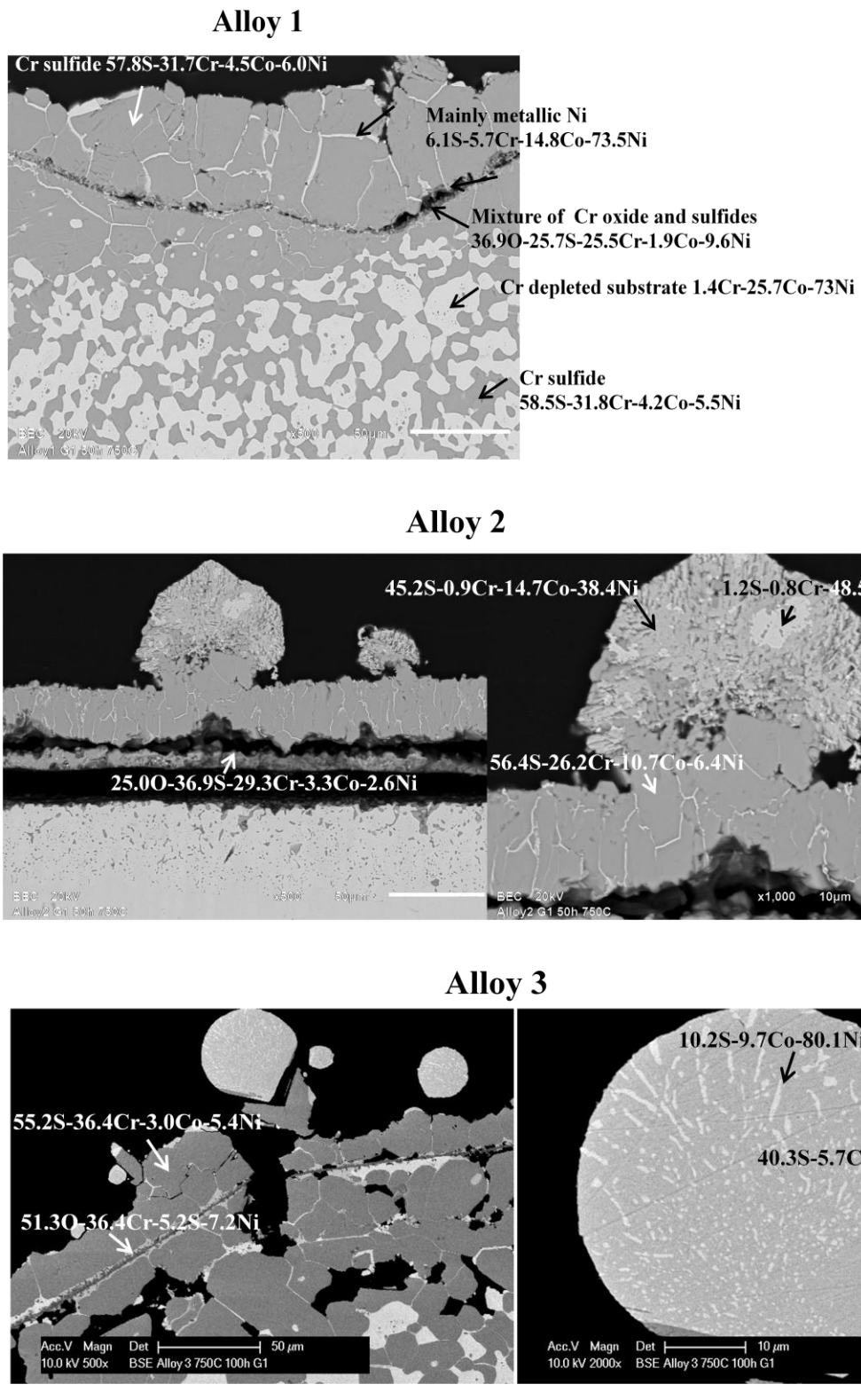

Figure 5.76 The magnified images of alloys after 50 hours in Gas 1

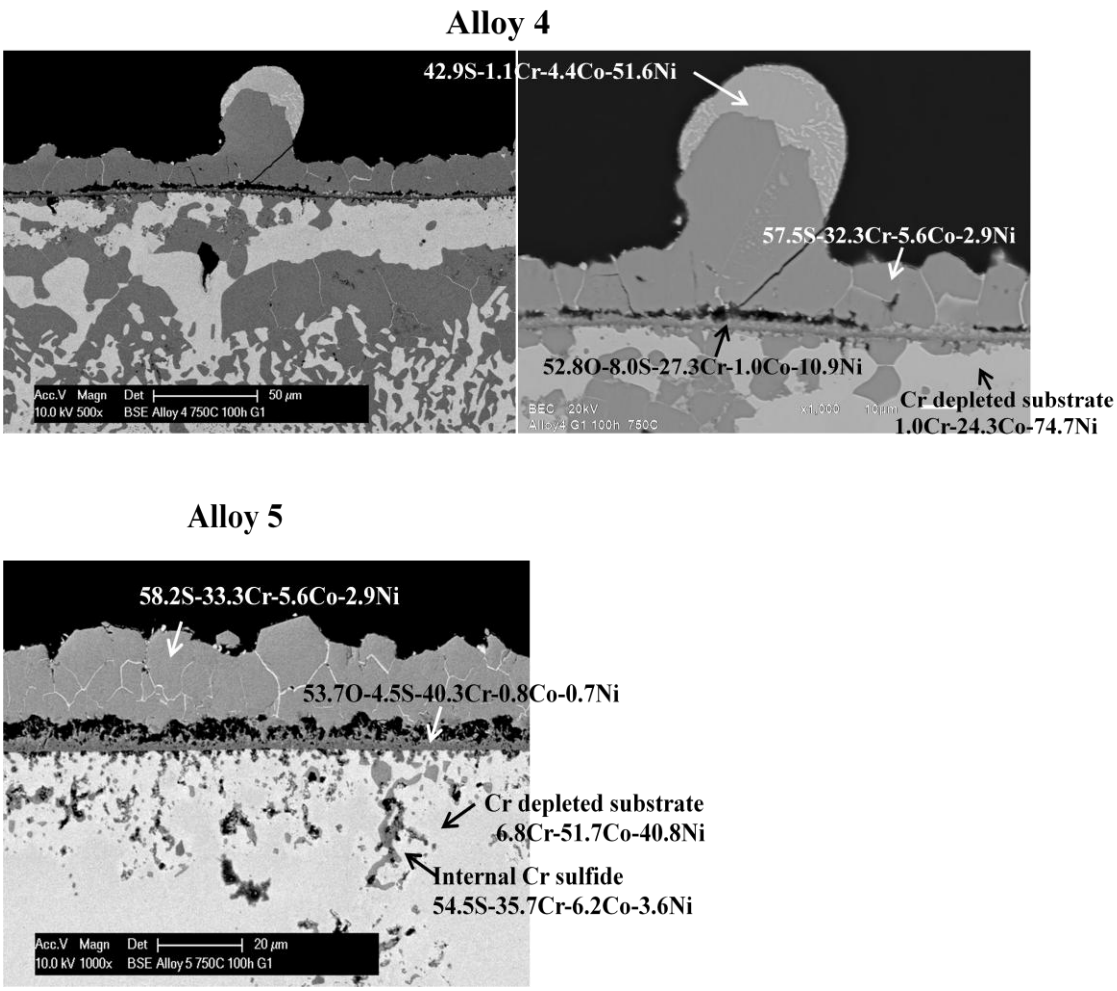

Figure 5.76 Continued Magnified images of alloys after 50 hours in Gas 1

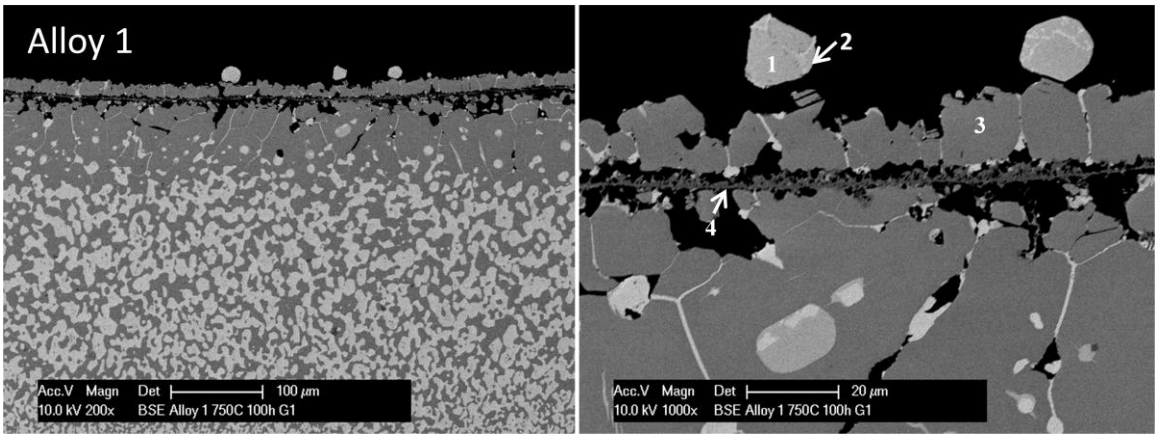

1 Ni sulfide 42.9S-0.8Cr-7.6Co-48.7Ni

2 Metallic Ni and Co 6.5S-0.9Cr-16.8Co-75.8Ni

3 Cr sulfide 56.8S-31.8Cr-5.0Co-6.4Ni

4 Cr_2O_3 enriched layer

Figure 5.77 Cross-sectional images of the model alloys after testing for 100 hours in Gas1

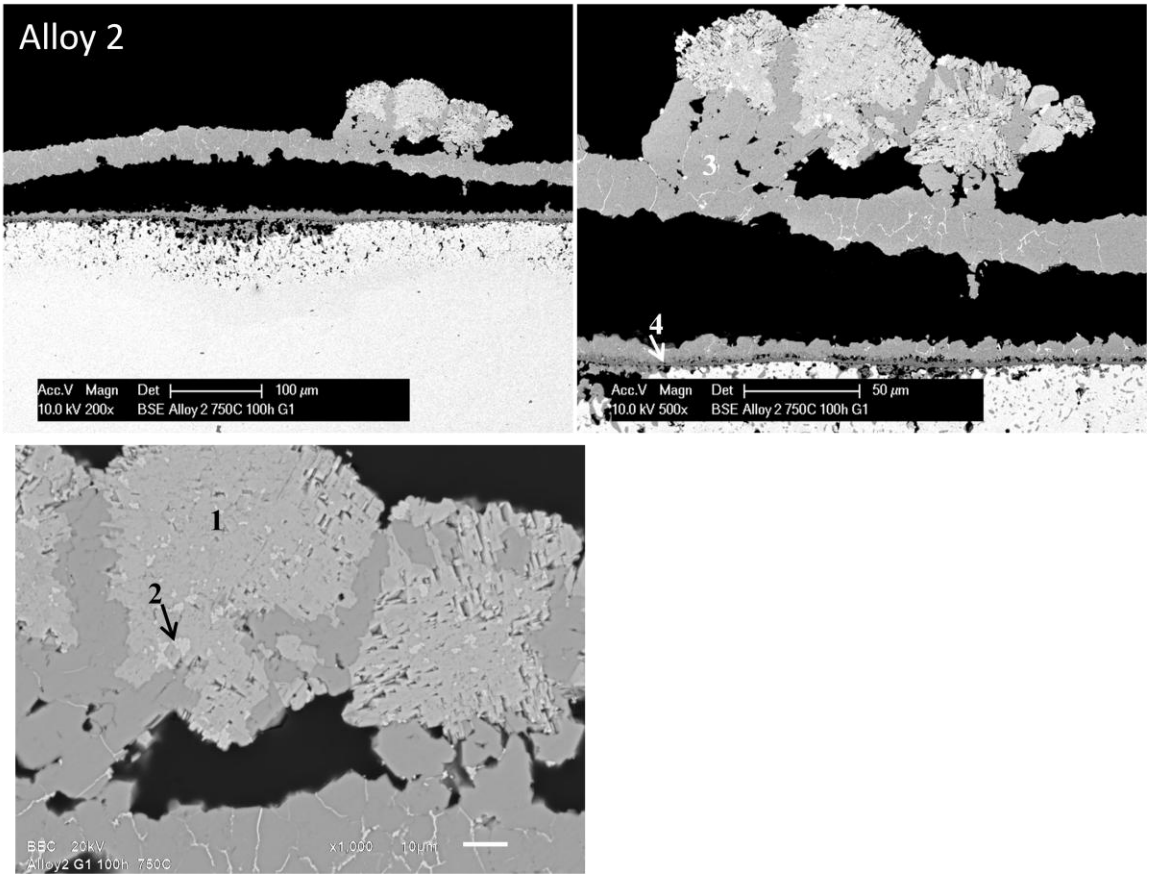

1 Ni sulfide 41.9S-0.6Cr-16.6Co-40.9Ni

2 Metallic Ni and Co 3.4S-0.9Cr-32.8Co-63.0Ni

3 Cr sulfide layer 54.1S-29.5Cr-10.9Co-5.6Ni

4 Cr_2O_3 enriched layer 50.5O-8.6S-39.8Cr-1.0Co

Figure 5.77 Continued Cross-sectional images of the model alloys after testing for 100 hours in Gas1

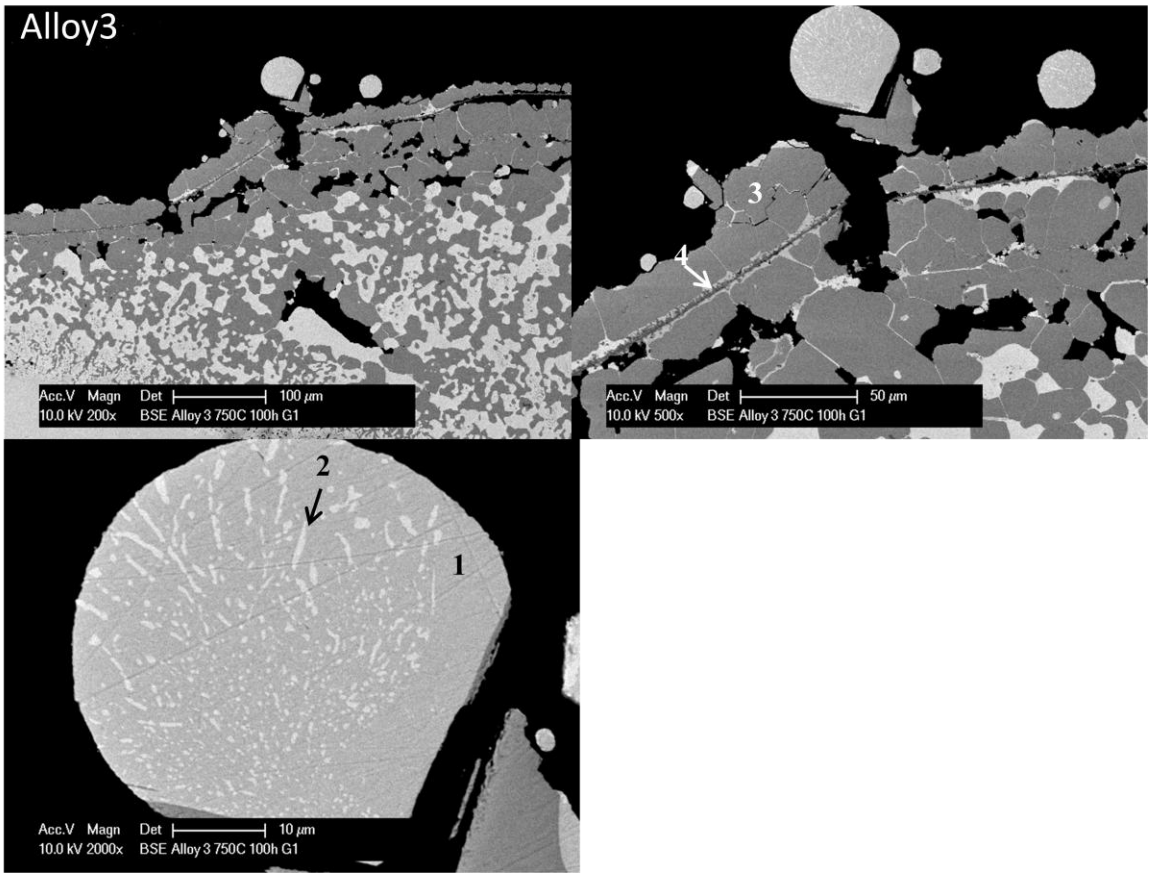

1 Ni sulfide 40.3S-5.7Co-54.0Ni

2 Metallic Ni and Co 0.2S-9.7Co-80.1Ni

3 Cr sulfide 55.2S-36.4Cr-3.0Co-5.4Ni

4 Cr_2O_3 enriched layer 51.3O-36.4Cr-5.2S-7.2Ni

Figure 5.77 Continued Cross-sectional images of the model alloys after testing for 100 hours in Gas1

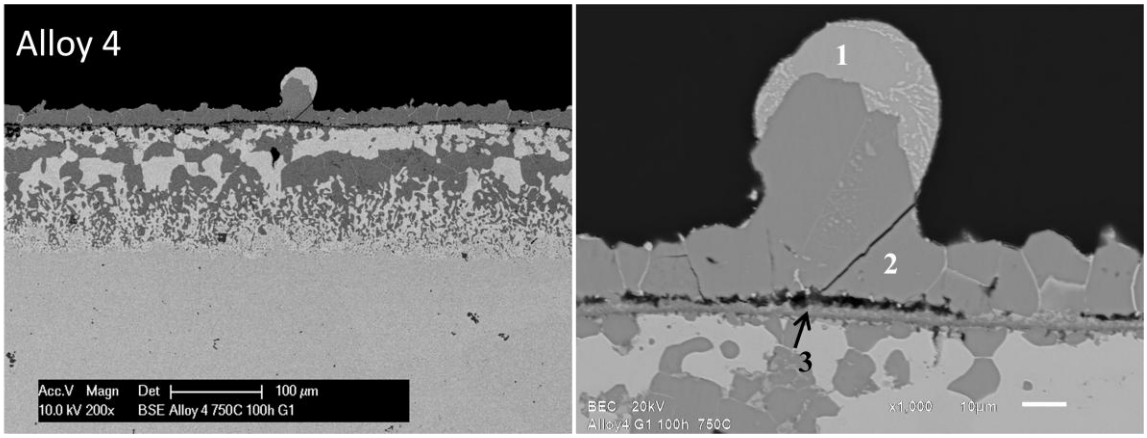

1 Ni sulfide 42.9S-1.1Cr-4.4Co-51.6Ni

2 Cr suflide 57.5S-32.3Cr-5.6Co-2.9Ni

3 Cr_2O_3 enriched layer 52.8O-8.0S-27.3Cr-1.0Co-10.9Ni

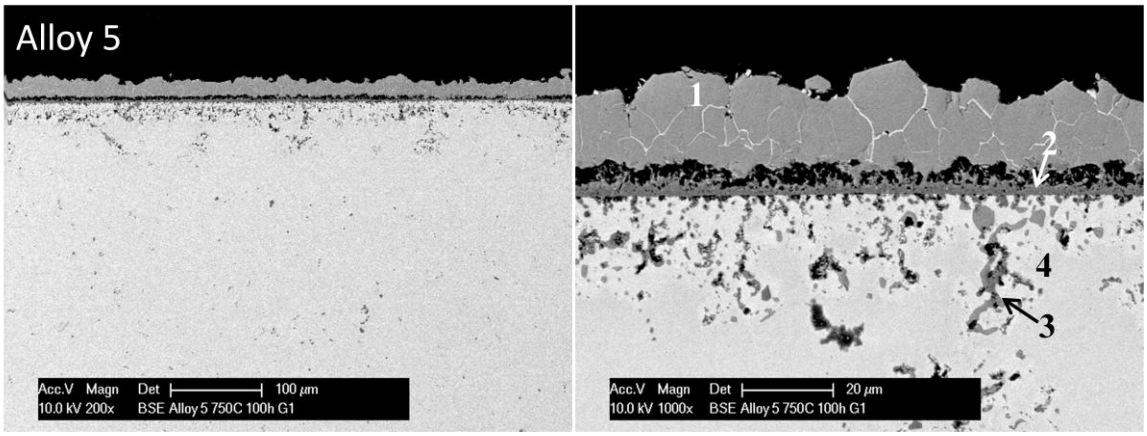

1 58.2S-33.3Cr-5.6Co-2.9Ni

2 Cr_2O_3 enriched layer 53.7O-4.5S-40.3Cr-0.8Co-0.7Ni

3 Internal Cr sulfide 54.5S-35.7Cr-6.2Co-3.6Ni

4 Cr depleted substrate 6.8Cr-51.7Co-40.8Ni

Figure 5.77 Continued Cross-sectional images of the model alloys after testing for 100 hours in Gas1

5.2.1.3 Summary

In order to complement the results for the commercial alloys, five model alloys were tested for 25, 50 and 100 hours at 750^{o}C in Gas 1. Inferences can be drawn as follows:

(1) The results from the model alloys verified the findings from the commercial alloys, which is, when the Ni/Co major-element ratio is near unity the alloy has better sulfidation resistance with less weight gain.

(2) The results from the model alloys confirmed the established beneficial effects of Cr and Co on sulfidation resistance. In the range of the current experiments, 10-40wt%Co, weight gain decreases with an increase in the alloy's Co content at a constant Cr level. Similarly, weight gain decreases with the increase in the alloy Cr content at a constant Co level.

(3) The results from the model alloys show that the tendency to form liquid Ni-Ni_3S_2 eutectic increases with an increase in the Ni content in the alloys.

5.2.2 Model alloys with the addition of minor alloying elements

To begin this section it is useful to review the results from the commercial Alloys 160 and 263. Although Alloy 263 contains less amounts of Cr and Co than Alloy 160, yet the former exhibited superior corrosion resistance due, it is believed, to the presence of minor amounts of Al, Ti and Mo. In order to verify the effects of these minor alloying elements, model Alloys 1, 2 and 4 were modified by the addition of 2.5wt.%Al-2.5wt.%Ti-5wt.%Mo to arrive at Alloys 6, 8 and 7, respectively. The Cr content and Ni/Co ratio of the modified alloys were kept the same as the parent alloys. The compositions of the three modified model alloys 6, 7 and 8 are shown in Table 4.4.

5.2.2.1 Weight-gain kinetics

The three modified alloys were tested in Gas 1 for 25, 50 and 100 hours at 750^{o}C. The weight gains of each alloy were compared with the representative parent alloy, as shown in Figure 5.78. It is clear from the figures that each modified alloy had less weight gain and thus better sulfidation resistance than its parent alloy.

To better determine how all the parent alloys and modified alloys behaved, Figure 5.79 shows the weight gains of the six alloys and compares them to the model Alloy 5, which has the best sulfidation resistance among the model Alloys 1-5(reported in section5.2.1).

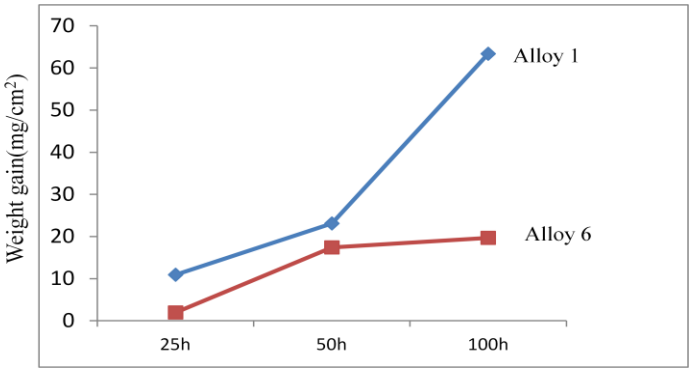

Alloy 1: 58Ni-22Cr-20Co Ni/Co=2.9

Alloy 6: 50.6Ni-22Cr-17.4Co-2.5Al-2.5Ti-5Mo Ni/Co=2.9

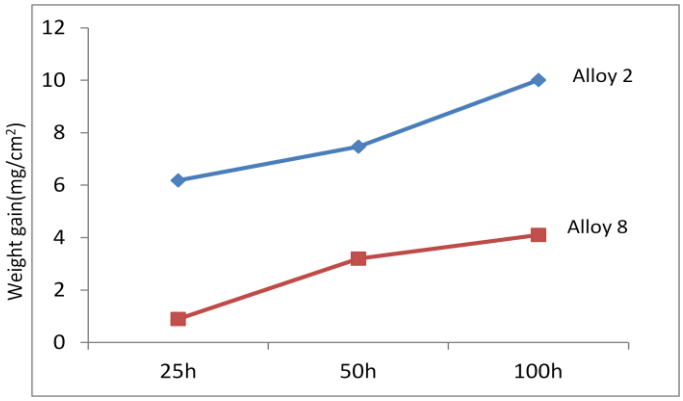

Alloy2: 38Ni-22Cr-40Co Ni/Co=0.95

Alloy8: 33.1Ni-22Cr-34.9Co-2.5Al-2.5Ti-5Mo Ni/Co=0.95

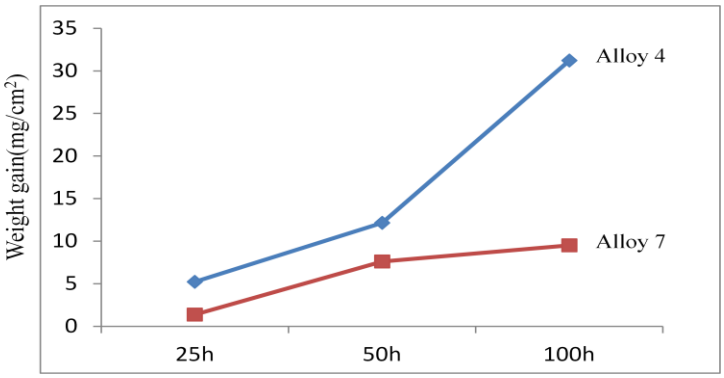

Alloy4: 52Ni-28Cr-20Co Ni/Co=2.6

Alloy7: 44.8Ni-28Cr-17.2Co-2.5Al-2.5Ti-5Mo Ni/Co=2.6

Figure 5.78 Weight gains after testing for various times in Gas 1 at 750^{o}C

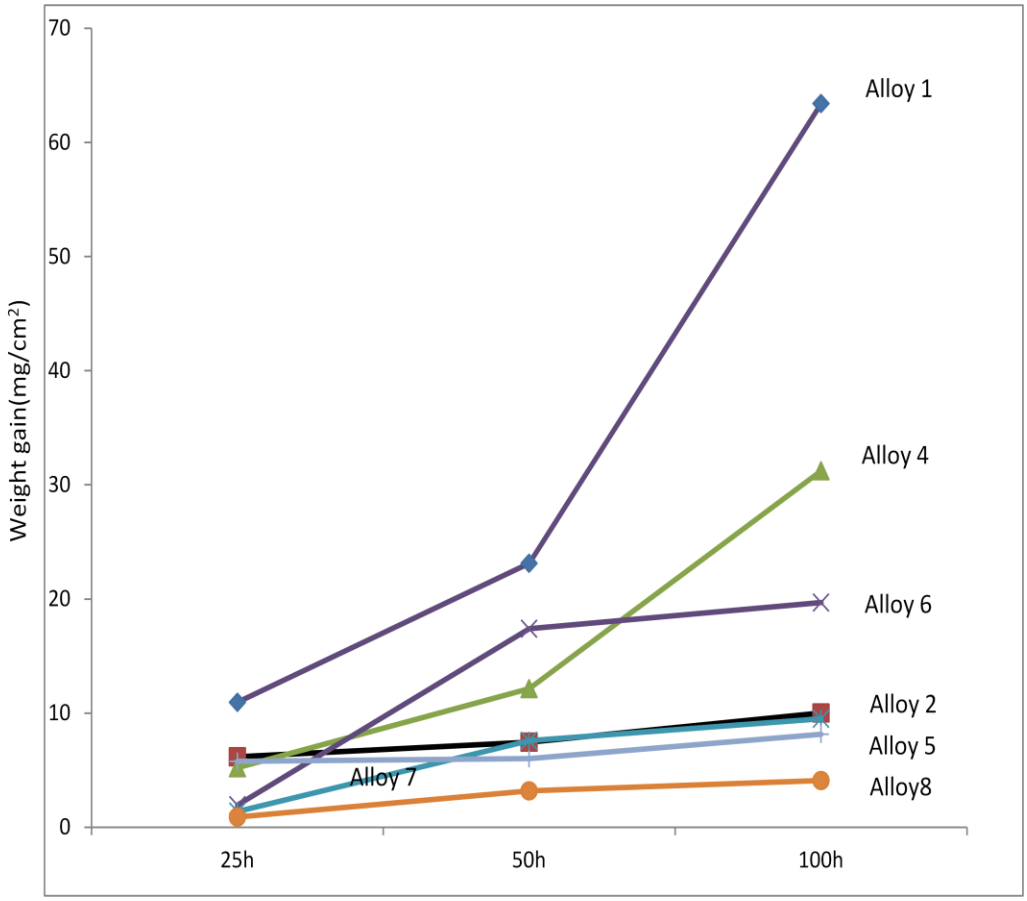

Figure 5.79 Weight gains as a function of time in Gas 1 at 750^{o}C

As shown in Figure 5.79, modified Alloy 8 has less weight gain than the best parent Alloy 5. Alloy 8 has the composition of 33.1Ni-22Cr-34.9Co--2.5Al-2.5Ti-5Mo. This results shows that optimum sulfidation resistance can be achieved by setting the Ni/Co base-metal ratio to near unity and adding relatively small amounts of Al, Ti and Mo. Remarkably, this is true even if the amount of Cr is as low as 22 wt.%.

The beneficial effect of having the Ni/Co base metal ratio near to unity was further demonstrated with model Alloys 6, 7 and 8. Figure 5.80 compares the weight gains of these alloys with the Ni/Co ratio indicated in the figure. It clearly shows that the alloy with Ni/Co ratio near to unity has less weight gain, and hence superior sulfidation resistance.

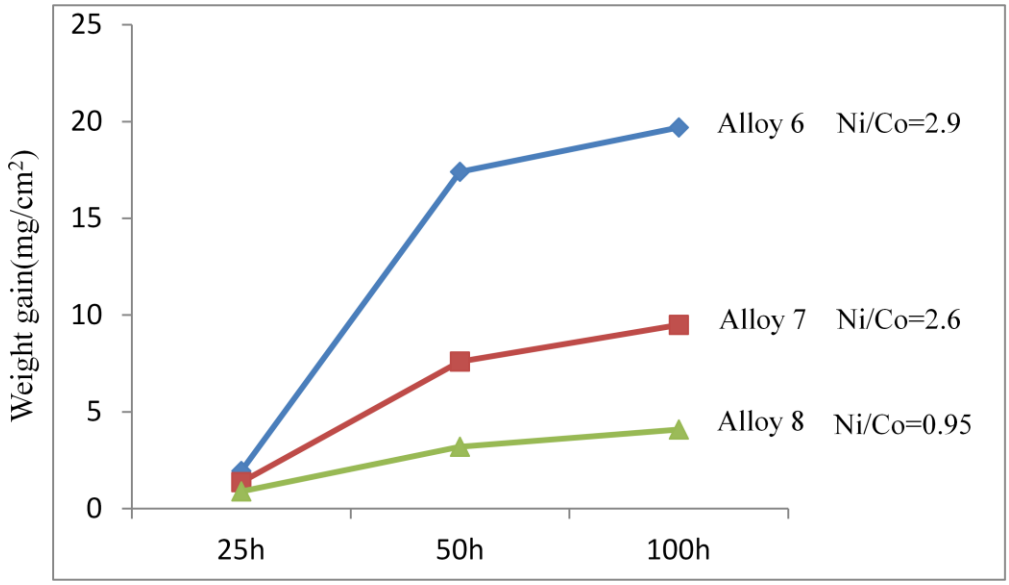

Figure 5.80 Weight gain of Alloys 6, 7 and 8 as a function of time in Gas 1 at 750°C

5.2.2.2 Morphological characteristics

As shown above in Figure 5.78 and Figure 5.79, sulfidation rate was significantly slowed with the addition of minor alloying elements. It is generally believed that there are two possible approaches to the inhibitation of sulfidation[143]. Firstly, according to the priciples set out by Wagner, defect concentration may be decreased with the

incorporation of minor alloying elements into the sulfide scales, which can lead to a decrease in the sulfidation rate since the reaction is controlled by the diffusion process. However, it is hard to realize this due to the lack of knowledge about the valence of dopants. For a P-type sulfide, if dopant cation has higher valency than host, rate constant K_p increases. While K_p decreases if dopant cation has lower valency than host. Another approach to inhibition of sulfidation is the development of a parial or complete diffusion barrier layer which slows down the outward diffusion of some base-meatal elements. Cross-sectional morphologies were analyzed to verify if the second mechnism works for the current study.

Figure 5.81 compares the cross-sectional images of Alloy 2 and Alloy 8 after testing for 25 hours in Gas 1 at 750^{o}C. Both alloys formed a double-layered scale comprised of an external Cr sulfide layer and an inner layer enriched with Cr oxide. It is clear that the Cr sulfide scale formed on Alloy 2 is almost four times thicker than that formed on Alloy 8, and the internal corrosion zone of Alloy 2 is also much thicker than that of Alloy 8. These results may be rationalized by invoking a more effective blocking effect by the inner Cr-oxide enriched scale of Alloy 8. The existence of 2.2at.%Al and 6.8 at.%Ti in the inner Cr_2O_3 enriched scale is believed to be a contributing factor for their enhanced blocking effect on the diffusion of base metal elements.

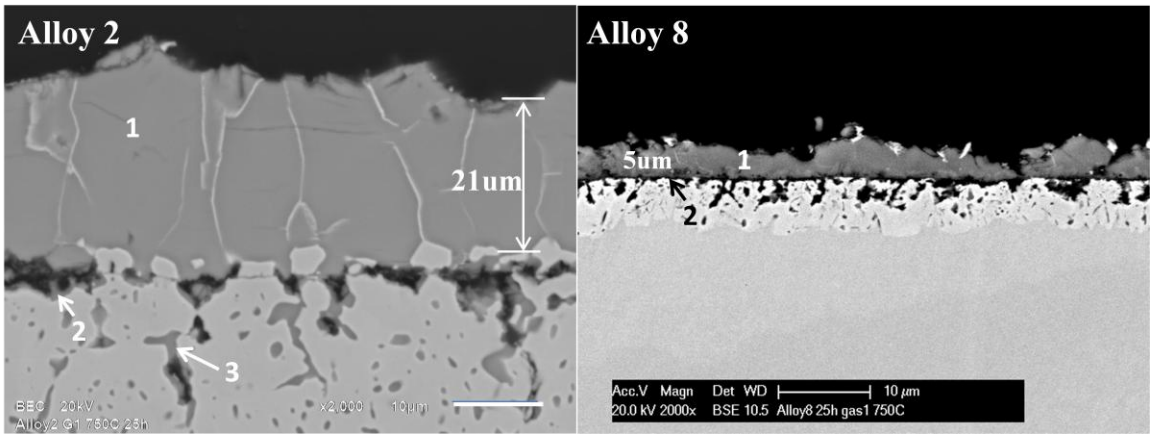

(1) Cr sulfide 59.2S-35.8Cr-4.4Co-0.6Ni (at.%) (2)Oxide enriched layer 17.8O-27.6Cr-16.8Co-15.2Ni-21.9S (3) Internal Cr sulfide 51.4S-34.2Cr-8.0Co-6.4Ni	(1)Cr sulfide 53.1S-43.8Cr-3.1Ni (at.%) (2)Oxide enriched layer 22.8O-27.6Cr-21.9S-2.2Al-6.8Ti-10.7Co-8.7Ni

Figure 5.81 Cross-sectional images of Alloys 2 and Alloy 8 after testing for 25 hours in Gas 1 at 750^{o}C

Figure 5.82 shows a magnified image of the oxide-rich inner scale on modified Alloy 8. The darker minority phase in the oxide layer identified by "1" in the figure is Al_2O_3 enriched, while the lighter oxide product indicated by "2", is Cr rich but also with relatively high levels of Ti and Al. Since both Al and Ti can form oxides which are more stable thermodynamically than Cr_2O_3, the addition of Al and Ti tends to promote greater oxide formation in the inner layer. Indeed, any oxide would serve to inhibit the outward diffusion of base-metal elements, thus reducing the outward sulfidation and internal corrosion. Accordingly, the greater amount of oxide formed in the inner scale region due to the presence of Ti and Al greatly leads to reduced sulfidation kinetics.

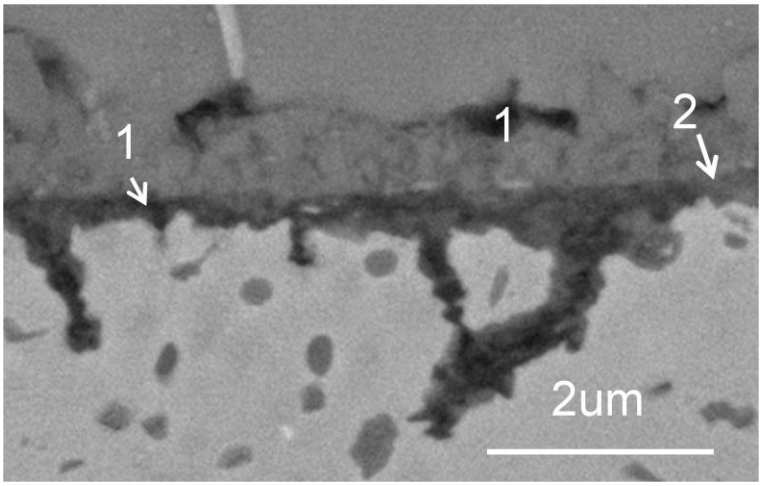

1 Dark phase: Al_2O_3 enriched 53.5O-38.1Al-6.8Cr-1.8Mo
2 Light phase: complex oxide 51.9O-19.8Cr-12.7Ti-9.0Al-6.6S

Figure 5.82 Magnified image of the Cr oxide enriched layer on Alloy 8

The formation of Al oxide at the alloy surface rather than internally can be understood with the help of the 1000°C oxide map shown in Figure 5.83. There are three regions in the figure. Region I corresponds to NiO external scale+Al_2O_3/ Cr_2O_3 internal oxides; region II is Cr_2O_3 external scale+Al_2O_3 internal oxides; region III is external scale of only Al_2O_3. Model Alloy 8, with 2.5wt.%Al and 22wt.%Cr, is indicated by the dot in this figure. It is located at the boundary of internal alumina and external alumina. Thus, the external formation of Al_2O_3 is rationalized. It is noted that the oxide map shown in Figure 5.83 was set up at the oxygen partial pressure of 1atm. The P_{O2} of the current study is 10^{-25}atm. The $\mathbf{N}_{\mathbf{Al}}^{*}$ boundary moves to lower Al level at low oxygen partial pressure, thus the oxygen partial pressure of current study more favors the formation of Al_2O_3.

The individual effect of Al was extensively studied and understood in Fe- and Ni-based alloys [20, 21, 97, 113]. In the sulfidizing-oxidizing atmospheres which are similar to the current study, the formation of Al_2O_3 provides protection, while in purely sulfidizing atmospheres, Al exists as $(Fe,Al)Cr_2S_4$, $(Cr\ Fe)Al_2S_4$ or, in some studies containing Mo, $Al_xMo_2S_4$. They all slow the outward diffusion of the base-metal elements, thus reducing the extent of external sulfide formation [20, 21, 97, 113].

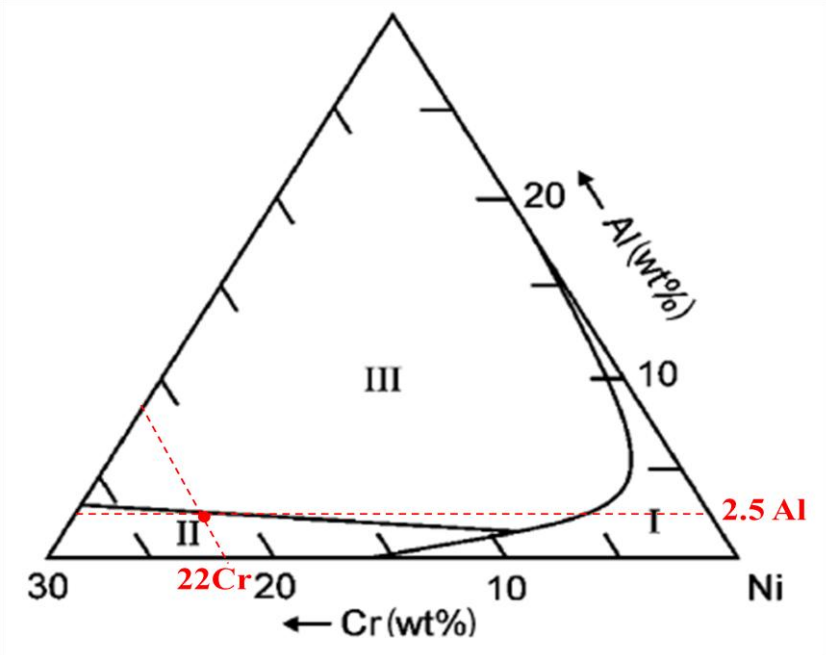

Figure 5.83 Compositional effects on the oxidation of Ni-Cr-Al ternary alloys at 1000°C, P_{O2}=1atm [144]

It is worth noting that no molybdenum was measured in the scales formed on Alloys 6, 7 and 8 even though 5wt.% Mo is present in the alloys. Sulfur K lines and the molybdenum L lines are both located at about 2.3 keV in the EDS spectrum, so it is hard to distinguish between molybdenum and sulfur. Thus, there might exist some amount of Mo sulfide since MoS_2 is stable in the testing gas (the dissociation pressure of MoS_2 is 1.49×10^{-11} atm at 750°C). It is also hard to distinguish the existance of Mo by XRD since the amount of MoS_2 would be small.

The individual effect of Mo on sulfidation resistance has been extensivley studied by others[44] [145]. As discussed in the literature survey of this thesis, Mo is highly resistant to sulfidation because the reaction rate of MoS_2 is comparable to the oxidation rate of Cr[44]. The addition of Mo to common base metals has also been studied, and the results suggested that it confers sulfidation resistance. For example, some reseachers[145] studied the effect of Mo in Ni-20 wt.% Cr and Ni-30wt.% Cr alloy in H_2-H_2S mixture at 700 °C and observed that Mo addition has a beneficial effect on the sulfidation behavior. The authors of that study concluded that the existence of MoS_2 in the internal sulfidation zone lowers the rate at which sulfur diffuses into the alloy. Furthermore, MoS_2 coexisting with Cr sulfide in the scale acts as a barrier to the outward migration of nickel.

Similar to Alloys 8 and 2, the Cr-sulfide scale that formed on Alloy 7 is much thinner than that formed on Alloy 4. Some amounts of Al and Ti were also observed in the inner Cr_2O_3-enriched inner layer of Alloy 7. Cross-sectional images of Alloys 4 and 7 are shown in Figure 5.84.

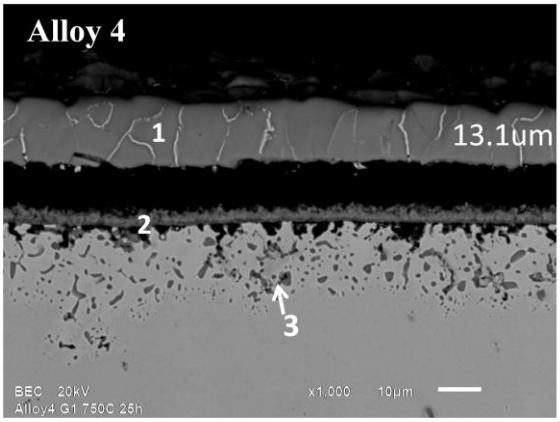

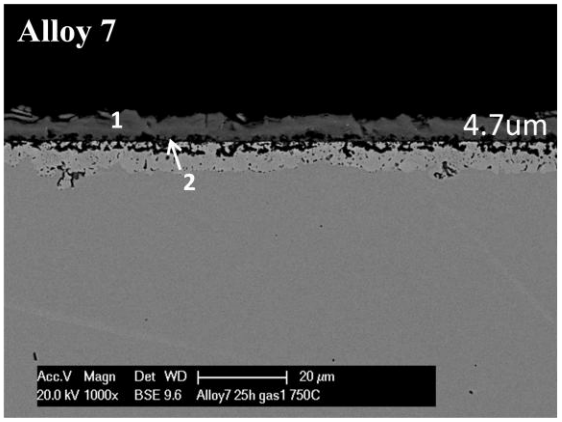

(1)Cr sulfide 58.9S-35.3Cr-2.5Co-3.4Ni (at.%) (2) Cr oxide enriched layer 43.6O-34.7Cr-0.9Co-2.8Ni-17.2S (at.%) (3)Internal Cr sulfide 34.7S-22.1Cr-12.7Co-30.5 (at.%)	(1) Cr sulfide 54.7S-42.3Cr-3.0Ni (at.%) (2) Cr oxide enriched layer 38.9O-34.8Cr-1.9Co-4.0Ni-12.3S-2.1Al-6.0Ti (at.%)

Figure 5.84 Cross-sectional images of Alloys 4 and Alloy 7 after testing for 25 hours in Gas 1 at 750^{o}C

Different from Alloys 7 and 8, it is seen from Figure 5.85 that Ni sulfide formed locally on Alloy 6 after 25 hours in Gas 1. The Ni/Co ratio of Alloy 6 (Ni/Co=2.9) is the highest among the three alloys, so there was a greater propensity for Ni-sulfide formation on Alloy 6. For Alloy 8 with Ni/Co=0.95, Ni sulfide started to form after 50 hours in Gas 1, while Ni sulfide already completely covered the surfaces of Alloys 6 and 7(Ni/Co=2.9 for Alloy 6, Ni/Co=2.6 for Alloy 7) at that time, as shown in Figure 5.86. This observation is quite analogous to the results obtained with the commercial alloys 120, 160, 188 and 282. Alloy 160 with its Ni/Co ratio near to unity formed an outer scale layer that was mainly Cr sulfide after 25 hours in Gas 1; for Alloy 120 and 282 with Ni/Co>1, Ni sulfide coexists with Cr sulfide in the outer sulfide scale, as was shown in Figure 5.14.

The effect of Ni/Co ratio was summarized in Figure 5.22. When the Ni/Co ratio is greater than unity, the availability of Ni is high, and therefore the Ni reaction is dominant. When Ni/Co is near or at unity, Ni and Co availabilities are low, so both Ni and Co reactions are minimal.

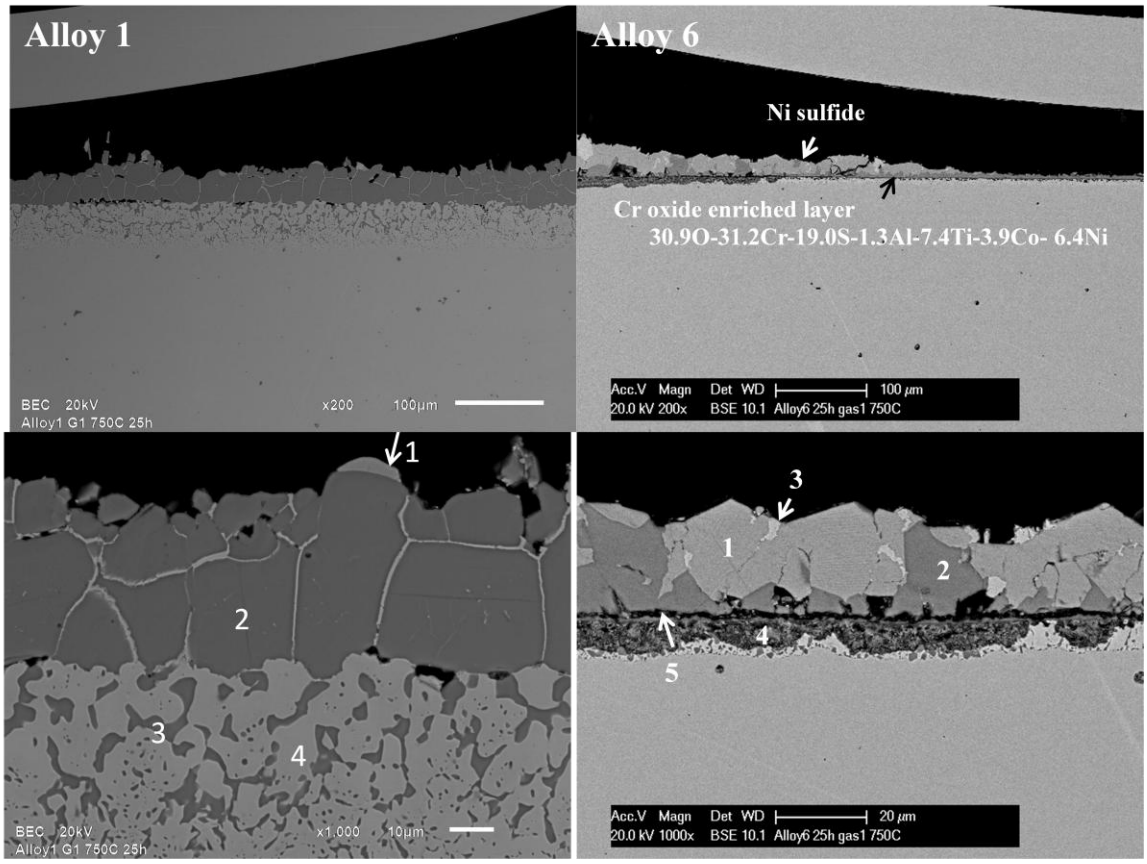

(1) Ni sulfide 43.3S-1.6Cr-6.2Co-48.9Ni (2)Cr sulfide layer 58.0S-32.7Cr-4.0Co-5.4Ni (3)Internal Cr sulfide 50.0S-25.7Cr-6.7Co-17.7Ni (4)Cr depleted substrate 2.2Cr-26.1Co-71.6Ni (at.%)	(1)Ni sulfide 36.8S-13.2Co-50.0Ni (2)Cr sulfide 50.6S-30.6Cr-8.7Co-10.2Ni (3)Metallic Ni and Co 2.9S-20.4Co-76.7Ni (4)Mixture of internal oxide and sulfide 16.6O-41.6S-18.5Cr-3.4Co-4.7Ni-9.4Al-5.7Ti (5)Cr oxide enriched layer 30.9O-31.2Cr-19.0S-1.3Al-7.4Ti-3.9Co-6.4Ni (at.%)

Figure 5.85 Cross-sectional images of Alloy 1 and Alloy 6 after testing for 25 hours in Gas 1 at 750^{o}C

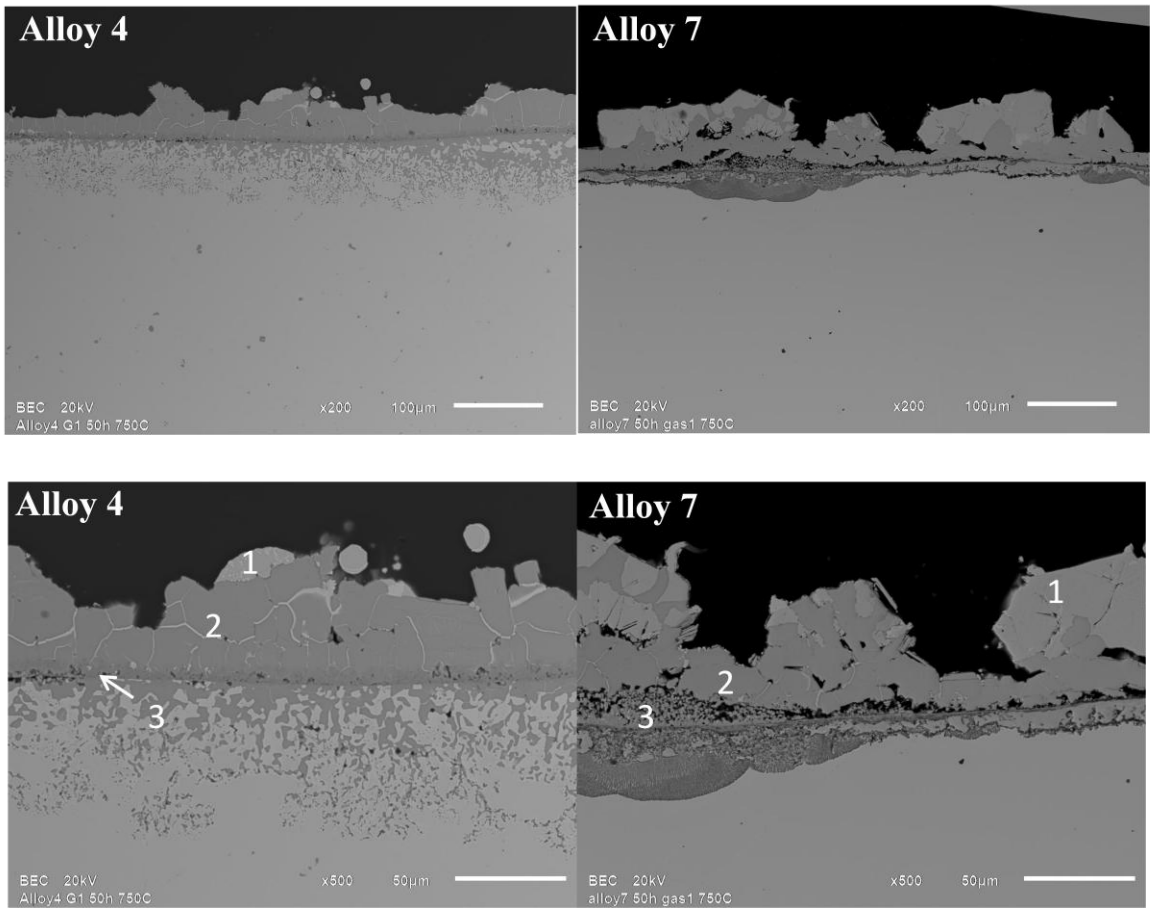

(1)Ni sulfide 44.2S-48.9Ni-1.1Cr-5.9Co (2)Cr sulfide 58.2S-5.4Ni-32.2Cr-4.2Co (3)31.8O-27.3S-3.6Ni-35.3Cr-2.0Co	(1)Ni sulifde 44.3S-0.4Cr-12.7Co-42.5Ni (2)Cr sulfide 55.9S- 276Cr-7.7Co- 8.8Ni (3)35.1O-9.5Al-0.5Si-27.5S-5.8Ti-19.0Cr-1.2Co-1.4Ni

Figure 5.86 The cross sectional images of modified Alloys 6, 7 and 8 and parent Alloys 1,4 and 2 after testing for 50 hours in Gas 1 at 750^{o}C

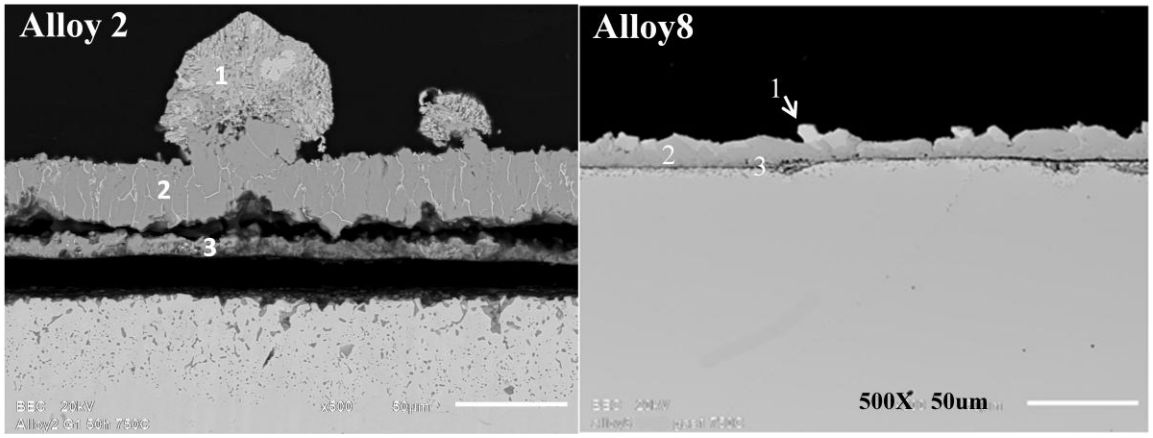

(1)Co and Ni sulfide 45.2S-0.9Cr-14.7Co-38.4Ni (2)Cr sulfide 56.4S-26.2Cr-10.7Co-6.4Ni (3)25.0O-36.9S-29.3Cr-3.3Co-2.6Ni	(1)Co and Ni sulfide 49.2S-1.3Cr-36.1Co-13.4Ni (2) Cr sulfide 54.4S-22.2Cr-16.2Co-7.2Ni (3)23.4O-7.8Al-39.9S-4.8Ti-17.0Cr-4.7Co-2.4Ni

Figure 5.86 Continued The cross sectional images of modified Alloys 6, 7 and 8 and parent Alloys 1,4 and 2 after testing for 50 hours in Gas 1 at 750^{o}C

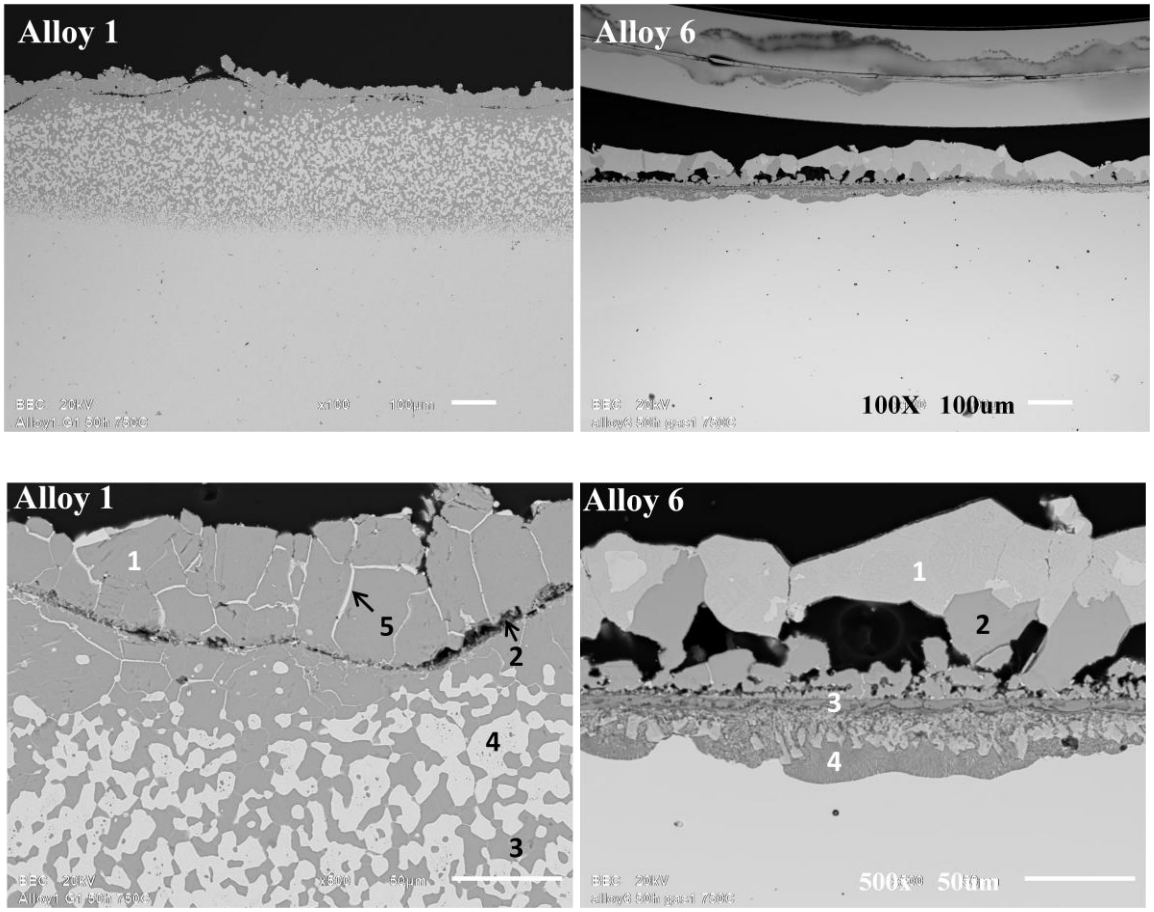

(1)Cr sulfide 57.8S-31.7Cr-4.5Co-6.0Ni (2)36.9O-25.7S-25.5Cr-1.9Co-9.6Ni (3)Internal sulfide 58.5S-31.8Cr-4.2Co-5.5Ni (4)Cr depleted substrate 1.4Cr-25.7Co-73Ni (5)Metallic Ni and Co 6.1S-5.7Cr-14.8Co-73.5Ni	(1)Ni sulfide 64.6S- 0.3Ti-21.1Cr-3.2Co- 4.9Ni-5.9Al (2)Cr sulfide layer 55.9S-27.0Cr-7.7Co-9.4Ni (3)36.6O-6.0Al-23.8S-2.4Ti-26.6Cr-2.3Co-2.4Ni (4)34.8O-9.6Al-32.2S-5.5Ti-15.3Cr-1.3Co-1.3Ni

Figure 5.86 Continued The cross sectional images of modified Alloys 6, 7 and 8 and parent Alloys 1,4 and 2 after testing for 50 hours in Gas 1 at 750^{o}C

Figure 5.87 compares the cross section of Alloys 6, 7 and 8 to their parent Alloys 1, 2 and 4 after 100 hours in Gas 1.

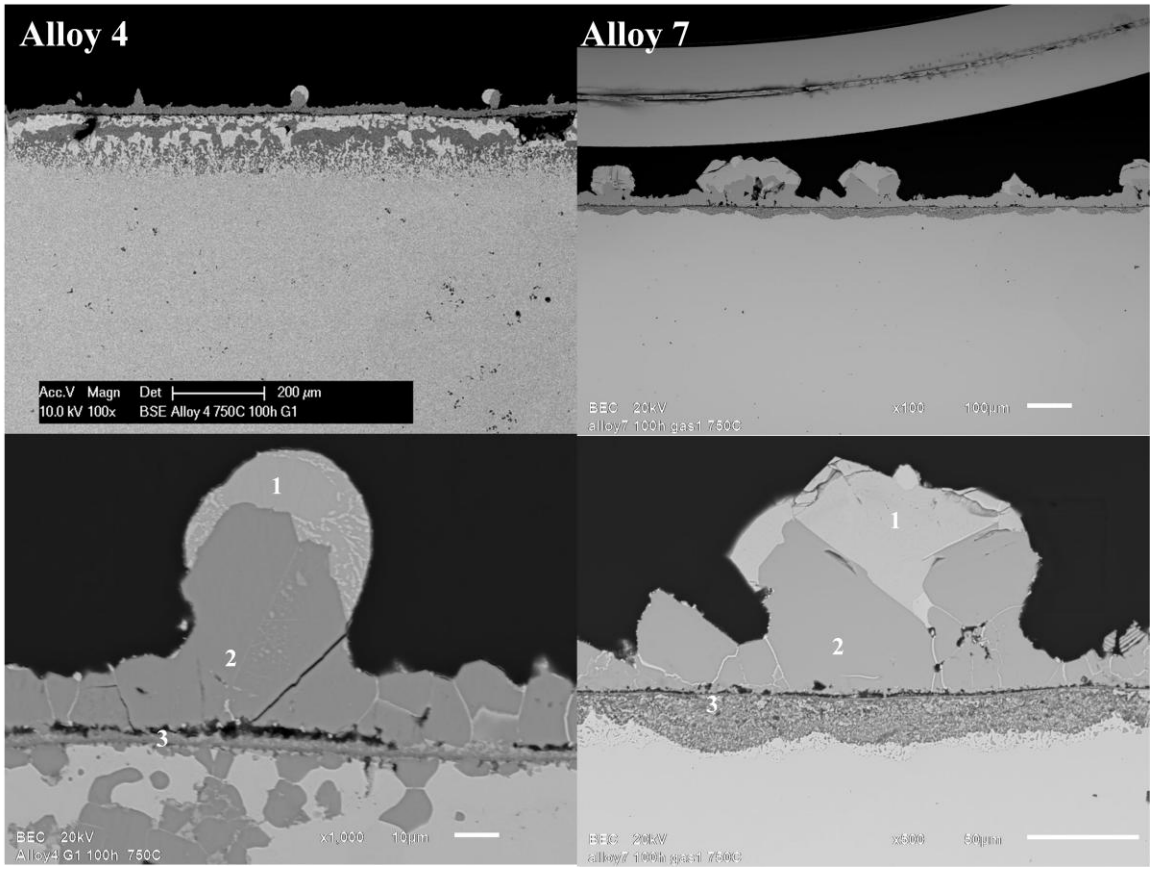

(1)Ni sulfide 42.9S-1.1Cr-4.4Co-51.6Ni (2)Cr sulfide 57.5S-32.3Cr-5.6Co-2.9Ni (3)52.8O-8.0S-27.3Cr-1.0Co-10.9Ni	(1)Ni sulfide 43.9S- 0.5Cr-11.1Cr-44.5Ni (2)Cr sulfide 55.9S- 29.4Cr- 6.7Co- 7.9Ni (3)38.7O-9.9Al-27.4S-5.8Ti-15.1Cr-1.3Co-2.0Ni

Figure 5.87 Cross-sectional images of modified Alloys 6, 7 and 8 and parent Alloys 1,2 and 4 after testing for 100 hours in Gas 1 at 750^{o}C

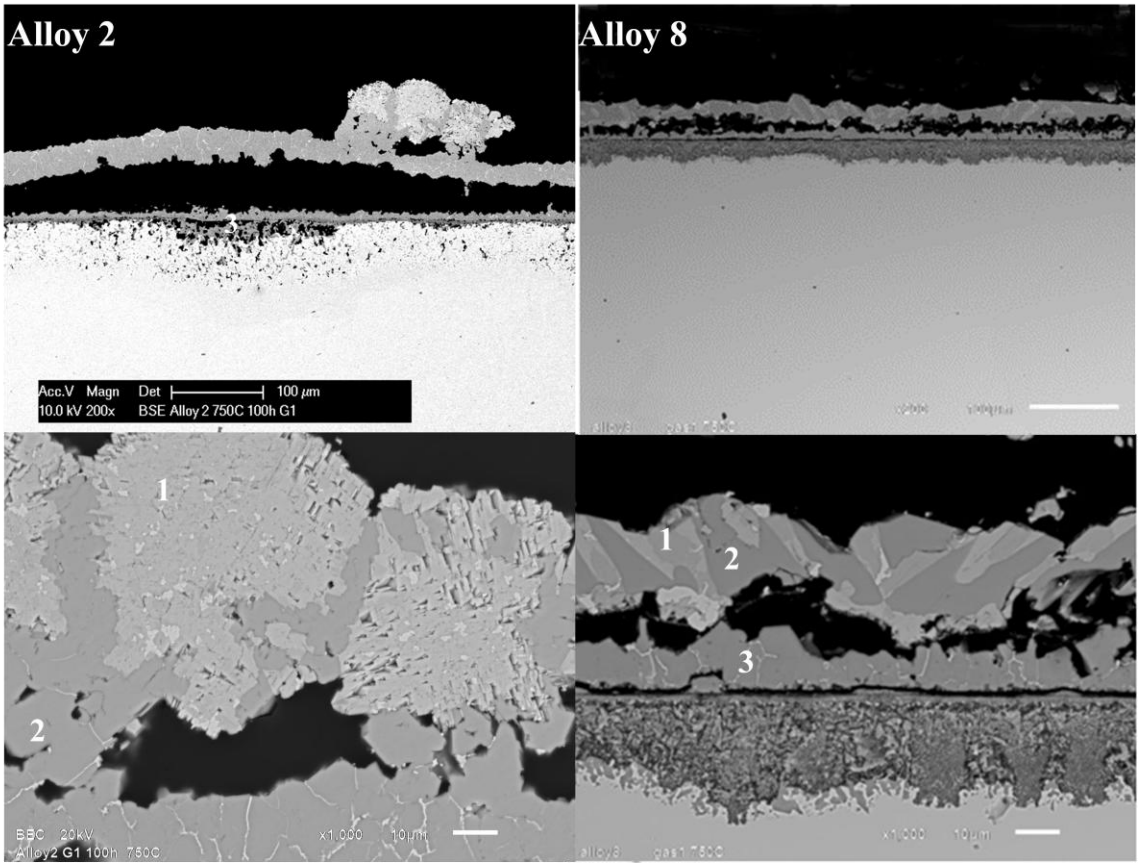

(1)Ni sulfide 41.9S-0.6Cr-16.6Co-40.9Ni (2)Cr sulfide 54.1S-29.5Cr-10.9Co-5.6Ni (3)50.5O-8.6S-39.8Cr-1.0Co	(1)Ni sulfide 50.5S- 0.8Cr- 13.4Co- 34.7Ni (2)Cr sulfide 58.6S- 0.5Ti-23.0Cr-10.9Co-7.1Ni (3)68.4O-8.8Al-7.3S-10.6Ti-0.9Cr-1.4Co-1.4Ni

Figure 5.87 Continued Cross-sectional images of modified alloys 6, 7 and 8 and parent alloys 1,2 and 4 after testing for 100 hours in Gas 1 at 750^{o}C

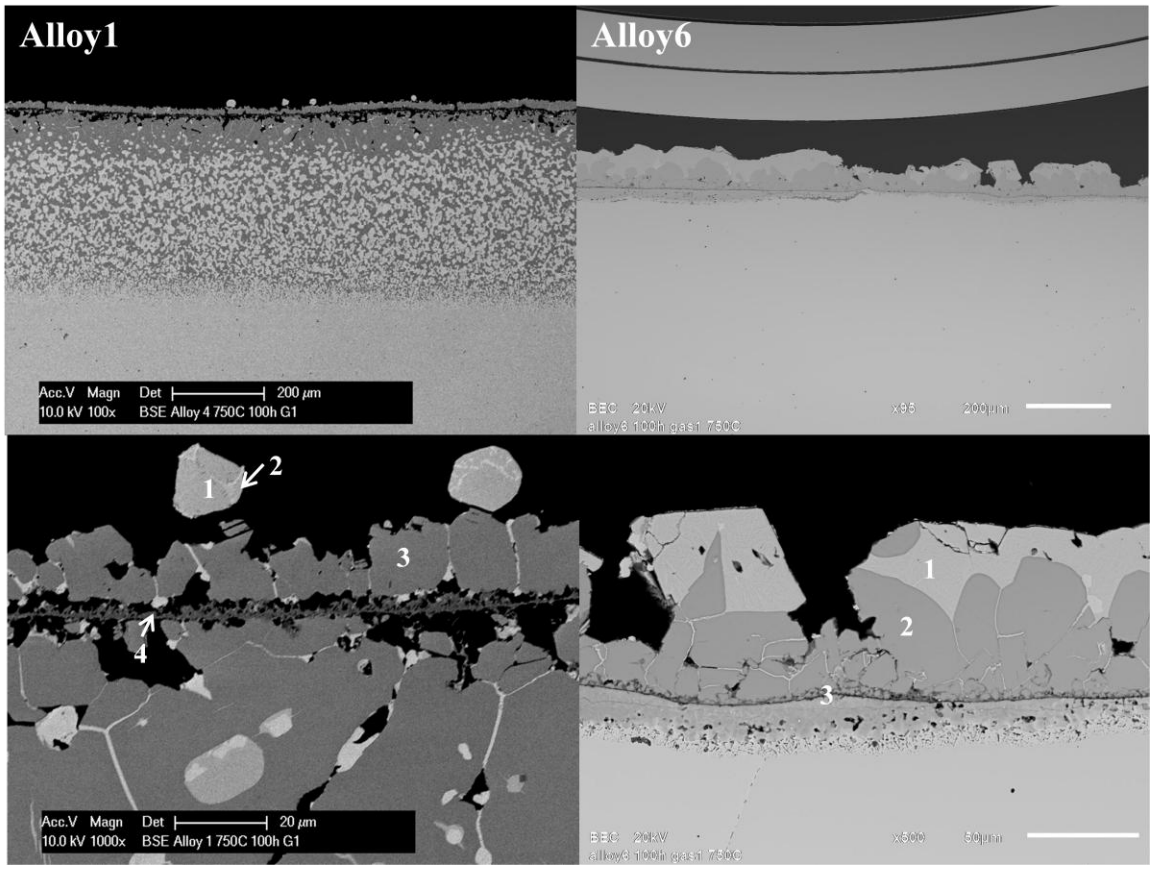

(1)Ni sulfide 42.9S-0.8Cr-7.6Co-48.7Ni (2)Metallic Ni and Co 6.5S-0.9Cr-16.8Co-75.8Ni (3)Cr sulfide 56.8S-31.8Cr-5.0Co-6.4Ni (4)Cr_2O_3 enriched layer 56.5O-35.3Cr-3.4S-0.7Co-4.1Ni	(1)Ni sulfide 46.5S- 0.8Cr- 13.4Co-39.3Ni (2) Cr sulfide 57.5S- 26.8Cr-7.9Co- 7.8Ni (3)64.8O-0.7Al-0.2Si-5.7S-23.7Ti-2.9Cr-0.8Co-1.2Ni

Figure 5.87 Continued Cross-sectional images of modified alloys 6, 7 and 8 and parent alloys 1,2 and 4 after testing for 100 hours in Gas 1 at 750^{o}C

5.2.2.3 Summary

In order to verify the effects of minor alloying elements such as Al, Ti and Mo, Alloys 1,2 and 4 were modified by adding these minor alloying elements to result in alloys 6, 7 and 8. The three modified model alloys were tested for 25, 50 and 100 hours in Gas 1 at 750^{o}C. The inferences that can be drawn are as follows:

(1) The modified alloys 6, 7 and 8 underwent less weight gain and hence offered better corrosion resistance than their parent alloys without minor alloying addition. This verified that with the judicious addition of Al, Ti and Mo, lower (Cr+Co) containing alloys can be highly sulfidation resistant.

(2) The modified alloys further verified the previous findings that when Ni/Co base-metal ratio is near unity, the alloy has better sulfidation resistance.

(3) Remarkable sufidation resistance can be obtained by maintaining a Ni/Co base-metal mass ratio near unity and adding minor amounts of Al, Ti and Mo. The best sulfidation-resistant model Alloy 8 has the composition Ni-22Cr-35Co--2.5Al-2.5Ti-5Mo (in wt.%).

(4) The addition of Al and Ti promotes the formation of an oxide-enriched inner layer which serves to inhibit the outward diffusion of base metal elements, thus mitigating the outward sulfidation and internal corrosion.

5.2.3 Model alloys with different Ti levels

As discussed in 5.2.2, the individual addition of Al and Mo is beneficial for improving sulfidation resistance. However, it is not clear about the individual effect of Ti. As reviewed in chapter 2.4, results on the effect of Ti are variable. To date, little work has been done on the effect of Ti in Ni-based alloys on sulfidation resistance. In order to clarify the individual effect of Ti, some model alloys with different Ti levels were prepared for further study.

The compositions of the new model alloys were designed based on results obtained from the commercial alloys. As was shown in Figure 5.3, the weight gains of Alloys 617, 282 and 41 were within about 4mg/cm^2 of each other after 100h exposure to Gas 1. The three alloys have similar composition, with the most significant difference being the Ti content. Alloy 41 contains the highest Ti content (3.1wt.%) and showed the least weight gain. Alloy 617 with 0.3 wt.%Ti had the most weight gain among the three alloys. Alloy 282 with 2.2 wt.%Ti had a weight gain value in the middle.

To clarify whether the differences in weight gains were caused by the difference in Ti contents, compositions of the model alloys were designed based on the compositions of these three commercial alloys. Accordingly, the new model alloys had the composition of Ni-20Cr-13Co-3Fe-0.5Si-5Mo-1.5Al-x**Ti** with three different Ti levels of 0.5Ti, 1.5Ti and 3Ti (the composition is in wt.%).

These new model alloys with different Ti levels were tested for 25, 50 and 100 hours in Gas 1 at 750^{o}C. They were also tested in Gases 2 and Gas 3 for 100 hours at 750^{o}C.

5.2.3.1 Weight-gain kinetics

The weight gains of the three alloys after testing for 25, 50 and 100 hours in Gas 1 are presented in Figure 5.88. It seems that the three Ti contents of the alloys did not bring about significantly different behavior. However, the three alloys behaved differently in Gas 2 obtained by bubbling Gas 1 through water at 0^{o}C and Gas 3 obtained by bubbling Gas 1 through water at 25^{o}C. Figure 5.89 summarizes the weight gains of the alloys after 100 hours in Gases 2 and 3. Alloy 3Ti exhibited the least weight gain, and Alloy 0.5Ti the most. Ti addition ostensibly exerted a beneficial effect on the sulfidation behavior in Gases 2 and 3.

The different behaviors in Gases 1, 2 and 3 show that there is a complex interplay between alloy compositions, specifically the relative amount of Ti, and environment. In Gas 1, which is the most sulfidizing, any effect of Ti is not apparent. However, in Gases 2 and 3 where the oxygen partial pressure is higher than that in Gas 1, Ti does appear to have an effect to improve the corrosion resistance.

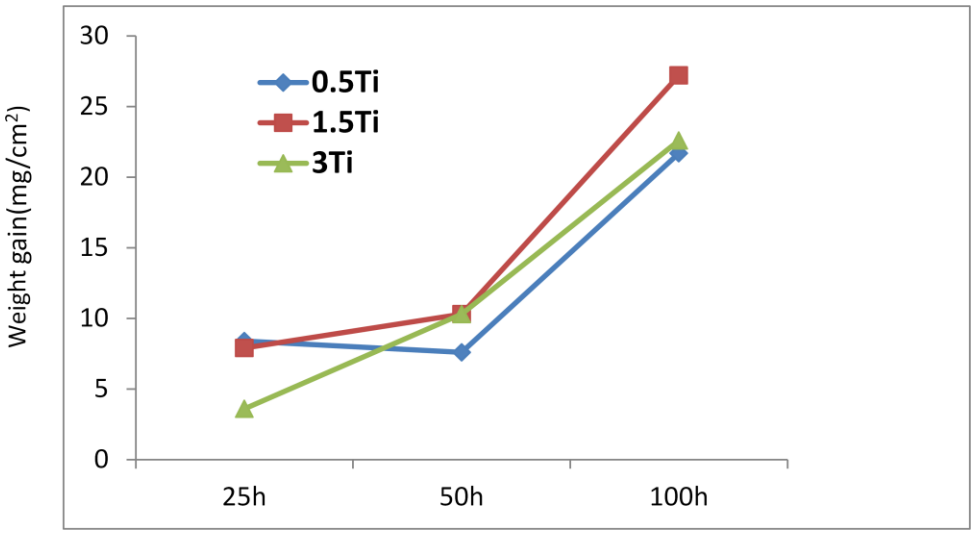

Figure 5.88 Weight gain as a function of testing time in Gas 1 at 750°C

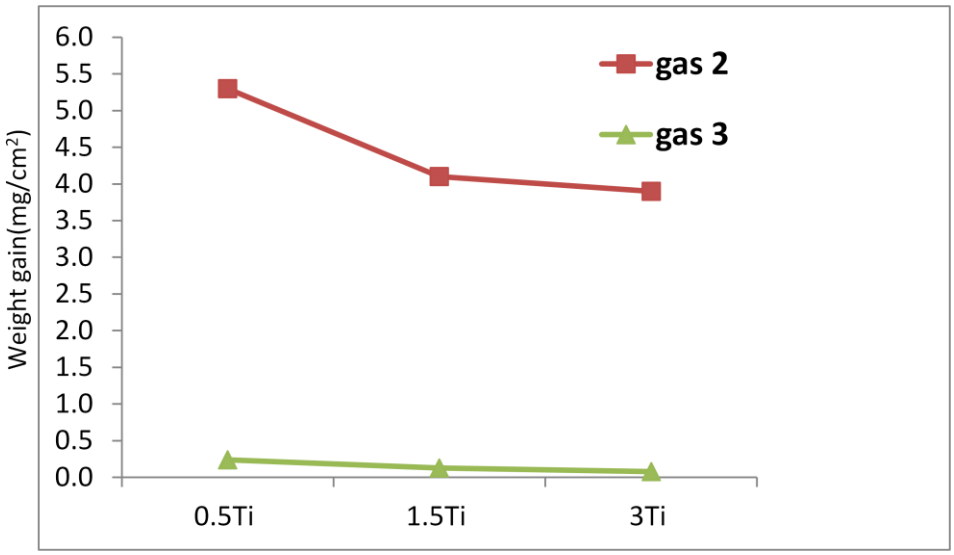

Figure 5.89 The weight gain of the three alloys after testing for 100 hours in Gas 2 and 3 at 750°C

5.2.3.2 Morphological characteristics

Figure 5.90 shows surface images of the model alloys with different Ti contents after testing in Gas 1 for 25 hours at 750^{o}C. The surface images are seen to look similar. According to XRD, Ni_3S_2 and Co_9S_8 formed on the surface.

Figure 5.91 shows cross-sectional images of the three alloys after 25 hours in Gas 1. The alloys have a multi-layered microstructure with the outermost layer being mainly Ni sulfide, the intermediate layer is Cr sulfide, and the inner layer is a mixture of Cr oxide and Cr sulfide. The compositions of each layer are shown in the table directly below the images. After testing for 50 hours, the cross-sectional images look similar to those after 25 hours except that the outer Ni sulfide layer became thicker, as seen in Figure 5.92. The three model alloys also had similar cross-sectional images after 100 hours in Gas 1, as seen in Figure 5.93.

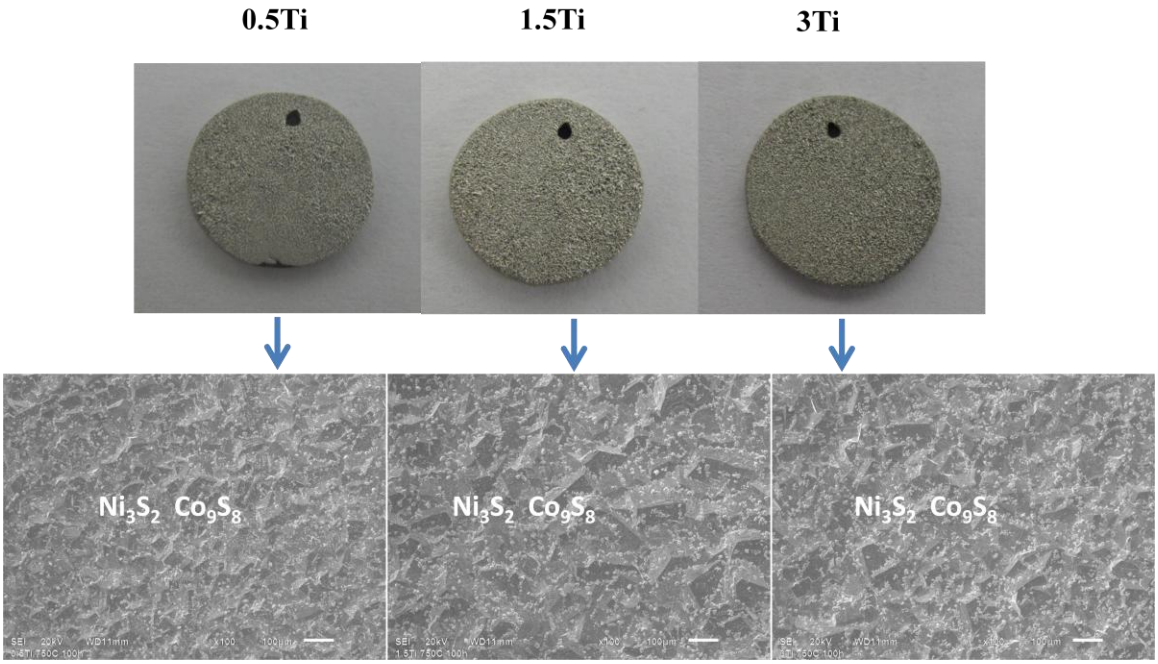

Figure 5.90 Surface images of model alloys with different Ti contents after 25 hours in Gas 1 after 25 hours

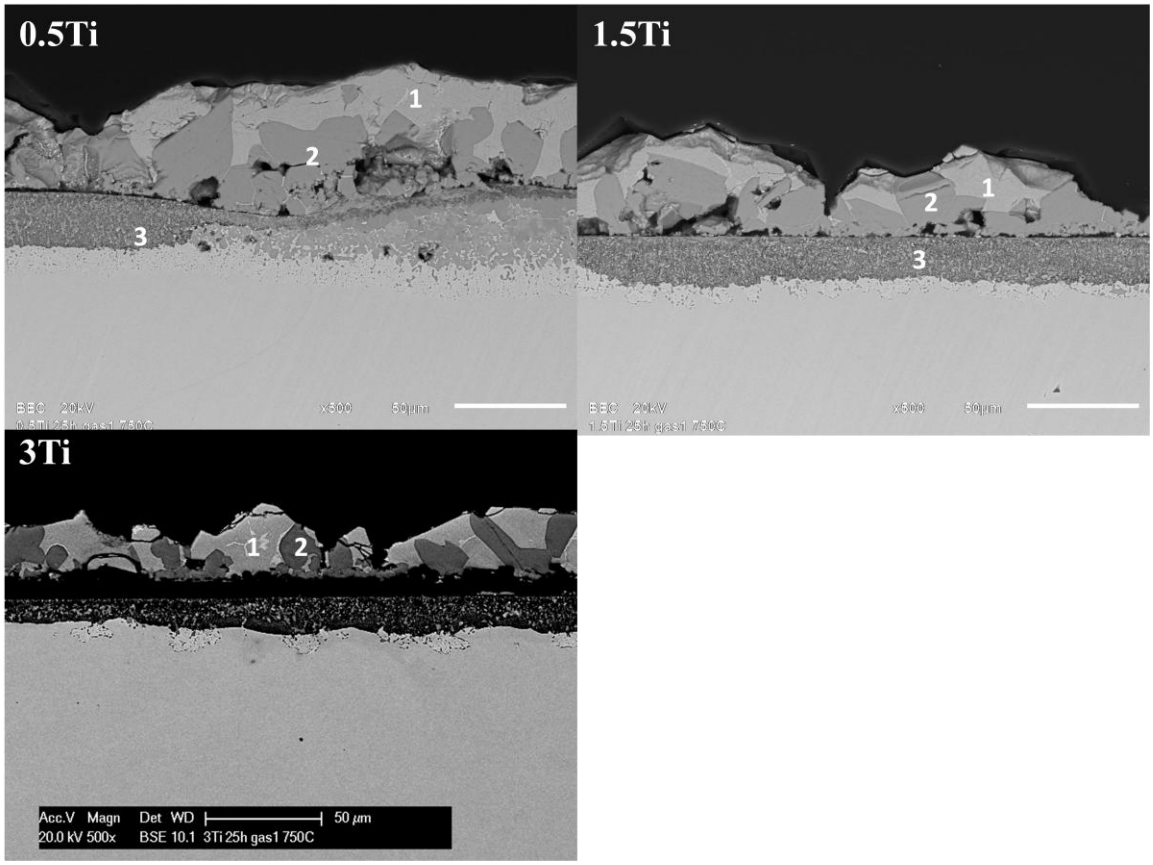

0.5T1	1.5Ti	3Ti
(1)Ni sulfide and Co sulfide 45.3S-42.6Ni 1.8Fe-10.3Co (2)Cr sulfide 56.4S-28.8Cr-1.7Fe-5.0Co-8.0Ni (3)25.7O-6.8Al-2.6Si-41.7S-1.6Ti-15.5Cr-1.9Co-4.2Ni	(1) Ni sulfide and Co sulfide 42.1S-48.1Ni 2.0Fe-7.8Co (2) Cr sulfide 57.1S-28.5Cr-1.40Fe-5.3Co-7.8Ni (3)28.8O-5.7Al-1.9Si-39.27S-3.1Ti-16.1Cr-1.7Co -3.5Ni	(1)Ni sulfide and Co sulfide 34.2S-45.9Ni-9.0Cr-1.5Fe-9.3Co (2) Cr sulfide 54S-30.9Cr-6.2Co-8.9Ni (3)16.4O-23.1Cr-5.4Al-43.0S-7.0Ti-5.2Ni

Figure 5.91 Cross-sectional images of alloys with different Ti contents after 25 hours in Gas 1

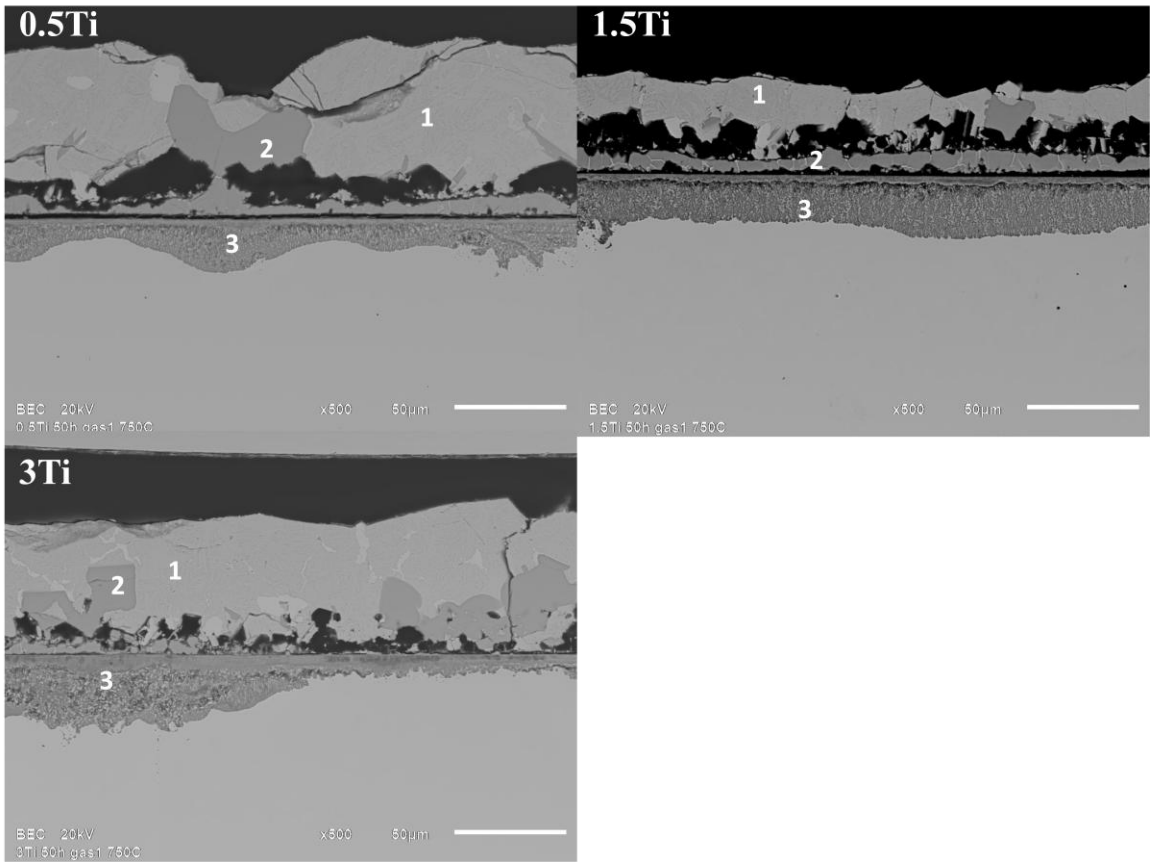

0.5Ti	1.5Ti	3Ti
(1) Ni sulfide 43.1S-0.5Cr-1.8Fe-8.50Co-46.0Ni (2) Cr sulfide 55.7S-27.6Cr-1.5Fe-5.7Co-19.5Ni (3) 33.9O-5.2Al-2.6Si- 34.9S-1.0Ti- 16.3Cr-0.5Fe- 2.0Co-3.8Ni	(1) Ni sulfide 43.3S-0.64Cr-1.9Fe-9.4Co-44.9Ni (2) Cr sulfide 57.34S-30.9Cr-1.3Fe-4.5Co-5.9Ni (3) 47.1O-4.8Al-1.7Si-21.7S-2.0Ti-19.7Cr-0.4Fe-0.9Co-1.7Ni	(1) Ni sulfide 44.2S-0.5Cr-2.0Fe-10.8Co-43.2Ni (2) Cr sulfide 56.0S-27.4Cr-1.6Fe-5.9Co-9.1Ni (3) 41.6O-4.0Al-1.5Si-21.7S-4.3Ti-23.7Cr-0.3Fe-0.9Co-2.0Ni

Figure 5.92 Cross-sectional images of alloys with different Ti contents after 50 hours in Gas 1

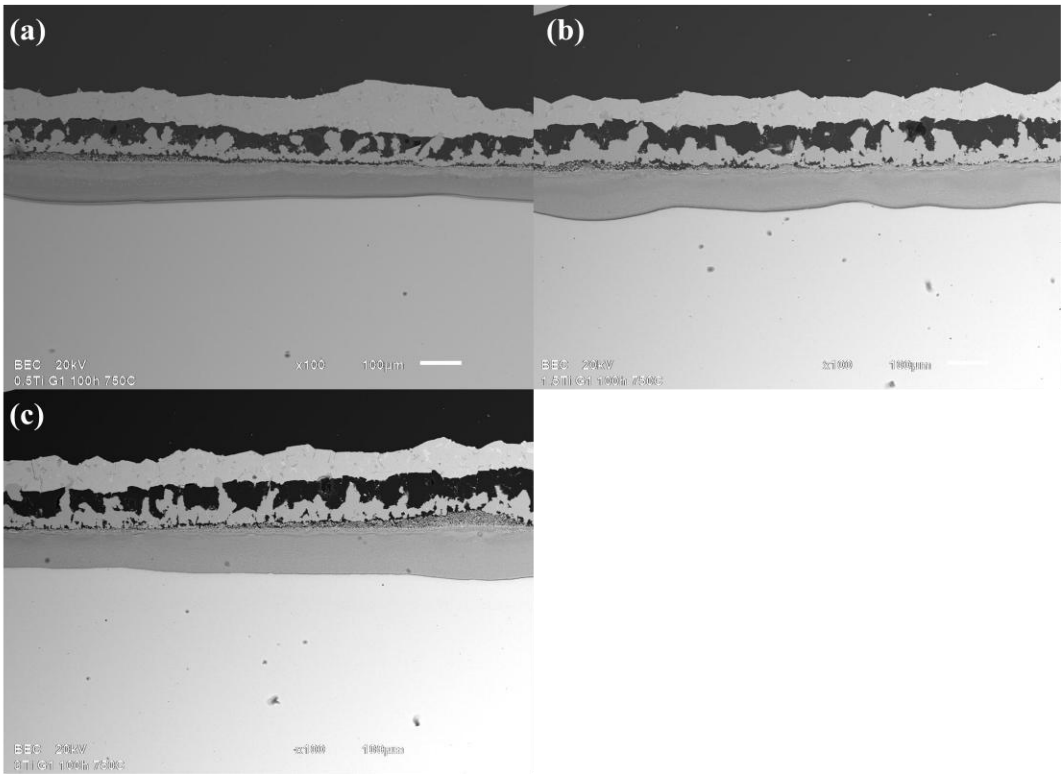

Figure 5.93 Cross-sectional images of alloys with different Ti contents after 100 hours in Gas 1 at 750^{o}C, (a)0.5Ti, (b) 1.5Ti (c) 3Ti

The three model alloys behaved similarly in Gas 1 after 25, 50 and 100 hours of exposure. However, they exhibited different behaviors in Gases 2 and 3. Figure 5.94 shows the surface images of the three alloys after 100 hours in Gas 2. Most of the surface of the alloy with 0.5Ti is covered with Ni sulfide; while for the alloy with 1.5Ti, Ni sulfide is only observed in some localized areas; Cr oxide covers the surface of the alloy with 3Ti. The different morphologies of the three alloys can be more clearly seen in the cross-sectional images in Figure 5.95. For the alloy with 0.5Ti, it is inferred that the initially-formed Cr-oxide scale broke down and Ni sulfide formation ensued. For the

alloy with 1.5Ti, Ni sulfide formed locally on the Cr-oxide layer. While on the alloy with 3Ti, a continuous Cr-oxide layer formed, containing 13.2 at.% Ti. This amount of titanium will beyond the reported solubility in Cr_2O_3 [146, 147]. A possible explanation for the high concentration of Ti in Cr_2O_3 is the formation of a complex chromium-titanium oxide $Cr_2Ti_2O_7$, which was verified by XRD analysis shown in Figure 5.96. The formation of $Cr_2Ti_2O_7$ is believed to act as a barrier to the outward diffusion of base metal elements. Wang et al.[148] also observed the existence of $Cr_2Ti_2O_7$ in the Cr_2O_3 scale formed on Alloy Fe-25wt.%Cr-4.3wt.%Ti after testing in H_2-H_2O-H_2S mixtures at 750°C. They proposed that $Cr_2Ti_2O_7$, together with Cr_2O_3, acts as a barrier to suppress sulfide formation.

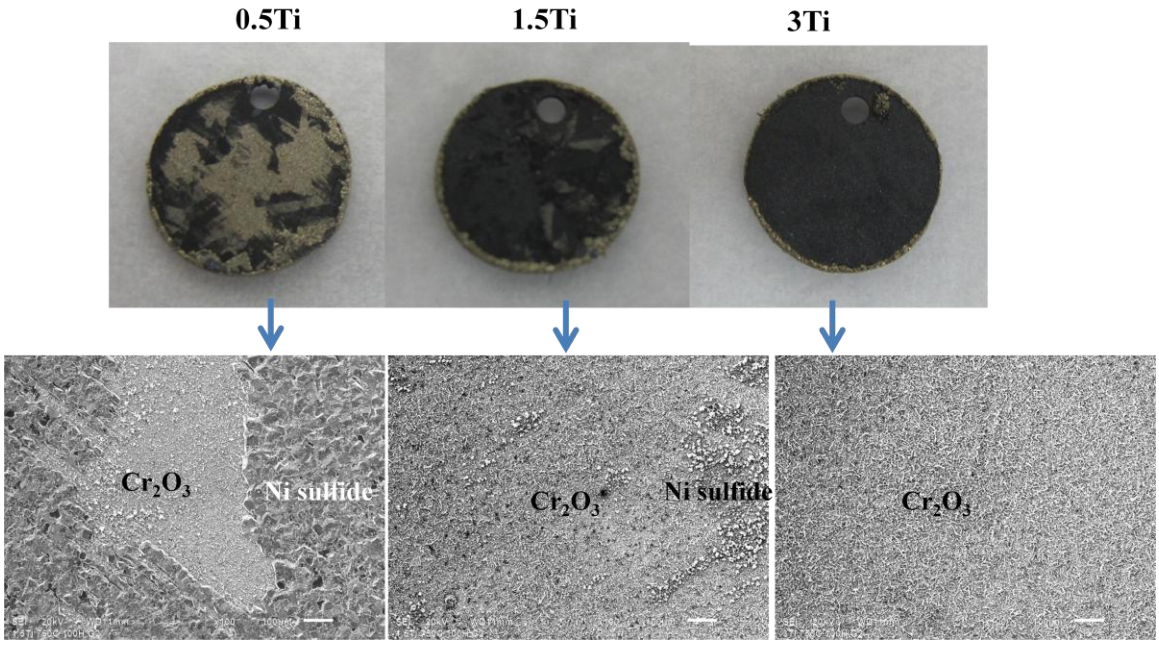

Figure 5.94 Surface images of model alloys after 100 hours in Gas 2

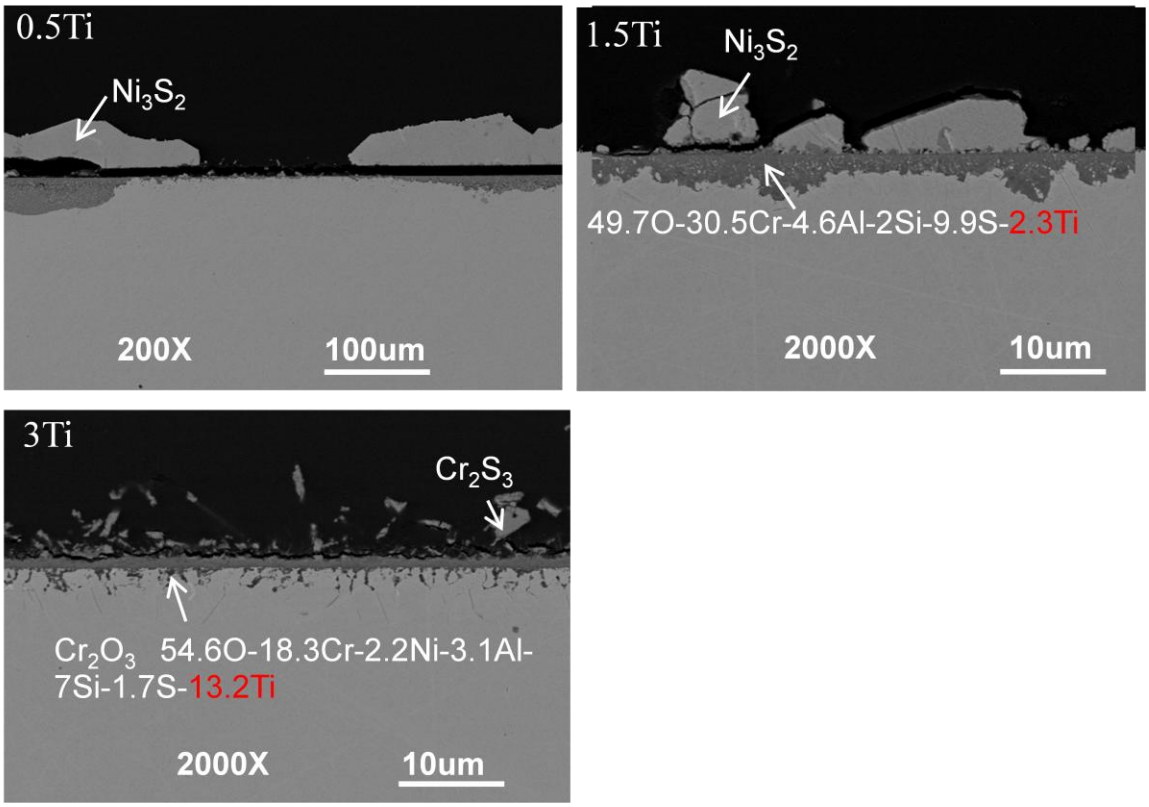

Figure 5.95 Cross sectional images of model alloys after 100 hours in Gas 2

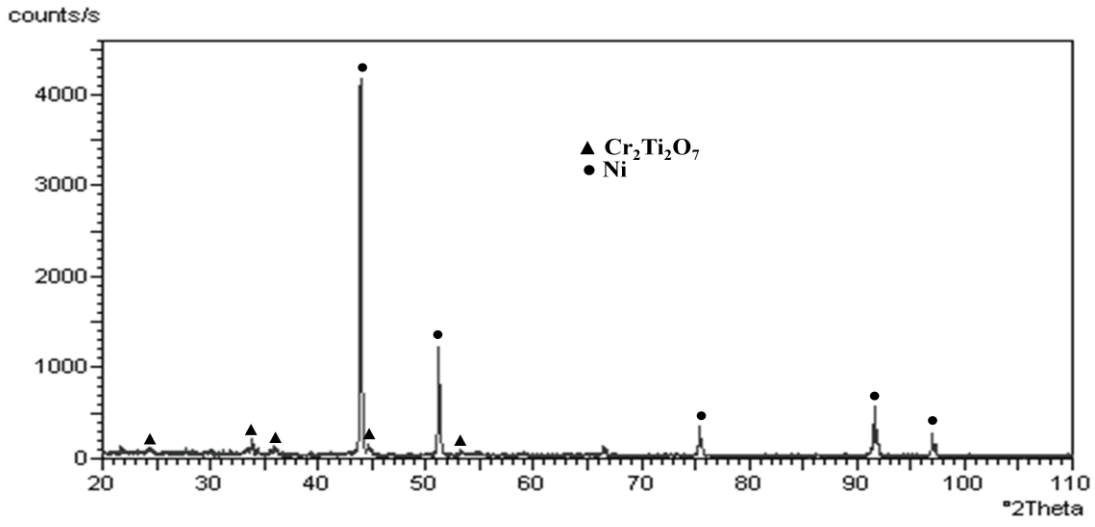

Figure 5.96 XRD pattern of Cr oxide enriched scale

Obviously, the presence of Ti in the Cr_2O_3 scale had the beneficial effect to promote and maintain the formation of oxide scale. The presence of Ti also helped to block the outward diffusion of base metal elements such as Ni. This blocking effect was more obvious with greater amounts of Ti in the alloy. The reason why Ti can promote the formation of oxide scale will be discussed later.

Figure 5.97 shows cross-sectional images of the model alloys after 100 hours in Gas 3. The Cr_2O_3 scale formed on the Alloy 3Ti is thick and continuous compared to that formed on the alloy with 0.5Ti and 1.5T. 11.5at.% Ti was measured in the Cr_2O_3 scale formed on the alloy with 3Ti, which shows the effect of Ti in promoting the formation of an oxide-enriched scale.

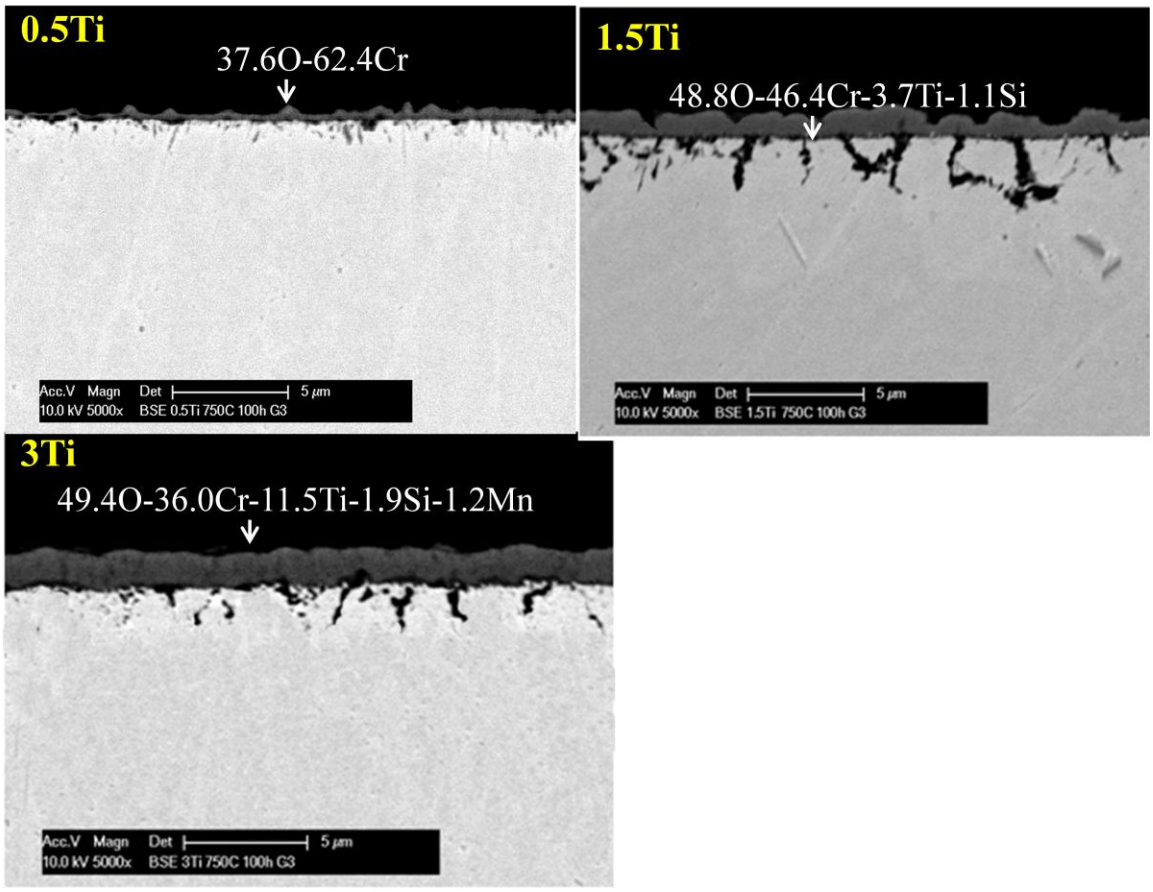

Figure 5.97 Cross-sectional images of model alloys after 100 hours in Gas 3

The scales formed on the three model alloys after testing in the three gases differed depending on the gas atmosphere. Figure 5.98 summarizes the primary type of scale formed on each alloy after 100 hours in the three gases at 750^{o}C. The dot and triangle represent oxide and sulfide, respectively. The dashed line represents an estimated threshold oxygen partial pressure above which protective Cr oxides scale forms. As shown in this figure, Ti content affects this threshold oxygen partial pressure. With an increase in Ti content, the threshold oxygen partial pressure decreases.

The information of the primary scale type can also be used to determine the kinetic boundary in the stability diagram. The stability diagram of the model alloys is shown in Figure 5.99. The diagram was set up on the assumption of ideal alloy behavior. Gases 1, 2 and 3 are indicated in this figure. Since there is not big difference in the alloy Ti content, the same diagram can be used for all three model alloys. Sulfide formed on the alloy with 3Ti after 100 hours in Gas 1, while oxide formed in Gases 2 and 3, so the kinetic boundary of the alloy with 3Ti is located somewhere between Gases 1 and 2. While for the alloy with 0.5Ti and 1.5Ti, sulfide formed in Gases 1 and 2, oxide formed in Gas 3. Thus the kinetic boundary for these alloys is located between Gases 2 and 3, as shown in Figure 5.99.

The beneficial effect of Ti on the location of the kinetic boundary was also reported in a study by Wang et al.[148]. They found that the addition of Ti to an Fe-Cr alloy shifted the kinetic boundary between Cr sulfide and Cr oxide to a lower oxygen partial pressure after testing in H_2-H_2O-H_2S mixture at 750^oC, as shown in Figure 5.100.

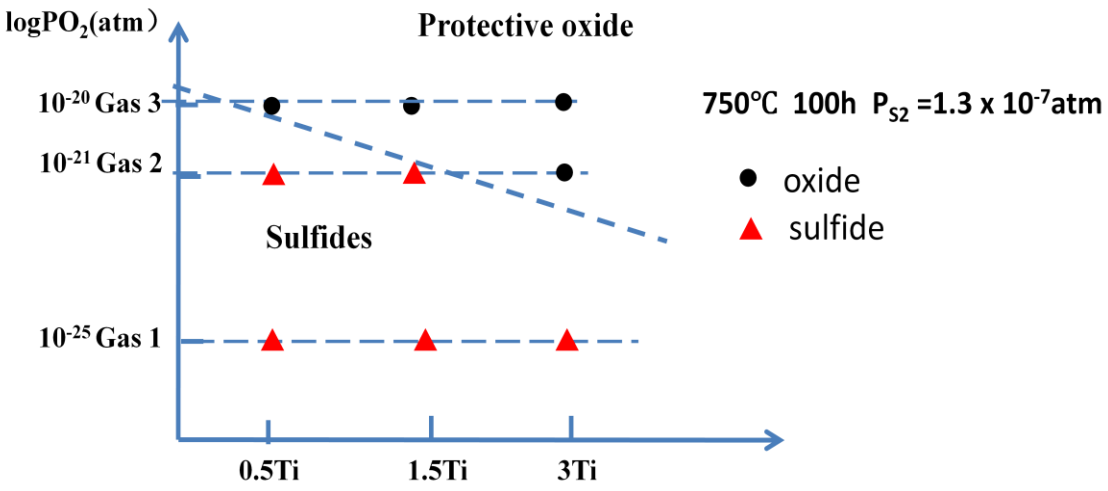

Figure 5.98 Influence of Ti content on the threshold oxygen partial pressure to form protective Cr_2O_3 scale

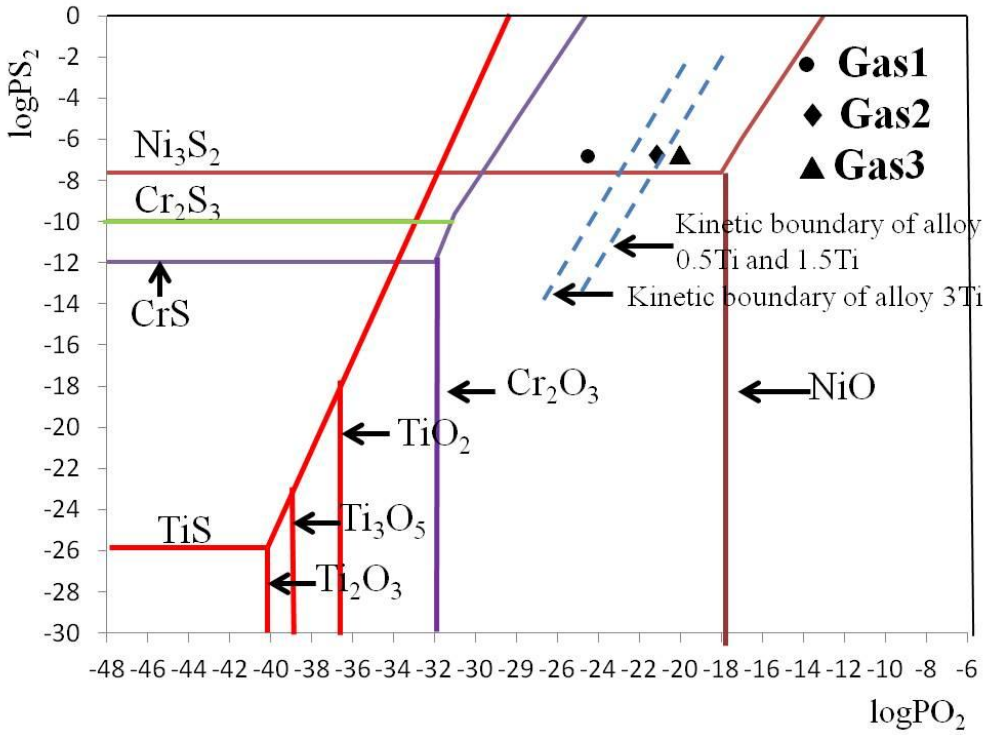

Figure 5.99 Phase stability diagram at 750°C for the alloys with 0.5Ti, 1.5Ti and 3Ti

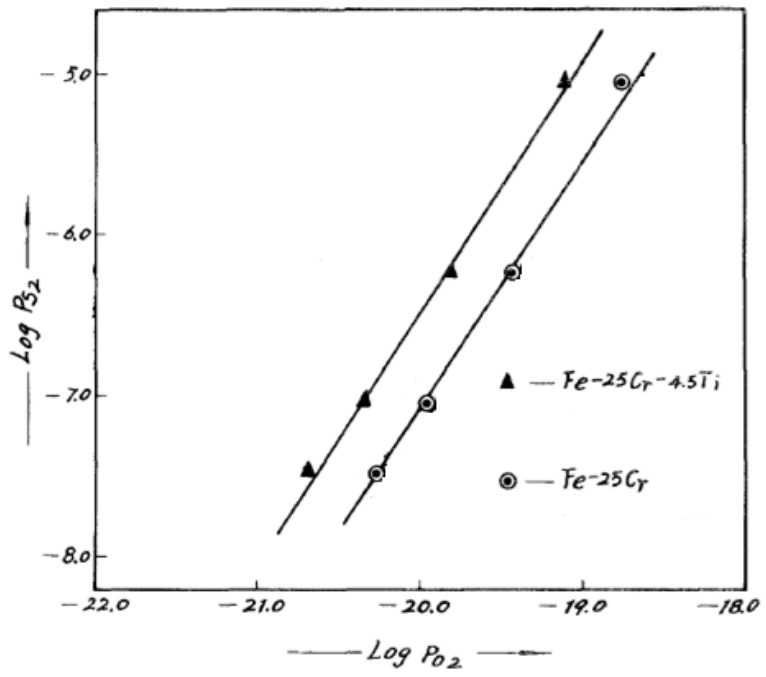

Figure 5.100 The kinetics boundary of Fe-25wt.%Cr and Fe-25wt.%Cr-4.3wt.%Ti at 750^{o}C, as reported by Wang et al.[148]

In order to investigate why Ti has the effect to shift the kinetic boundary and promote Cr_2O_3 scale formation, the alloys with 0.5 and 3Ti were tested in Gas 2 for 30 minutes. As shown in Figure 5.101, Ni sulfide covered the surface of the alloy with 0.5Ti, while Ni sulfide started to nucleate on the alloy with 3Ti after testing for 30 minutes in Gas 2. The X-ray diffraction measurements revealed the formation of complex oxides such as $Cr_{0.222}Ti_{0.778}O_{1.889}$ on the alloy with 3Ti, as shown in Figure 5.102.

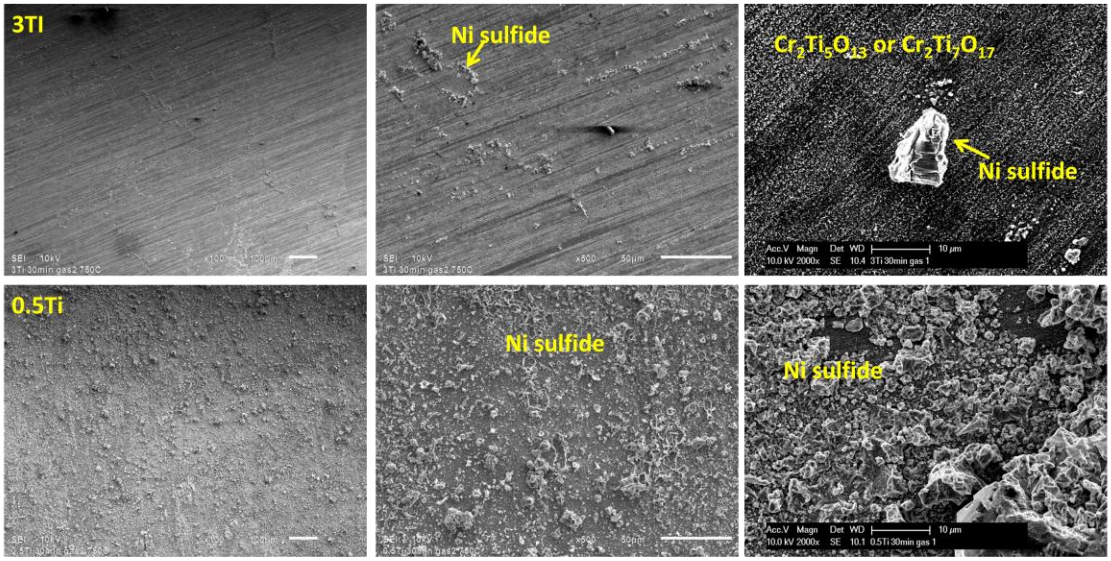

Figure 5.101 The surface images of Alloy 0.5Ti and 3Ti after 30 minutes in Gas 2

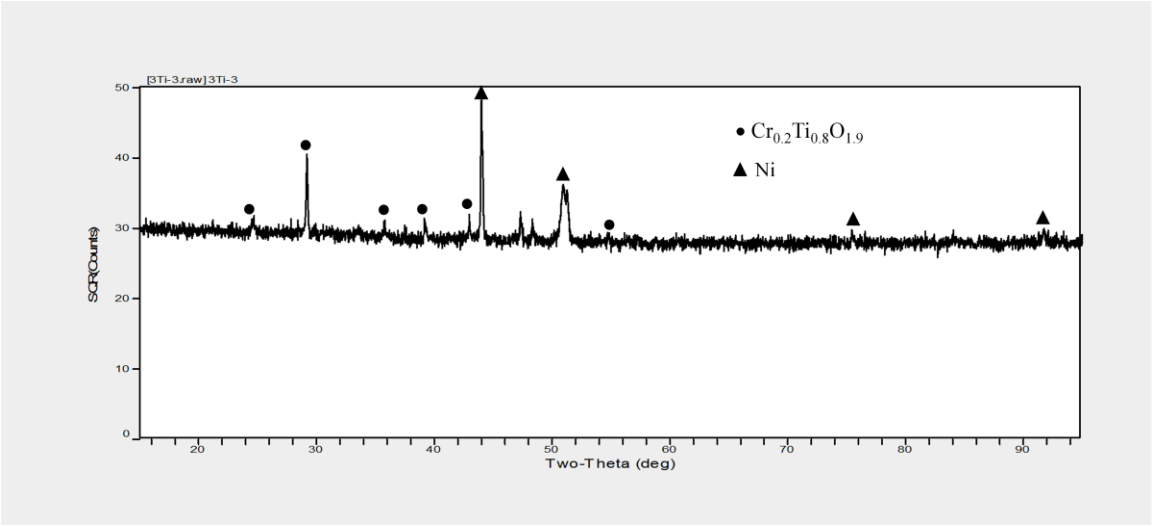

Figure 5.102 XRD pattern from the alloy with 3Ti after 30 min in Gas 2

Cross-sectional images of the two alloys are shown in Figure 5.103. A thin Cr and Ti complex oxide formed on the alloy with 3Ti, while double-layered sulfides were observed on the alloy with 0.5Ti, with a top Ni-sulfide layer and an inner Cr-sulfide layer. These results provide further evidence that Ti promotes the formation of an oxide layer.

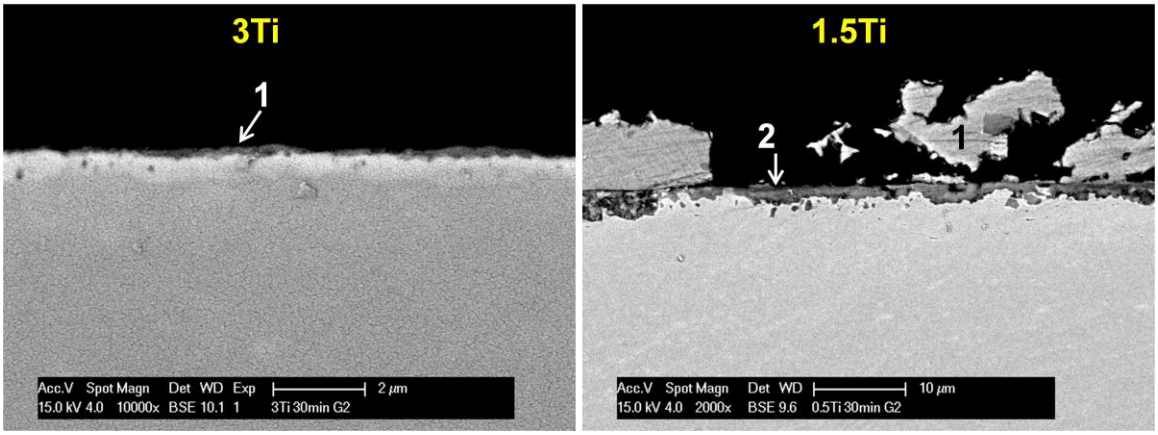

(1).48.5O-20.6Cr-4.6Al-8.6Ti-1.7Co-2.6Si-12.6Ni-1.6Fe (at.%)	(1).Ni sulfide 44.0S-54.8Ni-1.2Si (2).Cr sulfide 57.5S-35.6Cr-5.6Ni-1.2Al(at.%)

Figure 5.103 Cross-sectional images of the alloys with 0.5Ti and 3Ti after 30 minutes in Gas 2

As already discussed several times in the previous sections, the alloys used in low NO_x burner atmospheres rely on the formation and sustained growth of a protective oxide scale which acts as a barrier blocking the inward transport of oxidants, such as sulfur, and outward diffusion of base metals such as Ni. The formation of a protective oxide scale is complicated because nearly all alloying elements in the model alloys are able to form sulfide scale in Gas 1. The dissociation partial pressures of metal sulfides are shown in

Table 5.4. However, only some alloying elements, Al, Ti and Cr, can form stable oxides. All these sulfides and oxides will tend to nucleate and grow at preferred surface sites during the initial stage of reaction. Ti oxides are more stable thermodynamically than Cr_2O_3, and the growth rate of Ti oxides is favored during the very early stage of reaction. The early-formed Ti oxides may then promote the formation of Cr_2O_3 by, perhaps, serving as a sympathetic nucleation site. For instance, one possibility is that Ti_2O_3 particles formed and acted as a template for the nucleation of Cr_2O_3 as the primitive cell of both Ti_2O_3 and Cr_2O_3 have a rhombohedral structure (space group is R3C) with similar lattice constants, as shown in Figure 5.104. After the formation of Ti_2O_3 and Cr_2O_3, they reacted to form $Cr_{0.222}Ti_{0.778}O_{1.889}$. The formation of this complex oxide would hinder the sulfidation process. The effect of Ti to improve the protective oxide scale formation was also observed in a study on the high-temperature corrosion behavior of 310 stainless steel and Alloy 800 in oxidizing-sulfidizing gases[149].

Table 5.4 The dissociation pressure of some metal sulfides at 750°C

Sulfides	Dissociation pressure of sulfide at 750°C(atm)	Equilibrium sulfur pressure
Ni_3S_2	1.2×10^{-9}	1.3×10^{-7}
Cr_2S_3	1.5×10^{-11}	
CrS	5.1×10^{-14}	
Co_9S_8	1.5×10^{-8}	
MoS_2	1.49×10^{-11}	
FeS	1.3×10^{-10}	
Al_2S_3	8.3×10^{-20}	
TiS	4.9×10^{-26}	

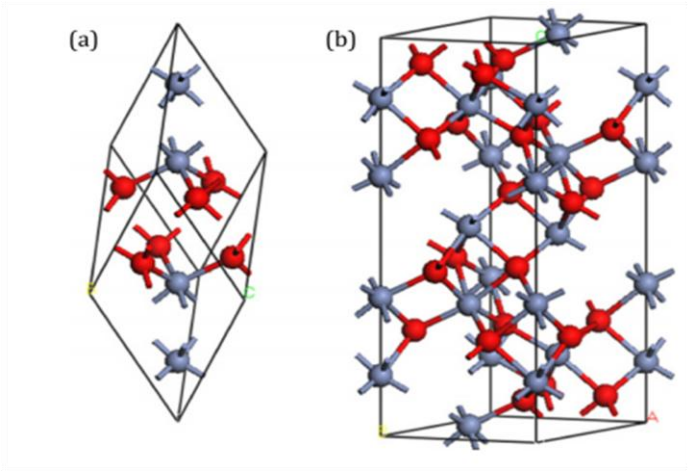

Gray dots: transition metal atoms;
Red dots: O

	Lattice constant (Å)	Angle (deg)
Ti_2O_3	5.431	56.583
Cr_2O_3	5.390	55.130

Figure 5.104 Crystal structure of Cr_2O_3 and Ti_2O_3[150, 151]. (a) rhombohedral primitive cell (b) hexagonal representation.

As seen in the table below the images in Figure 5.103, 8.6at.% titanium was observed in the oxide scale, while the total amount of oxygen and chromium in the oxide layer was 48.5at.% and 20.6at.%, respectively. This suggests that, except for the formation of $Cr_{0.222}Ti_{0.778}O_{1.889}$, there are extra amounts of oxygen and chromium in the scale. It is very possible that the remaining amounts of oxygen and chromium exist as Cr_2O_3. The Cr_2O_3 peaks were not identified in XRD analysis probably because that the soluble Ni and Fe in Cr_2O_3 shifted the lattice parameters of Cr_2O_3.

It is known now from this thesis study and others' research that the individual addition of Ti, Al and Mo is beneficial to improve sulfidation resistance. However, the co-addition of these three alloying elements has the most significant effect compared to any individual addition, as shown in Figure 5.9[120]. This shows that the tri-addition of Al, Ti and Mo combines the individual beneficial effect. The reaction products formed from the three alloying elements act, together with Cr oxide, to strengthen the barrier which blocks the outward diffusion of base-metal elements and inward diffusion of sulfur, and hence the tri-addition has a more significant effect compared to the individual addition.

5.2.3.3 Summary

In order to verify the effect of Ti on suflidation resistance, three model alloys with different Ti levels were prepared based on the compositions of commercial Alloys 41, 617 and 282. The three modified model alloys were tested for 25, 50 and 100 hours in Gas 1, and 100 hours in Gas 2 and 3 at 750^{o}C. The inferences that can be drawn from the results obtained are as follows:

(1) Titanium content (at least up to 3wt.%) influences the location of kinetic boundary. With an increase of Ti content, the kinetic boundary moves to the lower oxygen partial pressure. This serves as a beneficial effect of Ti being to promote the formation of the Cr_2O_3 scale.

(2) There is a complex interplay between alloy composition, specifically the relative amount of Ti, and environment. Ti did not have an obvious effect on sulfidation resistance in Gas 1; while Ti addition exerted a beneficial effect on sufidation behavior in Gases 2 and 3.

(3) Ti promotes the formation of complex Ti and Cr oxides. The complex oxides suppress the occurrence of sulfidation at the early stage of testing by acting as a barrier which impedes external sulfidation.

5.3 CORROSION BEHAVIOR OF IRON-MOLYBODLENUM -ALUMINUM ALLOYS IN SYNGAS

5.3.1 Alloy phase identification

Cast alloys of compositions Fe-30wt.%Mo-5wt.%Al and Fe-30wt.%Mo-10wt.%Al were annealed at 1000°C for 50 hours. The alloys can be represented in the 1000°C isothermal section of Al-Fe-Mo phase diagram, which is shown in Figure 5.105[140].

Figure 5.106 **s**hows the microstructure of the two alloys after annealing at 1000°C for 50 hours. A dark phase and a white phase can be clearly seen. The white phase is Mo-rich, μ for the 5Al alloy, but for 10Al alloy it is deduced to be a two-phase mixture of μ+Mo_3Al. μ-phase has a rhombohedral structure and is generally considered to be brittle[152]. The dark phase in 5Al is α-Fe, while in 10 Al it is α_1 (Fe_3Al). Table 5.5 summarizes the phase compositions and identities within the two alloys.

As indicated by the XRD spectra in Figure 5.107, the matrix phase in 5Al is α-Fe, which has the bcc structure, while the matrix phase in 10Al is Fe_3Al with an fcc structure. The difference in the matrix structures will influence the corrosion resistance, which will be discussed later.

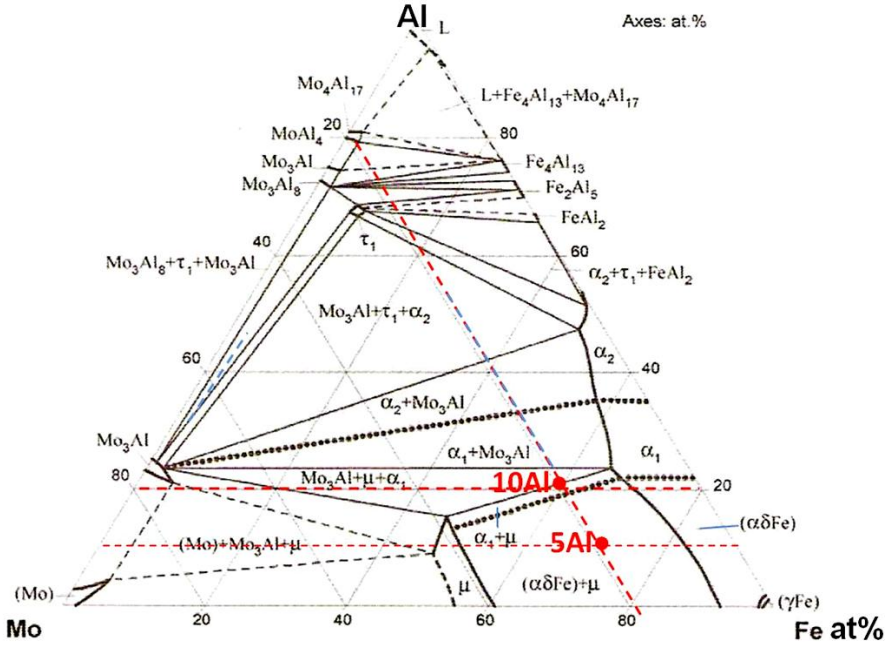

Figure 5.105 Al-Fe-Mo isothermal section at 1000°C[153]

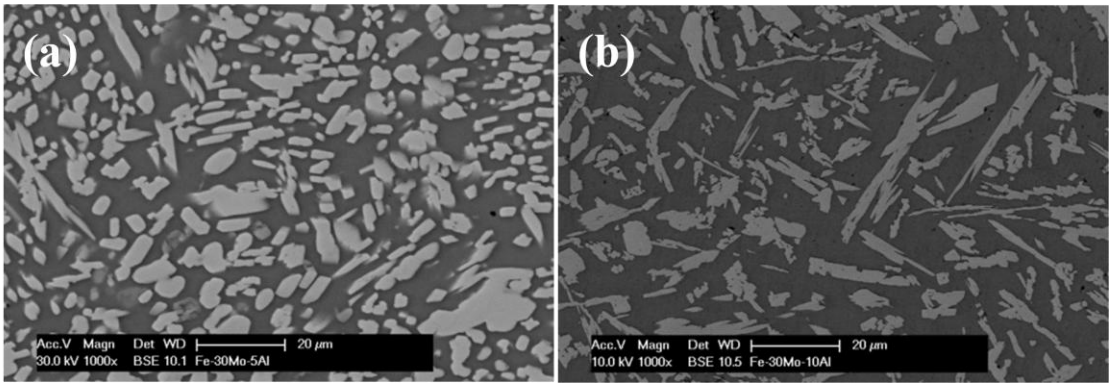

Figure 5.106 Microstructure of Fe-Mo-Al alloys after annealing at 1000°C for 50 hours, (A) Fe-30Mo-5Al, (B) Fe-30Mo-10Al

Table 5.5 Phase compositions and identities in the Fe-Mo-Al alloys studied

Alloy compositon	Dark phase (at.%)	White phase (at.%)
Fe-30wt.%Mo-5wt.%Al (Fe-18at.%Mo-10.5at.%Al)	74.5Fe-10.9Mo-14.6Al α-Fe	53.7Fe-38.8Mo-7.5Al μ
Fe-30wt.%Mo-10wt.%Al (Fe-18at.%Mo-21at.%Al)	62.6Fe-24.3Al-13.1Mo α_1-Fe_3Al	45.9Fe-36.4Mo-17.7Al μ+Mo_3Al

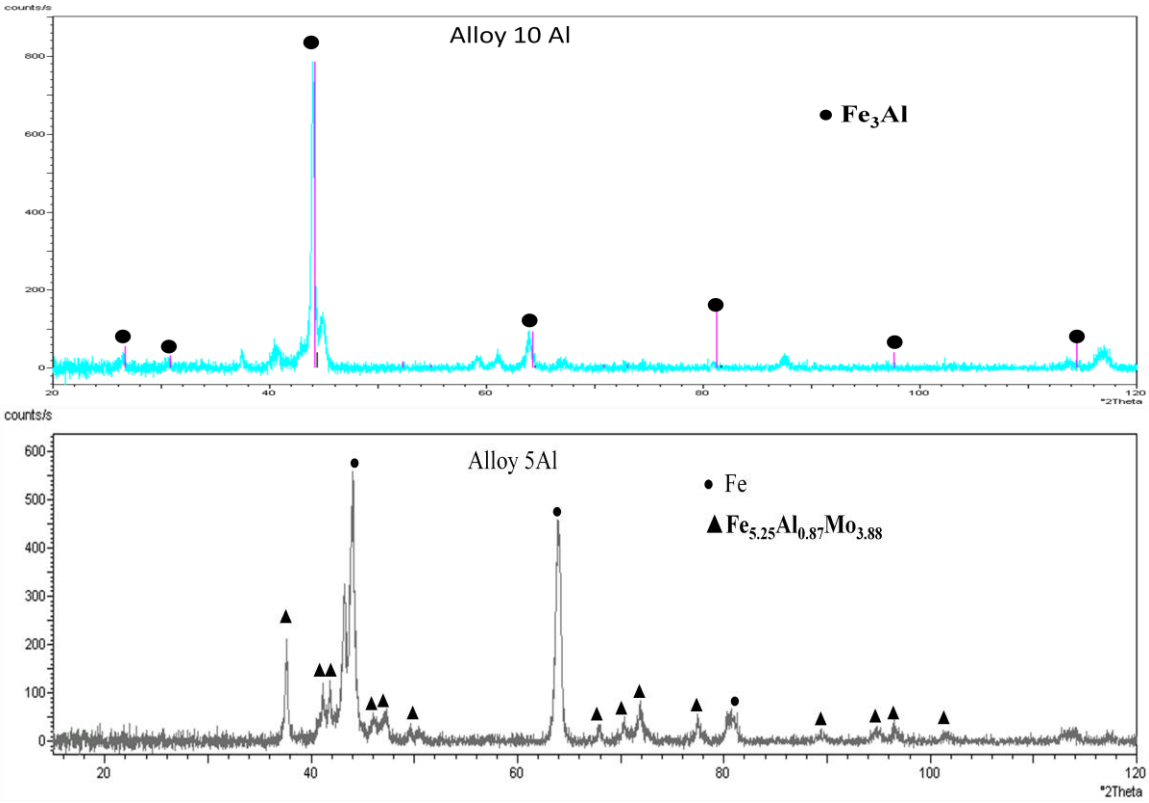

Figure 5.107 XRD pattern from Alloys 10Al and 5Al

5.3.2 Corrosion behavior and mechanism of alloy Fe-30Mo-5Al

Alloy Fe-30Mo-5Al was tested in Gas 4 (30%CO_2-1%CO-0.005%H_2S-19%H_2O-H_2) and Gas 5(30%CO_2-1%CO-0.01%H_2S-19%H_2O-H_2) for different times at 500 ^oC. Gas 5, with a higher amount of H_2S, is more aggressive than Gas 4, so the results shown below are mainly for Gas 5.

Figure 5.108 shows the weight-gain kinetics for Alloy Fe-30Mo-5Al in Gas 5. The alloy shows breakaway behavior. The weight-gain values are compared with the calculated weight gains from the experimental results summarized by Mrowec[44], where the Alloy Fe-30Mo-5Al was tested in H_2-H_2S mixture (with 0.01 atm sulfur vapor) at 500 ^oC. Unlike the breakaway kinetics observed in the current experiment, Alloy Fe-30Mo-5Al in Mrowec's study obeyed parabolic kinetics.

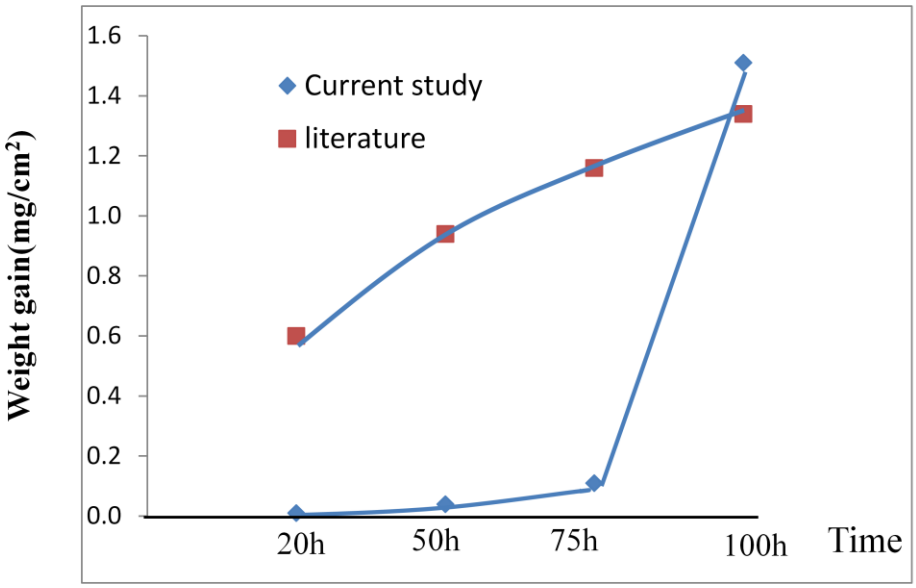

Figure 5.108 The weight gain with time of 5Al after testing for testing for 20, 50, 75 and 100 hours

Figure 5.109 shows a surface image of 5Al after testing for 20, 50, 75 and 100 hours. As shown in this figure, Al_2O_3 particles were clearly observed on the matrix ferrite phase after testing for 20 hours. EDS analysis showed about 7.9at.% oxygen in the matrix ferrite phase. After testing for 50 hours, the amount of particles increased; and oxygen content in the ferrite phase increased to 13.6 at.%. After testing for 75 hours, the ferrite phase was fully covered by FeS according to XRD analysis. The formation of FeS led to scale breakdown. This is probably because the Al level was not enough to form a thick protective Al_2O_3 layer, thus allowing Fe to diffuse outward and react with sulfur in the environment to form FeS. The FeS then grew laterally until it coalesced into a continuous outer layer which completely covered the sample surface, as indicated in Figure 5.109 (e). From 20 to 75 hours, there was no obvious composition change in the μ phase. The surface compositions of ferrite and μ-phase after testing for 20, 50, 75 hours are summarized in Table 5.6.

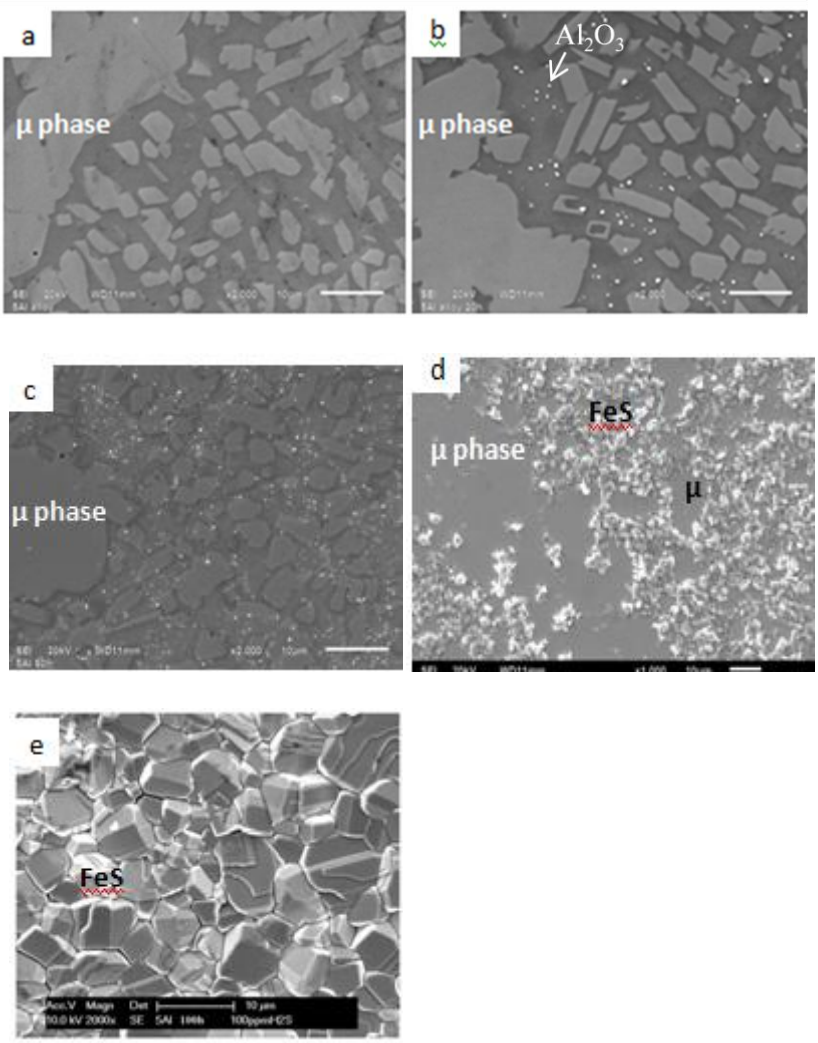

Figure 5.109 Surface image of 5Al after testing for 20, 50, 75 and 100 hours at 500 ^{o}C in Gas 2, (a) surface before testing, (b) 20 hours, (c) 50 hours, (d) 75 hours, (e) 100 hours

Table 5.6 Surface composition after testing for 20, 50, 75 and 100 hours

at.%		Fe	Mo	Al	S	O	Remarks
composition of μ phase	0 hr	56.0	36.8	7.2	-	-	
	20 hr	52.2	41.2	6.6	-	-	
	50 hr	52.5	40.9	6.6	-		
	75 hr	54.2	39.4	6.4	-		
	100 hr	-	-	-	-	-	
Composition of matrix ferrite	0 hr	80.0	5.1	14.9	-	-	
	20 hr	72.1	6.0	14.0	-	7.9	
	50 hr	69.1	4.6	12.7	-	13.6	
	75 hr	36.4	-	13.3	36.8	13.5	FeS started to form on ferrite
	100 hr	49.4	-	-	50.6		FeS completely covered sample surface

Figure 5.110 shows cross-sectional images of 5Al after 75 and 100 hours in Gas 5 at 500 ^{o}C. It is clearly shown from Figure 5.110 (a) that FeS initially formed on ferrite. Then FeS grew laterally, and finally covered the μ-phase, as shown in Figure 5.110 (b). It is also clear from Figure 5.110(b) that the ferrite was preferentially attacked phase. A thin layer underneath the outer FeS layer is a mixture of Al_2O_3 and $FeAl_2S_4$. The stability of Al_2O_3 with respect to $FeAl_2S_4$ is affected by the iron activity via the following reaction

$$2\ FeAl_2S_4 + 3O_2 = 2\ Al_2O_3 + 2Fe + 4S_2$$

Accordingly, the nature of the corrosion product is affected by the value of $(P_{S2})^4 * (a_{Fe})^2/(P_{O2})^3$, such that a higher iron activity will stabilize $FeAl_2S_4$ with respect to Al_2O_3. Iron activity decreases from inside of the preferential sulfidation zone to the interface

between the alloy and the FeS scale, thus iron activity at point 3 Figure 5.110 (b) is larger than that at point 2. Therefore, only $FeAl_2S_4$ was observed at point 3 and a mixture of Al_2O_3 and $FeAl_2S_4$ was observed at point 2. The composition of the outer FeS scale and the inner reaction zones are shown in Table 5.7. It is worth noting that there was significant Fe depletion from the preferentially attacked ferrite due to the outward diffusion of Fe, as seen by the composition indicated by points 2 and 3. There was no obvious change in the composition of μ phase, as seen by the compositions indicated by points 4 and 5.

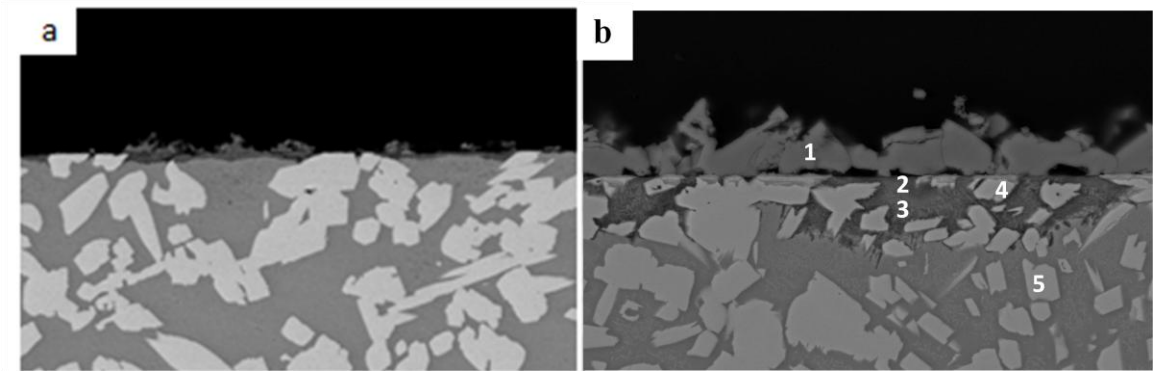

Figure 5.110 Cross-sectional images of 5Al after testing for 75 and 100 hours at 500^{o}C in Gas 2, (a) testing for 75 hours, (b) testing for 100 hours

Table 5.7 The composition of the scale on 5Al after testing for 100 hour in Gas 2

at.%		Fe	Mo	Al	S	O
1	FeS	46.8	-	-	53.2	-
2	Al_2O_3 $FeAl_2S_4$	8.1	-	27.6	34.6	29.7
3	$FeAl_2S_4$	16.2	-	22.6	61.2	-
4	μ phase	52.9	39.2	7.9	-	-
5	μ phase	53.2	38.9	7.9	-	

It is clear from Figure 5.109 that Al_2O_3 particles nucleate on ferrite but not on μ-phase. From a thermodynamic standpoint and conditions of local equilibrium, the chemical activity of Al in ferrite is same as that in μ phase, regardless how large the concentration difference may be. Therefore, it is the availability of Al, not its activity, that is more important [78]. We know from Table 5.5 that Al is enriched in ferrite, which would facilitate the formation of Al oxide on ferrite. By contrast, the Al content in μ-phase is relatively low; apparently too low to form Al_2O_3 externally.

From the above discussion, the mechanism of corrosion of the 5Al alloy can be depicted in Figure 5.111. After testing for time 1, Al_2O_3 forms on ferrite, but it doesn't provide protection against corrosion probably because there is not enough Al in the alloy to form a continuous Al_2O_3 layer. At time 2, Fe in ferrite diffuses outward and reacts with the atmosphere to form an iron sulfide layer on the Al_2O_3 layer. Iron sulfide layer then grows laterally until it finally covers the μ phase by time 3. Meanwhile, sulfur penetrates

through the alumina scale along flaws such as micro-cracks into the alloy and reacts with alloy elements to form internal sulfides.

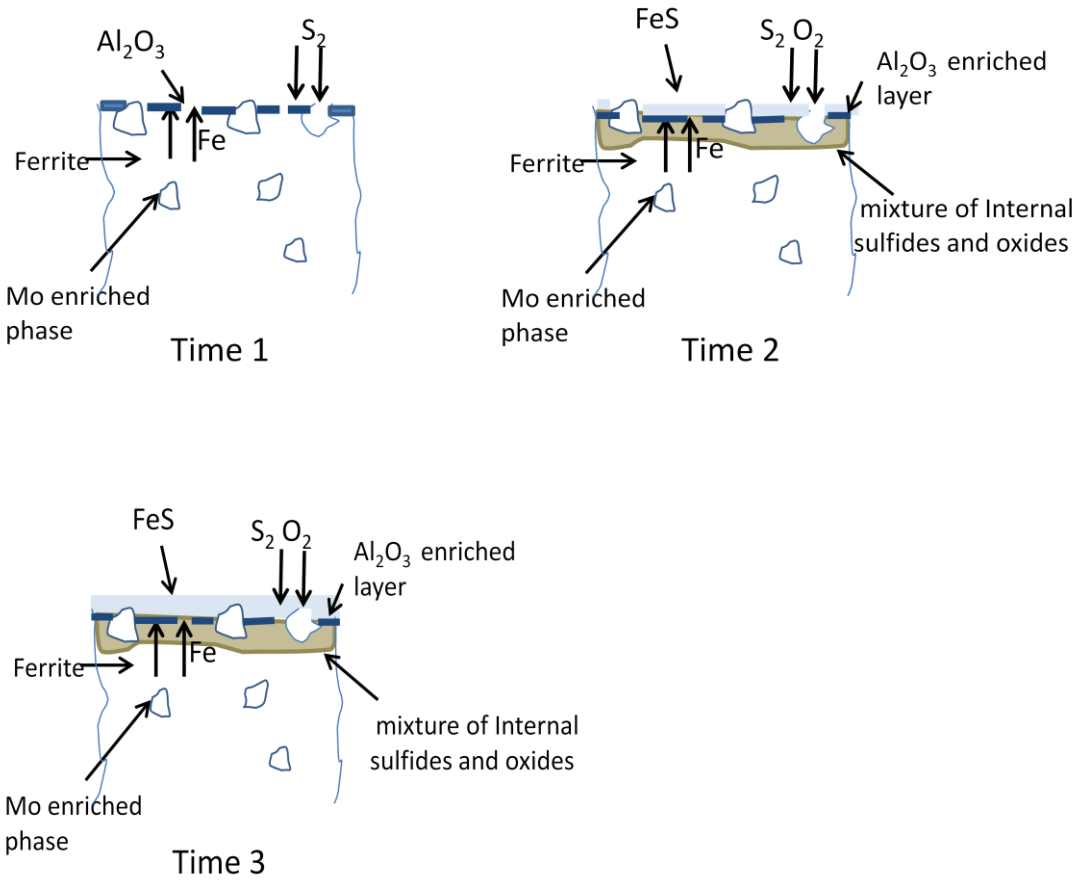

Figure 5.111 Schematic drawing of the growth of FeS scale on Alloy Fe-30Mo-5Al

In order to assess how Alloy Fe-30Mo-5Al behaves at higher temperature, it was tested at 600 ^{o}C for 100 hours in Gas 5. Figure 5.112 shows the surface and cross-sectional images of Alloy Fe-30Mo-5Al after 100 hours at 600^{o}C in Gas 5. The images are similar to those from the same alloy reacted at 500^{o}C.

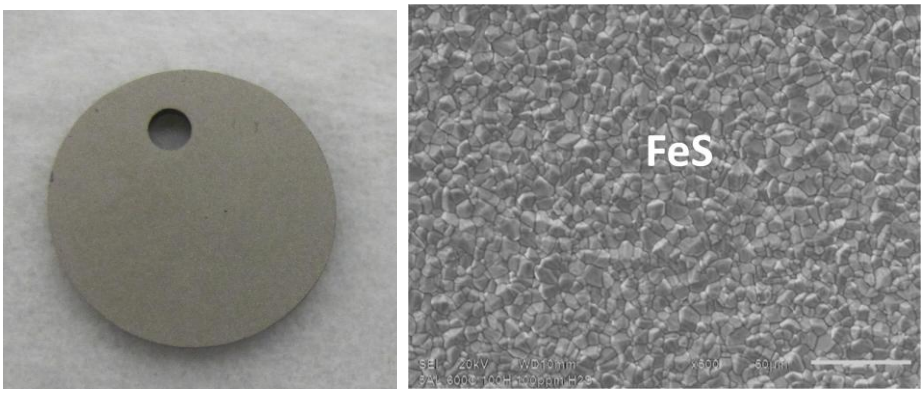

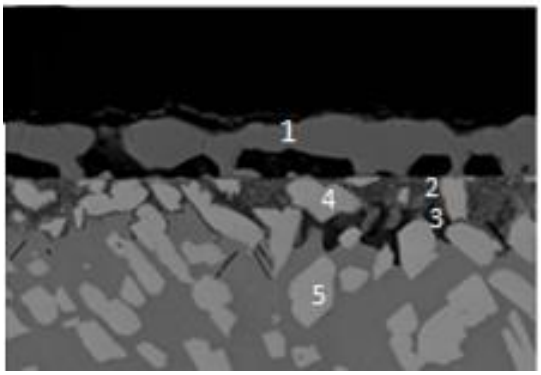

		Fe (at.%)	Mo (at.%)	Al (at.%)	S (at.%)	O (at.%)
1	FeS	52.1			47.9	
2	Al_2O_3 containing layer	17.3	8.7	19.3	19.5	34.9
3		27.7	9.3	15.1	17.2	30.7
4	μ phase	50.6	41.7	7.7		
5	μ phase	52.9	39.1	8.3		

Figure 5.112 Surface and cross-sectional images of Alloy Fe-30Mo-5Al after 100 hours at 600 ^{o}C in Gas 5

5.3.3 Corrosion behavior and mechanism of alloy Fe-30Mo-10Al

Alloy Fe-30Mo-10Al was tested at 500 ^{o}C in Gas 5 for 150 and 200 hours. There was little change in weight gain, as shown in Table 5.8. Moreover, no obvious change in appearance was observed on the surface, as seen in Figure 5.113. Since oxygen was observed on the surface using EDS, it is expected that an Al_2O_3 layer formed and provided protection against corrosion. But the Al_2O_3 layer was too thin to be observed in the cross-sectional image, as shown in Figure 5.114.

Table 5.8 Weight gain after testing for 150 and 200 hours at 500 ^{o}C in Gas 5

	150hours (mg/cm^2)	200 hours(mg/cm^2)
Fe-30Mo-10Al	0.002	0.003

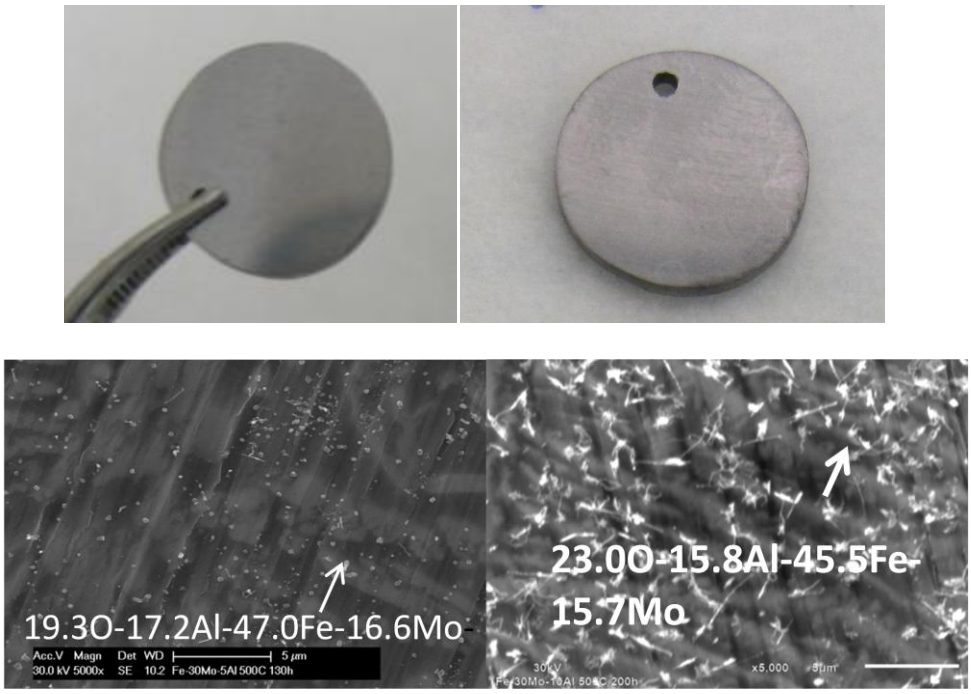

Figure 5.113 Surface images of Alloy Fe-30Mo-10Al after testing 150 and 200 hours in Gas 5

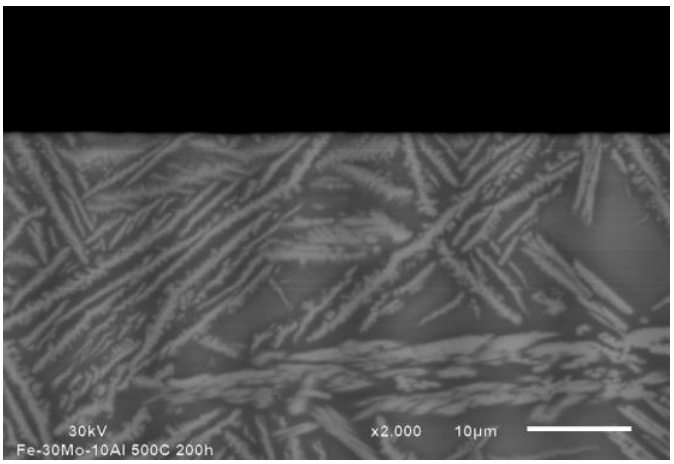

Figure 5.114 Cross-sectional image of Alloy 10Al after testing 200 hs in Gas 5

In order to verify the existence of a very thin Al_2O_3 layer, XPS analysis was conducted on 10Al after testing for 100 hours at 500 ^oC in Gas 5. Table 5.9 shows the composition as a function of emission angle. Relative to the nominal bulk composition, there is a significant deficit of Fe and excess of Al at both the outer surface (high angle) and near surface (low angle); only a trace amount of S was detected. Chemical shifts suggest that in the outer surface and near surface, both Fe and Al exist as oxides. It is inferred that oxidation, and not sufidation, dictated the measured surface compositions. The significant amount of Ca, Si and C on the sample surface might be due to contamination from the crucible. The pattern, shown in Figure 5.115, suggests that oxidation induces segregation of Al to the surface to form aluminum oxide.

The formation of an Al_2O_3 layer was also observed in a previous study[154]. For example, sputter-deposited Al-Mo alloys were tested in pure sulfur vapor at 10^3 pressure at the temperature range of 700-1000^oC and an alumina scale had formed, as determined by XPS analysis, due to the residual oxygen in the reactor[154].

Table 5.9 Composition as a function of emission angle

near-surface ⟷ top-surface

		Angle, degree			
At. %	Nominal Comp. of bulk	27	42	57	72
Si2s		8.85	7.8	11.58	9.83
O1s		44.85	42.67	41.91	39.43
Mo3d	16	3.08	2.47	1.46	0.93
Fe3p3	75	8.97	8.12	4.1	8.11
Ca2p		3.18	3.25	3.72	2.75
C1s		18.06	23.27	24.69	30.36
Al2s	19	13.02	12.42	12.54	8.59

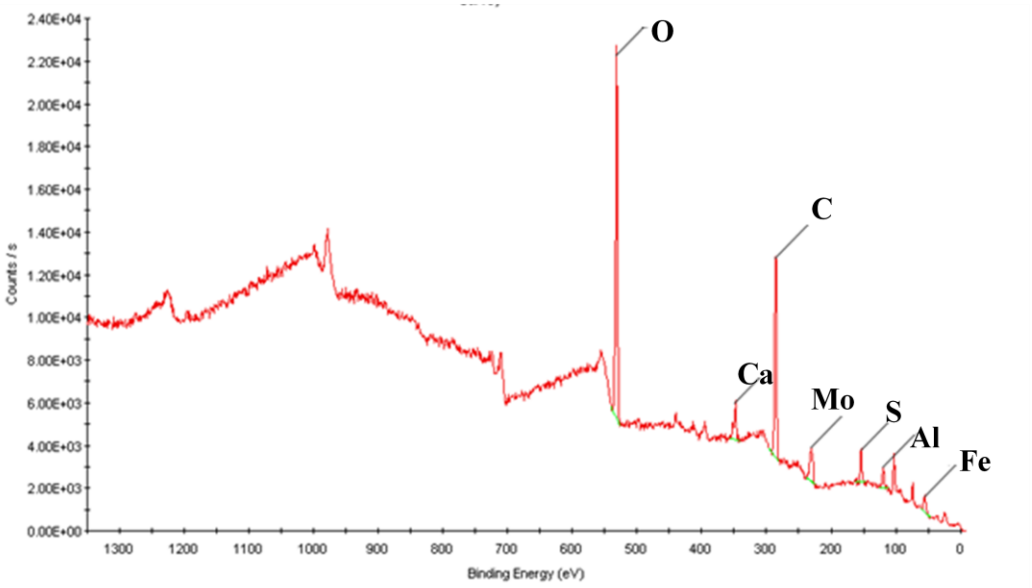

Figure 5.115 XPS analysis on 10Al after testing for 100h.

Alloy Fe-30Mo-10Al was also tested at 600^{o}C for as long as 300 hours in Gas 5. The surface and cross-sectional images are shown in Figure 5.116. A very thin Al_2O_3 layer can be distinguished in the cross-sectional image.

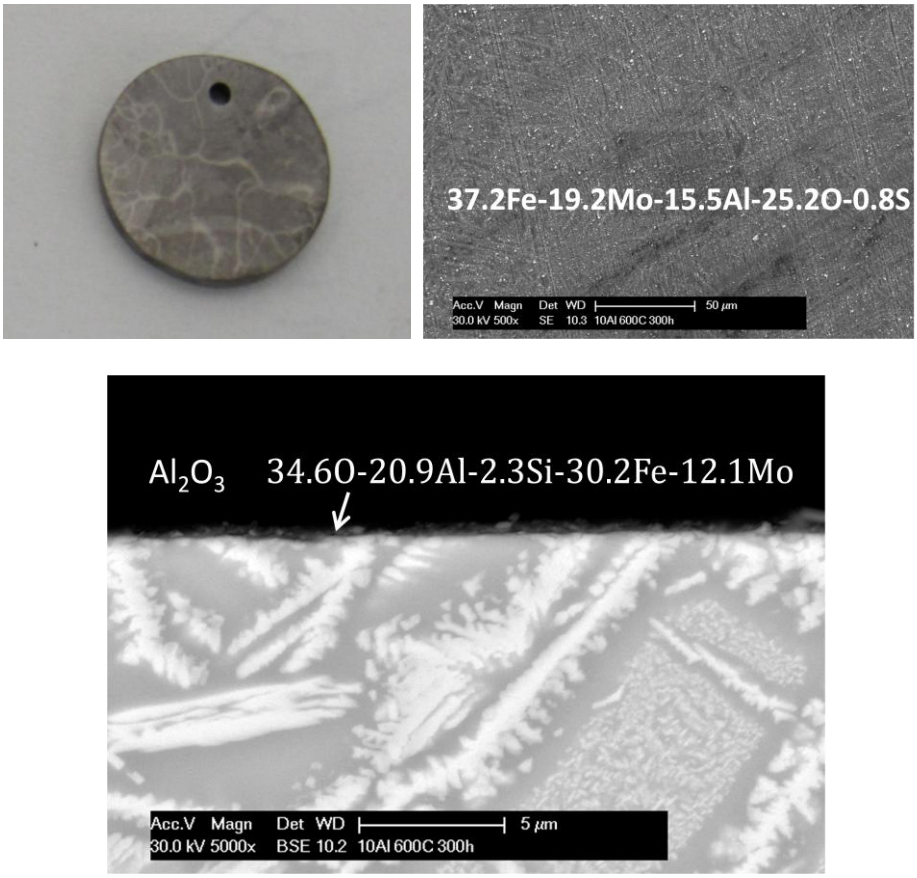

Figure 5.116 Surface and cross-sectional images of Alloy Fe-30Mo-10Al after testing for 300 hours at 600 ^{o}C in Gas 5

5.3.4 Alloying effects on sulfidation resistance

The matrix ferrite phase was preferentially attacked by sulfur while the shape and composition of the Mo-enriched phases in Alloy 10Al remained unchanged even after testing for 300 hours at 600^{o}C in Gas 5. Thus, the protection provided by the matrix phase determines sulfidation resistance provided that this matrix phase is of a significant volume fraction. When a continuous alumina scale forms over the matrix phase, the alloy will have the excellent sulfidation resistance. The formation of a protective Al_2O_3 layer depends on the composition of the matrix phase, especially Al content, since Al is enriched in this matrix phase (α Fe in Alloy 5Al and Fe_3Al in Alloy 10Al). As the overall Al content increases, the Al level in the matrix increases. Alloy 10Al has better sulfidation resistance than Alloy 5Al because of a higher level of Al.

The beneficial effects of Al on sulfidation resistance can be explained as follows. Firstly, a high Al level can help to stabilize the formation of Al_2O_3 which provides corrosion resistance. Secondly, both 5Al and 10Al have a two phase structure-a matrix phase and a Mo-enriched phase. Due to the difference in Al content, the matrix of 5Al is αFe with the bcc structure, while matrix phase of 10Al is Fe_3Al with an fcc structure. Fe diffuses faster in bcc than in fcc; thus Fe sulfide is more easily formed on 5Al than on 10Al. Thirdly, Al in ferrite can have the effect of blocking the outward diffusion of iron. As the overall Al content increases, the Al level in the matrix phases increases, leading to the more significant blocking effect.

Both the current and others studies[17, 19, 155] show that Mo in the matrix phase plays a limited role in improving the corrosion resistance. However, the concentration of Mo is also an important factor to improve corrosion resistance of Fe-Mo-Al alloys. The

addition of Mo leads the formation of μ phase (Mo_3Al), which reacts with sulfur at a very low rate. Wang et al.[20] compared the sufidation resistance of Fe-10Al and Fe-30Mo-Al in 0.01atm sulfur vapor at 700°C. The results showed that Alloy Fe-10Al sulfidized at a much higher rate than Fe-30Mo-Al. They proposed that a critical Al+Mo content is needed to provide sulfidation resistance, although they didn't mention the exact amount. Kai et al.[114] studied the corrosion behavior of Fe-xMo-7wt.%Al alloy in $H_2/H_2O/H_2S$ mixing gas at 900°C. The results showed that the corrosion rate is strongly dependent on the amount of Mo over the range of 10-20wt%, but less dependent on the amount of Mo over the range of 20-30wt.%.

5.3.5 The behavior of the alloy Fe-30Mo-5Al and Fe-30Mo-10Al in Gas 1

As mentioned in the previous literature review, most conventional oxidation-resistant alloys do not have acceptable sulfidation resistance under the condition where sulfidation is the favored mode of attack[8, 9]. The main reason for this is the greater extent of non-stoichiometry in sulfides [12]. Consequently, the diffusion through sulfide scales is very fast, and, hence, the growth rate of sulfides is fast. By contrast, a number of refractory metals, such as Mo and Nb, are highly resistant to sulfur corrosion, with the sulfidation rate comparable to the oxidation rate of Cr[13]. The excellent sulfidation resistance of refractory metals results from the very low deviations from stoichiometry, and thereby, the low defect concentrations in the sulfides of these metals. Research has shown that the predominant defects in these sulfides, as in refractory metal oxides, are S interstitials [12, 14, 118]. As a consequence, in contrast to common metals, sulfide scales on refractory metals grow relatively slowly by inward diffusion of sulfur. In order to compare the two

refractory metal Mo containing alloys with conventional commercial alloys, the two alloys were also tested in Gas 1 for 100 hours at 750^{o}C. The weight gains are compared to that of the best model Alloy 8, as shown in Figure 5.117. It is clear that Fe-Mo-Al alloys have better sulfidation resistance than model Alloy 8.

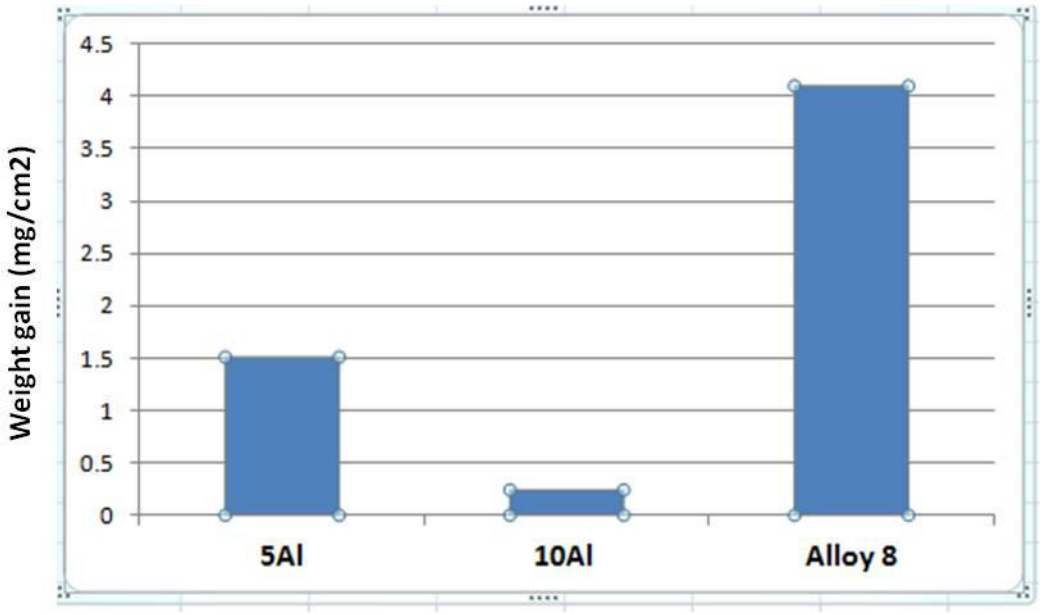

Figure 5.117 Weight gains of Alloys 5Al and 10Al and Alloy 5 after testing for 100 hours at 750^{o}C in Gas 1

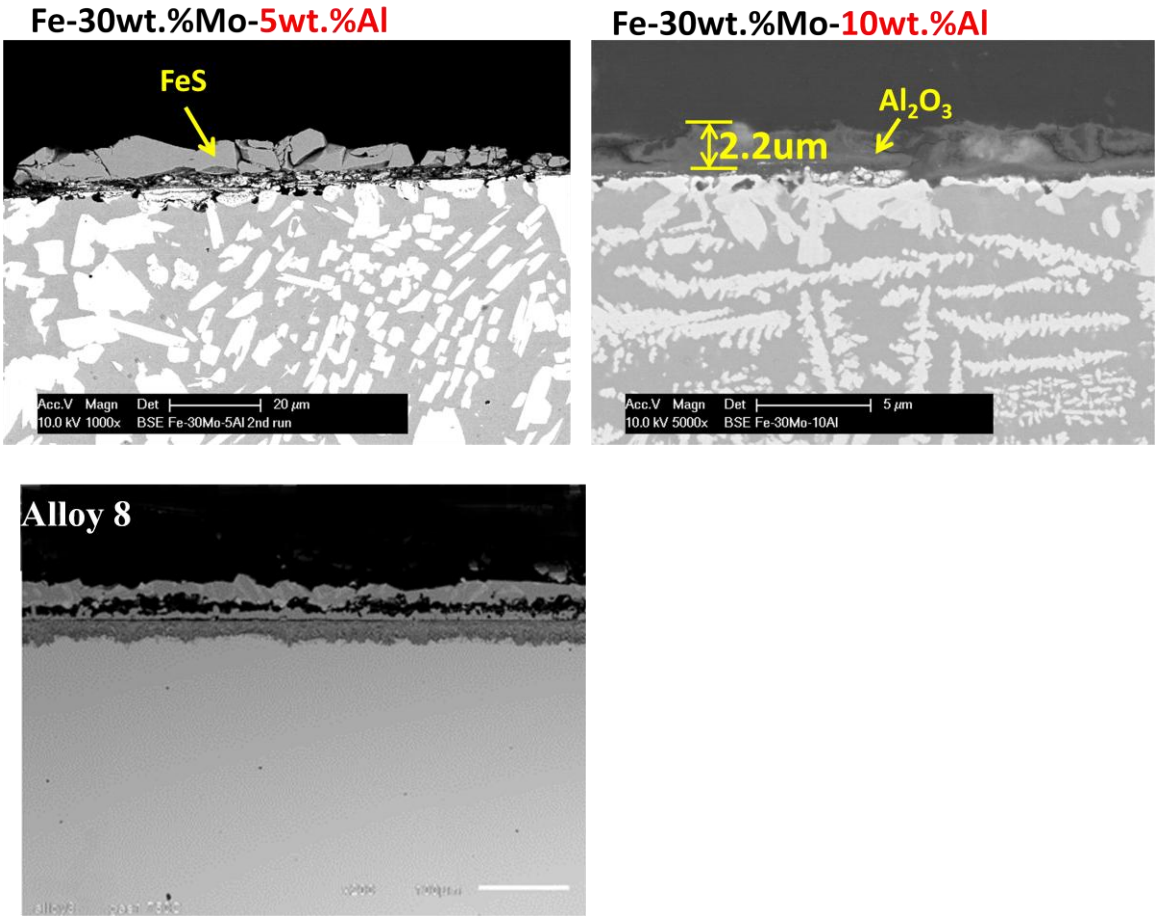

Figure 5.118 Cross-sectional images of Alloy 5Al, 10Al and Alloy 8 after testing for 100 hours at 750^{o}C in Gas 1

5.3.6 Summary

The corrosion resistance of Fe-30wt.%Mo-5wt.%Al and Fe-30wt.%Mo-10wt.%Al was studied in a simulated syngas atmosphere in which the H_2S content was up to 100ppm at 500^oC and 600^oC. The following conclusions can be drawn:

(1) Alloy Fe-30Mo-10Al exhibits excellent sulfidation resistance in the testing gases. The good corrosion resistance can be attributed to the formation of a very thin Al_2O_3 layer on the surface of the alloy, as identified by XPS analysis.

(2) Alloy Fe-30Mo-5Al showed breakaway behavior in the current study. Al_2O_3 initially nucleated on the surface of ferrite, but a continuous Al_2O_3 scale did not form due to the low Al content.

(3) The composition of the matrix phase, especially the Al content, determines sulfidation resistance. Firstly, a high Al level can help to stabilize the formation of Al_2O_3. Secondly, Al content influences the matrix phase structure. Alloy 10Al has a FCC matrix, while the matrix of 5Al has BCC structure. The FCC structure is preferred. Thirdly, Al in the matrix phase has the effect to block the outward diffusion of iron.

(4) Fe-30Mo-Al alloys have better sulfidation resistance than Ni-Cr-Co model alloys.

6.0 CONCLUSIONS

Eight chromia-scale-forming commercial alloys and eleven model alloys were tested at 750^{o}C in gases with a base composition of N_2-15%CO-3%H_2-0.12%H_2S. The effects of major alloying elements Cr, Co and Ni and minor alloying elements Ti, Al and Mo on sulfidation resistance were studied.

After testing the various commercial alloys in the simulated atmosphere of a low NO_x burner, the following conclusions can be drawn.

(1) Compared to Ni-Fe-based and Co-based alloys, the Ni-rich Ni-Co-based alloys studied showed the best corrosion resistance, with Alloys 160 and 263 exhibiting the best sulfidation resistance in all the three gases.

(2) In the case of Ni-based alloys, at a certain Cr level (~25wt. %), the Co content influences the weight gain and the onset of breakaway corrosion. An alloy has the longest time to breakaway when Ni/Co major element ratio is near unity, because both Ni and Co availability for reaction are low in such a case.

(3) Alloy 263 does not have high Cr and Co contents compared to Alloy 160, but the former has less weight gain due to relatively minor addition of Ti, Al and Mo. These elements can play an important role to improve sulfidation resistance due to their ability to promote and/or maintain protective oxide scale formation.

(4) At a given sulfur pressure, there is a threshold oxygen partial pressure beyond which a continuous protective chromia scale is developed. This threshold pressure decreases with an increase in the alloy Cr content. Even so, the kinetic boundary between sulfidation and oxidation is highly alloy dependent, beyond just total Cr content.

(5) In Gas 3, which has the highest oxygen potential, oxidation dominated over sulfidation; the chromium oxide layer formed to provide protection against corrosion. In Gas 1, where sulfidation dominates, all the alloys showed the worst corrosion resistance due to sulfides eventually forming over an initially-formed chromium oxide layer.

(6) Sulfide whisker growth is maintained by the outward diffusion of Ni. Such whisker formation on Alloy 120 is believed to be related to surface reaction control of the H_2S dissociation. The formation of whiskers indicates the occurrence of preferential growth, which is deduced to be due to an orientation dependence of the H_2S dissociation reaction.

(7) The Kirkendall effect and diffusional creep as a result of the stresses produced in the scale account for the initial development of voids in the scale. A dissociation process substantially leads to void growth, which may be extensive.

(8) The formation of nodules on some alloys is due to melting via Ni-Ni_3S_2 eutectic formation during the test.

Conclusion (2) from commercial alloy study was verified with studies on model alloys. Inferences drawn from the five model alloys, which were prepared to verify the Ni/Co major-element ratio, are as follows:

(9) The results from the model alloys confirmed that when the Ni/Co major-element ratio is near unity, the alloy has optimum sulfidation resistance.

(10) The results from the model alloys confirmed the established beneficial effects of Cr and Co on sulfidation resistance. In the composition range of the current experiments, 10-40wt%Co, weight gain decreases with an increase in the alloy Co content at a constant Cr level. Similarly, weight gain decreases with an increase in the alloy Cr content at a constant Co level.

(11) The results from the model alloys showed that the tendency to form liquid Ni-Ni_3S_2 eutectic increases with an increase in the Ni content in the alloys.

Conclusion (3) from commercial alloy study was also verified by the study of three model alloys. Conclusions about the effects of minor alloying elements Al, Ti and Mo can be drawn as follows.

(12) The modified Alloys 6, 7 and 8 underwent less weight gain and hence offered better corrosion resistance than their parent alloys without minor alloying addition. This verified that with the judicious addition of Al, Ti and Mo, lower (Cr+Co) containing alloys can be highly sulfidation resistant.

(13) The modified alloys further verified the previous findings that when Ni/Co base-metal ratio is near unity, the alloy has better sulfidation resistance.

(14) Remarkable sufidation resistance can be obtained by maintaining a Ni/Co base-metal mass ratio near unity and adding minor amounts of Al, Ti and Mo. The

best sulfidation-resistant model Alloy 8 has the composition Ni-22Cr-35Co-2.5Al-2.5Ti-5Mo (in wt.%). This composition represents a major alloy-development result stemming from this study.

(15) The addition of Al and Ti promotes the formation of an oxide-enriched inner layer which serves to inhibit the outward diffusion of base metal elements, thus mitigating the outward sulfidation and internal corrosion.

The individual effect of Ti on sulfidation resistance was also investigated and the conclusions can be drawn as follows.

(16) Titanium content (at least up to 3wt.%) influences the location of the kinetic boundary. With an increase of Ti content, the kinetic boundary moves to the lower oxygen partial pressure. This suggests that the beneficial effect of Ti is to promote sustained formation of the Cr_2O_3 scale.

(17) There is a complex interplay between alloy composition, specifically the relative amount of Ti, and the environment. Ti did not have an obvious effect on sulfidation resistance in Gas 1, while Ti addition exerted a beneficial effect on sufidation behavior in Gases 2 and 3.

(18) Ti promotes the formation of the complex Ti and Cr oxides. The complex oxides suppress the occurrence of sulfidation at the early stage of testing by acting as a barrier that impedes external sulfidation.

Fe-30wt.%Mo-5wt.%Al and Fe-30wt.%Mo-10wt.%Al had better sulfidation resistance than the conventional high-temperature alloys. The conclusions drawn from that study performed in a simulated syngas atmosphere are as follows.

(19) Alloy Fe-30Mo-10Al exhibits excellent sulfidation resistance in the testing gases. The good corrosion resistance was attributed to the formation of a very thin Al_2O_3 layer on the surface of the alloy, identified by XPS analysis.

(20) Alloy Fe-30Mo-5Al showed breakaway behavior in the current study. Al_2O_3 initially nucleated on the surface of ferrite, but a continuous Al_2O_3 scale did not form due to the low Al content.

(21) The composition of the matrix phase, especially the Al content, determines sulfidation resistance. Firstly, a high Al level can help to stabilize the formation of Al_2O_3. Secondly, Al content influences the matrix phase structure. Alloy 10Al has a FCC matrix, while the matrix of 5Al has BCC structure. The FCC structure is preferred. Thirdly, Al in the matrix phase has the effect to block the outward diffusion of iron.

(22) Fe-30Mo-10Al alloys have better sulfidation resistance than Ni-Cr-Co model alloys.

APPENDIX A

GAS PHASE DIFFUSION

When an alloy is put in a gas atmosphere, the oxidation or sulfidation process involves several processes[156]:

I. Transport of oxidant through the gas phase to the specimen surface.

II. Reaction at the surface including adsorption, dissociation, and incorporation into a solid reaction product.

III. Diffusion of anions and/or cations through the reaction product.

IV. Desorption of product gases.

V. Transport of product gases away from the specimen surface.

If step I and V are rate controlling, gas velocity has a substantial effect on the reaction kinetics. When the reacting gas is dilute in the atmosphere, the active gas molecules are rapidly depleted in the gas layers immediately adjacent to the specimen surface. In such a case, boundary-layer diffusion control may occur.

Subsequent reaction can only proceed if the molecule of the active species can diffuse through the boundary layer to the metal surface. The flux across this layer is

$$J_i = -\frac{D_i (P_i' - P_i'')}{RT\delta}$$

P_i' and P_i'' are concentration of the active species at metal surface and in the bulk gas. δ is the thickness of the boundary layer. This represents the maximum possible reaction rate observable. At the beginning of the reaction, the value of $P_i''_i$ is very low and can be neglected giving

$$J_i = -\frac{D_i P_i'}{RT\delta}$$

The reaction rate is thus directly proportional to P_i' , the partial pressure of the active species in the bulk atmosphere. If the boundary layer transport is rate controlling, the reaction rate increases with the increase of the partial pressure of the active species in the gas.

Another way to determine whether the reaction rate is controlled by the boundary diffusion is that the gas flow rate influences the reaction rate. If the gas flow rate increases, the thickness of the boundary layer, δ, decreases, correspondingly, the reaction rate increases.

REFERENCES

1. R.Viswanathan and W.Nakker, *Materials for Ultrasupercritical Coal Power Plants-Turbine Materials: Part II.* Journal of Materials Engineering and Performance, 2001. **10**(1): p. 81

2. R.M.Deacon, J.N.DuPont, and A.R.Marder, *High Temperature Corrosion Resistance of Candidate Nickel-Based Weld Overlay Alloys in a Low NOx Enviroment.* Materals Science and Engineering A, 2007. **460**: p. 392.

3. L. Paul and G. Clark., *Alternate Alloys for Weld Overlay of Boiler Tubes in Low NOx Coal Fired Boilers*, in *EPRI International Conference on Materials and Corrosion Experience for Fossil Plants*2003: Wild Dunes Resort, South Carolina.

4. Lai, G., *Performance of Automatic GMAW Overlays for Waterwall Protection in Coal-Fired Boilers*, in *EPRI Conference on Welding and Repair Technology for Power Plants*2002: Point Clear, Alabama.

5. K.Luer, et al., *Corrosion Fatigue of Alloy 625 Weld Claddings in Combustion Enviroments.* Materials at High Temperature, 2001. **18**(1): p. 11.

6. Cialone, H.J., I.G.Wright, and R.A.Wood, *Circumferential cracking of supercitical boiler water wall tubes*, in *Electric Power Reasearch Institute*, 1986: Palo Alto, CA.

7. F.Gesmundo, *The corrosion of Metallic Materials in Coal Gasification Atmosphere-Analysis of Data from COST 501(Round 1) Gasification Subgroup*, in *Concerted Actions on Materials COST 501 Advanced Materials for Power Engineering Components*March 1991, Comission of the European Communities Institue of Advanced Materials: JRC Petten, The Netherland.

8. Howes, M.A.H., *High Temperature Corrosion in Coal Gasification Systems*, in *Final Report GRI-87101521*987, Gas Research Institute: Chicago.

9. S.K.Verma, *Corrosion of Commercial Alloys in a Laboratory-Simulated Medium-BTU Coal Gasification Enviroment.* Corrosion, 1985. **85**: p. 336.

10. Gleeson, B., *Alloy Degradation Under Oxidizing-Sulfidizing Conditions at Elevated Temperatures.* Materials Research, 2004. **7**(1): p. 61.

11. B.Gleeson, D.L.Douglass, and F.Gesmundo, *Effect of Nb on the High-Temperature Sufidation Behavior of Cobalt.* Oxidation of metals, 1989. **31**(Nos.3/4).

12. S.Mrowec and K. Przybylski, *Transport Properties of Sulfide Scales and Sulfidation of Metals and Alloys.* Oxidation of metals, 1985. **23**(3): p. 107-139.

13. S.Mrowec and K. Przybylski, *Defect and Transport Properties of Sulfides and Sulifidation of Metals.* High Temp.Mater.Proc., 1984. **6**(1-2): p. 1.

14. Lee, B.S. and R.A. Rapp, *Gaseous Sulfidation of Pure Molybdenum at 700-950C.* J.Electrochem.Soc. , 1984. **131**(12): p. 2998.

15. Strafford, K.N., G.R. Winstanley, and J.M. Harrison, Werkst. Korros., 1974. **25**(187-201).

16. B.Gleeson, D.L.Douglass, and F.Gesmundo, *A Comprehensive Investigation of the Sulfidation Behavior of Binary Co-Mo Alloys.* Oxid. Met., 1990. **33**(5-6): p. 425.

17. Chen.M.F., D.L. Douglass, and F. Gesmundo, *High Temperature Sulfidation Behavior of Ni-Nb Alloys.* Oxid. Met., 1989. **31**(3/4): p. 237.

18. Wang, G., R.V. Carter, and D. D.L., *High-Temperature Sulfidation of Fe-Nb Alloys.* Oxid. Met., 1989. **32**(3/4): p. 273.

19. W.Kai, D.L.Douglass, and F.Gesmundo, *The Corrosion of Fe-Mo Alloys in $H_2/H_2O/H_2S$ Atmosphere.* Oxidation of Metals, 1992. **37**(5/6): p. 389.

20. Wang, G., D.L. Douglass, and F. Gesmundo, *High-Temperature Sulfidation of Fe-30Mo Alloys Containing Ternary Additions of Al.* Oxid. Met., 1991. **35**(5/6): p. 349.

21. B.Gleeson, D.L.Douglass, and F.Gesmundo, *The Sulfidation Behavior of Co-Mo Alloys Containing Various Ternary Additions.* Oxid. Met., 1990. **34**(Nos1/2): p. 123.

22. Ciferno, J. and J. Marano, *Benchmarking Biomass Gasification Technologies for Fuels , Chemicals and Hydrogen Production*, June 2002., National Energy Technology Laboratory,.

23. *Hydrogen Separation membranes*, in *Technical Brief*, EERC.

24. *Hydrogen from Coal Program RD&D Plan for the Period 2009 Through 2016*, Sep 2009., U.S.Department of Energy.

25. Hatlevik, O., et al., *Membranes for Hydrogen Separation and Production: History, Fabrication Strategies, and Current Performance.* Separation and Purification Technology, in press. **doi:10.1016/j.seppur.2009.10.020.**

26. Ayturk, M. and Y. Ma, *Electrodeless Pd and Ag Deposition Kinetics of the Composite Pd and Pd/Ag Membranes Synthesized from Agitated Plating Baths.* Journal of Membrane Science, 2009. **330**: p. 233-245.

27. Emerson, S.C., *Experimental Demonstration of Advanced Palladium Membrane Separators for Central High-Purity Hydrogen Production*, in *Progress Report for the DOE Hydrogen Program; DE-FC26-07NT43055;FY2008 Annual*, United Technologies Research Center:: East Hartford, CT.

28. Jack, D., *CO2 Capture and Hydrogen Production in IGCC Power Plants.*, in *Presented at the Gasification Technologies Conference*Oct 2008.: Washington, DC.

29. Balachandran, U., et al., *Hydrogen Separation by Dense Cermet Membranes.* Fuel, 2006. **85**: p. 150-155.

30. Gesmundo, F., D.J.Young, and S.K. Roy, *The High Temperature Corrosion of Metals in Sulfidizing-Oxidizing Enviroments: A Critical Review.* High Temp.Mater. Processes, 1989. **8**(3): p. 149.

31. Stroosnijder, M.F. and W.J. Quadakkers, *Review of High Temperature Corrosion of Metals and Alloys in Sulphidizing and Oxidizing Enviroments. II. Corrrosion of Alloys.* High Temp.Technol., 1986. **4**(3): p. 141.

32. Stringer, J. in *High-Temperature Oxidation and Sulphidation Processes,*. 1990. Pergamon Press,New York.

33. K.Natesan, *High-temperature Corrosion in Coal Gasification Systems.* Corrosion, 1985. **41**(11).

34. A.Roine, *HSC, Chemistry for Windows, Outokumpu Technology*: Finland, www.outokumputechnology.com, accessed Dec 2006.

35. Shatynski, S.R., *The Thermochemistry of Transition Metal Sulfides.* Oxid. Met., 1977. **11**(6): p. 307.

36. Lai, G.Y., *High Temperature Corrosion of Engineering Alloys*1990: ASM International.

37. Perkins, R.A., *Environmental Degradation of High Temperature materials, Series 3.* 1980. **2**(13): p. 5/1.

38. P.L.Hemmings and R.A.Perkin, *Thermodynamic phase Stability Diagrams for the Analysis of Corrosion Reactions in Coal Gasification/Combustion Atmospheres,* , E.R. FP-539, Editor: Lockheed Palo Alto Research Laboratories,Palo Alto,CA,1977.

39. Perkins, R.A. *Design of corrosion resistance alloys and coatings for coal conversion systems* in *Corrosion/Erosion of Coal Conversion Systems Materials Conferences* 1979. Berkeley, California.

40. R.W.Cahn, P.haasen, and E.J. Kramer, Corrosion and Enviromental Degradation 2000. **II**.

41. G.H.Meier, et al. in *Proc. Symp. High-Temperature Corrosion,*. March 1981. Houston,Texas,: National Association of COrrosion Engineers.

42. T.T.Huang, et al., *XPS and AES Studies of the High Temperature Corrosion Mechanism of Fe-30Mo Alloy.* Corrosion Science, 1984. **24**(3): p. 167.

43. C.Zhou, L.W.Hobbs, and G.J.Yurek. *Breakdown of Cr2O3 scales by sulfur*. in *Proceedings of the International Symposium on High-Temperature Oxidation and Sulphidation Processes*. August 1990. Hamilton, Ontario,Canada.

44. S.Mrowec, *The Problem of Sulfur in High-Temperature Corrosion.* Oxid. Met., 1995. **44**(1/2).

45. Heitjans, P. and J. Karger, *Diffusion in condensed matter: Methods, Materials, Models (2nd ed.)*. Karger, J., eds ed2005.

46. Young, D.J., in *High tempearture Oxidation and Corrosion of Metals*First edition, 2008. p. 55.

47. Birks, N., G.H.Meier, and F.S.Pettit, *Introduction to The High-Temperatuer Oxidation of Metals*. 2nd edition ed: Cambridge University Press.

48. A.Atkinson, R.I. Taylor, and A.E.Hughes, *A Quantitative Demonstration of Grain Boundary Diffusion Mechanism for the Oxidation of Metals.* Philosophical Magazine A, 1982. **45**(5): p. 823.

49. Young, D.J., *High Temperature Oxidation and Corrosion of Metals*. ELSEVIER CORROSION SERIES, ed. T. Burstein2008: Department of Materials Science and Metallurgy, University of Cambridge, Cambridge, UK.

50. Fick, A.E., Pogg. Ann., 1855. **94**(59).

51. C. Wagner, Z., Phys. Chem., 1920. **111**(78).

52. Rao, C.N.R. and K.P.R. Pisharody, *Transition Metal Sulfides.* Prog. Sol. State Chem., 1976. **10**(4): p. 207.

53. G.W.Samsonow, S.W.Drozdowa, and Sulfidy, *Metallurgia*1972, Moskwa.

54. L.M.Litz and J.M.Blocker, *High Temperature Materials Technology*, ed. e. J.E. Cambell and E.M. Sherwood. Vol. chap.13. 1968, Wiley,New York.

55. G.W.Samsonow, *Metallurgia*1978, Moskwa.

56. A.Davin and D. Coutsouradis, *Dry Corrosion of Cobalt, Chromium, and Co-Cr, Ni-Cr and Fe-Cr Alloys in Hydrogen Sulphide Atmosphere,.* Cobalt, 1962. **17**(12): p. 23-36.

57. H.Rau, *Range of Homogeneity and Defect Energetics in $Co_{1-x}S$.* Journal of Physics and Chemistry of Solids 1976. **37**(10): p. 931.

58. E.Fryt, W.W.Smeltzer, and J.S. Kirkaldy, *Chemical Diffusion and Point Defect Properties of Iron Sulfide at Temperatures 600-1000^{o}C.* J.Electrochem. Soc., 1979. **126** (4): p. 673.

59. M.Danielewski, S.Mrowec, and A.Stoklosa, *Defect Structure and Diffusion in Nonstoichiometric Ferrous Sulphide.* Solid State Ionics, 1980. **1**(3-4): p. 287.

60. Libowitz, G.G., *Energetics of defect formation and interaction in nonstoichiometric pyrhotite.* Reactivity of Solids 1972 p. 107.

61. Thiel, R.C., *On Interstitials and Vancancies in FeS.* Physca Status Solidi(b), 1970. **40**(1): p. 17.

62. Libowitz, G.G., *Energetics of Defect Formation and Interaction in Nonstoichiometric pyrhotite*. Reactivity of Solids1972, Chapman and Hall,London.

63. H.Rau, *Range of Homogeneity and Defect Interaction in High Temperature Nickel Sulfide $Ni_{1-x}S$.* J.Phys.Chem.Solid, 1975. **36**(11): p. 1199.

64. Brusq, H.L. and J.P.Delmaire, Tev. Inst. Htes. Temp.Refract., 1974. **11**: p. 193.

65. H.Rau, *Defect Enegetics and Range of Homogeneity of a-MnS.* J.Phys.Chem.Solids, 1978. **39**(4): p. 339.

66. K.N.Strafford and A.F.Hampton, *Physico-Chemical Properties of Chromium Sesquisulphide.* J.Mat.Sci., 1973. **8**(11): p. 1534.

67. M.Mikami, K.Igaki, and N.Ohashi, *Electrical and Magnetic Properties of the Chromium Sulfide with Deviation from Stoichiometric Compostion Cr_2S_3.* J.Phys. Soc., Japan, 1972. **32**: p. 1217.

68. P.Kofstad and K.P.Lillerud, *On High Temperature Oxidation of Chromium II. Properties of Cr2O3 and the Oxidation Mechanism of Chromium.* J.Electrochem.Soc., 1980. **127**(11): p. 2410.

69. Kofstad, P. and K.Lillerud, *Chromium Transport through Cr_2O_3 Scales I On Lattice Diffusion of Chromium.* Oxid.Met., 1982. **17**(3-4): p. 177.

70. H.Rau, *Estimation of the Homogeneity Range of MoS_2.* J.Phys.Chem.Solids, 1980. **41**(7): p. 765.

71. Mrowec, S., Oxid. Met., 1995. **44**(Nos.1/2).

72. Mrowec, S., A. Stoklosa, and M. Danielewski, *A New Thermobalance for Studying the Kinetics of High-Temperature Sulfidation of Metals.* Oxidation of Metals, 1977. **11**(6): p. 355.

73. B.Gleeson, *High-Temperature Corrosion of Metallic Alloys and Coatings*, in *Materials Science and Technology A Comprehensive Treatment*, R.W.Cahn, P.haasen, and E.J.Kramer, Editors. 2000, WILEY-VCH.

74. K.Natesan and D.J.Baxter, in *Proc. Conf. on Corrosion-Erosion-Wear of Materials at Elevated Temperatures*, N. A.V. Levy Ed., Editor 1987: Houston.

75. C.M.Packer and R.A.Perkin, in *Conference on Materails to Satisfy the Energy Demand*,, E.B.H.a.A.M. Eds.ASM, Editor 1981: OH. p. 205.

76. C.M.Packer and R.A.Perkin, in *Conf. on Behavior of High Temperature Alloys in Aggressive Enviroments*, J.B.M. I.Kirman, M.Merz, P.R.Sahm, D.P.Whittle Eds. The Metals Soc., Editor 1980: London. p. 813.

77. R.A.Perkin and S.J.Vonk, *Materials Problems in Fluidized-Bed Combustion Systems*, 1979.

78. M.P.Brady, B.Gleeson, and I.G.Wright, *Alloy design strategies for promoting protective oxide-scale formation* JOM Journal of the Minerals, Metals and Materials Society 2000. **52**(1).

79. Mitchell, D.R.G., D.J. Young, and W. Kleeman, *Caburization of Heat-Resistant Steels.* Mater.Corros., 1998. **49**(4): p. 231.

80. Chen, I.C. and D.L. Douglass, *The Internal-Nitriding Behavior of Co-Fe-Al Alloys.* Oxid. Met., 1999. **52** (3-4): p. 195.

81. Giggins, C.S. and F.S. Pettit, *Oxidation of Ni-Cr Alloys Between 800^{o} and 1200^{o}C.* Transaction of the Metallurgical Society of AIME, 1969. **245**: p. 2495-2507.

82. Pint, B.A., J. Leibowitz, and J.H. DeVan, *The Effect of an Oxide dispersion on the Critical Al Content in Fe-Al Alloys.* Oxid. Met., , 1999. **51**(1-2): p. 181.

83. Seltzer, M.S. and B.A. Wilcox, *Diffusion of Chromium and Alumium in Ni-20Cr and TDNiCr(Ni-20Cr-2THO$_2$)* Metall. Trans., 1972. **3**: p. 2357.

84. Desforges, C.D., Rev. Int. Hautes Temp. et Refract., 1977. **14**(28).

85. S.Mrowec and T.Werber, *Gas Corrosion of Metals*, in *Mat. Bureau of Standard*1978: Warsaw.

86. T.Biegun, A.Bruckman, and S. Mrowec, *High-Temperature Sulfide Corrosion of Cobalt-Chromium Alloys.* Oxid. Met., 1978. **12**(2): p. 157.

87. Mrowec, S., T.Werber, and M.Zastawnik, *The Mechanism of High Temperature Sulfur Corrosion of Nickel-Chromium Alloys.* Corr. Sci., 1966. **6**(2): p. 47.

88. D.P.Whittle, S.K.Verma, and J.Stringer, *Effect of Chromium Content on the Sulfidation Behavior of Co-Cr Alloys in H_2/H_2S Mixtures.* Corr. Sci., 1973. **13**(4): p. 247.

89. Mrowec, S., T.Walec, and T.Werber, *High Temperature Sulfur Corrosion of Iron-Chromium Alloys.* Oxid. Met., 1969. **1**(1): p. 93.

90. T.Narita and K.Nishida, *On the High-Temperature Corrosion of Fe-Cr Alloys in Sulfur Vapor.* Oxid. Met., 1973. **6**(3): p. 157.

91. T.Narita, W.W.Smeltzer, and K.Nishida, *Sulfidation Properties of Fe-Cr Alloys at 1073K in H_2S-H_2 Atmospheres of Sulfur Pressure 10^{-2} and 10^{-5} Pa.* Oxid. Met., 1982. **17**(299).

92. A.Davin and D.Coutsouradis, Cobalt, 1962. **17**: p. 23.

93. S.K.Verma, D.P.Whittle, and J.Stringer, *Sulfidation of Cobalt-based Alloys.* Corr. Sci., 1972. **12**: p. 545-554.

94. Blough, J.L., V.L.Hill, and B.A. Humphreys, *The Properties and Performance of Materials in the Coal Gasification Enviroment.* American Society For Metals, 1981: p. 225.

95. M.A.H.Howes, *High Temperature Corrosion in Coal Gasification System*, F.R. GRI-8710152, Editor Aug 1987, Gas reasearch Institute, Chicago.

96. Nagarajan, V., R.G. Miner, and A.V. Levy, *The Role of Silicon Additions in the Corrosion Resistance of Chromium-Forming Alloys in Coal Gasification Atmospheres.* J. Electrochem. Soc., 1982. **129**(4): p. 782.

97. K.Natesan, in *ASM Metal Congress*October10-16, 1987: Cincinnati,OH.

98. Grabke, H.J., J.F. Norto, and F.G. Casteels. in *Conf.on High temperature Alloys for Gas Turbines and Other Applications*. 1986. Dordrecht: D.Reidel Pub.Co.

99. G.Y.Lai, *Sulfidation-resistance of Co-Cr-Ni Alloy with Critical Content of Silicon and Cobalt. US. Patent 47,117,63*.

100. Azaroff, L.V., *Role of Crystal Structure in Diffusion. II. Activation Energies for Diffusion in Closest-Packed Structures.* J Appl Phys, 1961. **32**(9): p. 1663.

101. Cox.M.G.C., McEnancy.B, and V.D. Scott, *A Chemical Diffusion Model for Partitioning of Transition Elements in Oxide Scales on Alloys.* Phil.Mag, 1972. **26**(4): p. 839.

102. R.A.Perkin, W.C. Coons, and S.J.Vonk, Rep.EPRI-CS-2452, 1982.

103. Perkins, R.A. in *Proc 3rd Ann Conf on Materials for Coal Conversion and Utilization*. 1978. Gaithersburgh,USA.

104. R.A.Perkins, W.C. Coons, and S.J. Vonk, *Materials Problems in Fluidized-bed Combustion and Coal Gasification Systems*, R. EPRI-CS-2452, Editor 1982.

105. R.W.Bradshaw and R.E.stoltz, in *Corrosion-Erosion in Coal Conversion System Materials*1979, A.V. Levy Ed.

106. T.C.Tiearney and K.Natesan, *Sulfidation-Oxidation of Advanced Metallic Materials in Simulated Low-Btu Coal-Gasifier Enviroments.* Oxid.Met., 1982. **17**(1-2): p. 1.

107. R.W.Bradshaw, R.E.stoltz, and D.R.Adolphson, *Report SAND77-8277,Sandia Laboratories*, 1977: Livermore,CA.

108. K.Natesan. in *Corrosion-Erosion in Coal Conversion System Materials*. 1979. Houston: A.V. Levy Ed.,NACE.

109. D.J.Baxter and K.Natesan. in *9th Intern.Congr. on Metallic Corrosion*. 1984. NRC Canada,Ottawa.

110. H.J. Grabke, J.F. Norton, and F.G. Casteels. in *High temperature Alloys for Gas Turbines and Other Applications*. 1986. Dordrecht: D.Reidel Pub.Co.

111. R.G.Dickinson and L.Pauling, *The Crystal Structure of Molybdenite.* J.Am.Chem.Soc., 1923. **45**: p. 1466.

112. Kibsgaard, J., in *Interdisciplinary Nanoscience Center(iNANO), and Department of Physics and Astronamy*2008, University of AARHUS.

113. M.F.Chen and D. D.L., *Effect of Some Ternary Additions on the Sulfidation of Ni-Mo Alloys.* Oxid. Met., 1990. **33**(1-2): p. 103.

114. W.Kai and Douglass, *The High-Temperature Corrosion Behavior of Fe-Mo-Al Alloys in $H_2/H_2O/H_2S$ Mixed -Gas Enviroments.* Oxidation of Metals, 1993. **39**(3/4): p. 281.

115. Sims, C.T., *Superalloys*1987, New York, USA.

116. W., E. and C.T. Sims, *Ni-based Alloys*, in *Superalloys II*1987, A Wiley-Interscience Publication.

117. Weronski, A. and T. Hejwowski, *Thermal Fatigue of Metals*1991, New York: Marcel Dekker, Inc.

118. Mrowec, S. and K.Przybylski, High Temp.Mater. Processes 1984. **6**: p. 1.

119. G.Y.Lai, *High Temperature Corrosion and Materials Applications*2007.

120. Hiroshi Yakuwa, et al., *Development of a sulfidation-corrosion resistant Ni-based superalloy for FCC Power Recovery Turbine Rotors*, in *Proceedings of the 27th Turbomachinery Symposium*1998.

121. Kneeshaw, J.A., I.A. Menzies, and J.F.Norton, *Factors Influencing the Performance of a Cr-Ni-Fe Alloy Exposed to Sulfidising/Oxidising/Carburising Environments at 800°C.* Werkstoffe Und. Korrosion 1987. **38**: p. 473.

122. M.Benlyamani, F. Ajersch, and G. Kennedy. in *Proceedings of the Symposium on High Tempearuter Materials Chemistry-IV*. 1988. Pennington, NJ The Electochem. Soc. Inc.

123. F.Gesmundo, D.J.Young, and S.K.Roy, *The High Temperature Corrosion of Metals in Sulfidizing-Oxidizing Enviroments:A Critical Review*. High Temp.Mater. Processes, 1989. **8**(3).

124. A.Bruckman, *The Mechanism of Transport of Matter Through the Scales During Oxidation of Metals and Alloys.* Corr.Sci., 1967. **7**(1): p. 51.

125. S.Mrowec, *On the Mechanism of High Temperature Oxidation of Metals and Alloys.* Corro.Sci., 1967. **7**(9): p. 563.

126. Kofstad, P., *On the Formation of Porosity and Microchannels in Growing Scales.* Oxid. Met., 1985. **24**(5/6): p. 265.

127. Jackson, K.A., *Kinetic Process*2004, WILEY-VEC Verlag CmbH&Co. KGaA, Weinheim.

128. Lillerud, K.P., B.Haflan, and P.Kofstad, *On the Reaction Mechanism of Nickel with SO2+O2/SO3.* Oxid. Met., 1984. **21**(3/4): p. 119.

129. J.P.Orchard and D.J.Young, *Morphological Evolution During Sulfidation of an Iron-Nickel Alloys.* Oxidation of Metals, 1989. **31** (1-2): p. 105.

130. Winn, E.B., *The Temperature dependence of the Self-Diffusion Coefficients of Argon, Neon, Nitrogen, Oxygen, Carbon Dioxide and Methane.* Physical Review, 1950. **80**(6): p. 1024.

131. Chen, N.H., *New Generalized Equation for Gas Diffusion Coefficient.* Journal of Chemical and Engineering Data, 1962. **7**(1): p. 37.

132. M., B., Encyclopedia of Chemical Technology, 1949. **5**(88).

133. G.M.Raynaud and R.A.Rapp, *In Situ Observation of Whiskers, Pyramids and Pits During the High-Temperature Oxidation of Metals.* oxid.Met., 1984. **21**(1-2): p. 89.

134. M.W.Barsoum, et al., *Driving Force and Mechanism for Spontaneous Metal Whisker Formation.* Phys.Rev. Lett. 93,20614(2004), 2004.

135. Pilling, N.B. and R.E. Bedworth, J. Inst. Met., 1923. **29**: p. 529.

136. Twiss, R.J. and E.M. Moores, *Structural Geology*.

137. A.G.Evans and T.G. Langdon, Progr.Mat.Sci., 1976. **21**(177).

138. *Physical Metallrugy*. Fourth,Revised and Enhanced ed. Vol. II Chapter 13, Interficial and Surface Microchemistry. 1996.

139. N.Birks, G.H. Meier, and F.S. Pettit, *Introduction to the High-Temperature Oxidation of Metals*. 2nd Edition ed2006.

140. A.Bruckman and J.Romanski, *On the Mechanism of Sulfide Scale Formaton on Iron.* Corrion Science, 1965. **5**(3): p. 185.

141. Harper, M.A. and J.O.Cotner, *Mixed Sulfidation/Carburization Attack on Several Heat-Resistant.* Oxidation of Metals, 2000. **53**(5-6): p. 427.

142. Cheng Fang, H.Y., Matsuho Miyasaka, Toshio Narita, *Sulfidation Properties of Ni-20Cr and Ni-13.5Co-20Cr Alloys at 873K under Low Sulfur Pressures in H2S-H2 Atmospheres.* Oxid. Met., 2000. **53**(Nos.5/6): p. 597.

143. K.N.Strafford, *The Sulfidation of Metals and Alloys.* Metallrugical Rev., 1969. **14**(1): p. 153.

144. C.S.Giggins and F.S.Pettit, *Oxidation of Ni-Cr-Al Alloys Between 1000^{o} and 1200^{o}C Solid State Science-Techical Papers.* J.Electrochem.Soc., 1971. **118**(11): p. 1782.

145. D.J.Young, W.W.Smeltzer, and J.S.Kirkaldy, *The Effects of Molybdenum Addition to Nickel-Chromium Alloys on Their Sulfidation Properties.* Metallrugical Transactions A, 1975. **64**(June): p. 1205-1215.

146. S.Somiya, S.Hirano, and S.Kamiya, J.Sol.State. Chem., 1978. **25**(273).

147. W.Lee, Deut. Keram.Gesell.Ber., 1970. **47**(169).

148. C.R.wang, W.O.Zhang, and R.Z.Zhu, *High-Temperature Corrosion of Titanium-,Niobium-, and Manganese-Rich Fe-25Cr Alloys in H2-H2O-H2S Gas Mixtures.* Oxidation of metals, 1990. **33**(1/2): p. 55.

149. Nagelberg, A.S. and R.W.Bradshaw, *Chemical Characterizaiton of Complex Oxide Products on Titanium-Enriched 310SS.* J. Electrochem. Soc., 1981. **128**(12): p. 2655-2650.

150. Yuzheng Guo, S.J. Clark, and J. Robertson, *Electronic and Magnetic Properties of Ti_2O_3,Cr_2O_3, and Fe_2O_3 Calculated by the Screened Exchang Hybid Density Functional* J.Phys. Condens., 2012. **24**(32): p. 8.

151. Newnham, R.E. and Y.M.d. Haan, *Refinement of the α Al2O3, Ti2O3, V2O3 and Cr2O3 structures.* Zeitschrift für Kristallographie - Crystalline Materials, 1962. **117**(No. 2-3): p. 235-237.

152. Chosh, G., *Aluminium-Iron-Molybdenum.* MSIT.

153. Ghosh, G., *Aluminium-Iron-Molybedenum*, in *Landolt-Börnstein - Group IV Physical Chemistry*2008, Springer-Verlag Berlin Heidelberg. p. 96.

154. Habazaki, H., et al., *The sulfidation and Oxidation Behaviour of Sputter-Deposit Amorphous Al-Mo Alloys at High Tempearture.* Corr. Sci., 1993. **34**: p. 183.

155. Chen, Y., D.J.Young, and S.Blairs, *High-Temperature Sulfidation Behavior of Fe-Mo-Mn-Al Alloys.* Oxid. Met., 1993. **40**(Nos.5/6): p. 433.

156. G.H.Meier, F.S.Pettit, and N.Birks. *Interactive mechanism in the high-temperature oxidation of metals*. in *Proceedings of the International Symposum on High-Temperature Oxidation and Sulphidation Process,*. August 1990. Hamilton,Ontratia,Canada.